MODELING AND SIMULATION OF SILICON CARBIDE BASED MICROELECTROMECHANICAL ULTRASONIC TRANSDUCER

THIS THESIS IS SUBMITTED IN PARTIAL FULFILLMENT OF THE REQUIREMENTS FOR THE DEGREE OF DOCTOR OF PHILOSOPHY

MOUMITA PAL

MZU REGN NO : 1800283

PH. D REGN NO : MZU/PH.D/1288 OF 16.08.2018

DEPT. OF ELECTRONICS & COMMUNICATION ENGINEERING
SCHOOL OF ENGINEERING AND TECHNOLOGY

SEPTEMBER 2021

MODELING AND SIMULATION OF SILICON CARBIDE BASED MICROELECTROMECHANICAL ULTRASONIC TRANSDUCER

BY

MOUMITA PAL
Department of Electronics & Communication Engineering

Name of Supervisor : Dr. Reshmi Maity

Submitted

In partial fulfillment of the requirement of the Degree of Doctor of Philosophy in Electronics & Communication Engineering of Mizoram University, Aizawl

Department of Electronics And Communication Engineering
School of Engineering and Technology
MIZORAM UNIVERSITY
(*A Central University*)
Tanhril**,** Aizawl - 796 004, Mizoram

CERTIFICATE

This is to certify that the thesis entitled **"Modeling and Simulation of Silicon Carbide Based Microelectromechanical Ultrasonic Transducer"** submitted to Mizoram University for the award of the degree of **Doctor of Philosophy Electronics and Communication Engineering** by **Moumita Pal**, Ph.D Registration No. **MZU/Ph.D/1288 of 16.08.2018**, is Ph.D scholar in the Department of Electronics and Communication, under my guidance and supervision and has not been previously submitted for the award of any degree in any Indian or foreign University. She has fulfilled all criteria prescribed by the UGC (Minimum Standard and Procedure governing Ph.D. Regulations). She has fulfilled the mandatory publication (Publication enclosed) and completed Ph.D. course work. It is also certified that the scholar has been admitted in the Department through an entrance test, followed by an interview as per UGC Regulation of 2016.

Date: September, 2021
Place: Aizawl

(Dr. Reshmi Maity)
Supervisor

MIZORAM UNIVERSITY
Aizawl - 796 004

September 2021

DECLARATION

I, **Moumita Pal**, hereby declare that the subject matter of this thesis entitled "**Modeling and Simulation of Silicon Carbide Based Microelectromechanical Ultrasonic Transducer**" is the record of work done by me, that the contents of this thesis did not form basis of the award of any previous degree to me or to do the best of my knowledge to anybody else, and that the thesis has not been submitted by me for any research degree in any other University/Institute.

This is being submitted to the Mizoram University for the degree of Doctor of Philosophy in **Electronics and Communication Engineering**.

Date:

(Moumita Pal)
Candidate

(Dr. Reshmi Maity)
Supervisor

(Dr. Niladri Pratap Maity)
Head of the Department
Electronics and Communication Engineering

Acknowledgement

At the outset, I am grateful to the almighty God for his blessing that had lead me successfully to the end of my work. I wish to express my heartfelt gratitude to my supervisor and mentor **Dr. Reshmi Maity**, for her constant support, guidance, encouragement and patience throughout my research work. I am also thankful to **Dr. N. P. Maity**, the Head of Department of Electronic and Communication for extending all the facilities. Also, I am thankful to all the faculties and technical staff for their help, support and kind cooperation.

I would like to express my deepest gratitude to Dr. Indranath Sarkar, Associate Professor, JIS college of Engineering and colleagues of JIS College of Engineering for their kind support, without whom, this work would not have been possible.

I owe my gratitude to Ranjana Ray, Munmun Pramanik for providing opportunity, constant support due to which I was able to manage my responsibilities in the institution and simultaneously completing my Ph.D. I am deeply thankful to Himeli Chakrobarti for her suggestions, and encouragements, which helped me to conduct my research from various aspects.

Also, I would like to thank my parents Sitaram Pal and Sipra Pal, my daughter Shouraseni Saha, my husband Dr. Sirsanu Saha for their constant support, motivation, love and prayers. Last but not the least; I place on record, my sense of gratitude to one and all who, directly or indirectly, have lent their helping hand in this venture.

MOUMITA PAL

Table of Contents

Contents	**Page No.**
Acknowledgment	(i)
Table of Contents	(ii) – (iv)
List of Figures	(v) –(xiii)
List of Tables	(xiv)
List of Abbreviations	(xv-xvi)
Chapter 1 Introduction	
1.1 Micro Electro Mechanical Systems	1
1.1.1 Elements of MEMS	1-2
1.1.2 Application of MEMS	3
1.2 Micro machined Ultrasonic Transducer	3-4
1.2.1 Types of MUT	4-6
1.2.2 Competency of CMUT over PZT transducer	6-7
1.3 Operating principles of CMUT	7-8
1.4 Scope of the study	9-10
1.5 Preface to thesis	10-12
References	13-15
Chapter 2 CMUT- A Review	
2.1 Brief overview of CMUT	16-18
2.2 Fabrication technology engaged in CMUT design	18
2.2.1 Fabrication using surface micromachining	18-19
2.2.2 Fabrication using wafer bonding	19
2.2.3 Fabrication by bulk micromachining	20
2.3 Review on usage of various membrane materials	20-22
2.4 Review on structures developed using SiC	22-23
2.5 Various Geometrical shape of CMUT membrane	24-25
2.6 Application of CMUT	25-27
2.7 Study of various CMUT parameters	28-30
References	31-44
Chapter 3 Device Capacitance	
3.1 Introduction	45
3.1.1 Transducer capacitive action	45-46
3.1.2. Various geometrical structures	46-47
3.1.3 Silicon Carbide (SiC) as structural material	47
3.1.4 Inclusion of insulation layer	47-48
3.1.5 High-K material as insulation layer	48-49
3.2 Effect of fringing fields	49
3.3 Improved capacitance modeling of an non-insulated element	50-51
3.4 FEM Simulation	52
3.5 Comparative analysis of Si_3N_4 / SiC actuation layers	53-56
3.6 Device capacitance comparison between insulated and non-insulated structure	56-57
3.6.1 Excellence of SiC based insulated CMUT	57-58
3.6.2 Si_3N_4 insulated structure with SiC actuation layer	58-59

	3.6.3 Competency of insulated structure over non-insulated cell	59-61
3.7	Analysis of cavity and insulation layer capacitances of insulated CMUT	61-62
3.8	Analysis of fringing effects in an insulated CMUT	63-67
3.9	Investigation of effect of Hafnium oxide material as the insulation layer	67-69
3.10	Summary	69-70
References		71-74

Chapter 4 Electrostatic Force

4.1	Operating principle of CMUT as electrostatic actuator	75-76
	4.1.1 Electrostatic transduction of capacitive element	76
4.2	Background survey of modeling of electrostatic actuation	76-77
4.3	Analytical force model of non-insulated element	77-80
	4.3.1 FEM Simulation	80
	4.3.2 Comparative analysis of static electrostatic force in Si_3N_4/ SiC actuation layer based non-insulated cell	81-85
4.4	Si_3N_4 insulated structure with SiC actuation layer	85
	4.4.1 Analytical force model of insulated element	85-86
	4.4.2 Enhancement of Electrostatic force in insulated structure	86-88
	4.4.3 Significance of fringing in insulated CMUT	88-93
4.5	Effect of HfO_2 as insulating material upon electrostatic force generation	94-97
4.6	Summary	98
References		99-101

Chapter 5 Displacement Profile

5.1	Introduction	102
5.2	Actuation layer deflection of a non-insulated CMUT using plate model	102
	5.2.1 Analytical modeling of plate deflection profile	103-108
	5.2.2 Analysis of plate deflection in non-insulated structure	109-110
5.3	Actuation layer deflection of a non-insulated CMUT using membrane model	110-111
	5.3.1 Analysis of membrane deflection in non-insulated structure using Mason's analysis	111-114
	5.3.2 FEM Simulation	114-116
	5.3.3 Comparative study between plate and actuation layer displacement for Si_3N_4 / SiC actuation layer based non-insulated cell	116-117
	5.3.4 Effect of fringing in Si_3N_4 / SiC actuation layer based non-insulated cell	117-120
5.4	Displacement profile analysis of insulated cell	121
	5.4.1 Analytical force model of insulated element	121-122
	5.4.2 Enhancement of displacement profile in insulated structure	122-125
	5.4.3 Analysis of fringing effect in insulated CMUT	125-130
5.5	Influence of HfO_2 upon actuation layer displacement	130-134

Table of Contents

5.6 Summary 134
References 135-136

Chapter 6 Collapse Voltage and Coupling Factor
6.1 Introduction 137
6.2 Significance of collapse voltage 138
6.3 Electro-mechanical Model of a CMUT element 138-139
6.3.1 Analytical modeling of collapse voltage 139-142
6.3.2 Effect of various structural parameters upon collapse voltage 142-144
6.4 Analytical modeling of collapse voltage with fringing field effect 145-147
6.4.1Analysis of fringing effect upon collapse voltage 148-149
6.5 Coupling Coefficient 149-150
6.5.1 Variation of coupling factor under influence of structural parameters 151-153
6.6 Influence of HfO_2 upon collapse voltage and coupling factor 153-157
6.7 Summary 158
References 159-160

Chapter 7 Frequency Response and Mechanical Impedance
7.1 Introduction 161-162
7.2 Analytical modeling of frequency and impedance response using Mason's Circular membrane Model 162-164
7.3 Analysis of Resonance Frequency Response Profile 165-167
7.4 Analytical modeling of Mechanical Impedance 167-169
7.5 Analysis of dynamic response and mechanical impedance under the influence of various structural parameters 169-176
7.6 Summary 177
References 178-180

Chapter 8 Conclusion and Future Work
8.1 Conclusion 181-184
8.2 Future Work 184-185

List of Publications 186-187
Brief Bio-data of candidate 188
Particulars of the candidate 189

List of Figures

Figure No.	Figure Description	Page no.
Fig. 1.1	Components of MEMS	2
Fig. 1.2	Application of MEMS	2
Fig. 1.3	Frequency range of ultrasound wave	4
Fig. 1.4	Schematic diagram of PMUT	5
Fig. 1.5	Schematic diagram of CMUT	5
Fig. 1.6	CMUT in transmitting mode	8
Fig. 1.7	CMUT in receiving mode	8
Fig. 2.1	Surface micromachining process	18
Fig. 2.2	Various wafer bonding techniques	20
Fig. 2.3	Fringing field lines in the air gap and insulator capacitors	21
Fig. 2.4	Various geometrical shapes of CMUT	24
Fig. 3.1	3D view of circular non-insulated cell	45
Fig. 3.2 (a)	Insulated Structure	48
Fig. 3.2 (b)	Non-insulated Structure	48
Fig. 3.3	FEM model Structure	52
Fig. 3.4	Device capacitance due to change in electrode radius	53
Fig. 3.5	E_C for varying electrode radius	54
Fig. 3.6	E_{SiC} for varying electrode radius	54
Fig. 3.7	Device capacitance due to change in air gap separation	55
Fig. 3.8	E_C for varying air gap separation	55
Fig. 3.9	E_{SiC} for varying air gap separation	55
Fig. 3.10	Device capacitance and thickness of actuation layer thickness	56
Fig. 3.11	E_C for varying actuation layer thickness	56
Fig. 3.12	E_{SiC} for varying actuation layer thickness	56
Fig. 3.13	Device capacitance variation with electrode radius	60
Fig. 3.14	Enhancement of device capacitance with electrode radius	60
Fig. 3.15	Device capacitance with variation of gap thickness	60
Fig. 3.16	Enhancement of device capacitance with gap thickness	60
Fig. 3.17	Comparison of capacitance due to variation of gap thickness	61
Fig. 3.18	Comparison of capacitance due to variation of electrode radius	61

List of Figures

Fig. 3.19	Variation of capacitance with gap thickness	62
Fig. 3.20	Variation of capacitance with Insulator thickness	62
Fig . 3.21	Variation of capacitance with electrode radius	62
Fig. 3.22	Variation of capacitance with various dielectric material	62
Fig. 3.23	E_K for various dielectric material	63
Fig. 3.24	Device capacitance variation with electrode radius	64
Fig. 3.25	Percentage of enhancement in capacitance due to fringing	64
Fig. 3.26	Device capacitance with varying gap	65
Fig. 3.27	Enhancement in capacitance with respect to gap thickness	65
Fig. 3.28	Variation of device capacitance with insulation thickness	65
Fig. 3.29	Enhancement in capacitance with respect to insulation thickness	65
Fig. 3.30	Variation of capacitance due to change in various dielectric material	66
Fig. 3.31	E'_C with respect to relative dielectric constant for various electrode radius	66
Fig. 3.32	Variation of capacitance due to change in various dielectric material	67
Fig. 3.33	The device capacitance for varying electrode radius for the same input pulse between HfO_2 vs. Si_3N_4 isolation for various HfO_2 thickness	68
Fig. 3.34	A plot of the device capacitance for varying Gap thickness	68
Fig. 3.35	A plot of the device capacitance for various dielectric material	69
Fig. 3.36	A plot of the device capacitance with insulation thickness	69
Fig. 4.1	2D model of biased actuation layer vibration in circular CMUT	75
Fig. 4.2	Electric potential profile	81
Fig. 4.3	Electrostatic force due to variation in electrode radius	82
Fig. 4.4	E_F for varying electrode radius	82
Fig. 4.5	E_{F_SiC} for varying electrode radius	82
Fig. 4.6	Variation of electrostatic force for varying air gap	83
Fig. 4.7	E_F for varying air gap	83
Fig. 4.8	E_{F_SiC} for varying air gap	83
Fig. 4.9	Variation of electrostatic force for varying thickness of actuation layer	84

List of Figures

Fig. 4.10	E_F for varying actuation layer thickness	84
Fig. 4.11	E_{F_SiC} for varying actuation layer thickness	84
Fig. 4.12	Variation of electrostatic force for varying bias	85
Fig. 4.13	E_F for varying bias	85
Fig. 4.14	E_{F_SiC} for varying bias	85
Fig. 4.15	2D structure of insulated CMUT	86
Fig. 4.16	Comparative analysis of electrostatic force with varying electrode radius	87
Fig. 4.17	$E_i^{'}$ for varying electrode radius	87
Fig. 4.18	Comparative analysis of electrostatic force due to variation of gap thickness	87
Fig. 4.19	$E_i^{'}$ for varying gap thickness	87
Fig. 4.20	Electrostatic force variation with electrode radius for a) t_g =450 nm, t_i =500 nm b) t_g =650 nm, t_i =300 nm c) t_g =300 nm, t_i =650 nm	89
Fig. 4.21	$E_F^{'}$ with varying electrode radius for a) t_g =450 nm, t_i =500 nm b) t_g =650 nm, t_i =300 nm c) t_g =300 nm, t_i =650 nm	89
Fig. 4.22	Electrostatic force for varying insulation thickness	89
Fig. 4.23	$E_F^{'}$ for varying insulation thickness	89
Fig. 4.24	Electrostatic force with material permittivity	90
Fig. 4.25	$E_F^{'}$ for varying material permittivity	90
Fig. 4.26	Variation of force due to simultaneous change in electrode radius and insulation thickness	91
Fig. 4.27	Variation of force due to simultaneous change in electrode radius and dielectric constant	91
Fig. 4.28	Variation of electrostatic force due to change in various dielectric material	92
Fig. 4.29	Variation of electrostatic force due to change in insulation thickness for a) r_e =55 µm, t_g =450 nm b) r_e =27.5µm t_g =300 nm	92
Fig. 4.30	Electrostatic force vs Gap thickness	92
Fig. 4.31	$E_F^{'}$ for varying cavity height	92

List of Figures

Fig. 4.32	Electrostatic force with changing bias	93
Fig. 4.33	$E_F^{'}$ for varying material for varying bias	93
Fig. 4.34	Variation of force due to simultaneous change in r_e and bias	93
Fig. 4.35	Variation of force due to simultaneous change in r_e & t_g	93
Fig. 4.36	Comparative analysis of electrostatic force for HfO_2/Si_3N_4 isolation	94
Fig. 4.37	Gain of electrostatic force (R) for HfO_2/Si_3N_4 isolation	94
Fig. 4.38	$E_{HfO_2}^{'}$ for variation in gap thickness	95
Fig. 4.39	Effect of high-k on electrostatic force due to change in electrode radius	96
Fig. 4.40	$E_{HfO_2}^{'}$ for variation in Electrode radius	96
Fig. 4.41	Comparative study of electrostatic force for varying dielectric material	96
Fig. 4.42	Enhancement with respect to 500 nm thickness	96
Fig. 4.43	Comparative study electrostatic force due to change in insulation thickness	97
Fig. 4.44	Enhancement of force for varying insulation thickness	97
Fig. 4.45	Comparison electrostatic force for change in bias voltage between HfO_2 Vs. Si_3N_4 isolation for various HfO_2 thickness	97
Fig. 5.1	Bending of plate due to uniform loading	103
Fig. 5.2	Bending moment of plate element abcd	104
Fig. 5.3	Deflection with change in actuation layer radius for a) t_g =500 nm b) t_g =350 nm	109
Fig. 5.4	Deflection with change in thickness of actuation layer for a) t_g =500 nm b) t_g =350 nm	109
Fig. 5.5	Deflection with change in bias voltage for a) a_e =25 μm b) a_e =12.5 μm	110
Fig. 5.6	Deflection with change in radial distance for a) V_{dc}=40 V b) V_{dc} =20 V	110
Fig. 5.7	FEM models of dissimilar membrane profile	115
Fig. 5.8	FEM model magnitude distribution of the proposed structures	115
Fig. 5.9	CMUT with circular shape model	115

List of Figures

Fig. 5.10	Isometric view of the meshed geometry	116
Fig. 5.11	Displacement profile of the simulated geometry	116
Fig. 5.12	Displacement with changing actuation layer radius	117
Fig. 5.13	Displacement with increasing radial distance	117
Fig. 5.14	Displacement with changing cavity height	117
Fig. 5.15	Displacement with changing actuation layer thickness	117
Fig. 5.16	Actuation layer displacement due to variation in actuation layer radius	118
Fig. 5.17	E_m for varying actuation layer radius	119
Fig. 5.18	E_{m_SiC} for varying actuation layer radius	119
Fig. 5.19	Actuation layer displacement due to variation in cavity gap	119
Fig. 5.20	E_m for varying cavity gap	120
Fig. 5.21	E_{m_SiC} for varying cavity gap	120
Fig. 5.22	Actuation layer displacement due to variation in actuation layer thickness	120
Fig. 5.23	E_m for varying actuation layer thickness	121
Fig. 5.24	E_{m_SiC} for varying actuation layer thickness	121
Fig. 5.25	Actuation layer displacement due to variation in bias	121
Fig. 5.26	E_m for varying bias	121
Fig. 5.27	Comparative analysis of actuation layer displacement due to variation of actuation layer thickness	123
Fig. 5.28	Enhancement in displacement for the variation of gap thickness	123
Fig. 5.29	Comparative analysis of actuation layer displacement due to variation of actuation layer radius	123
Fig. 5.30	Enhancement in displacement for the variation of actuation layer radius	123
Fig. 5.31	Comparative analysis of actuation layer displacement due to variation of bias voltage	124
Fig. 5.32	Comparative analysis of actuation layer displacement due to variation of actuation layer thickness	124
Fig. 5.33	Comparison between % enhancement in displacement	124
Fig. 5.34	Actuation layer displacement for varying actuation layer radius a) t_a =2 μm b) t_a =1 μm c) t_a =0.5 μm	126
Fig. 5.35	E'_m for varying actuation layer radius	126
Fig. 5.36	Actuation layer displacement for varying air gap for a) t_i =500 nm b) t_i =350 nm c) t_i =750 nm	126
Fig. 5.37	E'_m for varying air gap	126

List of Figures

Fig. 5.38	Displacement for varying relative dielectric constant for a) V_{dc} =40 V b) a) V_{dc} =20 V c) V_{dc} =60 V	127
Fig. 5.39	E'_m with respect to various relative dielectric constant	127
Fig. 5.40	Displacement for varying insulation thickness for a) r_a =55 μm, t_g =450 nm b) r_a =27.5 μm, t_g =300 nm c) r_a =65 μm, t_g =600 nm	128
Fig. 5.41	E'_m for variation in insulation thickness	128
Fig. 5.42	Variation of displacement with simultaneous change in r_a and K	129
Fig. 5.43	Variation of displacement with simultaneous variation in r_a and t_i	129
Fig. 5.44	Variation of displacement with simultaneous change in r_a and V_{dc}	130
Fig. 5.45	Comparative analysis of displacement with actuation layer radius for HfO_2 and Si_3N_4 insulation	131
Fig. 5.46	E''_{hfo2} with changing actuation layer radius for varying actuation layer thickness	131
Fig. 5.47	Comparative analysis of displacement with air gap for HfO_2 and Si_3N_4 insulation	131
Fig. 5.48	E''_{hfo2} for varying air gap	131
Fig. 5.49	Comparative analysis of displacement for varying relative dielectric constant with different insulation thickness	132
Fig. 5.50	Comparative analysis of displacement profile for HfO_2 and Si_3N_4 insulation	132
Fig. 5.51	Comparative analysis of displacement for change in bias between Si_3N_4 isolation and HfO_2 of various thickness	133
Fig. 5.52	E''_{hfo2} for varying bias	133
Fig. 6.1	Schematic diagram of CMUT at collapse condition	138
Fig. 6.2	First order lumped electro-mechanical model of CMUT	139
Fig. 6.3	Variation of collapse voltage and spring constant for various actuation layer Radius	143
Fig. 6.4	Variation of collapse voltage for changing electrode radius due to different values of actuation layer thickness	143
Fig. 6.5	Variation of spring constant and Collapse Voltage for changing actuation layer Thickness	144
Fig. 6.6	Variation of Collapse Voltage for changing actuation layer Thickness due to different values of actuation layer Radius	144
Fig. 6.7	Variation of Collapse Voltage for change in insulator	145

List of Figures

	thickness due to different values of actuation layer radius	
Fig. 6.8	Variation of Collapse Voltage for changing gap Thickness due to different values of actuation layer radius	145
Fig. 6.9	Variation of Collapse Voltage for changing actuation layer Radius for different values of actuation layer thickness	148
Fig. 6.10	Variation of Collapse Voltage for changing insulation thickness for different values of actuation layer radius	148
Fig. 6.11	Variation of Collapse Voltage for changing actuation layer thickness for different values of actuation layer radius	149
Fig. 6.12	Variation of Collapse Voltage for changing gap thickness for different values of actuation layer radius	149
Fig. 6.13	CMUT equivalent model in the transmitting mode	149
Fig. 6.14	Coupling factor with change in effective gap distance due to air gap	151
Fig. 6.15	Coupling factor with change in effective gap distance due to insulator thickness	151
Fig. 6.16	Coupling Factor with applied DC bias	151
Fig. 6.17	Coupling Factor with residual stress	151
Fig. 6.18	Coupling Factor with electrode radius	152
Fig. 6.19	Coupling Factor with actuation layer thickness	152
Fig. 6.20	Comparative analysis of coupling factor for combinational effect of actuation layer radius and gap thickness	149
Fig. 6.21	Comparative analysis of coupling factor for combinational effect of static bias and gap thickness	149
Fig. 6.22	Comparative analysis of coupling factor for combinational effect of t_a and t_i	153
Fig. 6.23	Comparative analysis of coupling factor for combinational effect of r_a and t_i	153
Fig. 6.24	Comparative analysis of collapse voltage with respect to actuation layer radius for Si_3N_4 isolation	154
Fig. 6.25	Comparative analysis of collapse voltage with respect to actuation layer radius for various actuation layer thickness	154
Fig. 6.26	Comparative analysis of collapse voltage for change in gap thickness	155
Fig. 6.27	Comparative analysis of collapse voltage with insulation thickness	155
Fig. 6.28	Comparative analysis of coupling factor for change in	156

List of Figures

	bias between HfO_2/Si_3N_4 isolation for various HfO_2 thickness	
Fig. 6.29	Comparative analysis of coupling factor for change in residual stress between Si_3N_4 isolation and HfO_2 of various thickness	156
Fig. 6.30	E_{k_w} with respect to residual stress	156
Fig. 6.31	Comparative analysis of coupling factor for change in gap thickness Si_3N_4 isolation and HfO_2 of various thickness	157
Fig. 6.32	E_{k_w} with respect to gap thickness	157
Fig. 6.33	Comparison of coupling factor for change in actuation layer thickness between Si_3N_4 isolation and HfO_2 of various thickness	157
Fig. 6.34	Comparison of coupling factor for change in electrode radius between Si_3N_4 isolation and HfO_2 of various thickness	157
Fig. 7.1	Frequency response of 110μm actuated membrane	170
Fig. 7.2	3dB bandwidth of CMUT	170
Fig. 7.3	3D Frequency response of 110μm actuated membrane	170
Fig. 7.4	Comparison of frequency profile for the same input pulse between HfO_2 Vs. Si_3N_4 isolation	171
Fig. 7.5	Comparison of frequency profile for change in insulating and structural material for the same input pulse	171
Fig. 7.6	Comparison of frequency profile for various actuation layer radius	172
Fig. 7.7	Comparison of frequency profile for various actuation layer thickness	172
Fig. 7.8	Comparison of frequency profile for various insulation thickness	172
Fig. 7.9	Primary resonance with respect to residual stress	173
Fig. 7.10	Primary resonance with respect to actuation layer radius	173
Fig. 7.11	Displacement with respect to bias	174
Fig. 7.12	Displacement with respect to gap separation	174
Fig. 7.13	Displacement with actuation layer thickness	174
Fig. 7.14	Displacement with respect to insulation thickness	174
Fig. 7.15	Displacement with radial distance	174
Fig. 7.16	Impedance profile with respect to frequency	175
Fig. 7.17	Comparative analysis of impedance profile for various	175

List of Figures

	actuation layer radius	
Fig. 7.18	Comparative analysis of impedance profile for various actuation layer thickness	175
Fig. 7.19	Comparative analysis of impedance profile between SiC and Si_3N_4 actuation layer	175
Fig. 7.20	3D plot of impedance profile with actuation layer radius	176
Fig. 7.21	3D plot of impedance profile with actuation layer thickness	176

List of Tables

Table No.	Table Description	Page no
Table 2.1	Comparative study on various fabrication technologies	20
Table 2.2	Comparative study on usage of various membrane materials	22
Table 2.3	Comparative study on structures developed using SiC	23
Table 2.4	Comparative study on various geometrical shapes of CMUT membrane	25
Table 2.5	Comparative study on various applications of CMUT	27
Table 3.1	Comparative study among various CMUT actuation layer materials	58
Table 3.2	Contribution of fringing effect	66
Table 5.1	Comparative study of enhancement in displacement due to variation of various CMUT parameters	125
Table 5.2	Comparative analysis of Displacement among various CMUT structure	133
Table 7.1	Percentage of difference between analytical and experimental data	170
Table 8.1	Comparative study of CMUT parameters for various structures	184
Table 8.2	Percentage improvement in parameters in comparison with Si3N4 based non-insulated	184

List of Abbreviations

MEMS - Micro electro mechanical system

IC - Integrated circuit

MUT - Micromachined ultrasonic transducer

NDT - Non destructive testing

PZT - Lead-zirconate-titanate

CMUT - capacitive micromachined ultrasonic transducer

PMUT - Piezoelectric micromachined ultrasonic transducer

UT - Ultrasonic transducer

PECVD - Plasma enhanced chemical vapor deposition

ICP - Inductively coupled plasma

RIE - Reactive ion etching

Al - Aluminum

Si_3N_4 - Silicon nitride

SiC - Silicon Carbide

HfO_2 - Hafnium oxide

a-SiC - Amorphous SiC

PolySiC - Polycrystalline SiC

NH_4F - Ammonium fluoride

µm - Micrometer

nm - Nanometer

MPa - Megapascal

dB - Decibel

dBi - Decibels relative to isotropic

Si - Silicon

Ge - Germanium

SiO_2 - Silicon dioxide

LIST OF PUBLLICATIONS

Referred Journal Publications :

1. M. Pal, N. P. Maity, R. Maity, "An improved displacement model for micro-electro-mechanical-system based ultrasonic transducer," *Microsystem Technologies*, vol. 25, pp. 4685-4692, 2019.

2. M. Pal, C. Lalengkima, R. Maity, S. Baishya, N. P. Maity, "Effects of fringing capacitances and electrode's finiteness in improved SiC membrane based micromachined ultrasonic transducers," *Microsystem Technologies*, vol. 27, pp. 3679-3691, 2021.

3. M. Pal, N. P. Maity, S. Baishya, R. Maity, "Performance Analysis of Nano-Electro-Mechanical-System Ultrasonic Sensor with Fringing Field Effects", *Transaction of Electrical and Electronic Material*, online published on 9th March, 2021, doi.org/10.1007/s42341-021-00297-1.

4. M. Pal, N. P. Maity, R. Maity, "Analysis of Fringing Effects in High-k Insulated and SiC Structural Layer based Capacitive Micromachined Ultrasonic Transducer," *Sensor Review*, Manuscript ID: SR-09-2021-0313, Under Review.

5. M. Pal, N. P. Maity, R. Maity, "An Efficient Electrostatic Actuation Model with Fringing Effects of High-k Insulated MEMS Based Micromachined Ultrasonic Sensor," *Sensor Review*, Manuscript ID: SR-12-2021-0463, Under Review.

Conference Publication

1. M. Pal, R. Maity, N. P. Maity, "Silicon Carbide Membranes for Microelectromechanical Systems Based CMUT with Influence Factors," *19th International Workshop on New Approaches to High-Tech: Nano-Design, Technology, Computer Simulations – NDTCS-2021*, Minsk, Belarus, 2021

2. M. Pal, R. Maity, N. P. Maity, "An Accurate Electrostatic Actuation Model with Fringing Effect of MEMS Based Ultrasonic Transducer," *International Conference on Energy Systems, Drives and Automations, Kolkata*, 2021. [Under Review]

3. M. Pal, N.P. Maity, R. Maity, "An improved model for MEMS based ultrasonic transducer", *International Conference on Energy Systems, Drives and Automations, Kolkata*, pp. 40-44, 2018.

4. M. Pal, N.P. Maity, R. Maity, "Performance Analysis and Verification of MEMS Based Micromachined Ultrasonic Transducer with High-k Insulation Layer," *International Conference on Energy Systems, Drives and Automations, Kolkata,* pp. 27, 2019.

BIO-DATA OF THE CANDIDATE

Name of Candidate	:	Moumita Pal
Date of Birth	:	23/07/1986
Contact	:	9903269420 moumitajisceece@gmail.com
Permanent Address	:	2/C, Block-1, Heaven Plaza, Teghoria Main Road, Near Loknath Mandir, Kolkata -700157
Married	:	Yes
Educational Details	:	
(a) B.Tech	:	Instrumentation and Control Engineering
(b) M.Tech	:	Electronics and Communication Engineering
(c) Ph.D Course work	:	SGPA of 7.67
Present Occupation Details	:	
Organization	:	JIS College of Engineering
Rank	:	Assistant Professor
Job Profile	:	Presently working as Assistant Professor in Department of Electronics and Communication Engineering at JIS College of Engineering.

PARTICULARS OF THE CANDIDATE

Name of Candidate	:	Moumita Pal
Degree	:	Ph. D
Department	:	Electronics and Communication Engineering
Title of Thesis	:	Modeling and Simulation of Silicon Carbide Based Microelectromechanical Ultrasonic Transducer
Date of Admission	:	16/08/2018
Approval of Research Proposal:		
1. DRC	:	8-9/4/2019
2. BOS	:	23/04/2019
2. School Board	:	30/04/2019
MZU Regn No	:	1800283
Ph. D Regn No	:	MZU/Ph.D/1288 of 16.08.2018
Extension	:	NO

_____

Dr. Niladri Pratap Maity
Head
Dept of Electronics and Communication Engineering

CHAPTER

1

Introduction

1.1 Micro Electro Mechanical Systems

Micro electro mechanical system (MEMS) is a combination of microdevices that interconnect mechanical parts and electronic components and are manufactured in sizes ranging from micrometers to millimeters utilizing integrated circuit (IC) compatible batch-processing methods. On a micro-scale, these systems can detect, regulate, and respond, and then perform independently or in arrays to achieve macro-scale effects. Since the mid-1970s, MEMS has emerged as a revolutionary technology, opening up new possibilities in chemical [1], physiological [2], and biomedical [3] sensors and actuators. Even though MEMS technology is based on IC fabrication techniques, its test methodologies [4] are significantly different. MEMS devices respond to both electrical and data inputs from the field. Due to technological advancements, we are now capable of making equipment so small that it is not visible to the naked eye. The size of MEMS devices is usually measured in micrometers. Thermal sensors, pressure gauges, accelerometers, viscoelastic actuators, repeaters, levers, gears, power transmitters, micro-mirrors, control valves, pumps, and motors can now be produced in the bulk manner on the same micro-dimensional level in the processing chip involving advanced materials [5].

1.1.1 Elements of MEMS

In the most basic form of MEMS, mechanical micro-structural elements, microsensors, embedded systems, and microelectronic devices are all merged onto a single silicon chip. Fig. 1.1 shows a schematic diagram of MEMS components. Microsensors reliably detect the change in the system's environment by measuring

mechanical, thermal, magnetic, chemical, or electromagnetic information or events. Microelectronics process the data and send signals to microactuators, which react and change the environment in some way. MEMS devices are largely comprised of small parts and are extremely compact. MEMS has been used to make anything from switches to gears to pistons to propellers and even steam turbines, as seen in Fig. 1.2 MEMS is more than just the miniaturization of mechanical components or the fabrication of objects out of silicon. MEMS is a manufacturing technique that employs batch fabrication methods to design and manufacture complicated mechanical devices and systems, as well as the electronics with which they are associated.

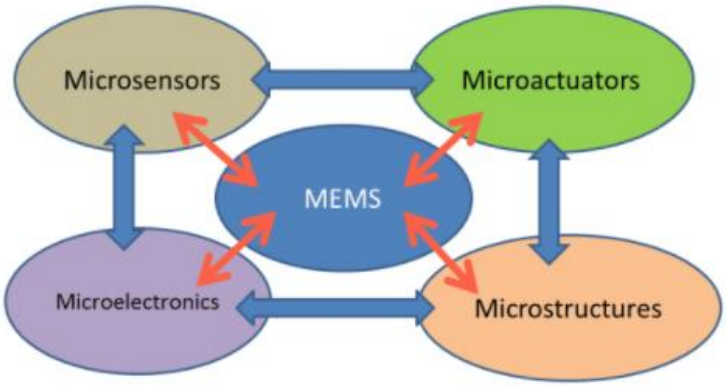

Fig. 1.1 Components of MEMS

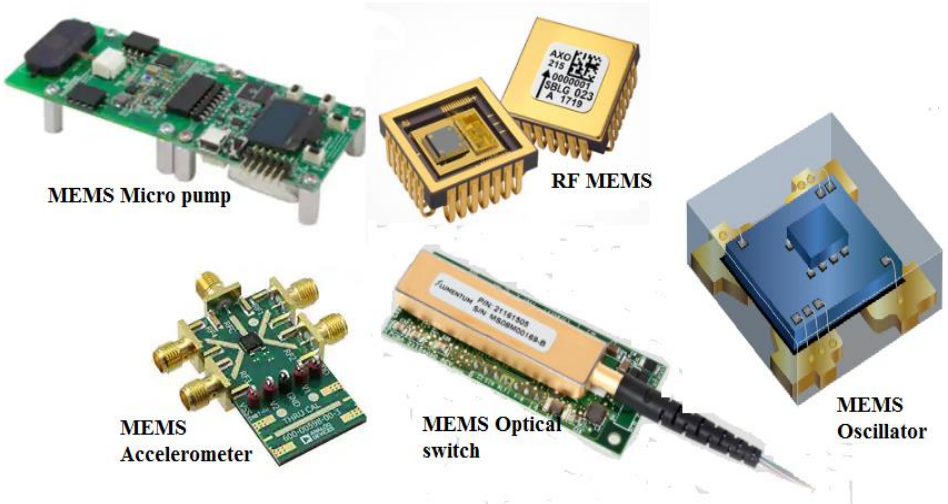

Fig. 1.2 Application of MEMS [6]

1.1.2 Application of MEMS

Over the previous several decades, MEMS practitioners and researchers have created a huge number of microsensors having practical sensing paradigms, such as heat, stress, surface tension, chemical reactions, electromagnetic field, radiation, and so on. Surprisingly, the performance of several of these micromachined sensors has excelled that of their macroscale equivalents. MEMS devices not only have outstanding performance but are also manufactured using batch fabrication procedures similar to those used in the IC industry, which can result in low per-device production costs as well as a range of other benefits. As a result, not only can high gadget performance be achieved, but it may also be delivered at a reasonable cost. Discrete silicon microsensors were swiftly commercialized, and the markets for these devices are presently rapidly developing. The MEMS research and development community has recently demonstrated microvalves for controlling gas and liquid flows, optoelectronic devices and reflectors for redirecting or regulating light beams, independently controlled micromirror arrays for displays, microresonators for a variety of applications, micropumps to develop positive fluid pressures, and micro flaps. Despite their small size, these microactuators can produce macroscale effects regularly; that is, these tiny actuators can perform mechanical feats far larger than their size would suggest. Scientists have fitted small microactuators on the leading edge of an airplane's airfoils and have demonstrated that these microminiaturized devices are capable of leading the aircraft alone.

1.2 Micromachined Ultrasonic Transducer

Ultrasonic transducers are a type of acoustic sensor that convert alternating voltages to ultrasound or convert ultrasound into an electrical signal in reverse. As shown in Fig. 1.3, ultrasounds occur at frequencies above hundreds of kilohertz which are higher than the limit of human hearing and are widely used in applications such as medical imaging, non-destructive testing (NDT) [7-8], sonar, flow metering [9-10], and ultrasonic range measuring [11].

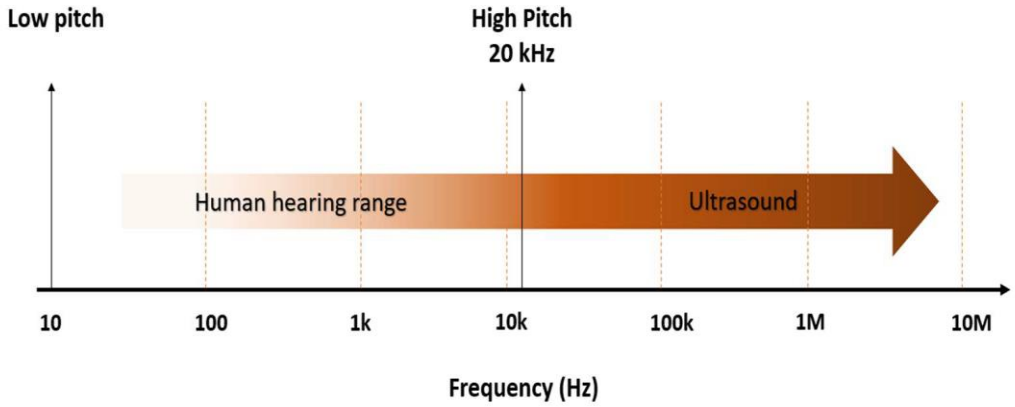

Fig. 1.3 Frequency range of ultrasound wave [12]

The ultrasonic imaging system, for example, in medical diagnostic imaging comprises an array of ultrasonic sensors and an imaging system. Ultrasound waves penetrate the objects, and subsequently, the items' reflected sound waves are acquired. The imaging system regulates the ultrasonic transducers that transmit and receive an ultrasound and generates an ultrasound image electronically using collected data from the transducers [14]. In immersion flow meter reading, a single ultrasonic transducer or a pair of transmitters and receivers calculates the distance between both the target and the ultrasound source using the pulse-echo measuring system and the speed of sound in air. From the supplied distance between the targets, it determines the sound transmitting time and speed [13]. Micromachined ultrasonic transducers (MUTs) have been developed as an alternative to traditional piezo composite UT in recent decades, although their concept remains the same [15-16].

1.2.1 Types of MUT

MUTs are of piezoelectric and capacitive types [17]. For many years, piezoelectric micromachined ultrasonic transducers (PMUTs) have been developed and widely used [12]. The piezoelectric effect describes a material's ability to create electricity when mechanical stress is applied, and to generate stress when an electric field is applied. Due to its high energy density and great effective stress piezoelectric coefficient, PMUT frequently employs lead-zirconate-titanate (PZT) film for sensing or actuating [18]. A PMUT device's

membrane is a micromachined multilayer with a piezoelectric layer layered between two metal electrode layers and an insulation layer separating it from the substrate (mostly silicon dioxide (SiO_2). The membrane's PZT thin layer is primarily employed to vibrate it, whereas the frequency of the PMUT is determined by the membrane's size and physical parameters [19]. A cross-section view of a basic PMUT device is shown in Fig. 1.4. Multiple capacitor cells are usually seen in capacitive micromachined ultrasonic transducers (CMUTs). Each cell has a substrate, which is a fixed electrode, and a membrane, which is a thin moveable electrode suspended over the substrate with a defined air gap as shown in Fig. 1.5. These transducers are made up of a large number of membranes that may be built onto silicon-based wafers using regular IC fabrication technology and silicon MEMS fabrication technology. The mechanical vibrations of the membranes in CMUTs produce ultrasonic waves. The electrode inserted in the membrane's structure electrostatically activates it [20].

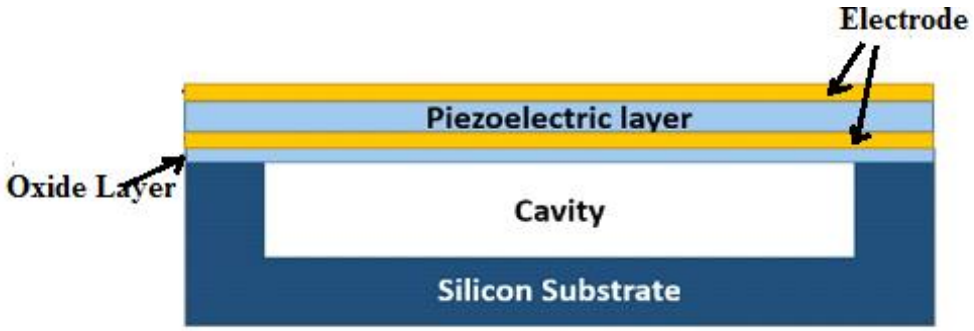

Fig. 1.4 Schematic diagram of PMUT

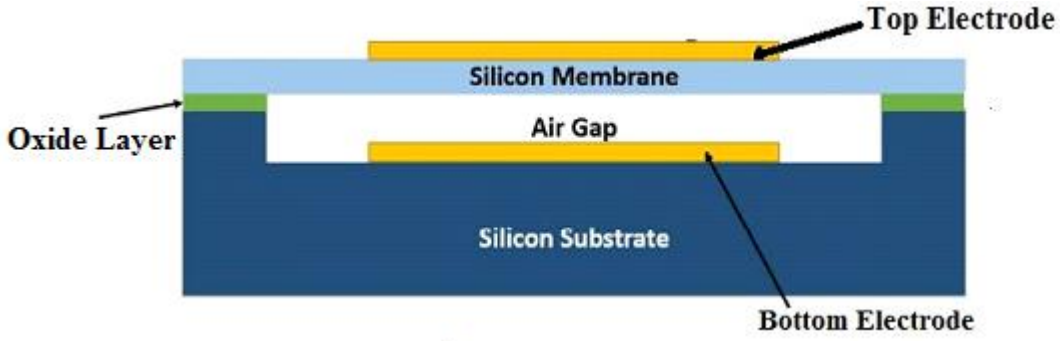

Fig. 1.5 Schematic diagram of CMUT

Ultrasonic transducers have been widely used in medical imaging in recent years, involving the use of various polymer crystals, piezoelectric materials, ceramics, and piezo composite materials for their high impact. MUTs have emerged in the study sector as a result of several shortcomings in the performance of piezoelectric transducers. CMUT is a type of MUT that works by varying capacitance and modulating the electrostatic force as a result.

1.2.2 Competency of CMUT over PZT transducer

CMUTs have numerous potential advantages over traditional PZT transducer materials which are enlisted below-

- A single operation can place several frequency elements in a single array.
- Precision dimensional control adjustable frequency range of 500 KHz to 50 MHz
- Unlike lead-based PZT devices, CMUTs are lead-free, and contain no hazardous ingredients, making them ideal for an intrusive ultrasound.
- Integration with electrical circuits in chip-scale packages, allowing for downsizing and lower form factors, as well as more dependable and resilient designs.
- The realization of 2D CMUT arrays provides a logical solution for 3D imaging.
- Manufacturing simplicity and predicted cost savings silicon micromachining techniques replace labour-intensive, element-based assembly in traditional PZT portable linear arrays.
- Because of their higher sensitivity and wide bandwidth functioning, CMUTs are an excellent choice for photoacoustic imaging.

Apart from the advantages listed above, CMUT is accepted in a large manner because of some special features. CMUTs provide greater acoustic matching to the propagation medium, resulting in increased immersion bandwidth and image resolution [21]. When compared to gas or liquid, piezoelectric components have high stiffness and thus a high acoustic impedance. Acoustic

power cannot be properly transmitted to low-density media due to this mismatch, hence quarter-wavelength matching layers must be inserted between the transducer and the external medium. The tiny moveable capacitor plate and the air cavity behind it result in a substantially reduced acoustic impedance for capacitive UT, allowing them to perform better in liquid or air-coupled applications even without matching. As piezoelectric UT's frequency response curve has a sharp resonant peak (high Q-factor), a dampening layer (backing layer or delay line) is frequently required for applications requiring a broader bandwidth. Capacitive UT, on the other hand, naturally generates broadband waves and does not require additional damping when properly designed. Ultrasonic systems necessitate circuitry to drive the transducers, as well as extra electronics to interpret the data received. The size of the entire ultrasonic system can be considerably decreased by merging the transducer and electronic circuitry on a single substrate.

Along with its monolithic integration, MUTs are excellent for this application. The photolithographic approach allows for exact size control of each transducer membrane, batch production, and easy 1D or 2D array construction, which are all benefits of CMUT over piezoelectric transducers. Although some piezoelectric sensors can be employed in high-temperature applications, the temperature sensitivity of traditional piezoelectric materials is frequently an issue. MUT based on the capacitive principle does not have this problem, and if made using a method similar to, they can endure temperatures as high as 600°C.

1.3 Operating principles of CMUT

The CMUT is a MEMS structure that consists of two electrodes facing each other, one stationary and the other moveable. The two electrodes are separated by an insulating layer and a vacuum-sealed gap. By transforming electrical energy into acoustic energy or vice versa through the movement of the movable electrode, CMUTs can work in both transmit and receive modes.

An alternating voltage is delivered between the membrane and the substrate backplate in the transmit mode as shown in Fig. 1.6. By supplying an ac voltage to

the membrane in transmit mode, electrostatic attraction force is exploited to cause the membrane to vibrate.

However, unipolar electrostatic force causes a constant attraction, causing the membrane to vibrate at twice the applied frequency. As a result, CMUT requires a dc bias voltage that is greater than the ac voltage amplitude for proper operation. Acoustic waves are generated in the surrounding medium by the shaking of the membranes. In receive mode, an incident acoustic wave causes

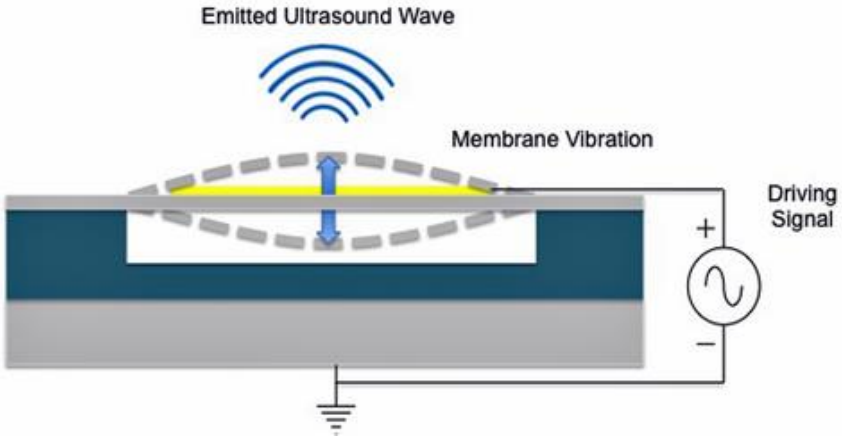

Fig. 1.6 CMUT in transmitting mode [12]

periodic vibration of the membranes. This vibration is recognised by capacitive sensing as shown in Fig. 1.7, which also necessitates a dc voltage. The total capacitance of the device is modulated by oscillation of the membrane. The difference in capacitance causes a current flow in the external electric circuit, which is amplified for further processing under the constant bias voltage supplied.

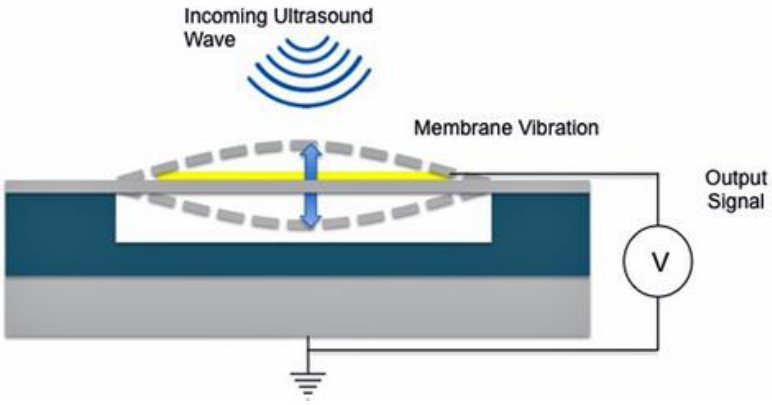

Fig. 1.7 CMUT in receiving mode [12]

1.4 Scope of the study

Ultrasound imaging is commonly done by transmitting a pulse and then detecting the echo that bounces back off the object's surface. Its vast usage in clinical imaging, non-destructive assessment, and acoustic microscopy is also praiseworthy. However, the application of ultrasound in acoustic and air medium demands perfect matching of coupling factor between the source and surrounding environment. Simultaneously high frequency ultrasound wave is required the most for capturing high intensity images of internal organs. In this context, CMUT is the fittest one to serve all these priorities compared to PZT. According to recent trends of miniaturization design of device need to be done in micro dimension. Non-insulated CMUT consist of membrane patterning below the top electrode which makes the electrodes far apart from other resulting reduction in device capacitance. Subsequent to this displacement of the membrane reduces and high frequency ultrasound could not be generated. Device engaged in clinical imaging, object detection requires device that are capable of generating high frequency ultrasound. To get rid of this limitation insulated structure can be considered for generating high frequency ultrasonic waves as it includes an insulation layer of lesser dimension compared to the membrane, patterning below the top electrode. This insulation layer will reduce the effective gap separation in comparison with the non-insulated one and will enhance direct device capacitance. Moreover, this layer will also prevent electrical hazards and take care of patients' safety. It is expected that enhanced device capacitance will certainly increase peak displacement of the membrane. Subsequent to which, reduction in impedance mismatch will occur. Undoubtedly, high coupling factor makes the device fittest to transmit ultrasound wave in acoustic and air medium. In this context insulated CMUT will be a good choice as enhanced membrane displacement will result in rising of coupling factor.

Among various structures of hexagonal, rectangular, circular, and square geometries, circular shaped capacitive element has maximum displacement [22]. As a consequence insulated circular CMUT will be taken into consideration. Moreover device having circular shaped electrode suffers from fringing field as electric field

lines bend at the edges of the plates [23]. An improved model of device capacitance will be incorporated here to express the excess capacitance which exists in the device for the fringing effect. Certainly this excess fringing capacitance will enhance device performance by enhancing membrane displacement and consequently coupling efficiency. This in turn will prove the device's potency to transmit maximum energy to the surrounding medium.

Structural material used for CMUT is one of the most important performance deciding factors. As device capacitance establishes a directly proportional relationship with the dielectric constant of the insulating material, hence the involvement of high-K material will improve the device performance. In this research work hafnium oxide (HfO_2) will be used as an insulating material due to its high relative dielectric constant. Insolvent of SiC as an actuation layer can enhance device sensitivity. These special features will enhance the penetration as it necessitates high-valued pressure transmission. Due to the high Young's modulus and low residual stress SiC will generate a high signal-to-noise ratio and expected to be one of the fittest materials for therapeutic application and medical imaging [24]. Though silicon nitride (Si_3N_4) is used as membrane material in many devices but SiC will be a better choice for its unique material properties. Displacement of the SiC layer will be modeled by Mason's model and plate model where lower valued residual stress and higher valued Young's modulus will be an influencing factor to enhance displacement compared to Si_3N_4 membrane. All the analytical result will be validated by FEM simulation and consideration of displacement model will be also done based on the result achieved by FEM simulation.

1.5 Preface to thesis

The thesis is organized as follows.

Chapter 2 states a review of CMUT, where various fabrication technologies adopted for device design are discussed. The existence of various geometrical shape of the membrane and their performance is depicted. The vast application of this capacitive transducer is also documented.

Chapter 3 deals with the analytical modeling of device capacitance for non-insulated and insulated structures. An improved model is incorporated for evaluating the device capacitance based on the fringing effect. Enhancement of device capacitance due to the fringing effect is proved in all aspects. The performance of SiC as actuation layer material is studied rigorously in the chapter. Effect of insulation upon device capacitance was also stated elaborately. Lastly effect of HfO_2 as an insulating material is examined from the various characteristic study.

Chapter 4 depicts the analytical modeling of electrostatic force generated in the device for capacitive action. As the CMUT is based on capacitive action, hence how the electrostatic force gets affected by the change in device capacitance is studied thoroughly. The dependency of electrostatic force upon various structural parameters is also characterized. Enhancement of device electrostatic force due to fringing is also described in an elaborative manner.

Chapter 5 deals with the displacement of the actuation layer with a comparative study of the plate model and Mason's membrane model. Performance enhancement in insulated elements compared to non–insulated elements is shown with various characteristic studies. Moreover, the overall enhancement in displacement due to the inclusion of fringing field capacitance is presented. Percentage enhancement in displacement due to the involvement of HfO_2 is investigated by varying device structural parameters.

Chapter 6 derives the collapse voltage and coupling factor of CMUT. The importance of evaluation of collapse voltage and coupling factor is also stated with various characteristic studies. Engagement of HfO_2 as an insulation material is also considered while the variations of collapse voltage and coupling factor are plotted against device parameters. The effect of fringing capacitance is also taken into consideration while the characteristic studies are presented.

Chapter 7 depicts the dynamic response of CMUT and impedance profile. Usage of this capacitive element is vast in medical imaging, acoustic, and air applications. In this context, impedance matching, bandwidth, resonance frequency has a great impact to characterise the device based on the application

field. Influences of device structural parameters upon the above-stated parameters are documented.

All the characteristic studies done in the chapters are validated by FEM simulation. At last, the whole research work has been concluded in a nutshell and the future scope of my research work is stated.

References

[1] K. Singh, S. Akhtar, S. Varghese, and J. Akhtar, "Design and development of MEMS pressure sensor characterization setup with low interfacing noise by using NI-PXI system," *Physics of Semiconductor Devices*, pp. 449-451, 2014.

[2] J.O. Dennis, A.Y. Ahmed, and M.-H. Khir, "Fabrication and characterization of a CMOS-MEMS humidity sensor," *Sensors*, vol. 15, no. 7, pp. 16674-16687, 2015.

[3] A. Hasan, M. Nurunnabi, M. Morshed, A. Paul, A. Polini, T. Kuila, M. Hariri, "Recent advances in application of biosensors in tissue engineering," *BioMed Research International*, vol. 2014, 2014.

[4] R. Ramadoss, R. Dean, and X. Xiong, "MEMS testing," *System-on-Chip Test Architectures*, pp. 591-651, 2008.

[5] D. M. Mills, "Medical imaging with capacitive micromachined ultrasound transducer (cMUT) arrays," *IEEE Ultrasonics Symposium Proceedings*, vol. 1, pp. 384-390, 2004

[6] M. Technology, "Medical MEMS Micro Pump Demonstration," ed: Microchip Technology, 2015, pp. https://www.microchip.com/en-us/solutions/medical/demonstrations-and-design-files/medical-mems-micro-pump.

[7] S. T. Hansen, B. J. Mossawir, A. S. Ergun, F. L. Degertekin, and B. T. Khuri-Yakub, "Air-coupled nondestructive evaluation using micromachined ultrasonic transducers," *IEEE Ultrasonics Symposium Proceedings*, vol. 2, pp. 1037-1040. 1999

[8] A. S. Ergun, G. G. Yaralioglu, and B. T. Khuri-Yakub, "Capacitive micromachined ultrasonic transducers: Theory and technology," *Journal of Aerospace Engineering*, vol. 16, no. 2, pp. 76-84, 2003.

[9] T. Folkestad and K. S. Mylvaganam, "Chirp excitation of ultrasonic probes and algorithm for filtering transit times in high-rangeability gas flow

metering," *IEEE Transactions on Ultrasonics, Ferroelectrics, and Frequency Control*, vol. 40, no. 3, pp. 193-215, 1993.

[10] M. S. Salim, M. Abd Malek, R. Heng, K. Juni, and N. Sabri, "Capacitive micromachined ultrasonic transducers: Technology and application," *Journal of Medical Ultrasound*, vol. 20, no. 1, pp. 8-31, 2012.

[11] J. Jung, W. Lee, W. Kang, E. Shin, J. Ryu, and H. Choi, "Review of piezoelectric micromachined ultrasonic transducers and their applications," *Journal of Micromechanics and Microengineering*, vol. 27, no. 11, pp. 113001-113017, 2017.

[12] B. S. Duy Le Nguyen, "Analytical modeling and simulation of capacitive micromachined ultrasonic transducer," Master of Science, Texas State University, 2020.

[13] W. Lee and Y. Roh, "Ultrasonic transducers for medical diagnostic imaging," *Biomedical engineering letters*, vol. 7, no. 2, pp. 91-97, 2017.

[14] E. Cianci, V. Foglietti, G. Caliano, and M. Pappalardo, "Micromachined capacitive ultrasonic transducers fabricated using silicon on insulator wafers," *Microelectronic engineering*, vol. 61, pp. 1025-1029, 2002.

[15] Y. Huang, A. S. Ergun, E. Haeggstrom, M. H. Badi, and B. T. Khuri-Yakub, "Fabricating capacitive micromachined ultrasonic transducers with wafer-bonding technology," *Journal of Microelectromechanical systems*, vol. 12, no. 2, pp. 128-137, 2003.

[16] J. Jung *et al.*, "A top-crossover-to-bottom addressed segmented annular array using piezoelectric micromachined ultrasonic transducers," *Journal of Micromechanics and Microengineering*, vol. 25, no. 11, p. 115024, 2015.

[17] P. Muralt, A. Kholkin, M. Kohli, and T. Maeder, "Piezoelectric actuation of PZT thin-film diaphragms at static and resonant conditions," *Sensors and Actuators* , vol. 53, no. 1-3, pp. 398-404, 1996.

[18] G.-H. Feng and H.-J. Liu, "Piezoelectric Micromachined Ultrasonic Transducers with a Cost-Effective Bottom-Up Fabrication Scheme for Millimeter-Scale Range Finding," *Sensors,* vol. 19, no. 21, pp. 4696-4700, 2019.

[19] S. T. McKinstry and P. Muralt, "Thin film piezoelectrics for MEMS," *Journal of Electroceramics,* vol. 12, no. 1, pp. 7-17, 2004.

[20] V. T. Rathod, "A review of electric impedance matching techniques for piezoelectric sensors, actuators and transducers," *Electronics,* vol. 8, no. 2, pp. 169-176, 2019.

[21] M. I. Haller and B. T. Khuri-Yakub, "A surface micromachined electrostatic ultrasonic air transducer," *IEEE Transactions on Ultrasonics, Ferroelectrics, and Frequency Control,* vol. 43, no. 1, pp. 1-6, 1996.

[22] R. Maity, N. P. Maity, K. S. Rao, K. Guha, and S. Baishya, "A new compact analytical model of nanoelectromechanical systems-based capacitive micromachined ultrasonic transducers for pulse echo imaging," *Journal of Computational Electronics,* vol. 17, no. 3, pp. 1334-1342, 2018.

[23] A. Mallik and A. Chattopadhyay, "The Impact of Fringing Field on the Device Performance of a p-Channel Tunnel Field-Effect Transistor With a High-K Gate Dielectric," *IEEE Transactions on Electron Devices,* vol. 59, no. 2, pp. 277-282, 2011.

[24] Q. Zhang, P.V. Cicek, K. Allidina, F. Nabki, and M. N. El-Gamal, "Surface-micromachined CMUT using low-temperature deposited silicon carbide membranes for above-IC integration," *Journal of Microelectromechanical Systems,* vol. 23, no. 2, pp. 482-493, 2014.

CHAPTER

2

CMUT- A Review

2.1 Brief overview of CMUT

Ultrasound is used for a variety of purposes, including sensing and actuation. In general, therapeutic applications such as lithotripsy, tissue ablation, and ultrasound detection are critical in all of these industrial cleaning applications. The imparted ultrasound must be detected via the coupling medium from the source. A solid coupling medium is used to measure wafer temperature, liquid for NDE and medical applications, and gaseous for air-coupled applications. [1-4]. A piezoelectric transducer has an impedance mismatch when used in fluid-coupled applications. MUTs are widely used as high-dynamic-range air transducers and for acoustic applications [5-9]. The use of ultrasound flow metering in medical therapy, as well as ultrasound microscopy, has been studied in many different ways. There are still a lot of unknown application areas since theoretical analysis prevents practical implementation. This capacitive transducer has proven its capability in acoustic applications, impedance matching, huge bandwidth, and high-frequency applications, reducing the need for piezoelectric transducers. Due to the use of photolithography, it is considerably less expensive than a piezoelectric transducer. The bottom electrode of a micro-dimensional capacitive element consists of an insulating layer on top of a conductive Si substrate. The top electrode is patterned with a metalized actuation layer consisting of polysilicon, which has a conducting nature. On the conductive substrate, an insulation layer prevents parallel electrodes from coming into contact with each other, and it also enhances the collapse voltage of a device by insulating it. For underwater imaging, acoustic sensors have been used since the early 20th century. The development of piezoelectric materials reached a critical mass at the end of the 20th century [9-10]. For transducer performance characterization,

significant developments in computer techniques necessitate more complicated algorithms. Air gaps are reduced as a result of technological empowerment through the application of micro fabrication technology. As a result, capacitive electrostatic transducers may create high electric field strengths, allowing them to compete with piezoelectric sensors. Integration with microelectronics, as well as greater bandwidth and large arrays with related electrical connections, are among the enhanced applications of CMUTs [11-12]. Rapid developments in characterization approaches have substantially improved, as has a good approach to working principles. The device's concept, methodology, and fabrication are all enhanced by a successful behavioural approach study. The static behaviour of the CMUT has a substantial impact on non-contact optical profilometers, which employ optical interferometry to scan the surface of the CMUT in a microscopic environment [13-14]. Using finite element method (FEM) simulation, the expressions show a correlation between the input and output variables along with the structural specifications [15]. CMUTs provide several advantages, including enhanced bandwidth, huge fabrication approaches in a variety of application domains, as well as excellent sensitivity and quick response times [16]. CMUTs have recently been able to overcome the challenges of two-dimensional array fabrication and are capable of capturing real-time three-dimensional images [17] owing to extensive study. Collapsed mode CMUT under proper biasing is essential for high power transmission [18-19]. The creation of an air-coupled ultrasonic transducer array without grating lobes that operates at 40 KHz frequency is a challenging task. Dimension of grating lobes causes limitation in the presence of air while acoustic imaging is performed. Excluding the grating lobes, a one-dimensional air-coupled phased array transducer is formed which can operate at 40 KHz. Keeping the transducer size less than 4.3 mm this challenge can be overcomed [20].

2.2 Fabrication technology engaged in CMUT design

Various fabrication schemes for CMUT have been developed by many researchers. Surface micromachining, bulk micromachining, and wafer bonding, as well as their combination, are among these approaches [21-25].

2.2.1 Fabrication using surface micromachining

Surface micromachining was first involved in building CMUT at Stanford University. In this process, a bottom electrode is formed upon a non-conductive substrate followed by sacrificial layer deposition. Better dimensional control of the membrane is achieved in this process by pre patterning the sacrificial layer, later on, forming an anchor with the membrane around it as shown in Fig. 2.1. The structural layer of the membrane is then deposited upon it and etching is done with release openings. The membrane of the device is thus suspended upon the substrate by removal of the sacrificial layer.

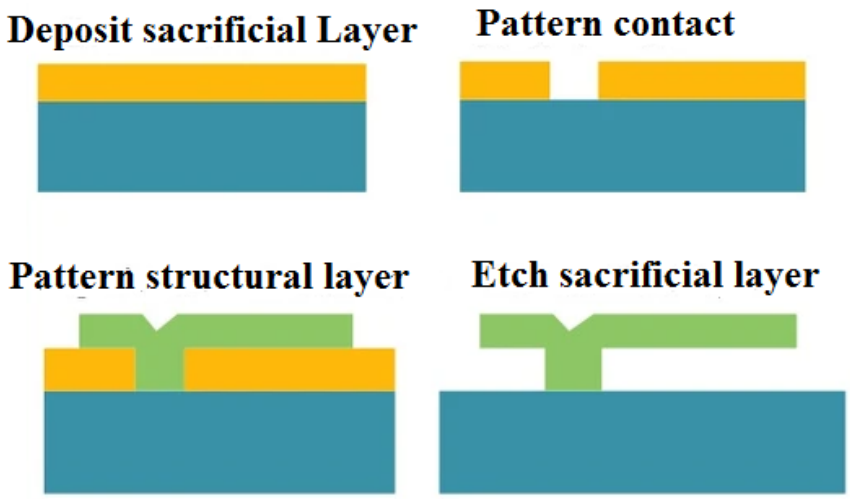

Fig. 2.1 Surface micromachining process

To make the membrane conductive, often metallization is carried over. Protection of the device is attained by depositing a final sealing layer if it is involved in a liquid environment. Many researchers have attempted to integrate electronics with surface-micromachined CMUT. A flip-chip bonding through silicon was engaged to connect the CMUT array electrically with an IC substrate [23]. IC dielectric layers are involved as the membrane of CMUT and the IC metallization layer act as a sacrificial layer to form the cavity after etching of metal [24]. In [25], the polysilicon layer is used as a membrane material where the oxide layer is used as a sacrificial layer. Moreover, transducers may also be fabricated after the completion

of IC in an alternative manner. Here fabrication of CMUT is done successfully upon the top of an IC substrate involving PECVD silicon nitride membrane at 250˚C sputtering chromium sacrificial layer [26].

2.2.2 Fabrication using wafer bonding

Instead of engaging the sacrificial layer, etching of cavities is done directly onto a wafer to create a capacitive gap by wafer bonding techniques. The bonding of this wafer is executed with another substrate by suspending the membrane layer upon a handle wafer as shown in Fig. 2.2. This handle wafer is finally dissolved from double-bonded substrates, keeping the thin CMUT membranes suspended in etched cavities. The wafer bonding process is advantageous in two aspects. First, the membrane layer is made of high quality epitaxial film whose growth is controlled at a tight thickness. Thus, improvement in uniformity in membrane thickness and dependability takes place for large-sized membranes [27-29]. Implementation of a narrow gap with a large size membrane can be materialized by this technique. In contrast to these, wafer bonding suffers from limitations due to its rigorous necessity of substrate cleanness and flatness. The requirement for additional substrate and removal of the handle wafer enhance the material cost for this process. Moreover, fabrication of CMUT using this process is found to be quite difficult to get integrated with monolithic IC due to its constraint of high temperature. A patent [30] from National Semiconductor defines the way to get rid of these difficulties by transferring the membrane into the IC substrate.

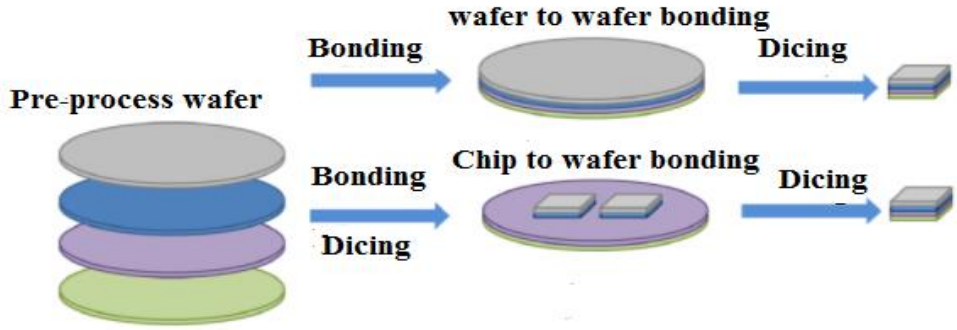

Fig. 2.2 Various wafer bonding techniques

2.2.3 Fabrication by bulk micromachining

A reverse process is executed as an adverse process of surface micromachining through wet etching of silicon from the wafer backside [31-32]. This unique process allows the exposure of the bottom electrode from the CMUT membrane. Moreover, released holes are also sealed in the top electrode by keeping the reliability of the material and structure of the active bottom electrode. In consideration of the difficulties aligned with the bulk machining process, the wafer front side is filled with polymer backing material to enhance the flexibility of CMUT arrays [33-35]. In Table 2.1 a comparative study on various fabrication technologies is established.

Table 2.1: Comparative study on various fabrication technologies

Referred paper	Membrane layer	Sacrificial layer	Remarks on fabrication
J. Wang [25]	Polysilicon layer	Oxide layer	Surface micromachining
J. Zahorian [26]	PECVD silicon nitride	Oxide layer	Surface micromachining Si_3N_4 sputtered at 250˚C
K. Park [28]	Si_3N_4	Nitride oxide layer	local oxidation of silicon (LOCOS) and direct wafer-bonding
A. I. H. Chen [29]	Low stress Nitride	Oxide layer	Wafer bonding
A. Coppa [31]	LPCVD Si_3N_4	DF-PECVD Si_3N_4	Top to bottom each layer is formed
Proposed Model	SiC	Polyimide	Dry release involved to eliminate risk of stiction

2.3 Review on the usage of various membrane materials

Massive advances in material science have opened up the possibility of using a wide range of materials for MEMS manufacturing, depending on the basic requirements in various application areas. For membrane construction, metals such as nickel(Ni), aluminium(Al), non-metals such as silicon(Si), germanium(Ge), polymers such as SU8, polyimide such as diamond, silicon carbide (SiC), silicon nitride (Si_3N_4), silicon dioxide (SiO_2) are used [36]. The shape and substance of the membrane have been proven to have a substantial impact on resonance frequency in many studies. Si_3N_4 performs admirably as a fine material for emission and detection

where surface micromachining technology is used for fabrication and Si_3N_4 for both the membrane and the insulation layer material. In another Si_3N_4 based CMUT, Si is employed as the membrane and as the insulating layer material SiO_2 is involved in wafer-bonded ultrasonic transducers [42]. The influence of collapse and snapback voltage is studied by modeling a CMUT cell with a circular shaped Si_3N_4 membrane and altering various electrode settings. A licensed FEM program (ANSYS 5.7) was used to validate the CMUT's static finite element calculations [43-44]. A breakthrough has been achieved by combining surface micromachining technology with dc-sputtered amorphous technology. This method is well suited for fabrication at the lowest temperature (to date) in a thermal budget of 200 °C [45]. Because of its high Young's modulus and low residual stress, SiC-based CMUT can produce high-strength, flexible, and long-lasting CMUT membranes. In micro-dimensional circular shaped CMUT, actuation layer thickness and gap spacing are equivalent to the electrode diameters resulting in the electric field bending at the edges and ranges to adjacent distant spots as fringing fields is shown in Fig. 2.3. This fringing field increases the device's equivalent capacitance. In the meantime, the fringing field is responsible for the charge storing effect and has an impact on the linked capacitance. As a result, the deflection rises in proportion to the amplitude of the electrostatic force. This greater deflection will be the sole source of ultrasonic sound waves.

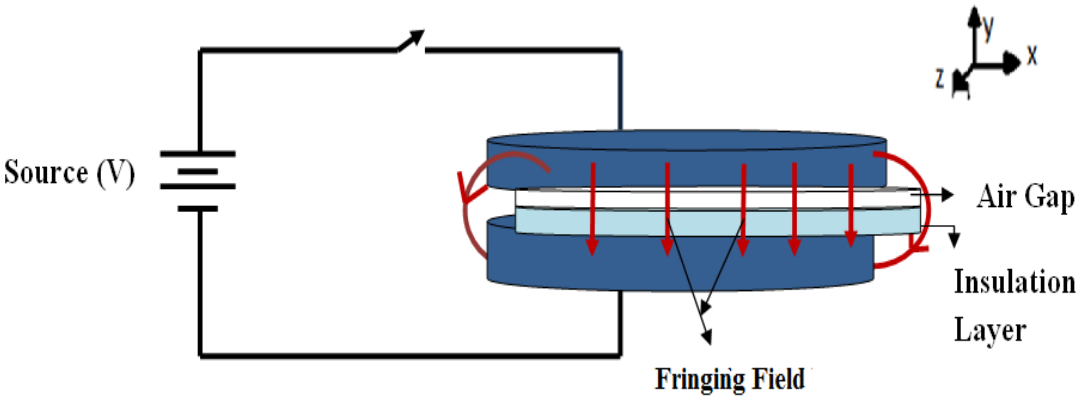

Fig. 2.3 Fringing field lines in the air gap and insulator capacitors

In Table 2.2 a comparative study on usage of various membrane materials is established.

Table 2.2: Comparative study on usage of various membrane materials

Referred Paper	Structural Layer	Young's Modulus (MPa)	Residual Stress (GPa)	Temperature required for fabrication	Remarks
A. Logan [36]	Si_3N_4	320	80	250ºC	Higher residual stress than SiC
M. Cetin [37]	Diamond	937.8	10.53	950ºC	Fabrication temperature is quite high
D. Gerardo [38]	Polymer	5.2	13.8	250ºC to 350ºC	Very low Young's Modulus
Q. Zhang [45]	SiC	260	30	200ºC	High Young's Modulus, Low residual stress and lowest temperature requirement

2.4 Review on the structures developed using SiC

Many systematic material selection strategies have been offered to tackle this challenge and make the design process more effective and efficient. Among four material selection process like material screening, comparing, selection, and optimization procedures Ashby's approach of material selection has been used the most commonly for MEMS devices [46]. The inception of research on SiC for MEMS applications traces back to the 1990s and was spearheaded by Mehran Mehregany's gathering at Case Western Reserve University [47].

SiC exists in three significant structures: single-crystalline, multi-crystalline, and amorphous. Due to its epitaxial nature, single-crystalline SiC has been widely explored for use in vicious climates. In MEMS, polycrystalline SiC (PolySiC) and amorphous SiC (a-SiC) are often utilized as structural and encapsulating layers because of their lower deposition temperatures [49-50]. SiC and polysilicon films with very low etching rates make excellent protective coatings [51]. Because of this, the deposition method and characteristics of SiC films determine whether they are

insulating, resistive, or highly conductive. a-SiC films have been found to have piezoresistive properties, and single-and poly-crystalline SiC has been employed as piezoresistive sensing materials [52]. A-SiC membranes prepared with NH_4F are biocompatible when used for cell culture [53-55]. In this thesis, the focus is on SiC films deposited at low temperatures since they enable MEMS to be created "above IC." The Young's modulus, residual stress, and deposition rate all vary depending on the deposition process. Both dry and wet etching methods can be engaged to pattern SiC films. The use of a molten potassium hydroxide and acid mixture to attack a-SiC and poly-SiC films has been demonstrated [56-57]. In addition to traditional micromachining techniques, laser ablation has been used to remove SiC layers [58-60]. In recent years, silicon-based MEMS matrix has attained a lot of attention as a micro-impulsion system. A SiC membrane is applied to the surface of micro-chambers to improve Si based MEMS ablation resistance. To create a high-quality cavity-free SiC membrane, a time-saving four-step deposition procedure is adopted [61]. One of the most promising materials for RF devices operating in hostile environments is SiC. "Silicon carbide-nanocrystalline diamond" has been discovered based on SiC film with controlled bending and matrices of very stable auto emission structures [62]. This proposed component base allows for a frequency range of GHz to THz to be covered. Table 2.3 establishes a comparative study on structures developed using SiC.

Table 2.3: Comparative study on structures developed using SiC

Referred paper	**Process Temperature(°C)**	**Residual Stress (MPa)**	**Deposition method**
R. Ghodssi [54]	200	750-65	PECVD
N. Ledermann [55]	400	1400-100	RF Sputtering
S. Inoue [56]	25	100	Reactive (Co-)sputtering
L. Gou [57]	200	260	DC sputtering
D. G. Jones [58]	<200	1250	Ion beam sputtering
Proposed model	200	260	Dry release of polyimide

2.5 Various geometrical shapes of CMUT membrane

CMUT exist in circular, hexagonal, rectangular and square shape as shown in Fig 2.4. Among various structures, the hexagonal one has the highest packaging density than rectangular, circular, and square geometries. High sensitivity and output pressure transducers are required for acoustic applications such as non-destructive testing, imaging, and treatments. Higher resolution is necessary for pulse-echo and photoacoustic imaging. Increased sensitivity enhances the detection of incoming pressure waves, resulting in higher image quality [63–64].

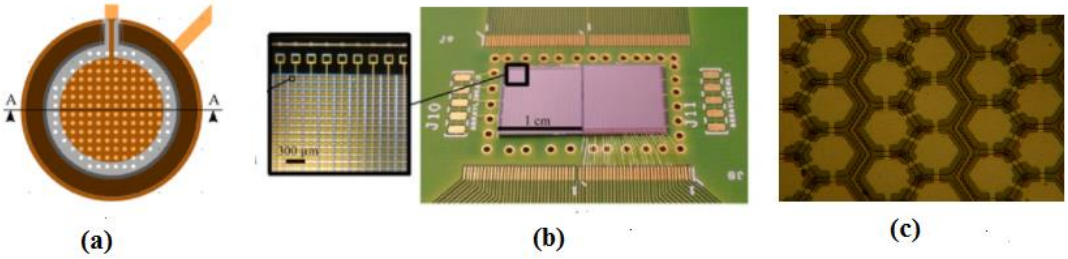

Fig. 2.4 Various geometrical shapes of CMUT (a) Circular membrane shaped CMUT (b) Square membrane shaped CMUT (c) Hexagonal membrane shaped CMUT [65]

High transmit output pressures boost penetration when it comes to pulse-echo imaging. By storing more energy in the tissue, heating can be hastened. It is necessary to maximize a cell's average output displacement to achieve high sensitivity and output pressure from CMUTs. To boost average output displacement, several research groups have proposed dual electrode topologies [66], non-uniform membrane designs [67–69], and modifying the fill factor and cell shape as viable design techniques.

During transmission, the main objective is to maximize average membrane deformation for a given received pressure (receiving efficiency) and average output pressure for a given operating voltage (transmission efficiency). An improved membrane design can benefit a CMUT with a fixed element size and operating frequency. The improvement can be attributed to three factors: 1) for a given pressure loading, a larger average membrane displacement; 2) for a given operating voltage and gap separation, a higher average electrostatic pressure; and 3) for a given

fill factor and parasitic capacitance, a higher fill factor, and lower parasitic capacitance. The hexagonal CMUT structure has the maximum package density among the rectangular, circular, and square geometries [70-73]. For hexagonal layers, a circular approximation is commonly used for mathematical reasons. The structural layer will deform, resulting in a large fluctuation in capacitance between the deformed layer and the fixed electrode [73]. According to various test results, the circular geometry produces strong repeatability and can be used for long-distance underwater object detection, distance measuring, and high intensity frequency applications. Table 2.4 proposes a comparative study on various geometrical shapes of CMUT membrane.

Table 2.4: Comparative study on various geometrical shapes of CMUT membrane

Referred paper	**Shape geometry**	**Features of various shape geometry**
Z. Zheng [70]	Rectangular	Generates deflection profiles that are in excellent agreement with finite element analysis (FEA) results for a wide range of geometry dimensions and loading conditions.
S. K. Tiwari [71]	Hexagonal	Highest packaging density they can be operated in the high temperature range and the transducer array can be fabricated at a lower cost.
M. Rahman [72]	Square	Provides higher accuracy compared to existing models has been presented
L. Jia [73]	Circular	Produces strong repeatability and can be used for long-distance underwater object detection, distance measuring, and high intensity frequency applications
Proposed model	Circular	Largest displacement among rectangular, square and hexagonal shape geometry

2.6 Application of CMUT

Ultrasonic sensors produce high-frequency sound pulses and analyze the echo they receive. To establish the distance to an object, sensors calculate the time between generating a signal and returning an echo. This approach can be used to determine wind speed and direction (anemometer), as well as tank fullness and other variables. An irregular blood flow rate is associated with many of these cardiovascular diseases. Blood flow can be measured quantitatively to provide important diagnostic information. A high-resolution, deep penetration

depth and real-time bidirectional display are all features of an implantable bidirectional PW Doppler blood flow meter [74].

The CMUT is used in a wide range of applications, and new designs have opened up new possibilities in the applications it supports. The CMUT is suitable for a range of applications because it can resolve good images in small or low-visibility locations. The CMUT was designed specifically for air-coupled applications. However, it began to concentrate on medical and underwater applications. The CMUT device is significant in the healthcare industry since it can take photographs of moving internal structures. Underwater imaging has a wide range of applications, including commercial, scientific, and military applications [75]. The commercial business would use the imaging to determine the location of fish or other catches. The CMUT imaging will boost fishing efficiency, especially in places where the water is muddy. The areas of sunken ships are frequently dark and have poor visibility. The location of wrecked ships can be determined using CMUT imagery [76]. The recovery of the ships allows them to be analyzed and the cause of the shipwreck to be determined. The CMUT device is both affordable and lightweight, rendering it even more appealing to medical professionals. CMUT imaging is employed in cardiac structures, the vascular system, the fetus and uterus, abdominal organs such the liver, kidneys, and gall bladder, and the eye for these reasons [77].

In modern piezoelectric-based systems, there is a considerable acoustic impedance mismatch between piezoelectric crystals (30 MRayl) and soft tissues (1.5 MRayl) [78-79]. Layers of high-density rubber that act as an acoustic matching layer are frequently placed between the transducer and the medium. The electromechanical coupling coefficient [80] is used to determine how efficient an ultrasonic transducer is. The coupling coefficient controls the bandwidth of piezoelectric transducers; whereas a high coupling coefficient is preferred for the useful vibration mode, a low coupling coefficient is sometimes required for competing modes to avoid erroneous response caused by mode coupling [81]. In CMUTs, a high coupling coefficient results in higher transducer sensitivity, bandwidth, and hence image resolution [82]. CMUTs have been

claimed to have an efficiency of up to 82%. The low mechanical impedance of the thin membrane clamped at the rim of the CMUT cell allows for better acoustic matching to the medium. As a result, CMUTs have a wide bandwidth [83]. Traditional piezoelectric arrays are manufactured by mechanically slicing piezoelectric crystals and filling the kerfs with a polymer [84-86]. It is extremely difficult to fabricate ultrasonic arrays with frequencies greater than 20 MHz using this method. CMUTs provide several benefits over piezoelectric transducers, but they also have many drawbacks [87-90]. Auditory crosstalk in CMUT transducers exacerbates the picture degradation caused by Stoneley waves at the membrane–water interface and Lamb waves propagating through the substrate [91]. Current CMUT designs have low receiving sensitivity, which has an impact on the signal-to-noise ratio and tissue penetration depth; this has been proven experimentally, with CMUT-based ultrasound probes having 10 dB less sensitivity than piezoelectric probes. Similar results were obtained in terms of penetration depth; however, when phased-array steering was used, the CMUTs outperformed piezoelectric probes in terms of signal-to-noise ratio; this was attributed to the larger acoustic radiation field experimentally recorded from CMUTs [92-94]. In Table 2.5 a comparative study on various application of CMUT is established.

Table 2.5: Comparative study on various applications of CMUT

Referred paper	**Application Domain**	**Frequency range**
M.S. Salim [74]	Non-destructive testing	2.3-2.5 MHz
R. Zhang [75]	Under water imaging	460KHz
O. Oralkan [76]	Pulse- echo imaging	3 MHz
B. T. Khuri-Yakub [77]	Medical imaging	2.5 MHz to 10 MHz
R. O. Guldiken [83]	High intensity focussed ultrasound generation	7.8 MHz
Proposed model	Air coupled transducer	1.62MHz

2.7 Study of various CMUT parameters

The mechanical portion of a CMUT is located on a parallel plate and can be represented in a variety of ways, including plate models, membrane displacement (Mason's Model), and electromechanical models. The mass-spring-damper system concept is used to approximate this electromechanical model. The most important parameters to consider in the described model are the spring constant, mass constant, and damping constant. In this model, the medium acoustic impedance is represented by a damper and a mass. A two-port network can be used to analyze the equivalent linear circuit model of CMUT's electrical and mechanical fields [95]. The single-dimensional CMUT's small-signal behaviour is taken into account when creating this two-port network model. As a function of frequency, electrical impedance calculations, and two-port network analysis for the transmitter (Tx) and reception (Rx) parts are done. Partially differential equations with specified solutions and complementary functions are evaluated with adequate boundary conditions for FEM analysis of various CMUT processes [96-98]. The structure, shape, and operating modes of the membrane all have an impact on CMUT performance. In recent years, a variety of finite element procedures dealt with such issues. Various small finite elements are studied as part of the simulation process in the finite element technique, and the exact answer is achieved by using a simpler function approximation. In this finite element model (FEM) approach, multiple linear equations are created to reduce the error between these differential solutions and the precise solution [99-102]. Various finite element tools, including as PZFlex, ANSYS, COVENTOR, COMSOL, and LS-DYNA, as well as custom-made modeling tools, are used to accurately study CMUT performance [103].

FE modeling and computer technologies are being carefully influenced by recent breakthroughs with the purpose of boosting sensitivity and bandwidth. In order to reach the ultimate goal of improving CMUT performance in diverse applications, innovative designs are used to investigate unfavourable arrays. These implementations are confined to collapsed mode operation as well as a certain type of CMUT in which the air gap between the plate and the substrate acts as a damper. These CMUTs are designed to be used in aeroplanes. This CMUT is suitable for

usage in both acoustic and airborne applications. As a result, modeling the vented cavity while considering fluid mechanics is challenging task. Consideration of mechanical and electrical attachments between the two electrodes is necessary for evaluating the nonlinear connection of electromechanical modeling during time domain analysis in collapsed mode CMUT operation [104-107]. Despite having less processing complexity than time-domain analysis, frequency domain analysis produces more efficient performance parameters [108]. The electrical resonance and anti-resonance frequency values are used to calculate the electromechanical coupling coefficient of each resonance [109-111].

The CMUT displacement profile can also be examined using the plate model. A steady pressure acting on a suspended membrane shape is taken into account when applying the plate theory. In this characterization of plate deflection, the plate form function is used, which includes plate radius as a function of radial distance, flexural rigidity, young modulus, plate thickness, and poison's ratio [112]. A stable deflection is taken into account while computing the uniform pressure analysis. This ensures that the greatest displacement occurs near the plate's center, where the top and bottom electrodes are close together, by maintaining a consistent electrostatic force across the plate. This straightforward assumption calculates critical mechanical parameters and assumes plate deflection in response to a voltage application. When considering the deflection of beams and plates, geometrical variations cause the reaction to vary unconditionally under axial force in a perpendicular position. Finite displacements in beams are caused by sufficiently massive loads [113]. After thorough research, it was determined that the dynamic behaviour of plates is well defined due to the significant downward deflection reaction of the structure [114-116]. The work done due to provided external energy produced dynamic pressure, and inertia forces to degenerate at the clamped plate are investigated using energy conservation laws for a discrete shaped plate and a beam [117]. Plates with uniform thickness, formed of stiff material, with large transverse sustainability, aligned with the plane and angular mass, as well as the influence of non-uniform bending, are maintained by the basic equations [118].

Each device has its inherent frequency. Resonance occurs when external energy is applied at a frequency that is similar to the device's inherent frequency. This type of resonance frequency is solely due to the membrane material and geometrical shapes. A CMUT membrane with a high density and low residual stress generates high resonance. Furthermore, micro dimensional CMUTs with a high working frequency range in the megahertz region have been found to be suitable for medical imaging. A 26 μm radius CMUT cell with a 4.85 MHz resonance frequency was created using a conceptual framework. Later, empirical evidence verified the theoretical finding, and the highest effective frequency was revealed to be 4.6 MHz, confirming the proximity between these [119]. In addition, in contrast to the results of experiments and simulations, the efficiency regulating parameters such as collapse voltage and membrane displacement is analyzed analytically and validated. In Table 2.6 a comparative study on various parameters of CMUT is done.

Table 2.6: Comparative study on various parameters of CMUT

Referred paper	Parameters calculated
A. Nikoozadeh [95]	A two-port network used to analyze the equivalent linear circuit model of CMUT's electrical and mechanical fields
A. Lohfink [96]	Calculation of frequency, electrical impedance done by partially differential equations with specified solutions and complementary functions
O. Oralkan [100]	Structure, shape, and operating modes of the membrane calculated by simpler function approximation involving FEM approach
B Bayram [102]	Dynamic analysis of CMUT
G. G. Yaralioglu [103]	FEM analysis done by COMSOL
B. Ma and N. Apte [104-105]	Vented cavity modeled considering fluid mechanics
N. Jones [112]	CMUT displacement profile examined using the plate model
R. Maity [119]	Collapse voltage and membrane displacement is analyzed analytically and validated
Proposed model	Static and dynamic displacement profile, collapse voltage, coupling coefficient, mechanical impedance is modeled involving fringing effect and validated by PZFlex FEM analysis.

References

[1] M. Turqueti, J. Saniie, and E. Oruklu, "Scalable acoustic imaging platform using MEMS array," *International Conference on Electronics/ Information Technology*, pp. 1-4, 2010

[2] F. L. Degertekin, J. Pei, B. T. Khuri-Yakub, and K. C. Saraswat, "In situ acoustic temperature tomography of semiconductor wafers," *Applied physics letters*, vol. 64, no. 11, pp. 1338-1340, 1994.

[3] F. L. Degertekin and B. Khuri-Yakub, "Hertzian contact transducers for nondestructive evaluation," *The Journal of the Acoustical Society of America*, vol. 99, no. 1, pp. 299-308, 1996.

[4] R. M. White, "Generation of elastic waves by transient surface heating," *Journal of Applied Physics*, vol. 34, no. 12, pp. 3559-3567, 1963.

[5] S. P. Kelly, R. Farlow, and G. Hayward, "Applications of through-air ultrasound for rapid NDE scanning in the aerospace industry," *IEEE Transactions on Ultrasonics, Ferroelectrics, and Frequency Control*, vol. 43, no. 4, pp. 581-591, 1996.

[6] A. Gachagan, G. Hayward, S. P. Kelly, and W. Galbraith, "Characterization of air-coupled transducers," *IEEE Transactions on Ultrasonics, Ferroelectrics, and Frequency Control*, vol. 43, no. 4, pp. 678-689, 1996.

[7] G. Hayward and A. Gachagan, "An evaluation of 1–3 connectivity composite transducers for air-coupled ultrasonic applications," *The Journal of the Acoustical Society of America*, vol. 99, no. 4, pp. 2148-2157, 1996.

[8] W. Manthey, N. Kroemer, and V. Magori, "Ultrasonic transducers and transducer arrays for applications in air," *Measurement Science and Technology*, vol. 3, no. 3, p. 249, 1992.

[9] D. Schindel and D. Hutchins, "Applications of micromachined capacitance transducers in air-coupled ultrasonics and nondestructive evaluation," *IEEE Transactions on Ultrasonics, Ferroelectrics, and Frequency Control*, vol. 42, no. 1, pp. 51-58, 1995.

[10] M. I. Haller and B. T. Khuri-Yakub, "A surface micromachined electrostatic ultrasonic air transducer," *IEEE Transactions on Ultrasonics, Ferroelectrics, and Frequency Control*, vol. 43, no. 1, pp. 1-6, 1996.

[11] D. W. Schindel, D. A. Hutchins, L. Zou, and M. Sayer, "The design and characterization of micromachined air-coupled capacitance transducers," *IEEE Transactions on Ultrasonics, Ferroelectrics, and Frequency Control*, vol. 42, no. 1, pp. 42-50, 1995.

[12] X. Jin, I. Ladabaum, F. L. Degertekin, S. Calmes, and B. T. Khuri-Yakub, "Fabrication and characterization of surface micromachined capacitive ultrasonic immersion transducers," *Journal of Microelectromechanical systems*, vol. 8, no. 1, pp. 100-114, 1999.

[13] A. S. Ergun, G. G. Yaralioglu, and B. T. Khuri-Yakub, "Capacitive micromachined ultrasonic transducers: Theory and technology," *Journal of Aerospace Engineering*, vol. 16, no. 2, pp. 76-84, 2003.

[14] T. Yu, W. Zhou, P. Xu, F. Yu, and Q. Qian, "Theoretical investigation on the dynamic performance of CMUT for design optimization," *Acta Mechanica Solida Sinica*, vol. 26, no. 1, pp. 99-110, 2013.

[15] I. Ladabaum, X. Jin, H. T. Soh, A. Atalar, and B. Khuri-Yakub, "Surface micromachined capacitive ultrasonic transducers," *IEEE Transactions on Ultrasonics, Ferroelectrics, and Frequency Control*, vol. 45, no. 3, pp. 678-690, 1998.

[16] O. Oralkan, A. Ergun, C. Cheng, J. Johnson, M. Karaman, T. Lee, and B. Khuri-Yakub,"Volumetric ultrasound imaging using 2-D CMUT arrays," *IEEE Transactions on Ultrasonics, Ferroelectrics, and Frequency Control*, vol. 50, no. 11, pp. 1581-1594, 2003.

[17] S. W. Smith, H. G. Pavy, and O. T. von Ramm, "High-speed ultrasound volumetric imaging system. I. Transducer design and beam steering," *IEEE Transactions on Ultrasonics, Ferroelectrics, and Frequency Control*, vol. 38, no. 2, pp. 100-108, 1991.

[18] O. T. Von Ramm, S. W. Smith, and H. G. Pavy, "High-speed ultrasound volumetric imaging system. II. Parallel processing and image display," *IEEE*

Transactions on Ultrasonics, Ferroelectrics, and Frequency Control, vol. 38, no. 2, pp. 109-115, 1991.

[19] B. Bayram, O. Oralkan, A. S. Ergun, E. Hæggstrom, G. G. Yaralioglu, and B. T. Khuri-Yakub, "Capacitive micromachined ultrasonic transducer design for high power transmission," *IEEE Transactions on Ultrasonics, Ferroelectrics, and Frequency Control,* vol. 52, no. 2, pp. 326-339, 2005.

[20] E. Konetzke, M.Rutsch, M. Hoffman, A. Hunger , "Phased array transducer for emitting 40-kHz air-coupled ultrasound without grating lobes," *IEEE International Ultrasonics Symposium (IUS),* pp. 1-4, 2015.

[21] M. Kobayashi, Y. Ono, C.K. Jen, and C.C. Cheng, "High-temperature piezoelectric film ultrasonic transducers by a sol-gel spray technique and their application to process monitoring of polymer injection molding," *IEEE Sensors Journal,* vol. 6, no. 1, pp. 55-62, 2006.

[22] L. Chen and M. Mehregany, "A silicon carbide capacitive pressure sensor for in-cylinder pressure measurement," *Sensors and Actuators,* vol. 145, pp. 2-8, 2008.

[23] I. O. Wygant, X. Zhuang, D. T. Yeh, O. Oralkan, A. S. Ergun, M. Karaman, "Integration of 2D CMUT arrays with front-end electronics for volumetric ultrasound imaging," *IEEE Transactions on Ultrasonics, Ferroelectrics, and Frequency Control,* vol. 55, no. 2, pp. 327-342, 2008.

[24] C. B. Doody, X. Cheng, C. A. Rich, D. F. Lemmerhirt, and R. D. White, "Modeling and characterization of CMOS-fabricated capacitive micromachined ultrasound transducers," *Journal of Microelectromechanical Systems,* vol. 20, no. 1, pp. 104-118, 2010.

[25] J. M. Rothberg, T. S. Ralston, A. G. Rothberg, J. Martin, S. A. Aliea, "Ultrasound-on-chip platform for medical imaging, analysis, and collective intelligence," *Proceedings of the National Academy of Sciences,* vol. 118, no. 27, 2021.

[26] J. Wang, Z. Zheng, J. Chan, and J. T. Yeow, "Capacitive micromachined ultrasound transducers for intravascular ultrasound imaging," *Microsystems & Nanoengineering,* vol. 6, no. 1, pp. 1-13, 2020.

[27] J. Zahorian, , R. Guldiken, G. Gurun, M. S. Qureshi, M. Balantekin, P. Hasler , "Single chip CMUT arrays with integrated CMOS electronics: Fabrication process development and experimental results," *IEEE Ultrasonics Symposium Proceedings*, pp. 386-389, 2008.

[28] K. Park, H. Lee, M. Kupnik, O. Oralkan, and B. Khuri-Yakub, "Fabricating capacitive micromachined ultrasonic transducers with direct wafer-bonding and LOCOS technology," *IEEE 21st International Conference on Micro Electro Mechanical Systems*, pp. 339-342, 2008.

[29] A. I. H. Chen, L. L. P. Wong, Z. Li, S. Na and J. T. W. Yeow, "Practical CMUT Fabrication With a Nitride-to-Oxide-Based Wafer Bonding Process," in *Journal of Microelectromechanical Systems*, vol. 26, no. 4, pp. 829-836, Aug. 2017.

[30] P. Smeys, P. Johnson, and G. Percin, "Method and system for forming a capacitive micromachined ultrasonic transducer," United State Patent 08222065, July 17, 2012.

[31] A. Coppa, E. Cianci, V. Foglietti, G. Caliano, and M. Pappalardo, "Building CMUTs for imaging applications from top to bottom," *Microelectronic engineering*, vol. 84, no. 5-8, pp. 1312-1315, 2007.

[32] A. Caronti, A. Coppa, A. Savoia, C. Longo, P. Gatta, B. Mauti , "Curvilinear capacitive micromachined ultrasonic transducer (CMUT) array fabricated using a reverse process," *IEEE Ultrasonics Symposium*, pp. 2092-2095, 2008.

[33] X. F. Zhuang, D. S. Lin, O. Oralkan, and B. T. Khuri-Yakub, "Fabrication of flexible transducer arrays with through-wafer electrical interconnects based on trench refilling with PDMS," *Journal of Microelectromechanical Systems*, vol. 17, pp. 446-452, 2008.

[34] A. S. Ergun, Y. L. Huang, X. F. Zhuang, O. Oralkan, G. G. Yaralioglu, and B. T. Khuri-Yakub, "Capacitive micromachined ultrasonic transducers: Fabrication technology," *IEEE Transactions on Ultrasonics, Ferroelectrics, and Frequency Control*, vol. 52, pp. 2242-2258, 2005.

[35] A. S. Ergun, Y. L. Huang, X. F. Zhuang, O. Oralkan, G. G. Yaralioglu, and B. T. Khuri-Yakub, "Capacitive micromachined ultrasonic transducers: Fabrication technology," *IEEE Transactions on Ultrasonics, Ferroelectrics, and Frequency Control*, vol. 52, pp. 2242-2258, 2005.

[36] A. Logan and J. T. W. Yeow, "Fabricating capacitive micromachined ultrasonic transducers with a novel silicon-nitride-Based wafer bonding process," *IEEE Transaction on Ultrasonics, Ferroelectrics and Frequency Control*, vol. 56, no. 5, pp. 1074-1084, 2009.

[37] M. Cetin and B. Bayram, "Diamond-Based Capacitive Micromachined Ultrasonic Transducers in Immersion", *IEEE Transaction on Ultrasonics, Ferroelectrics and Frequency Control*, vol. 60, no. 2, pp. 414-420, 2013.

[38] D. Gerardo , E. Cretu, R. Rohling, "Fabrication and testing of polymer-based capacitive micromachined ultrasound transducers for medical imaging*", Microsystems & Nanoengineering*, vol. 4, no. 19, pp. 568-579, 2018.

[39] R. Maity, N. P. Maity, K. S. Rao, K. Guha, and S. Baishya, "A new compact analytical model of nanoelectromechanical systems-based capacitive micromachined ultrasonic transducers for pulse echo imaging," *Journal of Computational Electronics*, vol. 17, no. 3, pp. 1334-1342, 2018.

[40] Y. Huang, X. Zhuang, E. O. Haeggstrom, A. S. Ergun, C.H. Cheng, and B. T. Khuri-Yakub, "Capacitive micromachined ultrasonic transducers with piston-shaped membranes: Fabrication and experimental characterization," *IEEE Transactions on Ultrasonics, Ferroelectrics, and Frequency Control*, vol. 56, no. 1, pp. 136-145, 2009.

[41] X. Jin, I. Ladabaum, and B. T. Khuri-Yakub, "The microfabrication of capacitive ultrasonic transducers,"*Journal of Microelectromechanical Systems*, vol. 7, no. 3, pp. 295-302, 1998.

[42] M. Meloche and S. Chowdhury, "Design of a MEMS discretized hyperbolic paraboloid geometry ultrasonic sensor microarray," *IEEE Transactions on Ultrasonics, Ferroelectrics, and Frequency Control*, vol. 55, no. 6, pp. 1363-1372, 2008.

[43] Y. Huang, A. S. Ergun, E. Haeggstrom, M. H. Badi, and B. T. Khuri-Yakub, "Fabricating capacitive micromachined ultrasonic transducers with wafer-bonding technology," *Journal of Microelectromechanical Systems,* vol. 12, no. 2, pp. 128-137, 2003.

[44] M. Chiurazzi, G. G. Garozzo, P. Dario, and G. Ciuti, "Novel Capacitive-Based Sensor Technology for Augmented Proximity Detection," *IEEE Sensors Journal,* vol. 20, no. 12, pp. 6624-6633, 2020.

[45] Q. Zhang, P.V. Cicek, K. Allidina, F. Nabki, and M. N. El-Gamal, "Surface-micromachined CMUT using low-temperature deposited silicon carbide membranes for above-IC integration," *Journal of Microelectromechanical Systems,* vol. 23, no. 2, pp. 482-493, 2014.

[46] Z. Mehmood, I. Haneef, and F. Udrea, "Material selection for Micro-Electro-Mechanical-Systems (MEMS) using Ashby's approach," *Materials & Design,* vol. 157, pp. 412-430, 2018.

[47] A. Fleischman, S. Roy, C. Zorman, M. Mehregany, and L. Matus, "Polycrystalline silicon carbide for surface micromachining," *Proceedings of Ninth International Workshop on Micro Electromechanical Systems*, pp. 234-238. 1996.

[48] A. C. Hoogerwerf, G. S. Durante, R. J. James, M.-A. Dubois, O. Dubochet, and M. Despont, "Silicon carbide pressure sensors for harsh environments," *20th International Conference on Solid-State Sensors, Actuators and Microsystems & Eurosensors*, pp. 2154-2157, 2019.

[49] L. Pakula, H. Yang, H. Pham, P. French, and P. Sarro, "Fabrication of a CMOS compatible pressure sensor for harsh environments," *Journal of Micromechanics and Microengineering,* vol. 14, no. 11, pp. 1478-1485, 2004.

[50] V. Rajaraman, L. Pakula, H. Pham, P. Sarro, and P. French, "Robust wafer-level thin-film encapsulation of microstructures using low stress PECVD silicon carbide," *IEEE 22nd International Conference on Micro Electro Mechanical Systems*, pp. 140-143, 2009.

[51] H. Zhang, H. Guo, Y. Wang, G. Zhang, and Z. Li, "Study on a PECVD SiC-coated pressure sensor," *Journal of Micromechanics and Microengineering,* vol. 17, no. 3, pp. 426-431, 2007.

[52] M. A. Fraga, "Comparison between the piezoresistive properties of a-SiC films obtained by PECVD and magnetron sputtering," *Materials Science Forum,* vol. 679, pp. 217-220, 2011.

[53] C. Iliescu, B. Chen, D. P. Poenar, and Y. Y. Lee, "PECVD amorphous silicon carbide membranes for cell culturing," *Sensors and Actuators B: Chemical,* vol. 129, no. 1, pp. 404-411, 2008.

[54] R. Ghodssi and P. Lin, *MEMS Materials and Processes Handbook*: Springer US, 2011.

[55] N. Ledermann, J. Baborowski, P. Muralt, N. Xantopoulos, and J.-M. Tellenbach, "Sputtered silicon carbide thin films as protective coating for MEMS applications," *Surface and Coatings technology,* vol. 125, no. 13, pp. 246-250, 2000.

[56] S. Inoue, T. Namazu, H. Tawa, M. Niibe, and K. Koterazawa, "Stress control of a-SiC films deposited by dual source dc magnetron sputtering," *Vacuum,* vol. 80, no. 7, pp. 744-747, 2006.

[57] L. Gou, C. Qi, J. Ran, and C. Zheng, "SiC film deposition by DC magnetron sputtering," *Thin Solid Films,* vol. 345, no. 1, pp. 42-44, 1999.

[58] D. G. Jones, R. G. Azevedo, M. W. Chan, A. P. Pisano, and M. B. Wijesundara, "Low temperature ion beam sputter deposition of amorphous silicon carbide for wafer-level vacuum sealing," *IEEE 20th International Conference on Micro Electro Mechanical Systems (MEMS)*, pp. 275-278, 2007.

[59] J. Edmond, J. Palmour, and R. Davis, "Chemical etching of ion implanted amorphous silicon carbide," *Journal of the Electrochemical Society,* vol. 133, no. 3, pp. 650-654, 1986.

[60] M. Farsari, G. Filippidis, S. Zoppel, G. A. Reider, and C. Fotakis, "Efficient femtosecond laser micromachining of bulk 3C-SiC," *Journal of Micromechanics and Microengineering,* vol. 15, no. 9, pp. 1786-1791, 2005.

[61] J. Zhu and S. Wang, "An investigation into the SiC anti-ablation membrane of MEMS microthrusters," *Symposium on Design, Test, Integration and Packaging of MEMS/MOEMS (DTIP)*, pp. 1-4, 2017.

[62] A. V. Lagosh, V. A. Golubkov, V. A. Ilyin, A. V. Korlyakov, and V. V. Luchinin, "Silicon carbide micromechanical and autoemission structure-based RF switches for harsh environments," *IEEE International Symposium on Radio-Frequency Integration Technology (RFIT)*, pp. 1-3, 2008.

[63] D. M. Mills, "Medical imaging with capacitive micromachined ultrasound transducer (cMUT) arrays," *IEEE Ultrasonics Symposium,* vol. 1, pp. 384-390, 2004.

[64] A. Caronti, G. Caliano, R. Carotenuto, A. Savoia, M. Pappalardo, E. Ciani, and V. Foglietti, "Capacitive micromachined ultrasonic transducer (CMUT) arrays for medical imaging," *Microelectronics Journal*, vol. 37, no. 8, pp. 770-777, 2006.

[65] R. Boubenia, P. Le Moal, G. Bourbon, E. Ramasso, and E. Joseph, "CMUT-Based Sensor for Acoustic Emission Application: Experimental and Theoretical Contributions to Sensitivity Optimization," *Sensors*, vol. 21, no. 6, pp. 2042-2046, 2021.

[66] R. O. Guldiken, J. McLean, and F. L. Degertekin, "CMUTS with dual electrode structure for improved transmit and receive performance," *IEEE Transactions on Ultrasonics, Ferroelectrics, and Frequency Control*, vol. 53, no. 2, pp. 483-491, 2006.

[67] M. N. Şenlik, S. Olcum, and A. Atalar, "Improved performance of CMUT with nonuniform membranes," *Proceedings IEEE Ultrasonics Symposium*, pp. 597-600, 2005.

[68] P. J. French and P. M. Sarro, “Surface versus bulk machining: The contest for suitable applications,” *Journal of Micromechanics and Microengineering,* vol. 8, pp. 45–53, 1998.

[69] S. Zhou, P. Reynolds, and J. A. Hossack, “Improving the performance of capacitive micromachined ultrasound transducers using modified membrane

and support structures," *IEEE Ultrasonics Symposium Proceedings*, pp. 1925–1928, 2005.

[70] Z. Zheng, W. Sun, X. Suo, L. L.P. Wong, Z. Sun, T.W. Yeow, "A novel deflection shape function for rectangular capacitive micromachined ultrasonic transducer diaphragms," *Sensing and Bio-Sensing Research*, vol. 5, pp. 62–70, 2015.

[71] S. K. Tiwari, B. S. Satyanarayana, A. Gopalkrishna Pai, K. K. Trivedi, N. S. Rahul and P. Sahay, "Hexagonal Capacitance Micromachined Ultrasonic Transducer," *International Conference on Computing, Communication and Networking*, pp. 1-4, 2008.

[72] M. Rahman and S. Chowdhury, "A new deflection shape function for square membrane CMUT design," *Proceedings of 2010 IEEE International Symposium on Circuits and Systems*, pp. 2019-2022, 2010.

[73] L. Jia, C. He, C. Xue, and W. Zhang, "The device characteristics and fabrication method of 72-element CMUT array for long-range underwater imaging applications", *Microsystem Technologies*, vol. 25, no. 7, pp. 1195–1202, 2019.

[74] M.S. Salim, M.F. Abd. Malek, N. Sabri, N.M. Noaman, K.M. Juni, " Survey on Ultrasonic Transducers Technology", *Australian Journal of Basic and Applied Sciences*,vol.7 , no. 2, pp- 639-651, 2013.

[75] R. Zhang, C. Xue, C. He, L. Jia, "Design and performance analysis of capacitive micromachined ultrasonic transducer (CMUT) array for underwater imaging" *Microsystem Technologies* , vol. 22, no. 3, pp. 2939–2947, 2016.

[76] O. Oralkan, A. S. Ergun, C. Cheng, J. A. Johnson, M. Karaman and B. T. Khuri-Yakub, "Underwater acoustic imaging using capacitive micromachined ultrasonic transducer arrays," *OCEANS '02 MTS*, vol. 4, pp. 2354-2360, 2002.

[77] B. T. Khuri-Yakub, O. Oralkan," Capacitive micromachined ultrasonic transducers for medical imaging and therapy", *Journal of Micromechanics and Microengineering*, vol. 21, no. 5, pp. 54004-54014, 2011.

[78] C. D. Gerardo , E. Cretu, R. Rohling, “Fabrication and testing of polymer-based capacitive micromachined ultrasound transducers for medical imaging*”, Microsystems & Nanoengineering*, vol. 4, no. 19, pp. 568-579, 2018.

[79] G. G. Yaralioglu, A. S. Ergun, B. Bayram, E. Haeggstrom and B. T. Khuri-Yakub, "Calculation and measurement of electromechanical coupling coefficient of capacitive micromachined ultrasonic transducers," in *IEEE Transactions on Ultrasonics, Ferroelectrics, and Frequency Control*, vol. 50, no. 4, pp. 449-456, 2003,

[80] Q. Zhou, K. H. Lam, H. Zheng, W. Qiu, and K. K. Shung, "Piezoelectric single crystal ultrasonic transducers for biomedical applications," *Progress in materials science*, vol. 66, pp. 87-111, 2014.

[81] J. Cho, M. Anderson, R. Richards, D. Bahr, and C. Richards, "Optimization of electromechanical coupling for a thin-film PZT membrane: I. Modeling," *Journal of Micromechanics and Microengineering*, vol. 15, no. 10, pp. 1797-1801, 2005.

[82] S. Ergun, G. G. Yaralioglu, and B. T. Khuri-Yakub, "Capacitive micromachined ultrasonic transducers: Theory and technology," *Journal of Aerospace Engineering*, vol. 16, no. 2, pp. 76-84, 2003.

[83] R. O. Guldiken, J. Zahorian, F. Yamaner, and F. L. Degertekin, "Dual-electrode CMUT with non-uniform membranes for high electromechanical coupling coefficient and high bandwidth operation," *IEEE Transactions on Ultrasonics, Ferroelectrics, and Frequency Control*, vol. 56, no. 6, pp. 1270-1276, 2009.

[84] K. K. Park, M. Kupnik, H. J. Lee, B. Khuri-Yakub, and I. O. Wygant, "Modeling and measuring the effects of mutual impedance on multi-cell CMUT configurations," *IEEE International Ultrasonics Symposium*, pp. 431-434, 2010.

[85] T. A. Ritter, T. R. Shrout, R. Tutwiler, and K. K. Shung, "A 30-MHz piezo-composite ultrasound array for medical imaging applications," *IEEE*

Transactions on Ultrasonics, Ferroelectrics, and Frequency Control, vol. 49, no. 2, pp. 217-230, 2002.

[86] O. Oralkan, S. T. Hansen, B. Bayram, G. G. Yaralioglu, A. S. Ergun, and B. T. Khuri-Yakub, "High-frequency CMUT arrays for high-resolution medical imaging," *IEEE Ultrasonics Symposium,* vol. 1, pp. 399-402, 2010

[87] C. Cheng, A. Ergun, and B. Khuri-Yakub, "Electrical through-wafer interconnects with sub-picofarad parasitic capacitance [MEMS packaging]," in *2001 Microelectromechanical Systems Conference*, pp. 18-21, 2001

[88] X. Zhuang, A. Ergun, O. Oralkan, Y. Huang and I. O. Wygant, "Through-wafer trench-isolated electrical interconnects for CMUT arrays," *IEEE Ultrasonics Symposium,* vol. 1, pp. 475-478, 2005

[89] C. Daft, S. Calmes, D. da Graca, K. Patel, P. Wagner, and I. Ladabaum, "Microfabricated ultrasonic transducers monolithically integrated with high voltage electronics," *IEEE Ultrasonics Symposium*, vol. 1, pp. 493-496, 2004

[90] S. Zhou and J. A. Hossack, "Reducing inter-element acoustic crosstalk in capacitive micromachined ultrasound transducers," *IEEE Transactions on Ultrasonics, Ferroelectrics, and Frequency Control,* vol. 54, no. 6, pp. 1217-1228, 2007.

[91] M. S. Salim, M. Abd Malek, R. Heng, K. Juni, and N. Sabri, "Capacitive micromachined ultrasonic transducers: Technology and application," *Journal of Medical Ultrasound*, vol. 20, no. 1, pp. 8-31, 2012.

[92] A. Caronti, G. Caliano, R. Carotenuto and V. Foglietti , "Capacitive micromachined ultrasonic transducer (CMUT) arrays for medical imaging," *Microelectronics Journal*, vol. 37, no. 8, pp. 770-777, 2006.

[93] D. M. Mills and L. S. Smith, "Real-time in-vivo imaging with capacitive micromachined ultrasound transducer (cMUT) linear arrays," *IEEE Symposium on Ultrasonics,* vol. 1, pp. 568-571, 2003.

[94] M. Legros, C. Meynier, R. Dufait, G. Ferin, and F. Tranquart, "Piezocomposite and CMUT arrays assessment through in vitro imaging performances," *IEEE Ultrasonics Symposium*, pp. 1142-1145, 2008.

[95] A. Nikoozadeh, B. Bayram, G Yaralioglu, B.T. Khuri Yakub," Analytical calculation of collapse voltage of CMUT membrane." *IEEE Ultrasonics Symposium*, pp. 256–259, 2004.

[96] A. Lohfink, P.C Eccardt, W Benecke, H. Meixner, "Derivation of a 1D CMUT model from FEM results for linear and nonlinear equivalent circuit simulation", *Proceedings IEEE Symposium on Ultrasonics, Honolulu,* pp. 465–468, 2003.

[97] A. Lohfink and P.C. Eccardt, "Linear and nonlinear equivalent circuit modeling of CMUTs." *IEEE Transactions on Ultrasonics, Ferroelectrics, and Frequency Control*, vol. 52,no. 2, pp. 2163–2172, 2005

[98] G. Yaralioglu, S Ergun, B.T. Khuri Yakub, "Finite-element analysis of capacitive micromachined ultrasonic transducers," *IEEE Transactions on Ultrasonics, Ferroelectrics, and Frequency Control*, vol. 52, no. 11, 2185–2198, 2005.

[99] M. Kupnik, I.O Wygant, B.T. Khuri Yakub, "Finite element analysis of stress stiffening effects in CMUTS," *IEEE Ultrasonics Symposium,* pp. 487–490 , 2008.

[100] O. Oralkan, B. Bayram, G. G. Yaralioglu, A. S. Ergun, M. Kupnik, D. T. Yeh, I. O. Wygant, and B. T. Khuri-Yakub, "Experimental characterization of collapse-mode CMUT operation," *IEEE Transactions on Ultrasonics, Ferroelectrics, and Frequency Control*, vol. 53, no. 8, pp. 1513–1523, 2006.

[101] A. S. Savoia, G. Scaglione, and B. Haider, "Combined use of Finite Element and Equivalent Circuit Modeling for System-Level Simulation of Integrated Capacitive Micromachined Ultrasonic Transducers (CMUT)," *IEEE International Ultrasonics Symposium (IUS)*, pp. 1-4, 2020.

[102] B Bayram, G. Yaralioglu, M Kupnik, A Ergun, O. Oralkan, A. Nikoozadeh, B. Khuri Yakub, "Dynamic analysis of capacitive micromachined ultrasonic transducers," *IEEE Transactions on Ultrasonics, Ferroelectrics, and Frequency Control*, vol. 52, no. 6, pp. 2270–2275, 2005.

[103] G. G. Yaralioglu, A. S. Ergun, and B. T. Khuri-Yakub, "Finite-element analysis of capacitive micromachined ultrasonic transducers," *IEEE*

Transactions on Ultrasonics, Ferroelectrics, and Frequency Control, vol. 52, no. 12, pp. 2185–2198, 2005.

[104] B. Ma, C. Chang, H.K. Oguz, K. Firouzi, B.T. Khuri Yakub, "Multi-parameter optimization of vented CMUTs for airborne applications, " *IEEE International Ultrasonics Symposium (IUS)*, pp. 1–4 , 2017.

[105] N. Apte, K.K. Park, B.T. Khuri Yakub, "Finite element analysis of CMUTs with pressurized cavities," *IEEE International Ultrasonics Symposium, Dresden, Germany,* pp. 979–982, 2012.

[106] N. Apte, K. Park, A. Nikoozadeh, B. T. Khuri Yakub, "Bandwidth and sensitivity optimization in CMUTs for airborne applications," *IEEE International Ultrasonics Symposium, Chicago,* pp. 166–169, 2014.

[107] O. Wygant, K. Mario, "Analytically Calculating Membrane Displacement and the equivalent Circuit Model of a Circular CMUT Cell", *IEEE International Ultrasonics Symposium* ,pp. 167-170, 2008.

[108] P. Eccardt, K. Niederer, T. Scheiter, and C. Hierold, " Surface micromachined ultrasound transducers in CMOS technology," *IEEE International Ultrasonics Symposium Ultrasonics Symposium*, pp. 959-962, 1996.

[109] Y. Nemirovsky and O. Bochobza-Degani, "A methodology and model for the pull-in parameters of electrostatic actuators," *Journal of Microelectromechanical Systems,* vol. 10, no. 4, pp. 601–615, 2001.

[110] N. Jones, "A Theoretical Study of the Dynamic Plastic Behavior of Beams and Plates with Finite-Deflections," *International Journal of Solids and Structures*, vol, 6, no. 12, pp. 1007-1029, 1971.

[111] N. Jones, "On the Mass Impact Loading of Ductile Plates, " *Defence Science Journal, Defence Research and Development Organisation,* vol. 53, no.1, pp. 15-24, 2003.

[112] N. Jones, "A Literature Review of the Dynamic Plastic Response of Structures," *The Shock and Vibration Digest*, vol. 7, no. 8, pp. 89-105, 1975.

[113] N. Jones, "Impulsive Loading of a Simply Supported Circular Rigid-Plastic Plate" *Journal of Applied Mechanics,* vol. 35, no.1, pp. 59-65, 1968.

[114] N. Jones, "The Credibility of Predictions for Structural Design Subjected to Large Dynamic loadings Causing Inelastic Behaviour," *International Journal of Impact Engineering,* vol. 53,no. 9, pp.106-114, 2013.

[115] N. Jones, "Damage of plates due to impact, dynamic pressure and explosive loads," *Latin American Journal of Solids and Structures* , vol.10, no. 11, pp. 767 – 780, 2000.

[116] M. Badi, G. Yaralioglu, A. Ergun, F. Degertekin, C. Cheng, B. Khuri-Yakub, "A First Experimental Verification of Micromachined Capacitive Lamb Wave Transducers", *Proc. IEEE Ultrasonics Symposium,* pp-311-314, 2000.

[117] H. H. J. Huynen, F. H. Dijkstra and T. Bouma: "Advance in ultrasonic trasducer development," *IEEE Transactions on Ultrasonics, Ferroelectrics, and Frequency Control*, vol. 27, no. 8, pp. 611–618, 2000.

[118] I. Matthew Haller and T. Butrus. Khuri-Yakub, "A new regime for operating capacitive micromachined ultrasonic transducers," *IEEE Transactions on Ultrasonics, Ferroelectrics, and Frequency Control*, vol. 43, no. 3, 1996.

[119] R. Maity, N. P. Maity, R. K. Thapa, S. Baishya, "Investigation of Silicon Nitride as an Excellent Membrane Material for MEMS Ultrasonic Transducers," *Applied Mechanics and Materials,*vol. 45, no. 17, pp. 567-571, 2017.

CHAPTER

3

Device Capacitance

3.1 Introduction

Ultrasonic transducers have been widely used in clinical imaging in recent years, involving the use of composites with different crystals, piezoelectric materials, ceramics, and piezo composite materials. MUTs have emerged in the research sector as a solution to the shortcomings of piezoelectric transducers. CMUT is a type of MUT that works by varying capacitance and then modulating electrostatic force.

3.1.1 Transducer capacitive action

Fabrication can be performed by surface micromachining technique or involving fusion bonding process at high temperature [1–4]. Square, circular or hexagonal geometry is included for constructing the diaphragm of a typical CMUT, which is supported on a fixed bottom electrode. This bottom electrode is separated from the top electrode by a small cavity filled with vacuum or air making the structure equivalent to a capacitor as in Fig. 3.1.

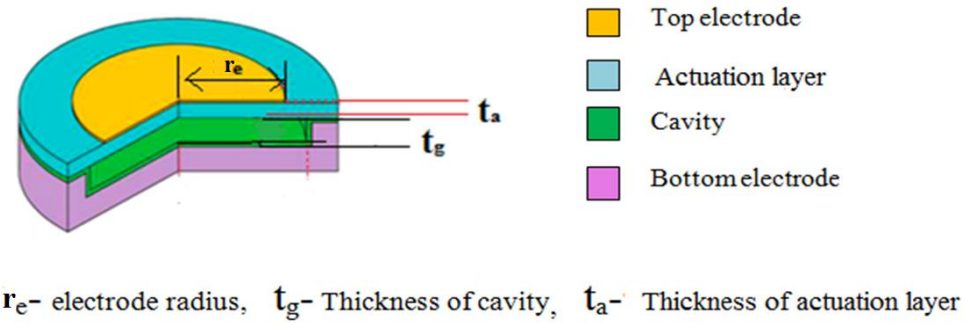

Fig. 3.1 3D view of circular non-insulated cell

Dimension of a typical CMUT used extensively for medical imaging includes structural layer thickness of 750 nm with 50 µm diameter, cavity height of 1µm, and top electrode thickness of 50 nm [5]. Many research papers have been analyzed

considering this dimension in order to facilitate the design as an electrostatic actuator for medical imaging for enhanced sensitivity [9].

Working of this transducer is based on capacitive action where the structure performs as a variable capacitor where the top electrode acts as a diaphragm and is free to move or deform against the bottom electrode. As a result, variation in capacitance takes place due to a change in distance between these two electrodes. Hence it can be considered as a capacitor cell that consists of a thin moveable film suspended upon a vacuum gap. The top electrode of the device sometimes becomes metal coated and is used as one of the electrodes for the capacitor. During transmitting mode, resonance takes place due to the application of bias voltage along with superimposed desired signal to the geometry. Consequently, an electrostatic force is generated which causes the diaphragm to vibrate and create ultrasonic vibration in the surrounding medium. During the receiving mode, the device gets exposed to the incident ultrasound wave, and as a result, deformation takes place in the diaphragm towards the fixed bottom electrode due to sound pressure. As the distance between the top and bottom electrodes changes so variation in capacitance occurs. The change in capacitance is then transformed to an equivalent electrical signal by a suitable microelectronic circuit. Accumulation of mechanical part along with microelectronic circuit tends this capacitive element to be considered as MEMS with capacitive working principle.

3.1.2. Various geometrical structures

Among various structures of CMUT, the hexagonal one has the highest packaging density among rectangular, circular, and square geometries [6-7]. For ease of mathematics, a circular approximation is usually carried out for hexagonal layers. Deformation will take place in the structural layer, leading to a forceful variation in the capacitance between the deformed layer and the fixed electrode [8]. During analytical modeling of deflection, this shape function is considered in accurate manner to explain the deflection of the deformed layer. In addition to that this shape function is also used to determine the effect of specific geometry parameters. Deflection shape functions of square and circular geometries have been widely studied by many authors. Modelling of rectangular layers is also worth

studying because they have exhibited the potential in improving the fill factor and the performance is compared with square ones. Based on different test experiments the circular geometry produces good repeatability and can be involved for long-distance underwater object detection, distance measurement as deflection is highest compared to other geometrical structures and can be utilised for high intensity frequency application.

3.1.3 Silicon Carbide (SiC) as a structural material

Materials used for structural layers are metals like nickel, aluminum, non-metals like silicon (Si), germanium (Ge), polymers like SU8, polyamide like a diamond, silicon carbide (SiC), silicon nitride (Si_3N_4), and silicon dioxide (SiO_2) [10-12]. Si_3N_4 is considered as one of the finest elements to be used that is quite capable of emitting and detecting ultrasonic waves in the air. Enhanced penetration by high pressure transmission and better signal to noise ratio can be achieved. Along with all these features, CMUT can also be involved in imagery application where tissue heating is done frequently. For this type of application, SiC can be adopted as the fittest one. The involvement of SiC will make the fabrication possible at a lower temperature compared to Si_3N_4 and can be considered as a suitable material for better mechanical and electrical properties while designing effectively for high frequency application. SiO_2 is commonly used to realize the dielectric spacer.

3.1.4 Inclusion of insulation layer

The gap between the top and bottom electrodes can be traversed during operation and can create an electrical shock during the full swing in transmit mode and at collapsed operation during receiving mode. Due to capacitive action, high electric field is generated between the two oppositely charged electrodes which generate adhesion force and electrical hazards. The hazards caused by improper insulation are a matter of concern when involved in biomedical imaging [13]. Necessity of insulation layer is stated through analytical modeling and characterization study of a SiC based insulated CMUT. A high-K dielectric layer exists between the electrodes as a preventive measure from being affected by electric shock. Inclusion of an insulation layer permits the patterning of the upper electrode

at the lower surface of the actuation layer as shown in Fig. 3.2 (a). A structure without an insulation layer is shown in Fig. 3.2(b) where the actuation layer is placed just below the top electrode to get prevented from electric shock.

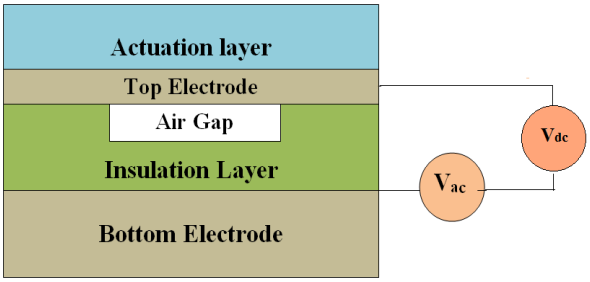

Fig. 3.2 (a) Insulated Structure

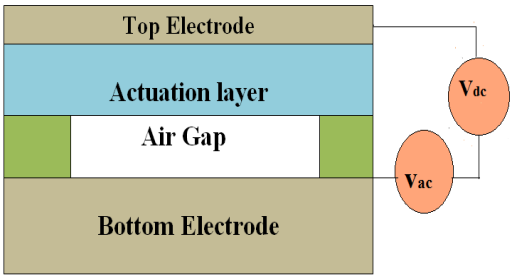

Fig 3.2 (b) Non-insulated Structure

The difference in work function raises the electrostatic force between the substrate and the surface which is responsible enough for the transition of electrons between the two electrical layers. When the top electrode comes into contact with the bottom one the energy becomes low and it remained stuck as the total removal energy reached the minimum level. This total energy consisting of energy restored for deformation and attraction is experienced by the surface.

3.1.5 High-K material as an insulation layer

Choice of the dielectric material for the insulation layer is done in such a manner so that it can endure the electric field generated in the device due to electrostatic attraction force [14-16]. As designing of sensitive CMUT is the most important criterion hence, the choice of high-K dielectric material should enhance the efficiency for generating high electric field by not decreasing the transduction gap and without further increasing in bias voltage both in transmitting and receiving mode. Mostly, high-K materials having a range of dielectric constant (K) between 3.9 and 200 are elaborated nicely in literature [17]. According to this, the breakdown strength E_{bd} of a dielectric material decreases with the increase in the value of the dielectric constant. As per the description done by thermochemical properties, reduction of ultimate breakdown strength takes place apparently with $K^{-1/2}$. Hence all high-K materials are not at all a good choice due to their insufficient amount of breakdown strength, which is quite essential for maintaining isolation thickness in

nanometer range. Keeping all these phenomenons under consideration, hafnium dioxide (HfO_2) can be considered as it maintains a balance between its breakdown strength and dielectric constant which is needed for low temperature fabrication process in nano dimensional features.

3.2 Effect of fringing fields

For a CMUT structure, the thickness of the actuation layer and gap separation becomes equivalent to the electrodes' diameters so the electric field curves at the boundaries and ranges to adjacent distant locations as the fringing fields. This fringing field augments the equivalent capacitance of the device. Meanwhile; the fringing field is also accountable for the charge storing effect; it similarly impacts the connected capacitance. In a circular-disk capacitor, Younes Ataiiyan's method [18] could be pragmatic to develop their connection. It embraces the static deformation convinced by the polarizing voltage and the fringing field. As a result, displacement profile including fringing effect supports the experimental and simulated outcomes stronger than that excluding it [19-21].

In order to model the capacitance, fringing field must be considered with suitable boundary settings. Fringing capacitances are evident in the actuation layer, the cavity, and the insulation layer. It increases the capacitance and the electrostatic force. Effects of fringing field in electrostatic actuator and in a time-varying serial capacitor of different models are discussed in [22-24]. This capacitor is pragmatic to the control of parallel-plate electrostatic microactuators [25]. Further, the modern approach is the practical principles derived centered on the experiments of ultrasonic waves. Certain latest works on the application of these capacitance prototypes are also seen, where amended capacitance model of radiofrequency (RF) MEMS shunt switching integrating fringing field effects of the perforated beam is derived [26]. Square diaphragm CMUT for fringing field effect has also been examined [27].

3.3 Improved capacitance modeling of a non-insulated element

A non- insulated element as in Fig. 3.2 (b) entails a thin metalized actuation layer of thickness 750 nm and electrode diameter 50 µm establishing one of the electrodes over very small gap of 500 nm over the profoundly doped Si. The upper surface of the Si base is metalized to form the lower electrode [9]. Comparative analysis is carried out between Si_3N_4 and SiC as actuation layers. The CMUT is sustained by pillars of SiO_2.

The metallization is prepared with aluminum (Al) as the upper metal. The direct capacitances for a fully metalized CMUT for gap and actuation layers are,

$$C_g = \left\{ \left(\varepsilon_g A \right) / t_g \right\} \tag{3.1}$$

$$C_a = \left\{ \left(\varepsilon_a A \right) / t_a \right\} \tag{3.2}$$

Where, t_g is gap separation, t_a is the thickness of actuation layer and $A = \pi r_e^2$ represents the area of the electrodes where r_e is the radius of the electrode. $K_a \varepsilon_g = \varepsilon_a$, denotes permittivity of actuation layer, K_a is the relative dielectric constant, ε_g is the permittivity of gap and the value is 8.85×10^{-12} $C^2/(N\text{-}m^2)$.

Equivalent device capacitance is derived as,

$$C_{eq} = \left(C_a \times C_g \right) / \left(C_a + C_g \right) \tag{3.3}$$

$$\frac{1}{C_{eq}} = \frac{t_g}{\varepsilon_g A} + \frac{t_a}{K_a \varepsilon_g A} = \frac{\varepsilon_g A}{t_g + \frac{t_a}{K_a}} = \frac{\varepsilon_g \pi r_e^{\,2}}{t_g + \frac{t_a}{K_a}} \tag{3.4}$$

A compact technique is available as Landau and Lifschitz approach. In this method the effective capacitance including fringing is,

$$C = \frac{\varepsilon \pi r^2}{d} + \varepsilon r \ln\left(\frac{16\pi r}{d} - 1\right) \tag{3.5}$$

ε is the permittivity of the dielectric, r and d are the radius and the separation between the electrodes respectively. Considering fringing effect, the total capacitance of the gap is C_{gf} and that of actuation layer is C_{af}. This gives, the following (3.6) and (3.7) respectively,

$$C_{gf} = \varepsilon_g \left[\left(\frac{\pi r_e^{\,2}}{t_g} \right) + r_e \ln \left\{ \left(\frac{16\pi r_e}{t_g} \right) - 1 \right\} \right] \tag{3.6}$$

$$C_{af} = \varepsilon_a \left[\left(\frac{\pi r_e^{\,2}}{t_a} \right) + r_e \ln \left\{ \left(\frac{16\pi r_e}{t_a} \right) - 1 \right\} \right] \tag{3.7}$$

Now the equivalent capacitance due to fringing C_{eqf} can be denoted as the series capacitance of the actuation layer and the air gap capacitance. Therefore it is written as,

$$C_{eqf} = \left(C_{af} \times C_{gf} \right) \Big/ \left(C_{af} + C_{gf} \right) \tag{3.8}$$

Putting the expressions of (3.6) and (3.7), in (3.8), it can be expressed as

$$C_{eqf} = \frac{\left\{ \frac{\varepsilon_g \pi r_e^{\,2}}{t_g} + \varepsilon_g r_e \ln\left(\frac{16\pi r_e}{t_g} - 1 \right) \right\} \left\{ \frac{K_a \varepsilon_g \pi r_e^{\,2}}{t_a} + K_a \varepsilon_g r_e \ln\left(\frac{16\pi r_e}{t_a} - 1 \right) \right\}}{\left\{ \frac{\varepsilon_g \pi r_e^{\,2}}{t_g} + \varepsilon_g r_e \ln\left(\frac{16\pi r_e}{t_g} - 1 \right) \right\} + \left\{ \frac{K_a \varepsilon_g \pi r_e^{\,2}}{t_a} + K_a \varepsilon_g r_e \ln\left(\frac{16\pi r_e}{t_a} - 1 \right) \right\}}$$

$$C_{eqf} = \frac{\left\{ \frac{\pi r_e}{t_g} + \ln\left(\frac{16\pi r_e}{t_g} - 1 \right) \right\} \left\{ \frac{K_a \pi r_e}{t_a} + K_a \ln\left(\frac{16\pi r_e}{t_a} - 1 \right) \right\}}{\left\{ \frac{\pi r_e}{t_g} + \ln\left(\frac{16\pi r_e}{t_g} - 1 \right) \right\} + \left\{ \frac{K_a \pi r_e}{t_a} + K_a \ln\left(\frac{16\pi r_e}{t_a} - 1 \right) \right\}} \tag{3.9}$$

3.4 FEM Simulation

Analytical modeling and simulation methods have equal importance for analyzing the transducer performance with various parameters. This computation technique is purely based on the mathematical generalization that generates a simple analysis to study the characteristics. It has a limitation to represent a real-time device as it only deals with the linear relationship between actuation layer deflection and applied force. It is needed to improve accuracy and precision by involving simulation method along with analytical modeling.

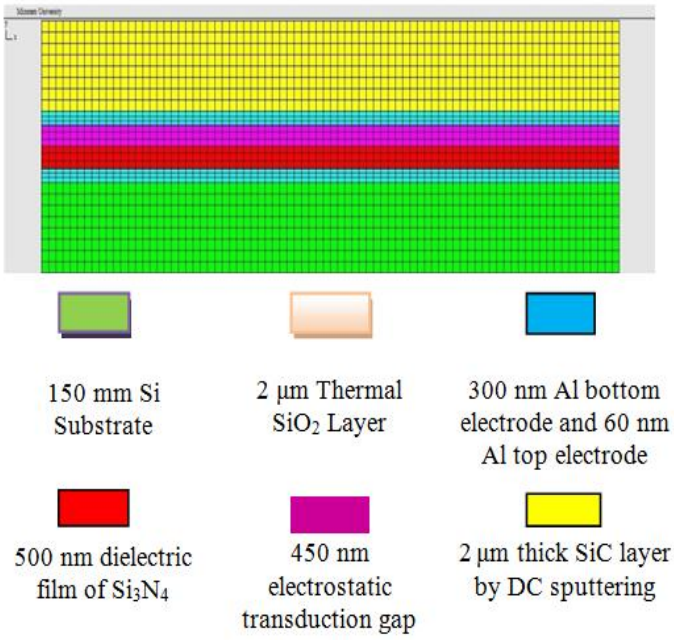

Fig. 3.3 FEM model Structure

In addition to this simulation can be considered in those cases, where formulation cannot be derived using analytical modeling as it provides analysis of parameters for each distinct case with a variety of function inputs. In this chapter finite element method (FEM) analysis is done to fully exemplify the device. Analyzed results are then validated with analytical modeling results. This will represent an insightful impact on CMUT behaviour. The dimension parameters such as device radius, actuation layer thickness, cavity depth, etc. are given in the geometry. The 2D FEM simulated insulated structure of the model is shown in Fig. 3.3 is done using PZFlex.

3.5 Comparative analysis of Si_3N_4 / SiC actuation layers

Keeping the basic structure of the CMUT unchanged; the material used in the actuation layer is changed to make a comparative study. As discussed in Fig. 3.2 (b) the actuation layer is altered by SiC as it has a comparatively higher dielectric constant, lower tensile stress, and higher Young modulus compared to Si_3N_4. Enhancement in device capacitance due to fringing is calculated as,

$$E_C = \left(\frac{C_{eqf} - C_{eq}}{C_{eq}} \right) \times 100 \tag{3.10}$$

Enhancement in device capacitance due to alteration of actuation layer by SiC is calculated as,

$$E_{SiC} = \left(\frac{C_{eqf\,(SiC)} - C_{eqf\,(Si_3N_4)}}{C_{eqf\,(Si_3N_4)}} \right) \times 100 \tag{3.11}$$

Where $C_{eqf\,(SiC)}$ and $C_{eqf\,(Si_3N_4)}$ are the device capacitances of a capacitive cell involving SiC and Si_3N_4 actuation layers respectively. Variation of capacitance due to change in electrode radius is shown in Fig. 3.4. As stated in (3.4) and (3.9) device capacitance is proportional to the square of the device radius; hence an increasing nature in device capacitance is observed.

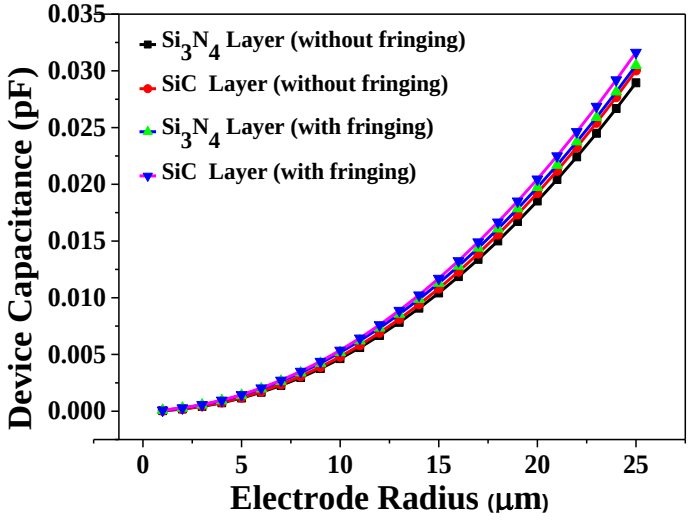

Fig. 3.4 Device capacitance due to change in electrode radius

The characteristic study shown in Fig. 3.5 depicts fringing capacitance contribution. The average E_C is 13% for Si_3N_4 and 15% for the SiC actuation layer. Moreover, in Fig. 3.6 capacitance enhancement of SiC cell compared to Si_3N_4 is plotted. A larger value of electrode radius produces higher enhancement. An average E_{SiC} of 9% is obtained. Hence larger impact in SiC actuation layer based device than Si_3N_4.

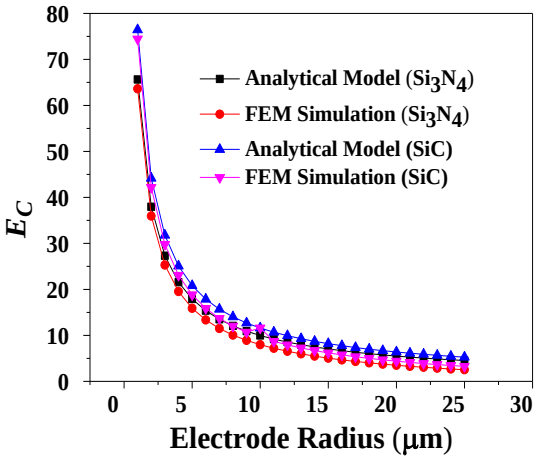

Fig. 3.5 E_C for varying electrode radius

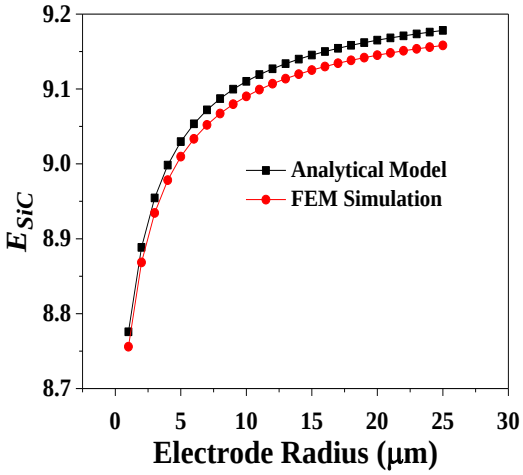

Fig. 3.6 E_{SiC} for varying electrode radius

Figure 3.7 shows the behavior of device capacitance due to a change in air gap separation. As depicted the decreasing nature proves the inverse proportionality between these two parameters. E_C and E_{SiC} variations with gap heights are shown in Figs. 3.8 and 3.9 respectively. The fringing effect is prominent mostly after 300nm of cavity height where an increasing slope is observed in the enhancement of device capacitance for both structures. Though initially, the difference between the E_C values was larger with increasing cavity height the difference diminishes gradually. Consequently, a decreasing nature of E_{SiC} is exhibited in Fig. 3.9. An average value of E_C is 4.32% for Si_3N_4 and 4.18 % for SiC actuation layer based structures. An average E_{SiC} of 6.4% is observed. Figure 3.10 shows device capacitance variation with the thickness of actuation layer. Similar to the variation with gap height, device capacitance also decreases due to increase in actuation layer thickness. Fringing effects are more profound at higher insulation thickness.

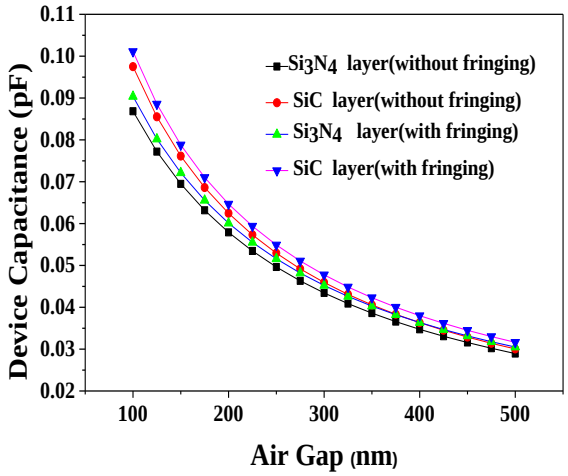

Fig. 3.7 Device capacitance due to change in air gap separation

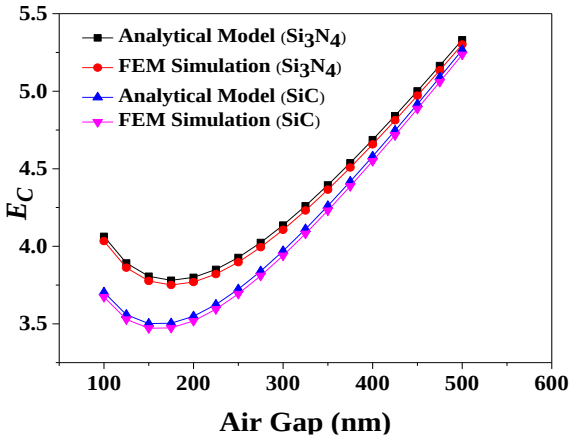

Fig. 3.8 E_C for varying air gap separation

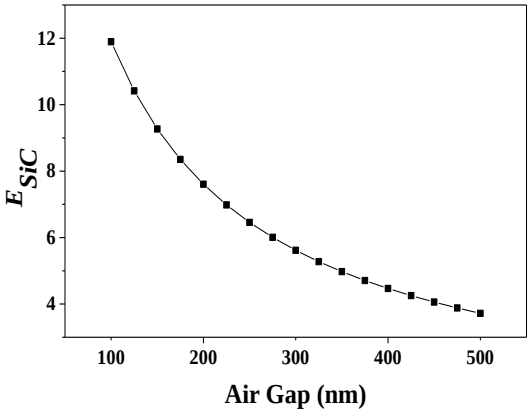

Fig. 3.9 E_{SiC} for varying air gap separation

E_C Value of SiC is comparatively higher than the same of Si_3N_4 for actuation layer thickness below 500nm but above it, the value becomes lower which is clearly depicted in Fig. 3.11. A plot of E_{SiC} with the variation of actuation layer thickness is shown in Fig. 3.12 where a sharp enhancement in device capacitance is observed due to the predominance effect of fringing. An average E_C of 5.01% is achieved in both Si_3N_4 and SiC actuation layers based elements. The involvement of SiC instead of Si_3N_4 produces an average E_{SiC} of 3.9% with the increase in actuation layer thickness. All the figures discussed in this section emphasize the usage of SiC as the fittest material for the actuation layer for achieving higher device capacitance. Henceforth an insulated structure is considered to have SiC as an actuation layer

[29]. Performance of insulated structure over non-insulated one is discussed in section 3.6 to investigate the necessity of insulation layer.

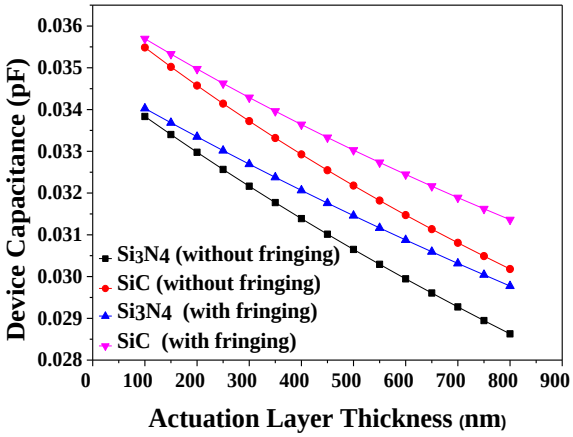

Fig. 3.10 Device capacitance and thickness of actuation layer

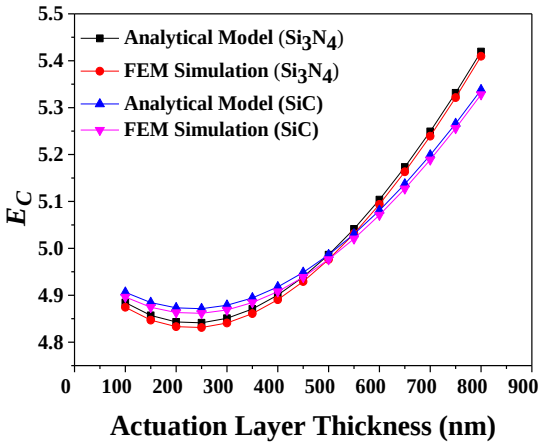

Fig. 3.11 E_C for varying actuation layer thickness

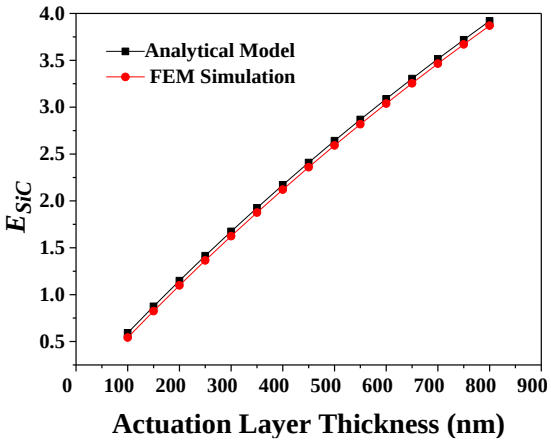

Fig. 3.12 E_{SiC} for varying actuation layer thickness

3.6 Device capacitance comparison between insulated and non-insulated structure

Comparatively better performance of SiC based non-insulated structure creates an acceptance for considering the material as actuation layer also in insulated structure. In addition to that its superior mechanical properties prove to be an efficient structural material for fabrication. Hence a comparative study is done in this section between SiC based non insulated and insulated structures. In insulated structure, above IC (Integrated Circuit) integration is materialized due to deposition of SiC at low temperature. As stated, this process is done at a very low thermal

budget below 200 ˚C for one hour [28]. High frequency application demands a high value of device capacitance which generally creates a large displacement value. Capacitance achieved at the above discussed non–insulated structure can be improved by involving an insulation layer of Si_3N_4 over the lower electrode. A capacitive structure having electrode radius a_e=55 µm, gap thickness $t_g = 450\,\text{nm}$, and actuation layer thickness t_a=2 µm is considered [28] for the purpose of characteristic study. The equivalent capacitance of a non-insulated structure is expressed in (3.9). Inclusion of an insulation layer allows the patterning of the upper electrode below the actuation layer as in Fig. 3.2 (a). The equivalent capacitance now consists of the series combination of the gap and the insulation layers.

3.6.1 Excellence of SiC based insulated CMUT

SiC exists in three significant structures: single-crystalline, multi-crystalline, and amorphous. On account of its excess deposition temperature, single-crystalline SiC has restricted use in MEMS that require customary sacrificial layer etching and material metallization. Due to its epitaxial nature, single-crystalline SiC has been widely explored for use in vicious climates. Examining the result set from Table 3.1 it is seen that SiC structure gives the highest aspect ratio. This aspect ratio has a great impact on higher order modes when its dynamic characteristic response is studied [32]. Increasing the aspect ratio fill factor can be increased which in turn increases the robustness of defects caused by fabrication. Fill factor consists the ratio of cavity area or active area of the device to the total device area. Involving SiC as actuation layer material for circular shaped structure the aspect ratio increases which gives a rise to fill factor. The increment in fill factor enhances the free-to-move area compared to the clamped perimeter of CMUT. Application of SiC based circular CMUT involves the combinational advantages of high Young's modulus (260 GPa) and low residual stress (30 MPa). Hence it can be used for extensive and robust displacement with the least deformation when kept at rest. Keeping the width of the actuation layer 30 µm with a separation of 3µm gap from the substrate generates flatness in an observable manner. Usage of polyimide reduces the risk of wet release method and involvement of hydrofluoric acid permits the placing of an upper

aluminum electrode directly below the SiC layer without any contamination. This optimized proximity between the upper and bottom electrode generates electromechanical coupling.

Table 3.1 Comparative study among various CMUT actuation layer materials

Type of CMUT	Electrode Radius (μm)	Type of Layers	Dielectric Constant of the Layer	Thickness of each Layer (nm)	CMUT Capacitance (pF)	% increment of capacitance value	Aspect Ratio of the CMUT
SiC based [28]	55	Si_3N_4	7.5	500	0.166	9.47	57.9:1
		air	1	450			
Si_3N_4 based [29]	25	Si_3N_4	7.5	400	0.0039	9.44	7:1
		air	1	150			
		Si_3N_4	7.5	250			
Diamond Based [30]	22	Diamond	5.7	1 000	0.0089	8.54	7.85:1
		SiO_2	3.9	230			
		air	1	1570			
Polymer Based [31]	50	SU8	3.2	670	0.1394	2.34	51.55:1
		air	1	300			

3.6.2 Si_3N_4 insulated structure with SiC actuation layer

Keeping the gap capacitance same as (3.6), considering $K_i\varepsilon_g = \varepsilon_i$ as the permittivity of the insulation layer and K_i as the dielectric constant of the insulation layer, equivalent capacitance is expressed in (3.12) as a series combination of the gap and the insulation layers,

$$C'_{eq} = \frac{\varepsilon_g A}{t_g + \frac{t_i}{K_i}} = \frac{\varepsilon_g \pi r_e^2}{t_g + \frac{t_i}{K_i}} \tag{3.12}$$

the insulation capacitance C_{if} is expressed as

$$C_{if} = \left(\frac{\varepsilon_i \pi r_e^{\,2}}{t_i} \right) + \left\{ \varepsilon_i r_e \ln \left(\frac{16\pi r_e}{t_i} - 1 \right) \right\} \tag{3.13}$$

Hence the equivalent device capacitance of an insulated structure can be expressed as,

$$C'_{eqf} = \frac{\left\{ \frac{\pi r_e}{t_g} + \ln \left(\frac{16\pi r_e}{t_g} - 1 \right) \right\} \left\{ \frac{K_i \pi r_e}{t_i} + K_i \ln \left(\frac{16\pi r_e}{t_i} - 1 \right) \right\}}{\left\{ \frac{\pi r_e}{t_g} + \ln \left(\frac{16\pi r_e}{t_g} - 1 \right) \right\} + \left\{ \frac{K_i \pi r_e}{t_i} + K_i \ln \left(\frac{16\pi r_e}{t_i} - 1 \right) \right\}} \tag{3.14}$$

The enhancement in capacitance in an insulated structure is calculated as,

$$E_i = \left(\frac{C'_{eqf} - C_{eqf}}{C_{eqf}} \right) \times 100 \tag{3.15}$$

3.6.3 Competency of insulated structure over non-insulated cell

Figures 3.13 and 3.15 show the comparative study of device capacitance due to the inclusion of insulation layer and that excluding it with various structural parameters. Enhancement in device capacitance E_i, are shown in Figs. 3.14 and 3.16. The device capacitance enhances by an average value of 27% than non-insulated counterpart with variation in electrode radius. Undoubtedly increase in capacitance produces greater capacitive force. Decrease in adhesion force and least occurrence of electrical shock hazards, structure with insulation layer is accepted immensely in case of utilizing it for patients' electrical safety. It's quite prominent from Fig. 3.15 that the difference in device capacitances almost diminishes with an increase in gap thickness above 650 nm.

A combinational effect of gap thickness and electrode radius is studied in Figs. 3.17 and 3.18. Increasing electrode radius enhances the device capacitance but with the increase in gap thickness, its decrement is vibrant in Fig. 3.17. Capacitance generated at 25 μm is less than that of 55μm. Similarly, lower cavity height causes higher value device capacitance as depicted in Fig. 3.18.

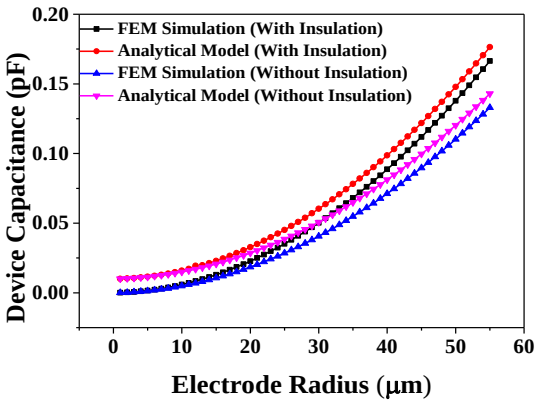

Fig. 3.13 Device capacitance variation with electrode radius

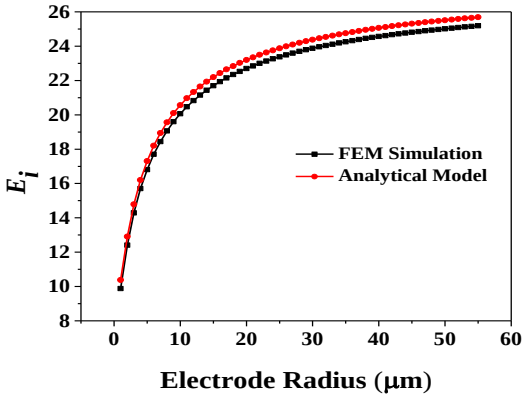

Fig. 3.14 Enhancement of device capacitance with electrode radius

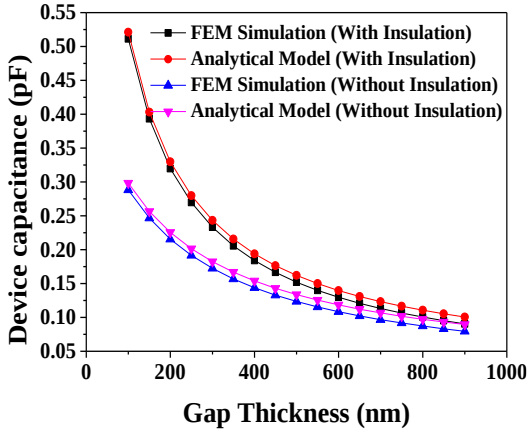

Fig. 3.15 Device capacitance with variation of gap thickness

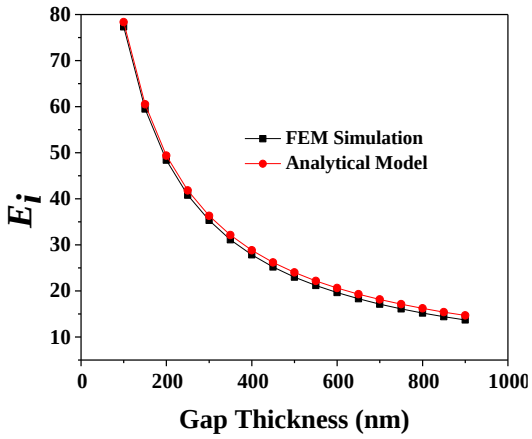

Fig. 3.16 Enhancement of device capacitance with gap thickness

Average E_i for both cases of 55 μm and 25 μm is 27%, whereas at 450 nm cavity height E_i is 27% and the same for 225 nm cavity height is 48%. In this context predominance nature of gap separation upon the device capacitance is evident. The overall conclusion is drawn from this section that device performance for high intensity application is initiated from an appreciable amount of capacitance generation which is comparatively larger valued for insulated structure. Moreover, insulated structure is competent enough regarding patient safety as it is free from electrical hazards. Gap and insulation capacitances are the prime factors for generating device capacitance and this intend to investigate the effect of gap and insulation capacitance upon it.

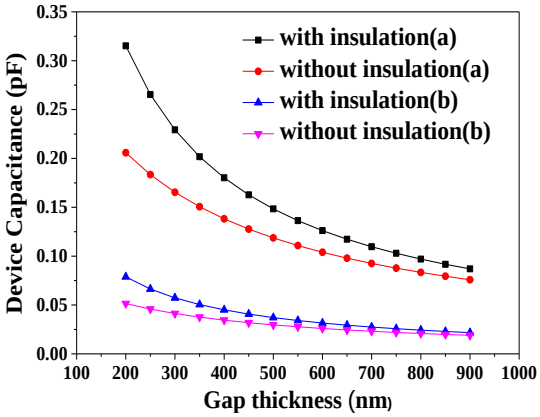

Fig. 3.17 Comparison of capacitance due to variation of gap thickness for a)r_e = 55 µm and b) r_e = 25 µm

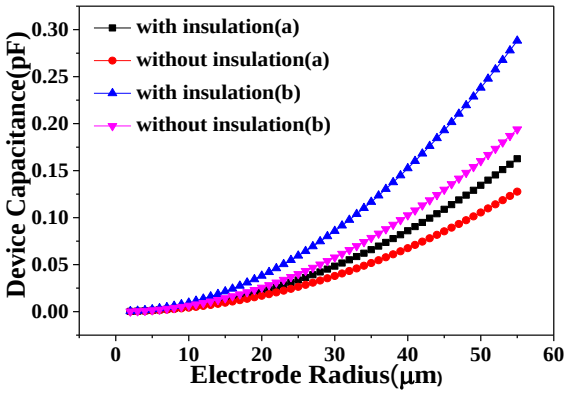

Fig. 3.18 Comparison of capacitance due to variation of electrode radius a) t_g =450 nm b) t_g =225 nm

3.7 Analysis of cavity and insulation layer capacitances of insulated CMUT

Figures 3.19-3.22 show that the gap capacitance predominantly determines the device capacitance. In Fig. 3.23 enhancement of device capacitance is plotted against insulating material of various dielectric constant keeping Si_3N_4 as reference.

Enhancement due to various materials is calculated as,

$$E_K = \left(\frac{C'_{eqf(K)} - C'_{eqf(Si_3N_4)}}{C'_{eqf(Si_3N_4)}} \right) \times 100 \qquad (3.16)$$

Here $C'_{eqf(Si_3N_4)}$ is device capacitance for Si_3N_4 and $C'_{eqf(K)}$ is device capacitance for other dielectric materials. The characteristic study shown in Figs. 3.22 and 3.23 express that engagement of high–K material as insulation layer enhances the device capacitance.

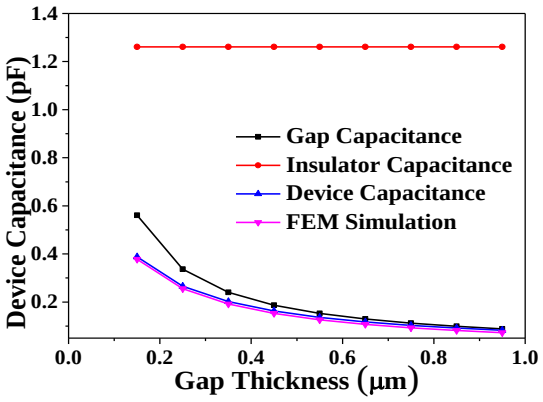

Fig. 3.19 Variation of capacitance with gap thickness

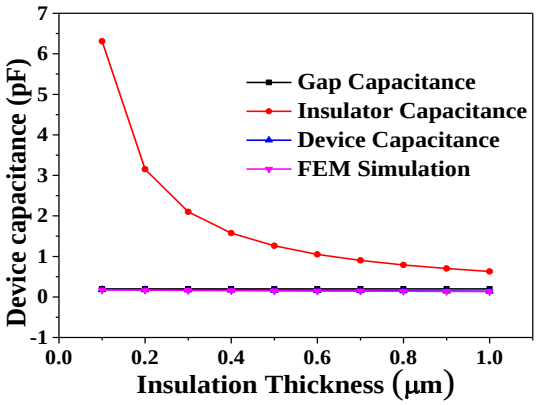

Fig. 3.20 Variation of capacitance with insulator thickness

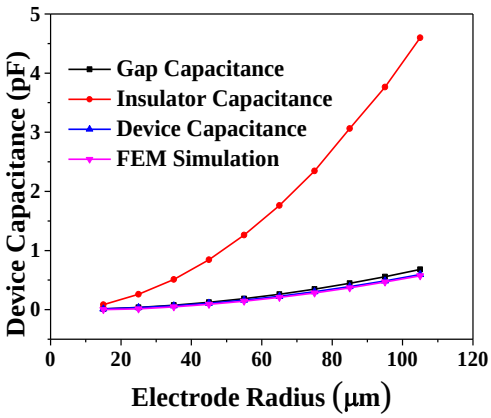

Fig. 3.21 Variation of capacitance with electrode radius

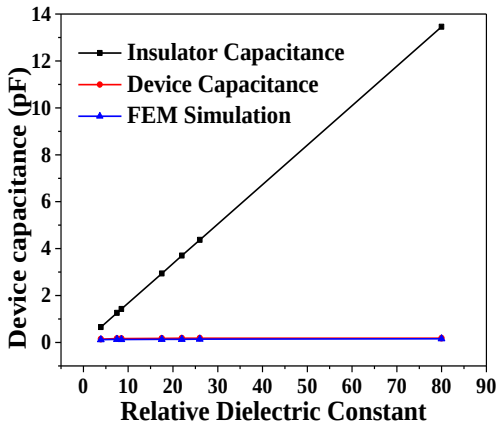

Fig. 3.22 Variation of capacitance with various dielectric material

Usage of HfO_2, Zirconium oxide (ZrO_2), Tantalum oxide (Ta_2O_3), Lanthanum(III) oxide (l_2O_3) than Si_3N_4 as insulating material keeps the capacitance of the device in appreciable range for which CMUT can generate ultrasound wave in acceptable frequency for high intensity application. It is observed clearly that the involvement of HfO_2 improves the device capacitance than involving Si_3N_4 as insulating material. Capacitance is determined primarily by the electrostatic transduction gap capacitance and the insulator capacitance has little effect in determining the overall capacitance of the device. The insulator layer aids in patterning the top electrode below the actuation layer which improves the overall capacitance of the device than a non-insulated structure.

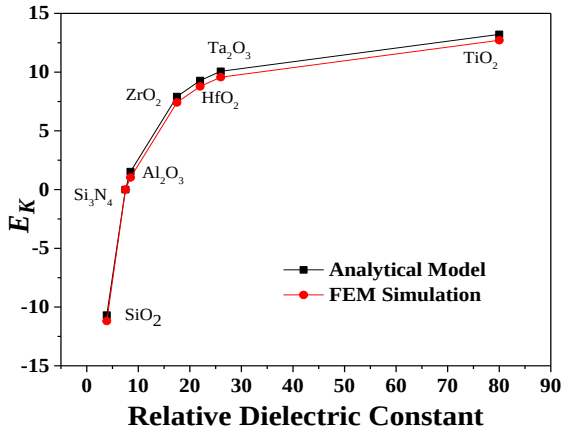

Fig. 3.23 E_K for various dielectric material

3.8 Analysis of fringing effects in an insulated CMUT

The inclusion of fringing capacitances helps in the evaluation of the effective device capacitance. In Fig. 3.24 the variation of device capacitance of an insulated element with electrode radius for various gap and insulation thickness is shown. A comparative approach can be studied from considering three cases a) t_g=450 nm, t_i=500 nm, b) t_g=650 nm, t_i=300 nm and c) t_g=300 nm, t_i=650 nm. Device capacitance for lower gap thickness and higher insulation thickness is capable for generating higher device capacitance from the dimension taken as a reference [29]. Though the reduction in gap thickness can increase device capacitance, still it will create hindrance in full swing for increased adhesive force.

Maintaining a tolerable gap separation can make the device efficient for generating high frequency ultrasound. Similarly increasing insulation thickness causes a reduction in device capacitance. Consequently, moderate gap thickness of 450 nm and the insulation thickness of 500 nm can be considered for better device performance and fit for ultrasound imaging. Fringing capacitance is more at lower electrode radius values as in Fig 3.25.

The enhancement in capacitance due to fringing is calculated as,

$$E'_C = \left(\frac{C'_{eqf} - C'_{eq}}{C'_{eq}} \right) \times 100 \qquad (3.17)$$

An average $E_C^{'}$ of 8.3% occurs in the electrode radius range of 35 to 55 µm. Below 10 µm of radius, the fringing effect is more profound.

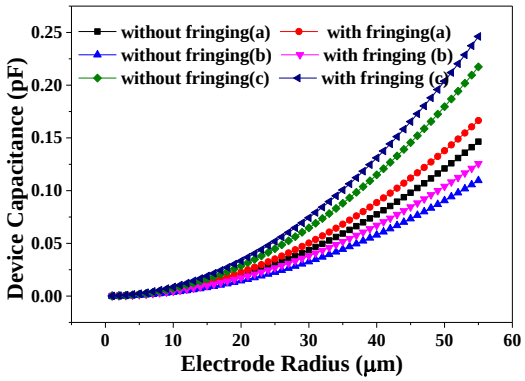

Fig. 3.24 Device capacitance variation with electrode radius for a) t_g =450 nm, t_i =500 nm b) t_g =650 nm, t_i =300 nm c) t_g =300 nm, t_i =650 nm

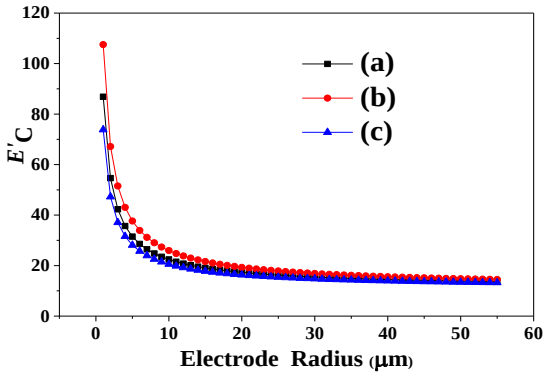

Fig. 3.25 Percentage of enhancement in capacitance due to fringing for a) t_g =450 nm, t_i =500 nm b) t_g =650 nm, t_i =300 nm c) t_g =300 nm, t_i =650 nm

Figure 3.26 shows the variation of device capacitance considering different gap thickness values. The capacitance decreases in a parabolic manner with respect to gap thickness. Higher electrode radius and lower insulation thickness produce comparatively higher device capacitance. Fringing capacitance increases with the gap thickness as in Fig. 3.27. Fringing effect has a greater impact for higher gap thickness, lower electrode radius, and higher insulation thickness. An average $E_C^{'}$ of 13.2% enhancement takes place for t_g =650 nm, t_i =300 nm, and 16.8% for t_g =300 nm, t_i =650 nm. Device capacitance variation due to change in insulation thickness is shown in Fig. 3.28, where the device capacitance exhibits dominant nature due to fringing for varying insulation thickness. Fringing has an insightful effect due to the change in insulation thickness among all other parameters discussed earlier. A uniform fringing capacitance contribution with insulation thickness is shown in Fig 3.29. The average $E_C^{'}$ attained from this characteristic is 13.2%.

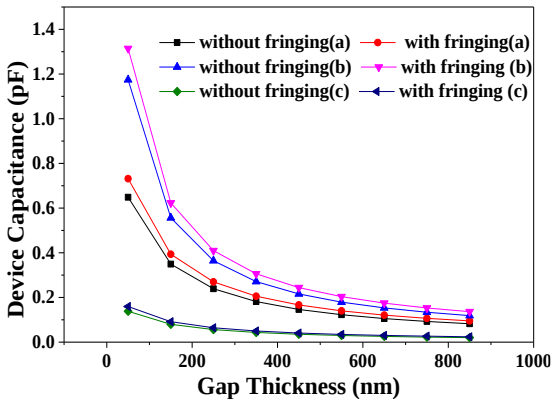

Fig. 3.26 Device capacitance with varying gap thickness for a) r_e =55 µm, t_i =500 nm b) r_e =65 µm, t_i =300 nm c) r_e =27.5 µm, t_i =650 nm

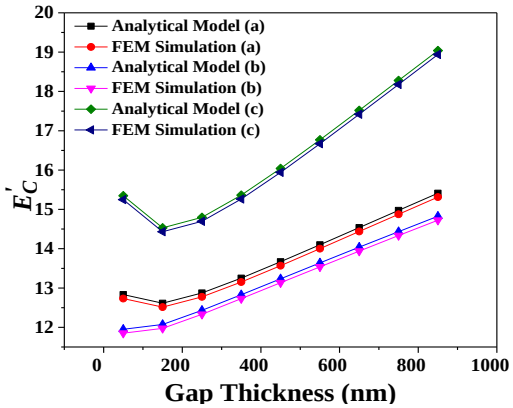

Fig. 3.27 E'_C with respect to gap thickness for a) r_e =55 µm, t_i =500 nm b) r_e =65 µm, t_i =300 nm c) r_e =27.5 µm, t_i =650 nm

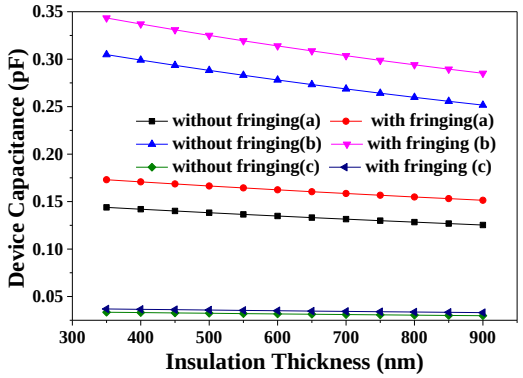

Fig.3.28 Variation of device capacitance with insulation thickness for a) r_e =55 µm, t_g =450 nm b) r_e =65 µm, t_g =300 nm c) r_e =27.5 µm, t_g =650 nm

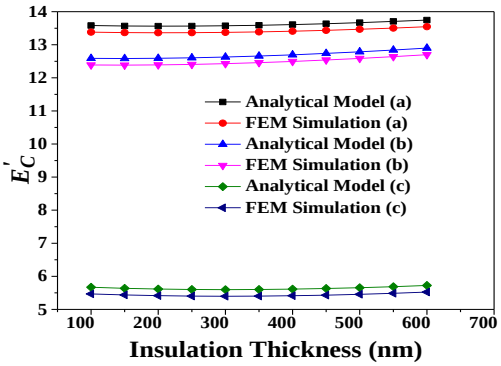

Fig. 3.29 E'_C with respect to insulation thickness for a) r_e =55 µm, t_g =450 nm b) r_e =65 µm, t_g =300 nm c) r_e =27.5 µm, t_g =650 nm

Characteristic study of device capacitance concerning change in various dielectric materials and electrode radius is plotted in Fig 3.30. Application of high-K dielectric material has a significant effect upon device capacitance as it is enhanced in a large manner compared to dielectric material of low dielectric constant. The purpose of selecting high-K dielectric material thus proves to be constructive for designing high performance CMUT. In Fig. 3.31 enhancement in device capacitance due to fringing is plotted with respect to dielectric material. An average value of E'_C attained from this figure is 7.4%. Figure 3.32 signifies that reduction in gap thickness and insulation thickness together can enhance device capacitance.

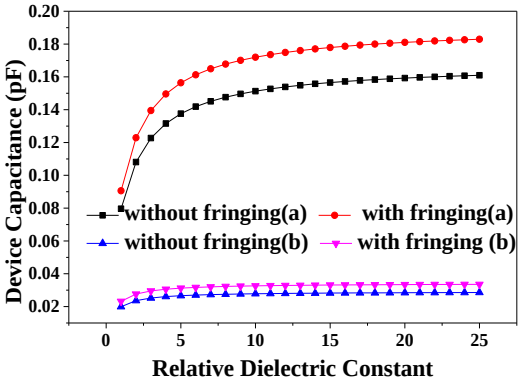

Fig. 3.30 Variation of capacitance due to change in various dielectric material for a) r_e =55 µm, b) r_e =27.5 µm

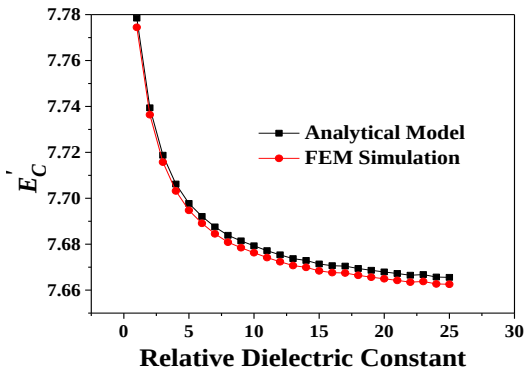

Fig. 3.31 E'_C with respect to material permittivity for r_e =55 µm

Selection of dielectric material is a prime factor while designing for high frequency application. In Table 3.2, a comparative study of the effect of fringing upon insulated CMUT is done for various structural parameters. One of these four parameters is varied and other values are kept constant. As depicted, enhancement in device capacitance is profound due to change in insulation and gap thickness and moderate when electrode radius and relative dielectric constant are taken into account.

Table 3.2: Contribution of fringing effect

Electrode radius (µm)	**Relative Dielectric Constant**	**Insulation thickness (nm)**	**Gap separation (nm)**	**Average E'_C (%)**
Variable	7.5	500	450	8.3
55	7.5	Variable	450	13.3
55	7.5	500	Variable	13.2
55	Variable	500	450	7.4

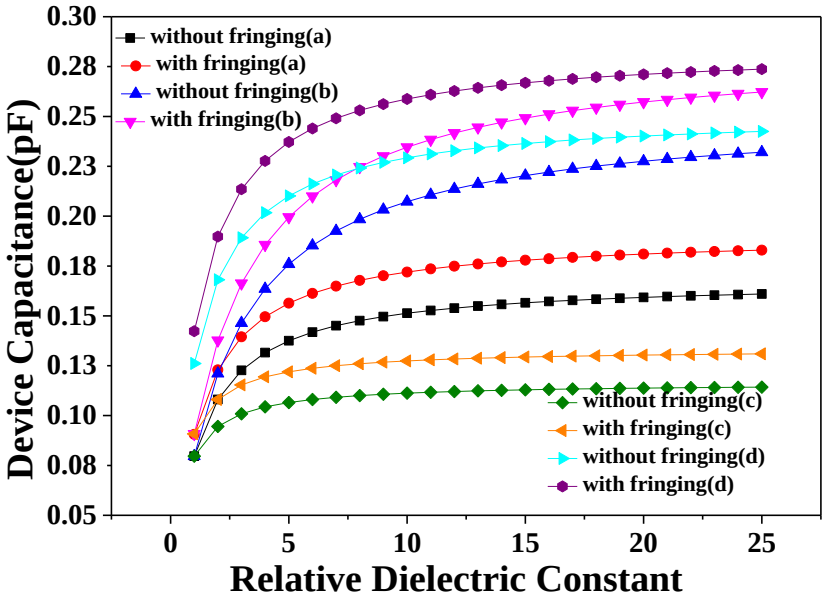

Fig. 3.32 Variation of capacitance due to change in various dielectric material a) t_g =450 nm, t_i =500 nm, b) t_g =300 nm, t_i =650 nm, c) t_g =650 nm, t_i =300 nm, d) t_g =300 nm, t_i =300 nm

3.9 Investigation of effect of HfO_2 material as the insulation layer

The above section witnesses that an insulated structure aids in higher device capacitance than the non-insulated counterpart which is beneficial to CMUT operation. This section investigates the involvement of different high-K materials that can be used as an insulating layer. A wide range of materials exists having a dielectric constant ranging from 9 to 200. But a nonlinear relationship exists between dielectric constant and dielectric breakdown strength which leads to an increase in dielectric strength for the decrease in dielectric constant and vice versa. Hence a balanced approach is required for the selection of such dielectric material having these two parameters to design a transducer with the desired efficiency along with high performance voltage requirements. As an example, dielectric materials having a balanced value of these two parameters are HfO_2, ZrO_2, L_2O_3, Si_3N_4, etc. Capacitance is directly proportional to the square of electrode radius and as the principal operation is capacitive hence the device capacitance also increases as the electrode radius enhances. Fig. 3.33 exhibits the variation of capacitance due to change in electrode radius respectively for the same input pulse between Si_3N_4 and HfO_2

isolation. Maintaining the standard fabricated thickness value for Si_3N_4, different isolation thickness of HfO_2 is taken under consideration. The characteristic study looks like a parabolic opening up nature. In addition to that effect of involving the high-K material is quite evident in Fig. 3.33 that 14% of device capacitance enhancement takes place due to a 50 nm HfO_2 insulation thickness compared to 500nm Si_3N_4 insulation. Fig. 3.34 represents the variation of capacitance with the gap separation. The graph shows the inversely proportional dependency upon gap thickness. The graph shows the inversely proportional dependency upon gap thickness. Increasing the separation gap between two electrodes yields the decrement of attraction force due to columbic force, henceforth the capacitance also decreases as gap separation increases.

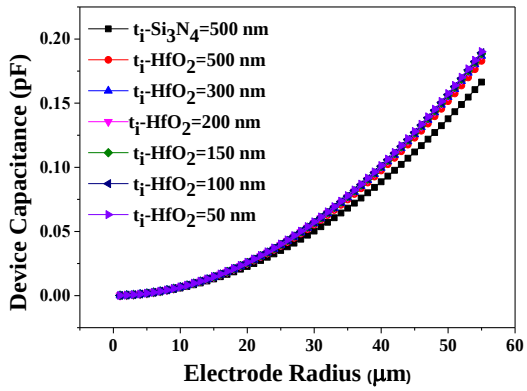

Fig. 3.33 The device capacitance for varying electrode radius for the same input pulse between HfO_2/Si_3N_4 isolation

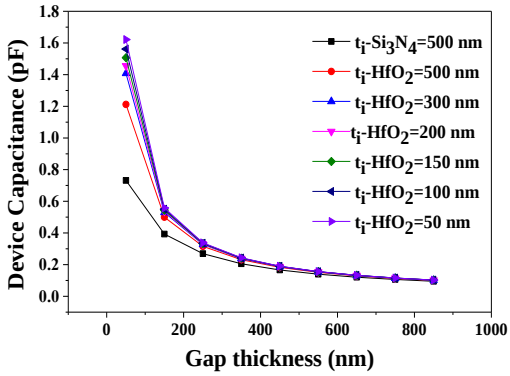

Fig. 3.34 A plot of the device capacitance for varying gap thickness

Device capacitance for 500 nm Si_3N_4 isolation layer is 0.166 pF whereas it becomes 0.183 pF when HfO_2 is used keeping the same thickness. But for 50 nm HfO_2 insulation thickness the capacitance is 0.190 pF. Figure 3.35 shows that the device capacitance of CMUT varies directly proportional to the dielectric constant of the insulating material. Considering different insulating materials the device capacitance has changed a lot like SiO_2 has a capacitance of 0.143 pF, Aluminum oxide has the same about 0.165 pF, whereas in the case of ZrO_2 and HfO_2 which are having comparatively high dielectric constant compared to Si_3N_4, have device capacitance as 0.175 pF and 0.179 pF respectively. Another high-K material such as Ta_2O_3 has a device capacitance of 0.181 pF which is a 10% larger value compared to

CMUT having a Si_3N_4 insulation layer. The result discussed here shows that these device capacitance mainly differs from each other due to the involvement of various insulation materials. Eventually, a decrease in insulation thickness also gives a rise in device capacitance which is quite evident from Fig. 3.35. A plot of the device capacitance for insulation thickness for the same input pulse between HfO_2 and Si_3N_4 isolation for various HfO_2 thickness and vacuum gap is shown in Fig. 3.36. It shows, at 500 nm Si_3N_4 the capacitance is 0.166 pF but for the same insulation thickness using HfO_2 capacitance becomes 0.183 pF. For 900 nm insulation thickness, the capacitance is 0.151 pF and 0.177 pF for Si_3N_4 and HfO_2 respectively.

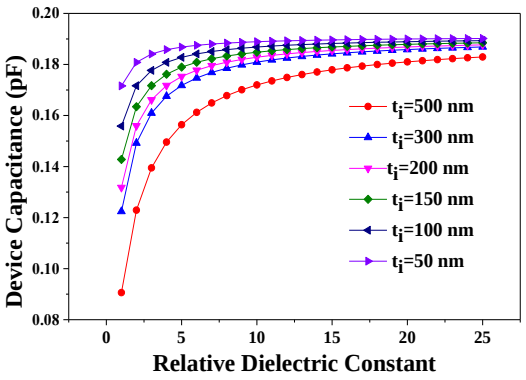

Fig. 3.35 A plot of the device capacitance for various dielectric material

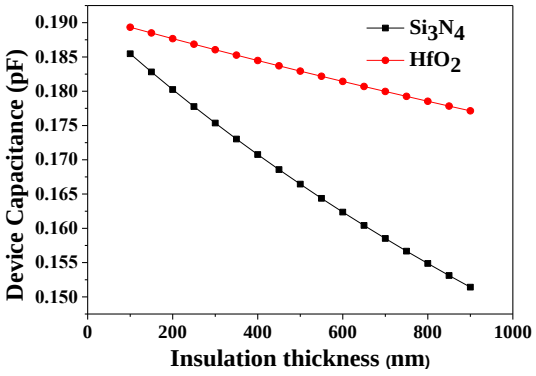

Fig. 3.36 A plot of the device capacitance with insulation thickness

3.10 Summary

The Landau technique for simulating the fringing field implication in CMUT is discussed in this chapter. This approach is used to determine the capacitances of the actuation layer, gap, and insulation. Because of its high Young modulus and low residual stress, SiC as a structural material makes the CMUT more capable of being produced with the smallest thermal budget. The addition of an insulating layer improves device selectivity and allows the CMUT to operate safely in high-voltage applications while being stable in high temperatures. The insulation layer is extremely beneficial in allowing CMUT to generate high-resolution imaging at a low cost, which can help develop medical imaging. The simulation result validates the Landau and Lifschitz approach for modeling the fringing field effect in CMUT. The simulation result is closest to the variation of device capacitance as a function of various factors. The use of HfO_2 in low-temperature manufacturing with an isolation

thickness of less than 100 nm is also possible using the atomic layer deposition (ALD) process. The performance of CMUT is improved in every aspect when HfO2 is used as an insulation layer instead of Si_3N_4. This enhancement in CMUT characteristics will undoubtedly make it more sensitive for high-frequency applications and also allow it to be used in an acoustic medium. The displacement, frequency, and impedance profile of a CMUT in a high-intensity application are all critical to its performance. Capacitance modeling sets the tone for the displacement profile, which is then followed by force modeling. In the following chapter, the evaluated device capacitance will be used for force modeling, and the effect of CMUT parameters on device capacitance will influence the force created by CMUT.

References

[1] M. I Haller and B. T Khuri-Yakub, ‘‘A surface micromachined electrostatic ultrasonic air transducer,*’’ IEEE Transaction on Ultrasonics, Ferroelectrics and Frequency Control*, vol. 43, no. 9, pp. 1–6, 1996

[2] X. Ladabaum, H. T Jin, A. Soh, Atalar, and B. T. Khuri Yakub, “Surface micromachined capacitive ultrasonic transducers,” *IEEE Transaction on Ultrasonics, Ferroelectrics and Frequency Control*, vol. 45, no. 3, pp. 678–690, 1998

[3] B. Bayram, O. Oralkan, A. Ergun, G. G. Yaralioglu and B. T. Khuri-Yakub, “Capacitive Micromachined Ultrasonic Transducer Design for High Power Transmission,” *IEEE Transaction on Ultrasonics, Ferroelectrics and Frequency Control*, vol. 49, no. 11, pp. 1596–1610, 2005

[4] J. Song, C. Xue, C. He, R. Zhang, L. Mu, J. Cui, "Capacitive micromachined ultrasonic transducers (CMUTs) for underwater imaging applications," *Sensors*, vol. 15, no. 9, pp. 23205-23217, 2015.

[5] R. Maity, N. P. Maity, R. Thapa, and S. Baishya, "Investigation of Silicon Nitride as an Excellent Membrane Material for MEMS Ultrasonic Transducers," *Applied Mechanics and Materials*, 2017, vol. 860, pp. 41-45.

[6] S. Zhou, P. Reynolds, and J. A. Hossack, "Improving the performance of capacitive micromachined ultrasound transducers using modified membrane and support structures,” *IEEE Ultrasonics Symposium Proceedings*, vol. 4, pp. 1925-1928.

[7] W. Zhang, H. Zhang, W. Hui, F. Yuan, “Simulation characterization of CMUT with vented square membrane”. *Proceedings of SPIE - The International Society for* Optical Engineering, pp. 9624-9629, 2015.

[8] L. Jia, C. He, C. Xue, and W. Zhang, "The device characteristics and fabrication method of 72-element CMUT array for long-range underwater imaging applications," *Microsystem Technologies*, vol. 25, no. 4, pp. 1195-1202, 2019.

[9] T.C. Cheng and T.-H. Tsai, "CMOS ultrasonic receiver with on-chip analog-to-digital front end for high-resolution ultrasound imaging systems," *IEEE Sensors Journal*, vol. 16, no. 20, pp. 7454-7463, 2016.

[10] R. Maity, N. P. Maity, R. Thapa, and S. Baishya, "An improved analytical and finite element method model of nanoelectromechanical system based micromachined ultrasonic transducers," *Microsystem Technologies*, vol. 23, no. 6, pp. 2163-2173, 2017.

[11] R. Maity, N. P. Maity, and S. Baishya, "Circular membrane approximation model with the effect of the finiteness of the electrode's diameter of MEMS capacitive micromachined ultrasonic transducers," *Microsystem Technologies*, vol. 23, no. 8, pp. 3513-3524, 2017.

[12] R. Maity, N. P. Maity, K. S. Rao, K. Guha, and S. Baishya, "A new compact analytical model of nanoelectromechanical systems-based capacitive micromachined ultrasonic transducers for pulse echo imaging," *Journal of Computational Electronics*, vol. 17, no. 3, pp. 1334-1342, 2018.

[13] G. G. Yaralioglu, A. S. Ergun, B. Bayram, E. Haggstrom, and B. T. Khuri-Yakub, "Calculation and measurement of electromechanical coupling coefficient of capacitive micromachined ultrasonic transducers," *IEEE Transactions on Ultrasonics, Ferroelectrics,and Frequency Control*, vol. 50, no. 4, pp. 449–456, 2003.

[14] N. Apte, K. K. Park, and B. T. Khuri-Yakub, "Finite element analysis of CMUTs with pressurized cavities," *IEEE International Ultrasonics Symposium*, pp. 979-982, 2012.

[15] B. Ahmad and R. Pratap, "Analytical evaluation of squeeze film forces in a CMUT with sealed air-filled cavity," *IEEE Sensors Journal*, vol. 11, no. 10, pp. 2426-2431, 2011.

[16] O. Wygant, M. Kupnik, and B. T. Khuri-Yakub, "Analytically calculating membrane displacement and the equivalent circuit model of a circular CMUT cell," *IEEE Ultrasonics Symposium Proceedings*, pp. 2111-2114, 2012.

[17] J.W. Mcpherson, J. Kim, A. Shanware, H. Mogul, J. Rodriguez, "Trends in the ultimate breakdown strength of high dielectric-constant materials," *IEEE Transactions on Device Electronics*, vol.50, no.8, pp.1771-1778, 2003.

[18] R. Maity, N. P. Maity, K. Guha, and S. Baishya, “Analysis of fringing capacitance effect on the performance of MEMS based micromachined ultrasonic air transducer, *IET Micro and Nano Letters,* vol 13, no. 6, pp. 872-877, 2018.

[19] R. Maity, N. P. Maity, K. S. Rao, K. Guha, and S. Baishya, "A new compact analytical model of nanoelectromechanical systems-based capacitive micromachined ultrasonic transducers for pulse echo imaging," *Journal of Computational Electronics,* vol. 17, no. 3, pp. 1334-1342, 2018.

[20] R. Maity, N. Maity, K. Guha, K. S. Rao, K. G. Sravani, and S. Baishya, "Study of 3D Hexagonal Membrane Structure for MEMS-Based Ultrasonic Transducer Using Finite Element Method," *Proceedings of ICDMC,* pp. 199-209.

[21] C. Maj and M. Szermer, "Influence of Fringing Fields on Parallel Plate Capacitance for Capacitive MEMS Accelerometers," *International Conference on the Perspective Technologies and Methods in MEMS Design*, pp. 82-85, 2020

[22] L. Vitaly and E. David, "Fringing field effect in electrostatics actuators," *Technical report ETR-2004–2, Israel Institute of Technology, Faculty of Mechanical Engineering,* 2004.

[23] M. Hosseini, G. Zhu, and Y.-A. Peter, "A new formulation of fringing capacitance and its application to the control of parallel-plate electrostatic micro actuators," *Analog Integrated Circuits and Signal Processing,* vol. 53, no. 2, pp. 119-128, 2007.

[24] F. Hunt, "The analysis of transduction and its historical back-ground," *Electroacoustics*: *Acoustical Society of America*, vol. 23, no. 7, pp. 123-126, 1982.

[25] M. J. Kumar, S. K. Gupta, and V. Venkataraman, "Compact modeling of the effects of parasitic internal fringe capacitance on the threshold voltage of high-K gate-dielectric nanoscale SOI MOSFETs," *IEEE Transactions on Electron Devices,* vol. 53, no. 4, pp. 706-711, 2006.

[26] K. Guha, M. Kumar, S. Agarwal, and S. Baishya, "A modified capacitance model of RF MEMS shunt switch incorporating fringing field effects of perforated beam," *Solid-State Electronics,* vol. 114, pp. 35-42, 2015.

[27] M. Rahman, J. Hernandez, and S. Chowdhury, "An improved analytical method to design CMUTs with square diaphragms," *IEEE Transaction on Ultrasonics, Ferroelectrics and Frequency Control,* vol. 60, no. 4, pp. 834-845, 2013.

[28] Q. Zhang, P. Cicek, K. Allidina, F. Nabki, and M. N. El-Gamal, "SurfaceMicromachined CMUT Using Low-Temperature Deposited SiC Membranes for Above-IC Integration", *IEEE Journal of Microelectromechanical. System,* vol. 23, no. 2, pp.482-*493, 2014.*

[29] A.Logan and J. T. W. Yeow, "Fabricating capacitive micromachined ultrasonic transducers with a novel silicon-nitride-Based wafer bonding process," *IEEE Transaction on Ultrasonics, Ferroelectrics and Frequency Control,* vol. 56, no. 5, pp. 1074-1084, 2009.

[30] M. Cetin and B. Bayram, "Diamond-Based Capacitive Micromachined Ultrasonic Transducers in Immersion", *IEEE Transaction on Ultrasonics, Ferroelectrics and Frequency Control,* vol. 60, no. 2, pp. 414-420, 2013.

[31] D. Gerardo , E. Cretu, R. Rohling, "Fabrication and testing of polymer-based capacitive micromachined ultrasound transducers for medical imaging*", Microsystems & Nanoengineering*, vol. 4, no. 19, pp. 568-579,2018

[32] S. H. Wong, M. Kupnik, X. Zhuang, D. Lin, K. Butts-Pauly, B.T. Khuri-Yakub, "Evaluation of wafer bonded CMUTs with rectangular membranes featuring high fill factor', *IEEE Transaction on Ultrasonics, Ferroelectrics and Frequency Control*, vol. 55, no. 9, pp 2053-2065, 2008.

CHAPTER

4

Electrostatic Force

4.1 Operating principle of CMUT as electrostatic actuator

Basic principle of CMUT operation is electrostatic transduction mechanism based on capacitive action. This capacitive action is built between one fixed electrode and another movable one which is capable to vibrate. A bias is needed for proper functioning of the device in active mode [1]. In addition to that a signal has to be superimposed on the bias voltage and applied between the bottom fixed electrode and movable top electrode. In consequence to that resulting electrostatic force is modulated and causes vibration in the actuation layer as shown in Fig. 1. Subsequent to that ultrasound is generated at the same frequency which is superimposed upon the bias. Due to application of bias between two electrodes the actuation layer gets attracted towards the substrate for electrostatic attraction force. This attraction force is developed based on the principle of columbic force [2].

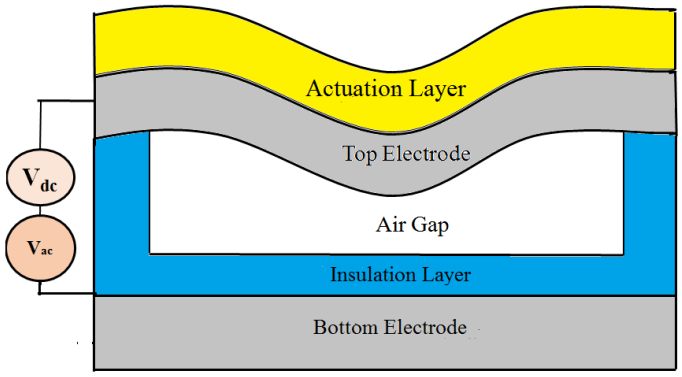

Fig. 4.1 2D model of biased actuation layer vibration in circular CMUT

Application of bias supplies the charge which gets modulated by the vibrating structural layer and ultrasound is generated for electrostatic actuation. In order to achieve harmonic movement of actuation layer in transmission mode bias plays an

important role. Generated electrostatic force gets balanced by the resulting bending firmness and residual stress of structural material.

4.1.1 Electrostatic transduction of capacitive element

The primary existence of capacitive transducer as electrostatic transducer is to operate in high electric field. It can produce an electric field approximately more than 108V/cm. Proper handling should be taken care of during the operating state with high electric field to maintain reproducibility and accuracy [3]. Excellent matching of mechanical impedance with the surrounding medium leads the device to be superior in comparison to piezoelectric and magnetostrictive transducers. Based on the structural layer shape hexagonal, square, circular elements are discussed in various research papers. Among these structures hexagonal transducer is operated in high temperature range and fabrication is not at all costly. In order to have good system repeatability and long distance under water application circular shape is accepted widely. Moreover sensitivity is also high for this structure while engaged in medical imaging.

4.2 Background survey of modeling of electrostatic actuation

As this research work considers the circular structured cell, hence more features of device along with analytical models were presented in many research papers [4-6]. These studies were based on approximation considering the parallel plate capacitive action. Later on calculation of actual deflection of the movable edge clamped top electrode was established by considering the pull in voltage and parameters derived from equivalent circuit model [7-8]. In this paper the top electro de was considered as a plate and effect of non-uniform load was considered for solving the structure. In paper [9] Galerkin method was considered for solving the electrostatic action upon a concentrically loaded plate. Increasing bias voltage causes the non uniform load distribution upon the top electrode and change in electrostatic force will occur due to variation in their separation. If the deflection of the top electrode does not happen more than half of the gap separation under pull-in condition then the consideration of top electrode as plate becomes unnecessary. Hence in [10] A simple solution is considered for solving the deflection of a circular

plate. In contrast to that, applying the concept of series expansion by trigonometric or polynomial basis function solution of square diaphragm is expressed in paper [11-12]. Another combined approach is executed in paper [13-14], where both the circular and square geometrical shape functions are considered for studying the electrostatic action that causes deflection. An electromechanical model used in paper [15] for capturing the behaviour using mass-spring-damper model. In some research paper concept of fringing is also applied in calculating the electrostatic force. Effect of fringing field enhances the device capacitance; subsequently electrostatic force was also affected. In circular-disk capacitor, the Younes Ataiiyan's method [16] could be realistic to develop their connection. Consequently this increased force enhances the displacement profile of structural layer [17-19].

4.3 Analytical force model of non-insulated element

Existence of bending electric field lines at the capacitive plate causes the fringing effect which is elaborately described in Chapter 3. Effect of fringing gives a rise to enhanced device equivalent capacitance which in turn effect the electrostatic force generated in the CMUT. Considering the capacitance modeling of Sec 3.3 and the CMUT structure [20] Fig. 3.2(b) analytical calculation of force is done in non-insulated cell with fully metalized actuation layer.

'u' is defined by potential energy. The value of *u* is calculated by,

$$u = \frac{1}{2} C_{eq} v(t)^2 \tag{4.1}$$

where, C_{eq} represents the direct series capacitance of actuation layer capacitance, C_a and the air gap capacitance, C_g resulting in an effective electrostatic force as in (4.2),

$$F = -\frac{du}{dt_g} \tag{4.2}$$

Putting the value of (4.1) in (4.2) , force can be expressed as

$$F = -\frac{du}{dt_g} = -\frac{1}{2} v(t)^2 \frac{dC_{eq}}{dt_g} \tag{4.3}$$

Here *v(t)* is applied voltage between two electrodes and t_g is air gap. Putting the device equivalent capacitance from (3.4), the following expression becomes,

$$\frac{dC_{eq}}{dt_g} = \frac{d}{dt_g}\left(\frac{C_a \times C_g}{C_a + C_g}\right) = C_a \frac{d}{dt_g}\left(\frac{C_g}{C_a + C_g}\right) \tag{4.4}$$

$$= \frac{C_a\left[\left(C_g + C_a\right)\frac{dC_g}{dt_g} - C_g \frac{d}{dt_g}\left(C_g + C_a\right)\right]}{\left(C_g + C_a\right)^2}$$

$$= \frac{C_a^{\,2}}{\left(C_g + C_a\right)^2} \cdot \frac{dC_g}{dt_g} \tag{4.5}$$

As, $\frac{dC_g}{dt_g} = \varepsilon_g\left[\frac{-\pi r_e^{\,2}}{t_g^{\,2}}\right]$, hence putting the value of $\left(\frac{dC_g}{dt_g}\right)$ and (4.5) , (4.3) can be rewritten as,

$$F = -\frac{du}{dt_g} = -\frac{1}{2}\frac{v(t)^2 C_a^{\,2}}{\left(\frac{C_a}{C_g}+1\right)^2 C_g^{\,2}} \times \frac{dC_g}{dt_g}$$

$$F = \frac{1}{2}\frac{v(t)^2 C_a^{\,2}}{C_g^{\,2}\left(\frac{C_a}{C_g}+1\right)^2}\left[\varepsilon_g \frac{\pi r_e^{\,2}}{t_g^{\,2}}\right] \tag{4.6}$$

The force on the actuation layer including the fringing capacitance, (4.3) can be rewritten as,

$$F_f = -\frac{1}{2} v(t)^2 \frac{dC_{eqf}}{dt_g} \tag{4.7}$$

Hence, putting the device equivalent capacitance from (3.9), the following expression becomes,

$$\frac{dC_{eqf}}{dt_g} = \frac{d}{dt_g}\left(\frac{C_{af} \times C_{gf}}{C_{af} + C_{gf}}\right) = C_{af} \frac{d}{dt_g}\left(\frac{C_{gf}}{C_{af} + C_{gf}}\right) \tag{4.8}$$

$$\frac{dC_{eqf}}{dt_g} = \frac{C_{af}\left[\left(C_{gf}+C_{af}\right)\frac{dC_{gf}}{dt_g} - C_{gf}\frac{d}{dt_g}\left(C_{gf}+C_{af}\right)\right]}{\left(C_{gf}+C_{af}\right)^2}$$

$$= \frac{C_{af}\left[\left(C_{gf}+C_{af}\right)\frac{dC_{gf}}{dt_g} - C_{gf}\frac{d}{dt_g}\left(C_{gf}+C_{af}\right)\right]}{\left(C_{gf}+C_{af}\right)^2} \tag{4.9}$$

Putting the value of (3.7) & (3.8), $\frac{dC_{gf}}{dt_g}$ can be written as (4.10)

$$\frac{dC_{gf}}{dt_g} = -\varepsilon_g\left[\frac{\pi r_e^{\,2}}{t_g^{\,2}} + \frac{r_e}{\frac{16\pi r_e}{t_g}-1}\cdot\frac{16\pi r_e}{t_g^{\,2}}\right] \tag{4.10}$$

Putting (4.10) in (4.9), the expression can be rewritten as,

$$\frac{dC_{eqf}}{dt_g} = \frac{-C_{af}^{\,2}\varepsilon_g}{\left(C_{gf}+C_{af}\right)^2}\left[\frac{\pi r_e^{\,2}}{t_g^{\,2}} + \frac{r_e}{\frac{16\pi r_e}{t_g}-1}\cdot\frac{16\pi r_e}{t_g^{\,2}}\right] \tag{4.11}$$

Hence considering (4.11) and putting the value in (4.7) electrostatic force is expressed as (4.12)

$$F_f = \frac{1}{2}\frac{v(t)^2 C_{af}^{\,2}}{C_{gf}^{\,2}\left(\frac{C_{af}}{C_{gf}}+1\right)^2}\left[\varepsilon_g\frac{\pi r_e^{\,2}}{t_g^{\,2}} + \frac{\varepsilon_g r_e}{\left(\frac{16\pi r_e}{t_g}-1\right)}\times\frac{16\pi r_e}{t_g^{\,2}}\right] \tag{4.12}$$

A comparative analysis is accomplished altering the actuation layer by SiC instead of Si_3N_4. To generate appreciable amount of electrostatic force in resonance with the operating frequency a large bias is delivered along than the signal.

Expression of total voltage is, $v(t) = V_{dc} + V_{ac}\cos\omega t$, where V_{dc} is the bias and V_{ac} is the signal. Hence, $v(t)^2 = V_{dc}^2 + 2\left(V_{dc}V_{ac}\right)c\,\mathrm{os}\,\omega t + V_{ac}^2 c\,\mathrm{os}^2\,\omega t$

$V_{ac}^2 \cos^2 \omega t$ is the second harmonic, which is quite less compared to the bias . As the applied bias is considerably greater than time varying one, considering the electrostatic force for applied bias (4.6) and (4.12) can be rewritten as,

$$F_{bias} = \frac{1}{2} \frac{V_{dc}^{\ 2} C_a^{\ 2}}{C_g^{\ 2} \left(\frac{C_a}{C_g} + 1 \right)^2} \left[\varepsilon_g \frac{\pi r_e^{\ 2}}{t_g^{\ 2}} \right] \tag{4.13}$$

$$F_{f_{bias}} = \frac{1}{2} \frac{V_{dc}^{\ 2} C_{af}^{\ 2}}{C_{gf}^{\ 2} \left(\frac{C_{af}}{C_{gf}} + 1 \right)^2} \left[\varepsilon_g \frac{\pi r_e^{\ 2}}{t_g^{\ 2}} + \frac{\varepsilon_g r_e}{\left(\frac{16\pi r_e}{t_g} - 1 \right)} \times \frac{16\pi r_e}{t_g^{\ 2}} \right] \tag{4.14}$$

Dynamic electrostatic force for signal is expressed as,

$$F_{f_{signal}} = \frac{V_{ac} V_{dc} C_{af}^{\ 2}}{C_{gf}^{\ 2} \left(\frac{C_{af}}{C_{gf}} + 1 \right)^2} \left[\varepsilon_g \frac{\pi r_e^{\ 2}}{t_g^{\ 2}} + \frac{\varepsilon_g r_e}{\left(\frac{16\pi r_e}{t_g} - 1 \right)} \times \frac{16\pi r_e}{t_g^{\ 2}} \right] \tag{4.15}$$

Electrostatic force $F_{f_{bias(SiC)}}$ is generated in the device for involving SiC as actuation layer and that same involving Si_3N_4 generates electrostatic force as $F_{f_{bias(Si_3N_4)}}$. Both values of electrostatic force are calculated from $C_{eqf(SiC)}$ and $C_{eqf(Si_3N_4)}$ using (3.8) putting relative dielectric constant as 9.7 and 7.5 respectively in (4.7).

4.3.1 FEM Simulation

The corresponding electric potential profile showing the fringing field line is shown Fig. 4.2. PZFlex is a user defined unit system. To simplify the model, we have applied symmetry to it. Applying symmetry conditions the structure is divided into two equal halves for making it simple for analysis at lesser simulation run time. Parametrical analysis for electrostatic potential a dc bias of 40V is applied in the parametric sweep of the study. Selecting the electrostatic study electrostatic potential is applied on the bottom surface boundary of the actuation layer and the top surface of bottom electrode. Afterwards a mesh is formed and computation is done.

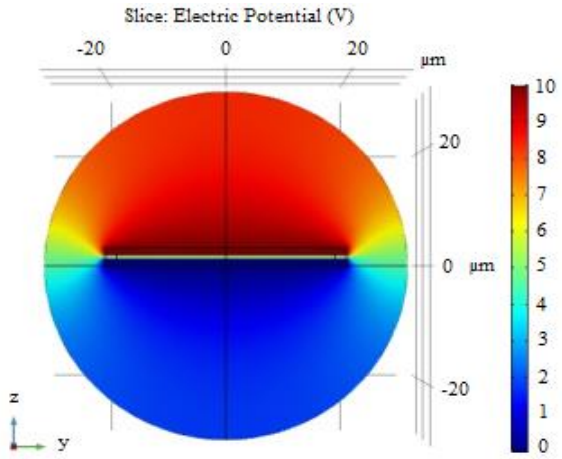

Fig. 4.2 Electric potential profile

4.3.2 Comparative analysis of static electrostatic force in Si_3N_4/ SiC actuation layer based non-insulated cell

Behaviour of electrostatic force against certain parameters like electrode radius, air gap, actuation layer thickness and bias of actuation layer based CMUT are discussed in this section. Fig. 4.3 shows the behavior of electrostatic force due to change in electrode radius. Increase in electrode radius gives a rise in device capacitance , subsequent to which electrostatic force also gets enhanced. The enhancement in electrostatic force due to fringing is expressed as

$$E_F = \left(\frac{F_{f_{bias}} - F_{bias}}{F_{bias}} \right) \times 100 \tag{4.16}$$

Enhancement in a cell with SiC actuation layer instead of Si_3N_4 is

$$E_{F\_SiC} = \left(\frac{F_{f_{bias(SiC)}} - F_{f_{bias(Si_3N_4)}}}{F_{f_{bias(Si_3N_4)}}} \right) \times 100 \tag{4.17}$$

Average E_F is 13% for Si_3N_4 and 15% for SiC actuation layer as shown in Fig. 4.4. Fringing effects are more for lower radius values. Moreover in Fig. 4.5 enhancement of electrostatic force in SiC cell compared to Si_3N_4 is plotted.

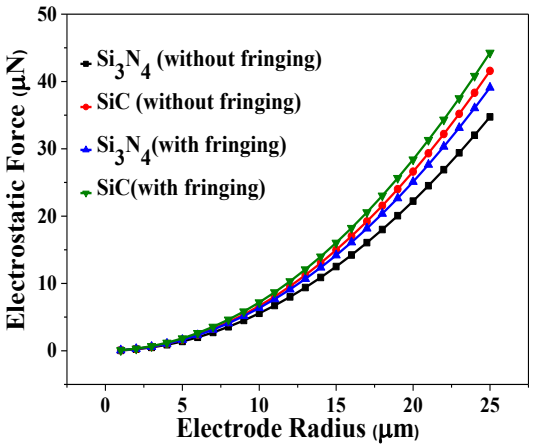

Fig. 4.3 Electrostatic force due to variation in electrode radius

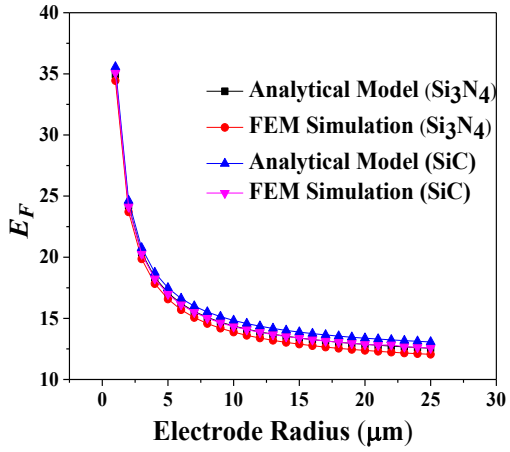

Fig. 4.4 E_F for varying electrode radius

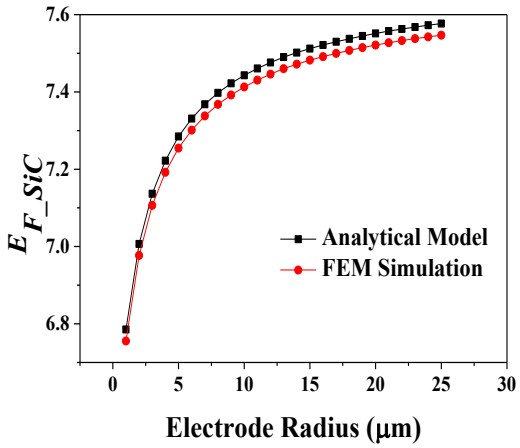

Fig. 4.5 E_{F_SiC} for varying electrode radius

Larger valued electrode radius produces more enhancements. An average E_{F_SiC} of 7.41 % is obtained. Hence larger impact in SiC actuation layer based device than Si_3N_4. The characteristic study shown in Fig. 4.6 depicts contribution of fringing effect in electrostatic force for varying air gap between two electrodes. Increase in gap separation decreases the device capacitance and same for electrostatic force, as electrostatic force has a inverse proportionality relationship with gap separation. In Figs. 4.7 and 4.8 variation of E_F and E_{F_SiC} is exhibited respectively for changing cavity height. An average value of E_F is 14.06 % and 14.93% for Si_3N_4 and SiC actuation layer based structures respectively. Above 300nm cavity height appreciable amount of enhancement is seen in SiC actuation layer based element.

Moreover a rising slope of force enhancement is evident in Fig. 4.8 due to fringing approach. An average value of E_{F_SiC} produced while plotted against cavity height is 26%.

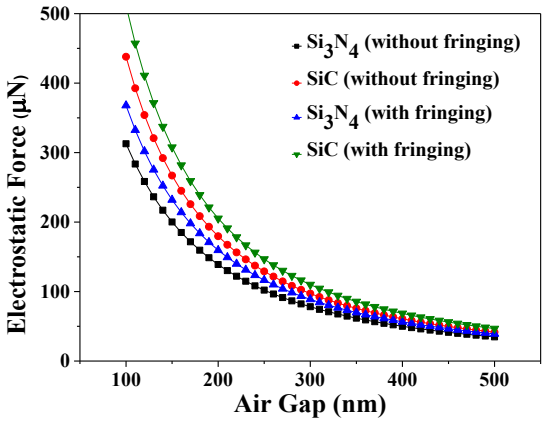

Fig. 4.6 Variation of electrostatic force for varying air gap

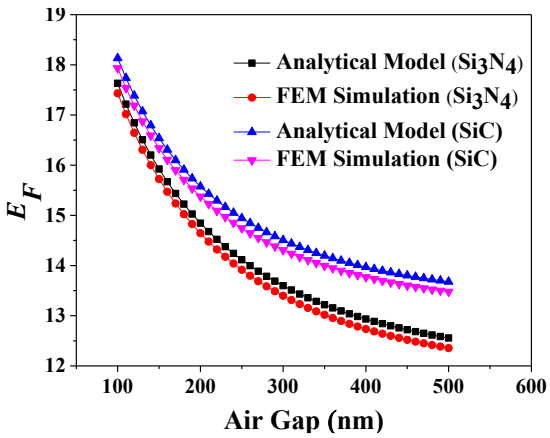

Fig. 4.7 E_F for varying air gap

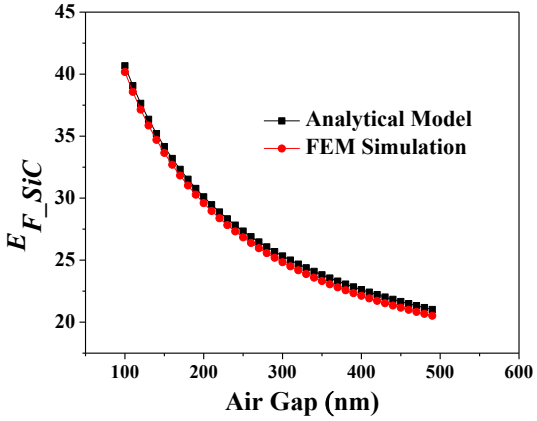

Fig. 4.8 E_{F_SiC} for varying air gap

Variation of electrostatic force with respect to thickness of actuation layer is shown in Fig. 4.9. Increase in actuation layer thickness contributes larger amount of force enhancement mostly after 300nm. A plot of E_F and E_{F_SiC} is depicted with respect to actuation layer thickness in Figs. 4.10 and 4.11 respectively. As increase in thickness of actuation layer increases the distance between two electrodes, hence reduction in capacitance takes place, which in turns reduces the electrostatic force. Certainly, contribution of fringing also has an insightful impact due to increasing thickness of actuation layer that yields to produce an average E_F of

11.89% for Si_3N_4 and 13.13% for SiC. Due to fringing an average E_{F_SiC} of 17.7% takes place.

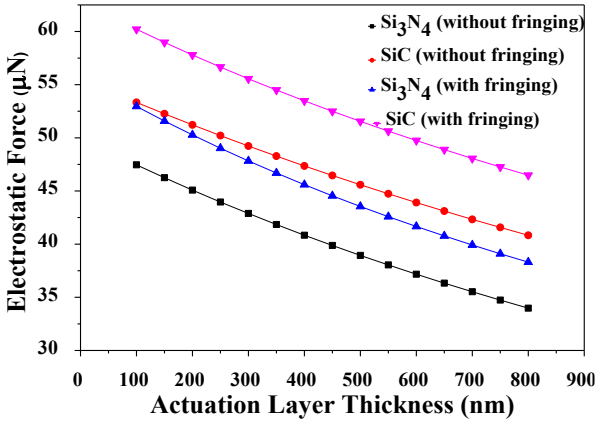

Fig. 4.9 Variation of electrostatic force for varying thickness of actuation layer

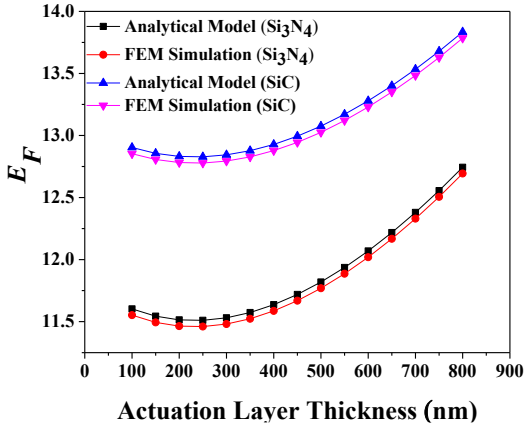

Fig. 4.10 E_F for varying actuation layer thickness

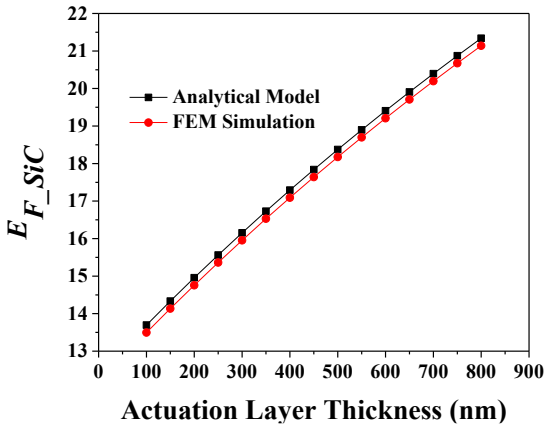

Fig. 4.11 E_{F_SiC} for varying actuation layer thickness

Bias is a prime deciding factor for analyzing the characteristic of device generated electrostatic force as it establishes non linear relationship with the square of applied bias voltage. Variation of electrostatic force with applied bias is shown in Fig. 4.12. Increase in applied bias enhances the electrostatic force and produce parabolic opening up nature. Average E_F of 11.92% for Si_3N_4 and 12.41% for SiC is shown in Fig. 4.13. Electrostatic force enhanced by 19.68% due to usage of SiC layer is exhibited in Fig. 4.14. Considering all the characteristic studies against structural parameters involvement of SiC is accepted unanimously as actuation layer material.

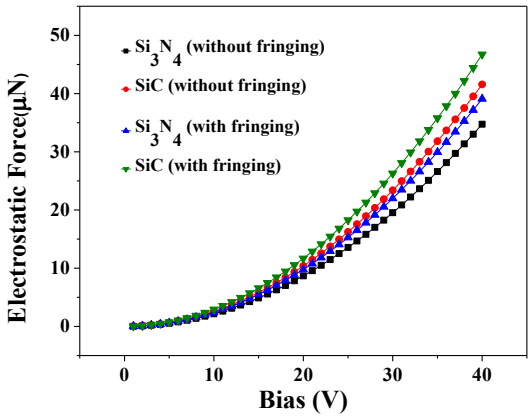

Fig. 4.12 Variation of electrostatic force for varying bias

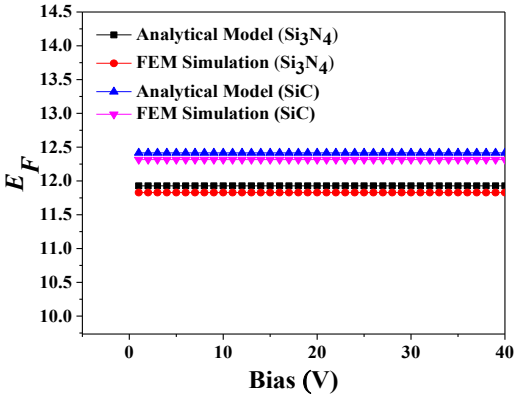

Fig. 4.13 E_F for varying bias

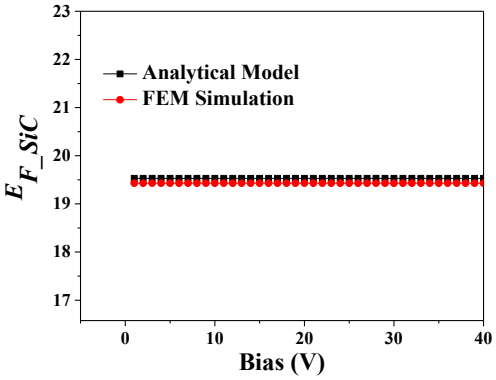

Fig. 4.14 E_{F_SiC} for varying bias

4.4 Si_3N_4 insulated structure with SiC actuation layer

The presence of the insulation layer as in Fig.4.15 permits the patterning of the upper electrode below the actuation layer which increases the overall capacitance of the device as already analyzed in Chapter 3.

4.4.1 Analytical force model of insulated element

Analyzing the results discussed in section 4.3.2, one conclusion can be drawn that usage of SiC as actuation layer improves the electrostatic force in all aspect. An analytical modeling of insulated CMUT (shown in Fig. 4.15) with SiC as actuation material is discussed in this section. The equivalent capacitance comprises now of the gap and insulator capacitances series combination. Based on the equivalent capacitance without fringing, electrostatic force is expressed by considering bias voltage and change in device equivalent capacitance.

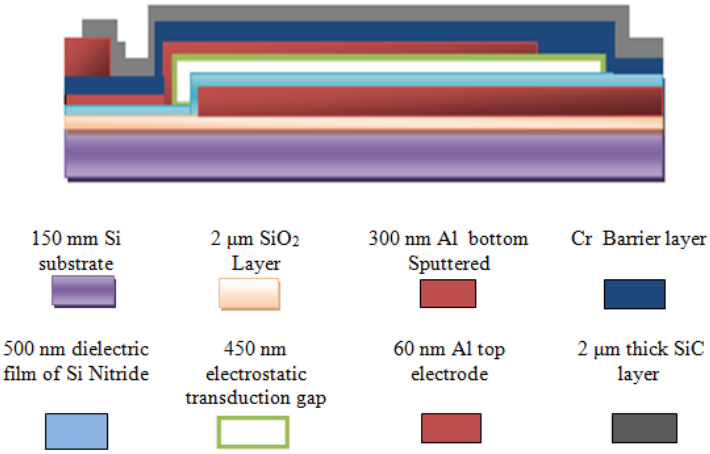

Fig. 4.15 2D structure of insulated CMUT

Hence force without fringing can be derived as

$$F'_{bias} = \frac{1}{2}\frac{V_{dc}^{\,2}C_i^{\,2}}{C_g^{\,2}\left(\frac{C_i}{C_g}+1\right)^2}\left[\varepsilon_g \frac{\pi r_e^{\,2}}{t_g^{\,2}}\right] \tag{4.18}$$

Considering the fringing effect the force can be expressed for this device by (4.19)

$$F'_{f_{bias}} = \frac{1}{2}\frac{V_{dc}^{\,2}C_{if}^{\,2}}{C_{gf}^{\,2}\left(\frac{C_{if}}{C_{gf}}+1\right)^2}\left[\varepsilon_g \frac{\pi r_e^{\,2}}{t_g^{\,2}} + \frac{\varepsilon_g r_e}{\left(\frac{16\pi r_e}{t_g}-1\right)}\times\frac{16\pi r_e}{t_g^{\,2}}\right] \tag{4.19}$$

4.4.2 Enhancement of Electrostatic force in insulated structure

Figure 4.16 shows the variation of electrostatic force with electrode radius. Enhanced electrostatic force is observed in insulated structure in comparison to a non-insulated counterpart. Generated force increases exponentially with respect to electrode radius. Here enhancement is calculated by

$$E'_i = \left(\frac{F'_{f_{bias}} - F_{f_{bias}}}{F_{f_{bias}}}\right)\times 100 \tag{4.20}$$

The characteristic study proves that inclusion of insulation layer tends the capacitance to get enhanced which consequently generates larger force than non-insulated cell. In this context average $E_i^{'}$ becomes 49.8% when enhancement of electrostatic force is plotted against electrode radius as shown in Fig. 4.17.

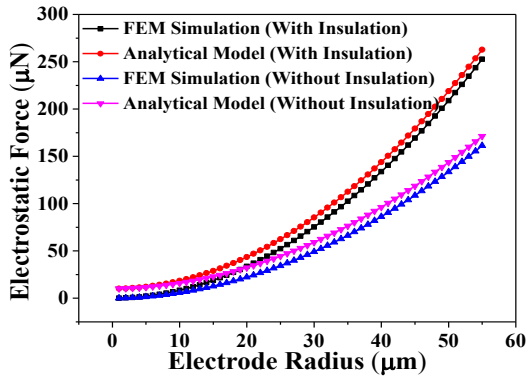

Fig. 4.16 Comparative analysis of electrostatic force with varying electrode radius

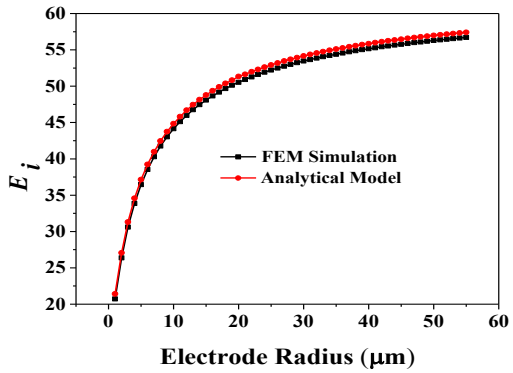

Fig. 4.17 $E_i^{'}$ for varying electrode radius

Figure 4.18 shows the comparative study of electrostatic force due to increase in gap thickness. Increase in gap thickness enhances the separation between two electrodes whose effect is visible in greater manner for non-insulated element. The enhanced force is profound between the range of gap thickness from 350nm to 500 nm. An average $E_i^{'}$ of 54.13% force enhancement takes place in insulated structure as depicted in Fig. 4.19.

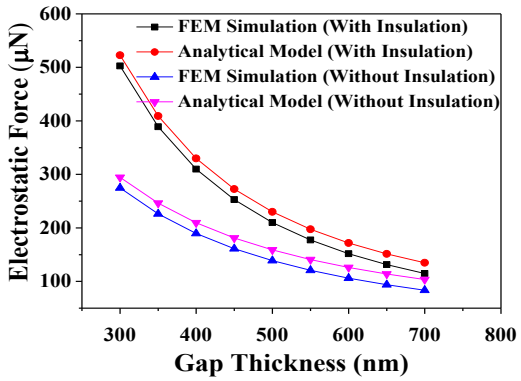

Fig 4.18 Comparative analysis of electrostatic force due to variation of gap thickness

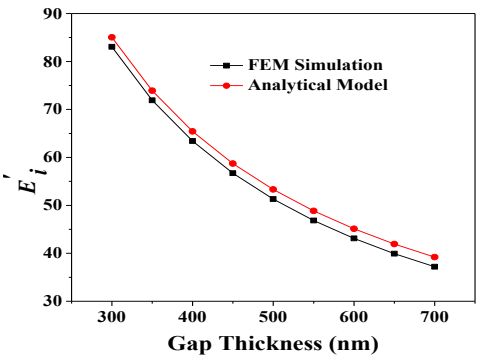

Fig. 4.19 $E_i^{'}$ for varying gap thickness

Moreover, added advantage is obtained from insulated device that, it will be free from any sorts of electrical shock which will improve device safety, sensitivity, free from parasitic capacitance and make the structure more effective from the marketing point of view.

4.4.3 Significance of fringing in insulated CMUT

Inclusion of fringing capacitances helps in evaluation of the effective device capacitance. This gives a certain rise in electrostatic force also. In Fig. 4.20 the variation of electrostatic force of an insulated element is shown with electrode radius for various gap and insulation thickness. A comparative approach can be studied from considering three cases a) t_g=450 nm, t_i=500 nm, b) t_g=650 nm, t_i=300 nm and c) t_g=300 nm, t_i=650 nm. Lower gap thickness invokes to enhance the device capacitance; consequently force gets enhanced. Though increasing electrode radius generates high electrostatic force still cavity gap has predominance effect upon it, when a combinational effect of insulation layer thickness is concerned. Lower gap thickness and higher insulation thickness is capable for generating higher electrostatic force maintaining t_g=450 nm, t_i=500 nm as reference. Though reduction in gap thickness can increase the generated force, still increased pull in voltage will restrict the actuation layer from full swing. Moderate gap separation should be considered in this regard to make the device efficient for generating high frequency ultrasound. Enhancement in electrostatic force due to the contribution of fringing is shown in Fig. 4.21. Fringing effect is more profound for lower electrode radius and this is quite evident from Fig. 4.21. Here enhancement due to fringing is expressed as

$$E_{F}^{'} = \left(\frac{F^{'}_{f_{bias}} - F^{'}_{bias}}{F^{'}_{bias}} \right) \times 100 \tag{4.21}$$

Insulation thickness is also a prime parameter along with the dielectric materials. The dimension of insulation thickness must be designed in such way so that it can withstand with the full scale generated electric field within the CMUT during operating mode. The thickness of the insulation is really important during collapse mode as this insulation layer prevent the cell from electric shock.

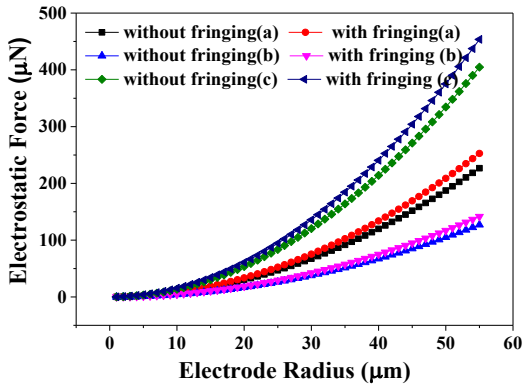

Fig. 4.20 Electrostatic force variation with electrode radius for a) t_g=450 nm, t_i=500 nm b) t_g=650 nm, t_i=300 nm c) t_g=300 nm, t_i=650 nm

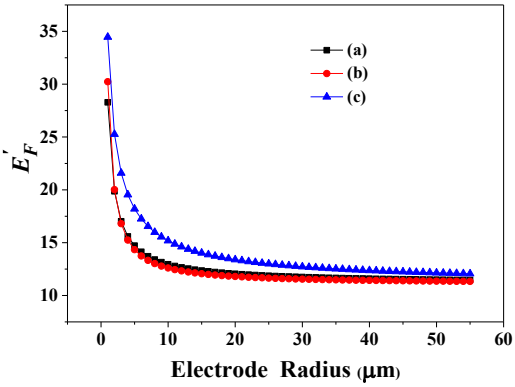

Fig. 4.21 E_F' with varying electrode radius for a) t_g=450 nm, t_i=500 nm b) t_g=650 nm, t_i=300 nm c) t_g=300 nm, t_i=650 nm

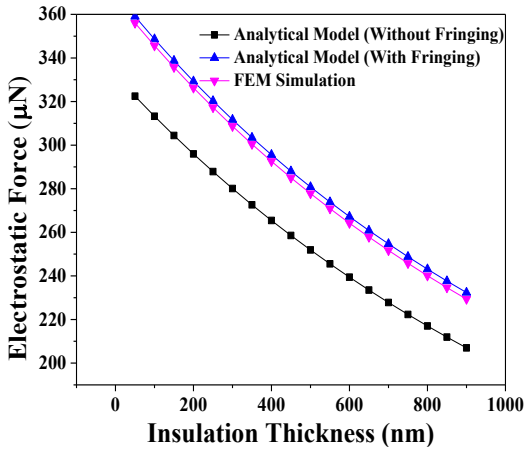

Fig. 4.22 Electrostatic force for varying insulation thickness

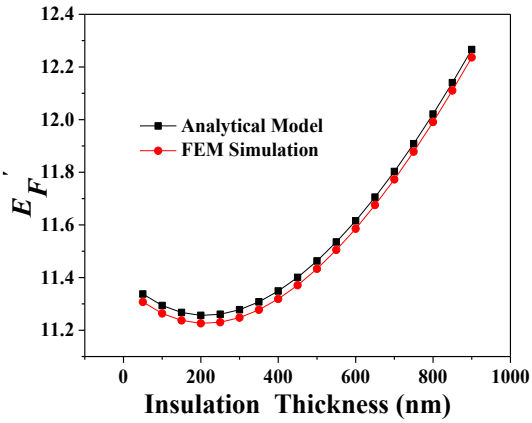

Fig. 4.23 E_F' for varying insulation thickness

Figure 4.22 shows the variation of electrostatic force with respect to insulation thickness where electrostatic force decreases with increase in insulation thickness of dielectric layer. Proper selection of dielectric insulation thickness is really important as it is one of the deciding factor for generating high sensitivity and electrostatic force. Fig. 4.23 also shows that enhancement of electrostatic force is profound involving fringing approach with respect to insulation thickness. Above 300 nm of insulation thickness fringing effect has greater impact than below. Average value E_F' of 11.14% is produced due to change on insulation thickness while design is done. As shown by Fig. 4.24, the variation of electrostatic force gets incremented with

increase in relative dielectric constant. A plot of $E_F^{'}$ with respect to relative dielectric constant is exhibited in Fig. 4.25. Fringing effect upon electrostatic force renders significant enhancement above dielectric constant value 10. Involvement of high-K material as insulation layer emphasizes the fringing effect in larger manner than materials having lesser dielectric constant. Performance of CMUT not only depends on insulation thickness and dielectric material but also depends upon the vacuum gap between two electrodes. Desired pressure output, actuation layer mass, stiffness is considered as a primary requirement.

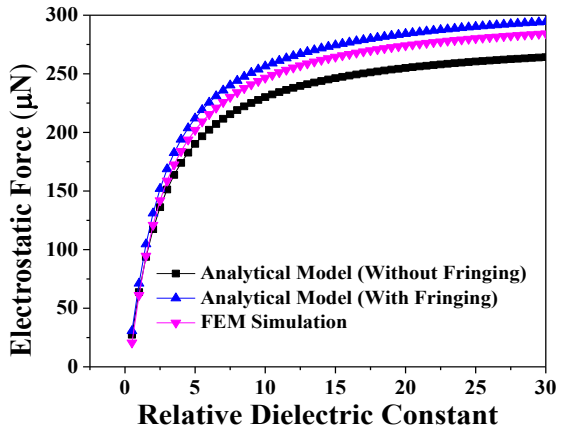

Fig. 4.24 Electrostatic force with relative dielectric constant

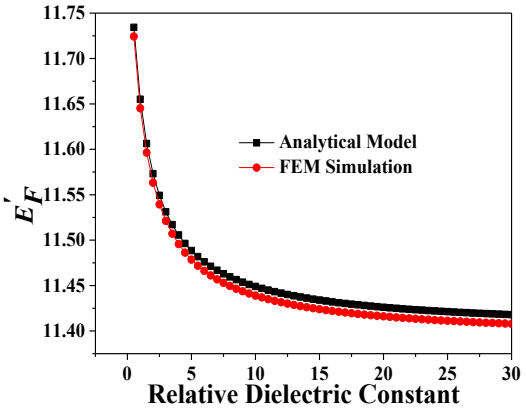

Fig. 4.25 $E_F^{'}$ for varying relative dielectric constant

Combining the variation of electrostatic force with electrode radius and insulation thickness, a 3D characteristic is exhibited in Fig. 4.26. Dependency of force with a simultaneous variation of electrode radius and relative dielectric constant is shown in Fig. 4.27. Enhancement of electrostatic force due to increase in electrode radius and decrement of the same for increasing insulation thickness is observed from Fig. 4.26. Subsequently maximum force is attained at maximum electrode radius and minimum insulation thickness. Similarly Fig. 4.27 depicts the behavioral approach of electrostatic force for increasing value of electrode radius and relative dielectric constant. Increase in both structural parameters cause enhancement in force, hence considering this combinational maximum force is achieved for maximum value of electrode radius and relative dielectric constant.

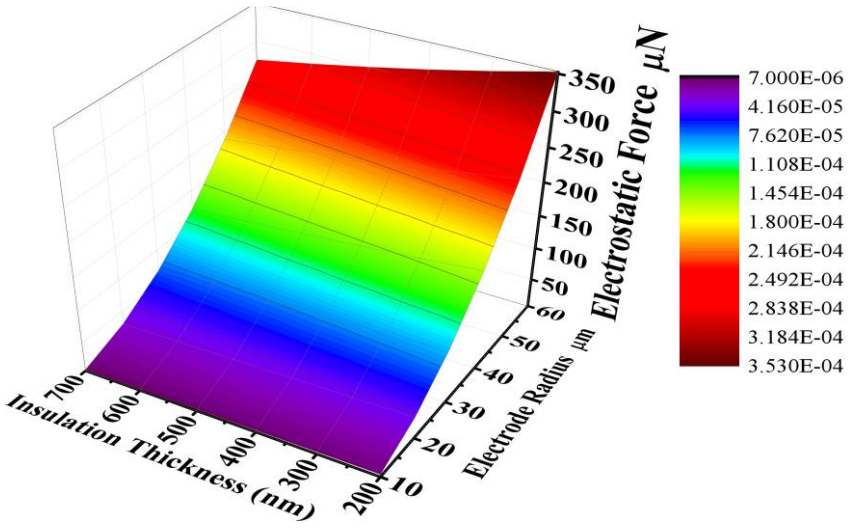

Fig. 4.26 Variation of force due to simultaneous change in r_e and t_i

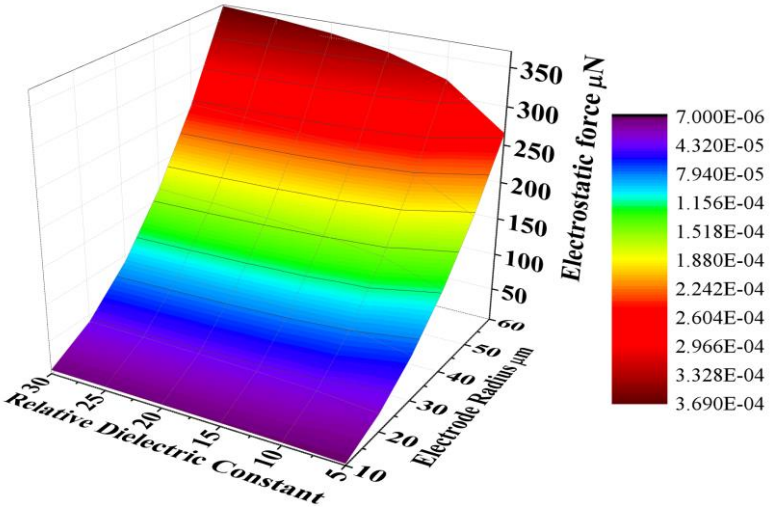

Fig. 4.27 Variation of force due to simultaneous change in r_e and K

Insightful impact of fringing modeling upon device generated force due to change in relative dielectric constant for various values of structural parameter is expressed through Fig. 4.28. Certainly higher valued electrode radius and lower gap thickness generates higher valued electrostatic force. In the contrary Fig. 4.29 shows that increase in insulation thickness decreases the generated force but combinational effect of reduced radius and increased gap thickness enhances the counterpart.

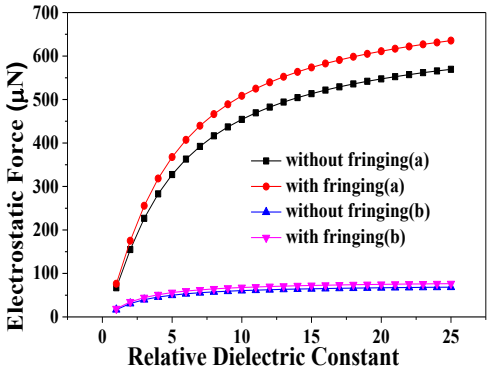

Fig. 4.28 Variation of electrostatic force due to change in various dielectric material for a) r_e=55 μm, t_g=300 nm, t_i=650 nm, b) r_e=27.5 μm t_g=450 nm, t_i=500 nm

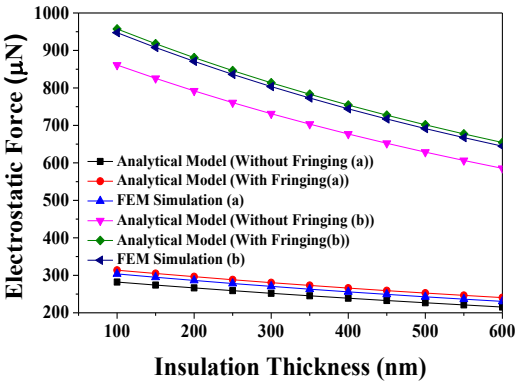

Fig. 4.29 Variation of electrostatic force due to change in insulation thickness for a) r_e=55 μm, t_g=450 nm b) r_e=27.5 μm t_g=300 nm

Figure 4.30 shows that higher value of increasing gap thickness produces lesser electrostatic force. Effect of fringing is quite vibrant within the fabricated [20] value between 350 nm-450 nm. Making the gap thickness less than this range will create a hindrance towards full swing and improving reproducibility. Figure 4.31 shows force enhancement for changing gap thickness which undoubtedly supports the decreased value of force for gap thickness above 500 nm. Average $E_F^{'}$ of 11.49% takes place in this characteristic study. Designing a CMUT for pulse echo imaging is feasible by applying high bias voltage. Usage of probe with high sensitivity requires proper biasing with the signal.

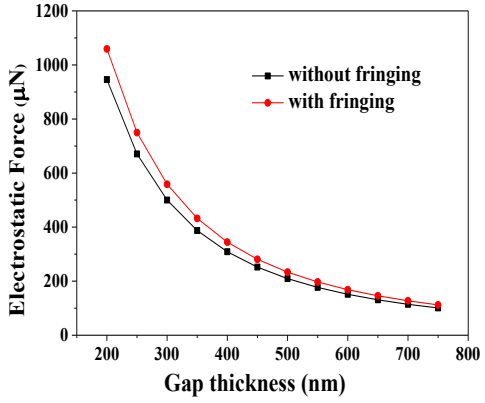

Fig. 4.30 Electrostatic force with t_g

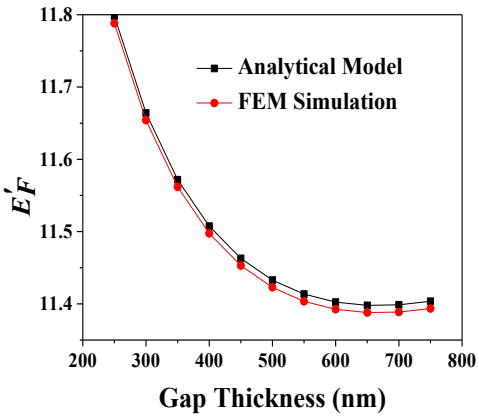

Fig. 4.31 $E_F^{'}$ for varying cavity height

As shown in Fig. 4.32 higher bias is capable enough to produce higher electrostatic force. Moreover in Fig. 4.33 an average $E_F^{'}$ of 11.5% is observed for increasing bias. Figure 4.34 exhibits a 3D representation of dual effect of electrode radius and bias voltage upon electrostatic force. For electrode radius 55 µm and bias voltage of 40 V produces maximum electrostatic force in the device. Figure 4.35 plots a 3D representation of electrostatic force for combining effect of electrode radius and gap thickness. Maximum force is generated for maximum electrode radius and minimum cavity gap.

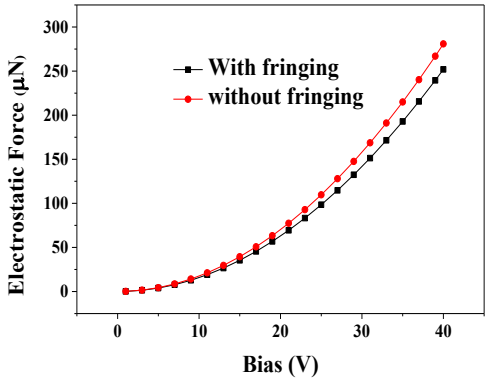

Fig. 4.32 Electrostatic force with bias

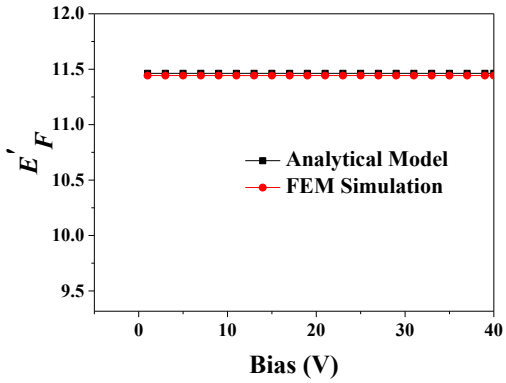

Fig. 4.33 $E_F^{'}$ for varying material for varying bias

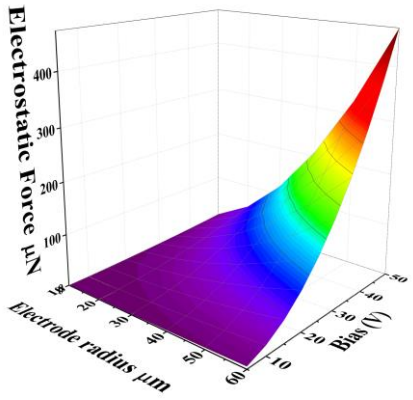

Fig. 4.34 Variation of force due to simultaneous change in r_e and V_{dc}

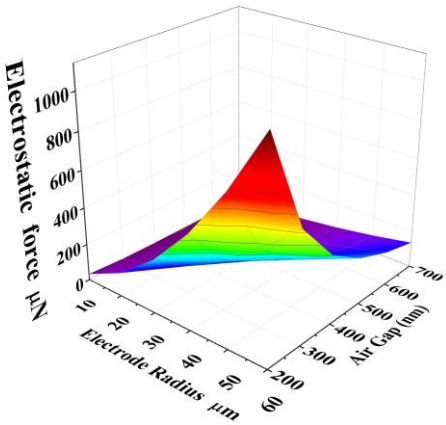

Fig. 4.35 Variation of force due to simultaneous change in r_e and t_g

4.5 Effect of HfO_2 as insulating material upon electrostatic force generation

Undoubtedly, insulated structure has proved to be more competent than non-insulated counterpart for its higher electrostatic force. Due to directly proportional relationship of capacitance and with relative dielectric constant and as per discussion from Section 3.9, in this section also device characteristics are compared specifically using HfO_2 and Si_3N_4 materials as insulation layer. Ability to achieve a full gap swing is calculated by the key parameter of CMUT electrostatic pressure. Achieving the similar full gap swing by giving a smaller input voltage depicts higher transmission sensitivity. Figure 4.36 exhibits comparative electrostatic force along with the gap separation. The electrostatic force is 252 μN for 500 nm Si_3N_4, where as for 50 nm insulation thickness involving HfO_2, the force becomes 330 μN at 500 nm gap separation.

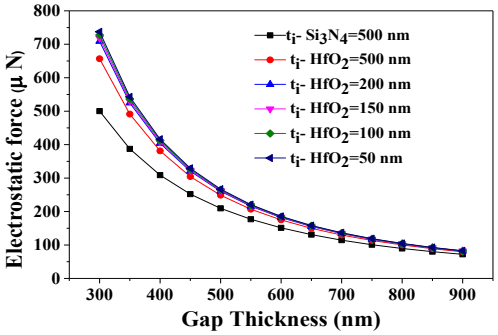

Fig. 4.36 Comparative analysis of electrostatic force for HfO_2/Si_3N_4 isolation

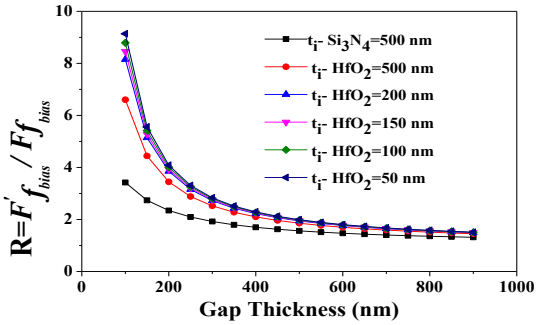

Fig. 4.37 Gain of electrostatic force (R) for HfO_2/Si_3N_4 isolation

Ratio of electrostatic force (R) generated by each device to that of an ideal parallel plate model without consisting isolation layer for the same input voltage is plotted in Fig 4.37. As SiC actuation layer is placed just below the top electrode to avoid stiction force and electrical hazards, CMUT structure without insulation layer produces larger valued electrostatic force compared to non-insulated one. Hence obviously the ratio R will be greater than unity. Involving HfO_2 as dielectric material instead of Si_3N_4 give rise to electrostatic force and by varying the thickness of HfO_2 insulation layer the enhancement is also visible in Fig 4.37. Reduction in insulation thickness reduces the separation between two parallel plates henceforth enhancement in force occurs. Keeping the insulation thickness at 50 nm, device can get rid of

electrical hazards and can produce higher electrostatic force than 500nm Si_3N_4 insulation which results generation of high intensity ultrasound. Enhancement due to HfO_2 insulating layer is calculated as,

$$E'_{HfO_2} = \left(\frac{F'_{f(HfO_2)} - F'_{f(Si_3N_4)}}{F'_{f(Si_3N_4)}} \right) \times 100 \tag{4.22}$$

where $F'_{f(Si_3N_4)}$ is the electrostatic force generated by structure having 500 nm Si_3N_4 layer and $F'_{f(HfO_2)}$ is measured as force generated from structure having HfO_2 insulation layer of various thickness within a range of 500 nm to 50 nm. An average E'_{HfO_2} of 17.05%, 20.9%, 22.7%, 24.6 % and 25.8 % is seen in Fig. 4.38 due to HfO_2 layer of 500 nm, 300 nm,200 nm,100 nm and 50 nm respectively.

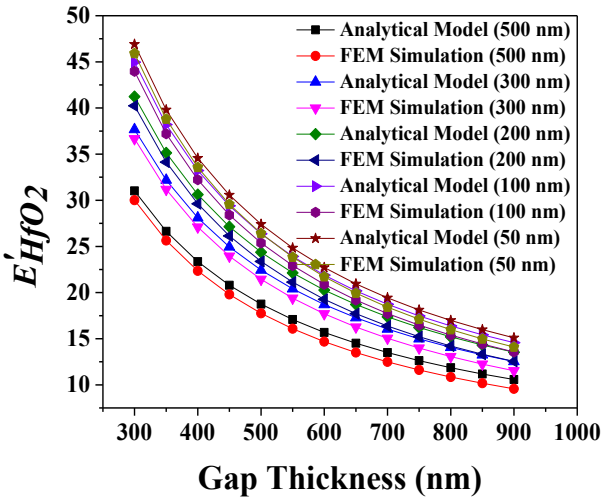

Fig. 4.38 E'_{HfO_2} for variation in gap thickness

Enhancement with radius for involving the high-K material is quite evident in Figs. 4.39 and 4.40, which shows and average 14% enhanced force due to a 50 nm HfO_2 insulation thickness compared to 500nm Si_3N_4 insulation.

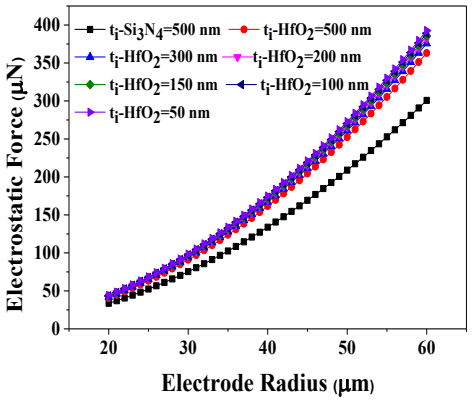

Fig. 4.39 Effect of high-K on electrostatic force due to change in electrode radius

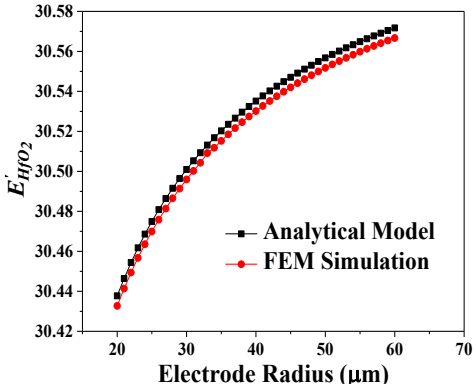

Fig. 4.40 E'_{HfO_2} for variation in electrode radius

Figure 4.41 also depicts a comparative approach that larger valued relative dielectric constant generates higher electrostatic force which is also effected by variation of insulation thickness. The relation between dielectric constant of a material is directly proportional with device capacitance. Enhancement of force due to high-K insulation is studied in Fig. 4.42, keeping insulation thickness 500 nm as standard value as relative dielectric constant changes. An average E'_F of 14% takes place while 50 nm insulation thicknesses is considered.

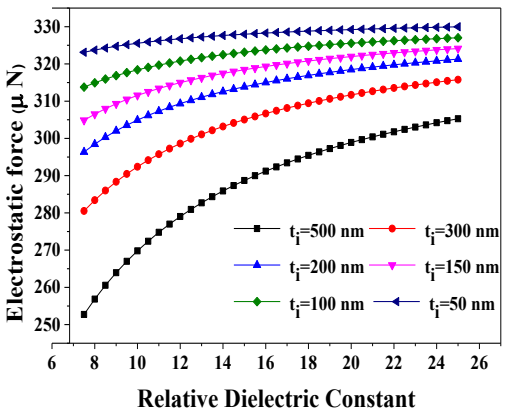

Fig. 4.41 Comparative study of electrostatic force for varying dielectric material

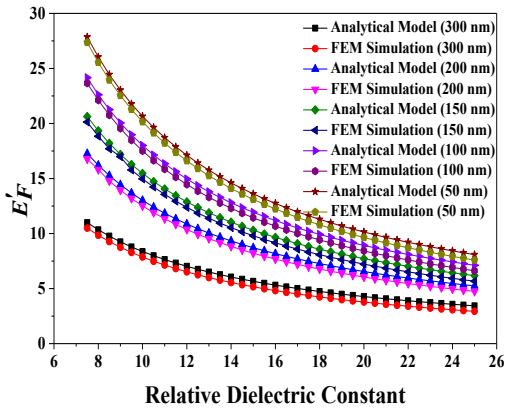

Fig. 4.42 Enhancement with respect to 500 nm thickness

In Fig. 4.43 electrostatic force is plotted due to change in insulation thickness involving Si_3N_4 and HfO_2 as insulating material where a non linear variation is seen for varying insulation thickness. Effect of high–K material gets

dominant more for the insulation thickness above 400 nm and the difference between the force generated by Si_3N_4 and HfO_2 become larger. Though higher insulation thickness makes the electrode far apart from other and reduces the force, still involving HfO_2 maintains the force within acceptable range. Figure 4.44 plots the enhancement of force against varying insulation thickness keeping the force generated by Si_3N_4 insulation layer as reference. An average force enhancement occurs by 24% due to HfO_2 insulation layer. Figure 4.45 exhibits the variation of electrostatic force is apparent that it intensifies from zero, which supports the logic of generating attraction force between two electrodes and simultaneously pulls down the actuation towards the substrate. As a result both the electrostatic force shows a parabolic opening up type characteristics due to given applied bias.

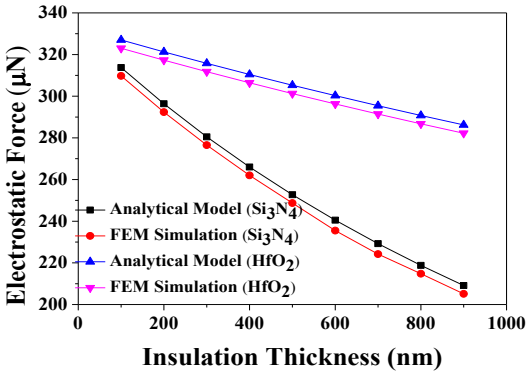

Fig. 4.43 Comparative study electrostatic force due to change in insulation thickness

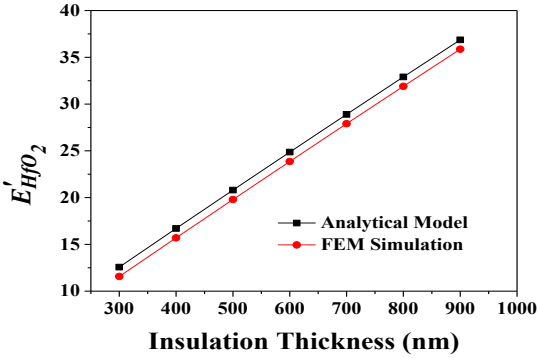

Fig. 4.44 Enhancement of force for varying insulation thickness

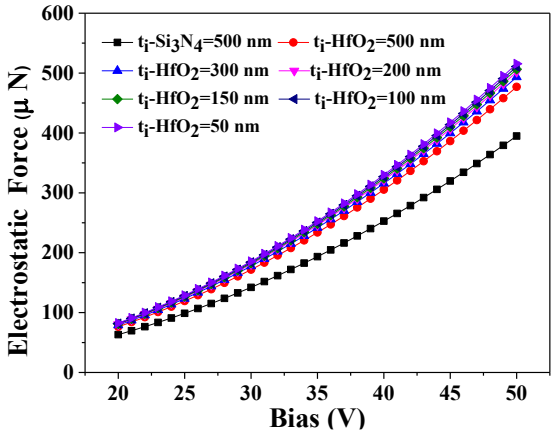

Fig. 4.45 Comparison electrostatic force for change in bias between HfO_2/ Si_3N_4 isolation

4.6 Summary

An improved analytical modeling of electrostatic force is carried out. This analysis deals with the Landau's technique for modeling the electrostatic force considering the fringing field capacitance in CMUT. Analytical data is validated by FEM simulation. Overall impact of fringing field is observed in electrostatic force in almost all types of capacitive device structure like actuation layer based, non-insulated and insulated CMUT. Based on performance insulated CMUT structure with SiC as structural material seem to be quite capable of generating high frequency ultrasound waves due to appreciable amount of force generation.. Introduction of an insulation layer enhances the device sensitivity and makes the CMUT ready to operate safely in high voltage as well high temperature. The insulation layer is quite helpful in enabling the CMUT to generate high resolution image at low cost. Such findings can serve the advancement of medical imaging in large scale. A comparative study between HfO_2 isolation and Si_3N_4 is done rigorously for insulation thickness from 500 nm to 50 nm.

References

[1] B. Bayram, E. Haeggstrom, G. G. Yaralioglu, B. T. Khuri-Yakub, "A new regime for operating capacitive micromachined ultrasonic transducers," *IEEE Transactions on Ultrasonics, Ferroelectrics, and Frequency Control*, vol. 50, no. 9, pp. 1184-1190, 2003.

[2] I. O. Wygant, M. Kupnik and B. T. Khuri-Yakub, "Analytically calculating actuationdisplacement and the equivalent circuit model of a circular CMUT cell," *IEEE Ultrasonics Symposium Proceedings,* pp. 2111– 2114, 2008.

[3] Y. Huang, A. S. Ergun, E. Hæggstr¨om, M. H. Badi, and B. T. Khuri- Yakub, "Fabricating capacitive micromachined ultrasonic transducers with wafer-bonding technology," *Journal of Microelectromechanical System*, vol. 12, no. 2, pp. 128–137, 2003.

[4] I. Ladabaum, X. Jin, H. T. Soh, A. Atalar, and B. T. Khuri-Yakub, "Surface micromachined capacitive ultrasonic transducers," *IEEE Transactions on Ultrasonics, Ferroelectrics, and Frequency Control*, vol. 45, no. 3, pp. 678–690, 1998.

[5] A. Caronti, G. Caliano, A. Iula, and M. Pappalardo, "An accurate model for capacitive micro machined ultrasonic transducers," *IEEE Transactions on Ultrasonics, Ferroelectrics, and Frequency Control,* vol. 49, no. 2, pp. 159–168, 2002.

[6] A. Lohfink and P.-C. Eccardt, "Linear and nonlinear equivalent circuit modeling of CMUTs," *IEEE Transactions on Ultrasonics, Ferroelectrics, and Frequency Control*, vol. 52, no. 12, pp. 2163–2172, 2005.

[7] A. Nikoozadeh, B. Bayram, G. Yaralioglu, and B. Khuri-Yakub, "Analytical calculation of collapse voltage of CMUT membrane," *IEEE Ultrasonics Symposium Proceedings*, vol. 1, pp. 256–259, 2004.

[8] H. Koymen, A. Atalar, E. Aydogdu, C. Kocabas, H. K. Oguz, S. Olcum, A. Ozgurluk, and A. Unlugedik, "An improved lumped element nonlinear circuit model for a circular CMUT cell," *IEEE Transactions on Ultrasonics, Ferroelectrics, and Frequency Control*, vol. 59, no. 8, pp. 1791–1799, 2012.

[9] B. Ahmad and R. Pratap, "Elasto-electrostatic analysis of circular microplates used in capacitive micromachined ultrasonic transducers," *IEEE Sensors Journal*, vol. 10, no. 11, pp. 1767–1773, 2010.

[10] S. Timoshenko and S. Woinowsky-Krieger, *Theory of Plates and Shells,* 2nd ed. Mcgraw-Hill College, 1959.

[11] R. L. Taylor and S. Govindjee, "Solution of clamped rectangular plate problems," *Communications in Numerical Methods in Engineering*, vol. 20, no. 10, pp. 757–765, 2004.

[12] M. Rahman, J. Hernandez, and S. Chowdhury, "An improved analytical method to design CMUTs with square diaphragms," *IEEE Transactions on Ultrasonics, Ferroelectrics, and Frequency Control*, vol. 60, no. 4, pp. 834–845, 2013.

[13] M. F. Lacour, T. L. Christiansen, J. A. Jensen and E. V. Thomsen, "Electrostatic and small-signal analysis of CMUTs with circular and square anisotropic plates," *IEEE Transactions on Ultrasonics, Ferroelectrics, and Frequency Control*, vol. 62, no. 8, pp. 1563-1579, 2015.

[14] M. F.Lacour, T. L. Christiansen, J. A. Jensen, and E. V. Thomsen, "Modelling of CMUTs with anisotropic plates," *IEEE Ultrasonics Symposium Proceedings*, pp. 588–591, 2012.

[15] Wygant, I.O., Kupnik, Mario and Khuri-Yakub, Pierre, "Analytically calculating actuation displacement and the equivalent circuit model of a circular CMUT cell", *IEEE Ultrasonics Symposium Proceedings,* pp. 2111 – 2114, 2008.

[16] R. Maity, N. P. Maity, K. Guha, and S. Baishya, "Analysis of fringing capacitance effect on the performance of MEMS based micromachined ultrasonic air transducer", *IET Micro and Nano Letters*, vol 13, no. 6, pp. 872-877, 2018

[17] R. Maity, N. Maity, K.S, Rao, K. Guha and S. Baishya, "New Compact Analytical Model of Nano-Electro-Mechanical-Systems Based Capacitive Micromachined Ultrasonic Transducers for Pulse Echo Imaging", *Journal of Computational Electronics,* vol. 17, pp. 1334-1342, 2018.

[18] R. Maity, N. P. Maity, K. Guha, and S. Baishya, "Analysis of fringing capacitance effect on the performance of MEMS based micromachined ultrasonic air transducer, *IET Micro and Nano Letters*, vol 13, no. 6, pp. 872-877, 2018.

[19] S. Burt, N. Finney, J. Young, Y. Ataiiyan, "Fringing Field Parallel Plate Capacitor", Department of Engineering and Physics", *AAPT 129th National Meeting*, Santa Rosa Junior College, pp. 1-8, 2017.

[20] Q. Zhang, P. Cicek, K. Allidina, F. Nabki, and M. N. El-Gamal, "Surface Micromachined CMUT Using Low-Temperature Deposited SiC Membranes for Above-IC Integration", *IEEE Journal of Microelectromechanical System,* vol. 23, no. 2, pp.482-493, 2014.

CHAPTER

5

Displacement Profile

5.1 Introduction

In transmitting and receiving mode, vibrating actuation layer generates and detects ultrasonic waves respectively. During transmission mode, the actuation layer responses with the applied voltage. This deformation is solely dependent on variations of capacitance and electrostatic force. Based on radial position magnitude of electrostatic force varies and deflection profile of actuation layer is calculated by the distribution of this force over the actuation layer. Uniform pressure generation from the total force has to be assumed while deflection is calculated. This assumption proved to be suitable as both the actuation layer and electrodes are having same diameter. Effect of fringing field is also studied. Noticeable amount of enhancement of device capacitance and electrostatic force are already discussed in Chapters 3 and 4, due to this fringing effect. This enhanced force indeed a prime cause for enhancement of displacement. Comparative analysis of various adopted displacement models is derived and an improved approach of displacement model is carried out in the following sections.

5.2 Actuation layer deflection of a non insulated CMUT using plate model

Generalized plate model is implied in order to achieve a functional representation of deformed clamped actuation layer in many research works [1] as exact shape of deformed layer is completely unknown. Calculation of deflection is carried out applying the boundary conditions, geometrical shape and loading condition of actuation layer. Considering CMUT structure of Fig. 3.2(b) analytical calculation of plate deflection is done in non-insulated cell with fully metalized actuation layer [2].

5.2.1 Analytical modeling of plate deflection profile

When a symmetrically distributed load acts upon a circular plate along the perpendicular axis of plate that passes through the centre, then the middle plane the plate will be deflected symmetrically. The expression of the deflected clamped circular plate is a function of radius under uniform pressure and was derived by Timoshenko [3]. All the equally distant points with respect to the centre will have same deflection and considered to be deflected in one diametral section along the symmetric axis. Considering the centre of the un-deflected plate as origin of coordinates in Fig. 5.1, distance from the centre is r and deflection at the centre is depicted by w_p in z direction. Slope of the deflected surface at any arbitrary point A is denoted by the ratio of change in deflection to the change in radial distance. The angle between the vertical plane to the deflected surface point A and the symmetry axis OB is φ. Small deflection at the diametral section r in the middle of the surface in any direction n is expressed as,

$$\frac{1}{r_n} = -\frac{d^2 w_p}{dr^2} = \frac{d\varphi}{dr} \tag{5.1}$$

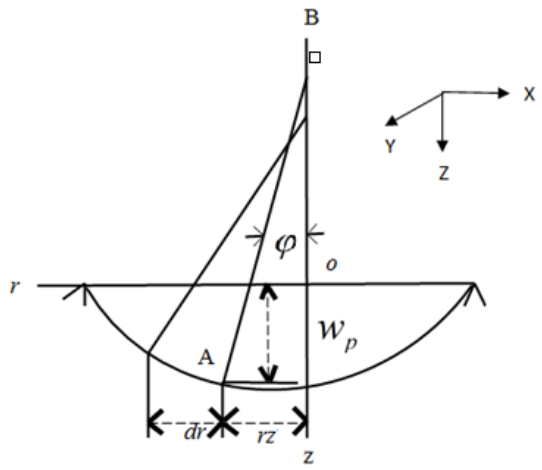

Fig. 5.1 Bending of plate due to uniform loading

According to the symmetry condition, between two principal curvatures those take place, one is $\frac{1}{r_n}$ at the deflected surface A and other one is parallel to the normal of AB and vertical to *rz* plane. Considering the twist at the surface, expression of deflection becomes,

$$\frac{1}{r_t} = -\frac{1}{r}\frac{dw_p}{dr} = \frac{\varphi}{r} \tag{5.2}$$

Hence , considering (5.1) and (5.2) as principal curvature expressions assuming the equation of pure bending conditions, bending moments per unit length is expressed by (5.3) and (5.4)

$$M_r = -F_r\left(\frac{d^2w_p}{dr^2} + \frac{\sigma_a}{r}\frac{dw_p}{dr}\right) = F_r\left(\frac{d\varphi}{dr} + \frac{\sigma_a}{r}\varphi\right) \tag{5.3}$$

$$M_t = -F_r\left(\frac{1}{r}\frac{dw_p}{dr} + \sigma_a\frac{d^2w_p}{dr^2}\right) = F_r\left(\frac{\varphi}{r} + \sigma_a\frac{d\varphi}{dr}\right) \tag{5.4}$$

The bending moment acts along the circumferential regions of the plate represented by 'abcd' M_r in Fig. 5.2. The figure is considered to depict a slice of a conical surface, with the apex at B. M_t acts along the diametric sections *rz* of the plate and F_r is the flexural rigidity and expressed as $F_r = \frac{Y_a t_a^3}{12(1-\sigma_a{}^2)}$. Here Y_a and σ_a are the plate material's Young's modulus and Poisson ratio, respectively.

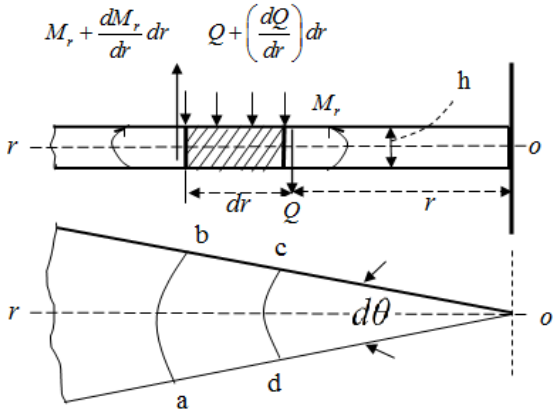

Fig. 5.2 Bending moment of plate element 'abcd'

As (5.3) and (5.4) is a function of either w_p or φ, hence can be derived by considering the balance condition of the plate element shown by abcd in Fig. 5.2 which is cut out from the bended plate by a pair of cylindrical section ab and cd by two diametral sections 'ad' and 'bc'. Expression of the coupling force acting on the 'cd' side of the element is ,

$$M_r r d\theta \tag{5.5}$$

and the same for 'ab' side is

$$\left(M_r + \frac{dM_r}{dr} dr\right)(r + dr)\, d\theta \tag{5.6}$$

Couple acting on the 'ad' and 'bc' are equivalent to $M_t dr$ and resultant couple acted on the *roz* plane is derived as $M_t dr d\theta$. The shearing force per unit length of the cylindrical section of radius *r* is denoted by Q . The total estimated shearing force operating on 'cd' of the element is along these two sections correspondingly expressed as, $Qrd\theta$ and corresponding force on the 'ab' side

$$\left[Q + \left(\frac{dQ}{dr}\right) dr\right](r + dr)\, d\theta \tag{5.7}$$

Eliminating the infinitesimal difference between the two opposite shearing force acting on the element sides, couple in the *rz* plane be expressed as,

$$Qrdrd\theta \tag{5.8}$$

Summing up the moments (5.5), (5.6), (5.7) and (5.8) and eliminating the moment due to the exterior load on the element, the below mentioned expression can be written.

$$\left(M_r + \frac{dM_r}{dr} dr\right)(r + dr)\, d\theta - M_r r d\theta - M_t dr d\theta + Qrd\theta dr = 0 \tag{5.9}$$

Neglecting infinitesimal small quantity of higher order,

$$M_r + \frac{dM_r}{dr} r - M_t + Qr = 0 \tag{5.10}$$

Putting the value of (5.3) and (5.4) for M_r and r the simplified form of (5.10) can be expressed as,

$$\frac{d^2\varphi}{dr^2}+\frac{1}{r}\frac{d\varphi}{dr}-\frac{\varphi}{r^2}=-\frac{Q}{F_r} \tag{5.11}$$

This also can be written in another form as,

$$\frac{d^3w_p}{dr^3}+\frac{1}{r}\frac{d^2w_p}{dr^2}-\frac{1}{r^2}\frac{dw_p}{dr}=\frac{Q}{F_r} \tag{5.12}$$

In case of homogeneously loaded circular shaped plate the shearing force Q can be evaluated simply by separating the load distributed within the circle having radius *r* by *2πr;* then (5.11) and (5.12) is used to establish the slope and deflection of the plate. Integrating (5.11) and (5.12) following forms are attained.

$$\frac{d}{dr}\left[\frac{1}{r}\frac{d(r\varphi)}{dr}\right]=-\frac{Q}{F_r} \tag{5.13}$$

$$\frac{d}{dr}\left[\frac{1}{r}\frac{d}{dr}\left(r\frac{dw_p}{dr}\right)\right]=\frac{Q}{F_r} \tag{5.14}$$

Q is expressed as a function of r and R.H.S of (5.14) as a function of pressure distributed over the plate. Multiplying both sides by 2πr, the equation becomes,

$$Q2\pi r=\int_0^r P2\pi r dr \tag{5.15}$$

Hence, the expression becomes as,

$$r\frac{d}{dr}\left[\frac{1}{r}\frac{d}{dr}\left(r\frac{dw_p}{dr}\right)\right]=\frac{1}{F_r}\int_0^r Prdr \tag{5.16}$$

Differentiating both sides, the equation becomes as.

$$\frac{1}{r}\frac{d}{dr}\left\{r\frac{d}{dr}\left[\frac{1}{r}\frac{d}{dr}\left(r\frac{dw_p}{dr}\right)\right]\right\}=\frac{P}{F_r} \tag{5.17}$$

For uniformly loaded circular plate, it is considered that the pressure P is distributed at the total surface and the shearing force at a radial distance r can be expressed as,

$$2\pi rQ=\pi r^2P$$

$$\Rightarrow Q=\frac{Pr}{2} \tag{5.18}$$

Substituting the value in (5.14), it can be evaluated as,

$$\frac{d}{dr}\left[\frac{1}{r}\frac{d}{dr}\left(r\frac{dw_p}{dr}\right)\right]=\frac{Pr}{2F_r} \tag{5.19}$$

Integrating (5.19), the following expression can be written,

$$\frac{1}{r}\frac{d}{dr}\left(r\frac{dw_p}{dr}\right)=\frac{Pr^2}{4F_r}+C_1 \tag{5.20}$$

Here C_1, is constant of integration. Multiplying both side of (5.20) by r and making second integration the following equations are expressed,

$$r\frac{dw_p}{dr}=\frac{Pr^4}{16F_r}+\frac{C_1r^2}{2}+C_2$$

$$\frac{dw_p}{dr}=\frac{Pr^3}{16F_r}+\frac{C_1r}{2}+\frac{C_2}{r} \tag{5.21}$$

Integrating the above equation, the displacement can be expressed as,

$$w_p=\frac{Pr^4}{64F_r}+\frac{C_1r^2}{4}+C_2\log\frac{r}{r_a}+C_3 \tag{5.22}$$

where r_a is the radius of the circular shaped actuation layer considered as plate in this displacement modeling. In case of circular plate with clamped edge, slope of deflection surface in the radial direction is zero at a radial distance $r=0$ and $r=r_a$, Applying the boundary condition in (5.21),

$$\left(\frac{Pr^3}{16F_r}+\frac{C_1r}{2}+\frac{C_2}{r}\right)_{r=0}=0 \tag{5.23}$$

$$\left(\frac{Pr^3}{16F_r}+\frac{C_1r}{2}+\frac{C_2}{r}\right)_{r=r_a}=0 \tag{5.24}$$

From (5.23), constant C_2=0, substituting the value in (5.24) evaluation of constant

C_1 is depicted as below,

$$C_1 = -\frac{\mathrm{P}\, r_a^{\,2}}{8F_r}$$

Putting the constant value in equation (5.21) the slope can be expressed as,

$$\varphi = -\frac{dw_p}{dr} = \frac{Pr}{16F_r}\left(r_a^{\,2} - r^2\right) \tag{5.25}$$

Equation (5.22) can be again written as,

$$w_p = \frac{Pr^4}{64F_r} - \frac{\mathrm{P}\, r_a^{\,2} r^2}{32F_r} + C_3 \tag{5.26}$$

Considering the boundary condition at $r = r_a$ the following equation can be achieved,

$$\frac{Pr_a^{\,4}}{64F_r} - \frac{\mathrm{P}\, r_a^{\,4}}{32F_r} + C_3 = 0 \tag{5.27}$$

Hence the constant C_3 can be written as,

$$C_3 = \frac{Pr_a^{\,4}}{64F_r}$$

and the displacement for symmetrically loaded plate can be expressed as,

$$w_p = \frac{P}{64F_r}\left(r_a^{\,2} - r^2\right)^2 \tag{5.28}$$

As displacement is maximum at the centre so, the equation can be rewritten as,

$$w_{p(\max)} = \frac{\mathrm{P}\, r_a^{\,4}}{64F_r}$$

Evaluation of plate deflection is dependent on upon P, which is evaluated from electrostatic force (4.2) generated in the device. Under static bias condition P is replaced by $P_{f_{bias}} = \frac{F_{f_{bias}}}{A}$ where, $F_{f_{bias}}$ is the electrostatic force with the inclusion of fringing fields as derived in (4.13) and the final expression becomes,

$$w_{pf_{bias}} = \frac{P_{f_{bias}} r_a^4}{64F_r} \tag{5.29}$$

5.2.2 Analysis of plate deflection in non-insulated structure

Under static bias condition the actuation layer is deflected towards the bottom electrode. Characteristic study of this deflection is analyzed by plate model under influence of various device parameters like electrode radius, actuation layer thickness, bias and cavity height. A comparative analysis is carried out between two non-insulated structure using SiC and Si_3N_4 actuation layer material. Pressure intensity upon the actuation layer is dependent on electrostatic force generated in the device. Considering $F_{f_{bias(Si_3N_4)}}$ as electrostatic force for Si_3N_4 actuation layer based element and $F_{f_{bias(SiC)}}$ for SiC actuation layer based device pressure is calculated. Calculation of flexural rigidity is also done separately by actuation layer material's Young's modulus and respective Poisson ratio. Here Young's modulus of Si_3N_4 is considered as 320 GPa and that of SiC is 260GPa. Figure 5.3 shows the plate deflection with respect to change in actuation layer radius. Increasing actuation layer radius increases the deflection and a parabolic opening up characteristic is exhibited. A comparative approach is also shown in the figure for a) t_g =500 nm and t_g =350nm.

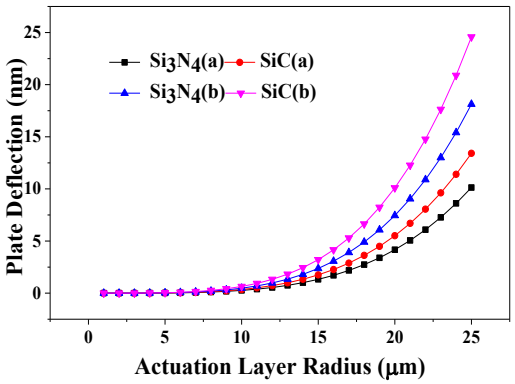

Fig. 5.3 Plate deflection with change in actuation layer radius for a) t_g =500 nm b) t_g =350 nm

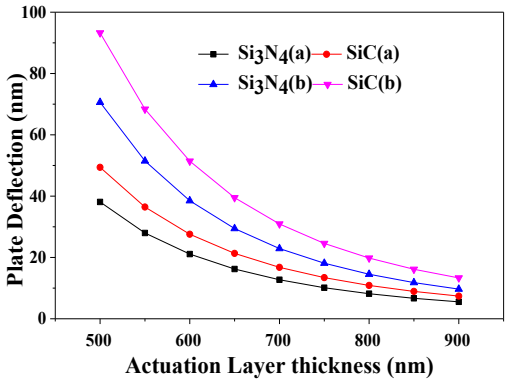

Fig. 5.4 Plate deflection with change in thickness of actuation layer for a) t_g =500 nm b) t_g =350 nm

Lower gap thickness causes higher deflection as the capacitive plates come close to each other and produce larger capacitance. Consequently, larger capacitance generates larger electrostatic force and deflection. Figure 5.4 shows an exponentially

decreasing characteristic of deflection for increasing actuation layer thickness. Lower value of cavity height and actuation layer thickness produces higher deflection. Figures 5.5 and 5.6 reflect the variation of plate deflection with the change of bias and radial distance from the centre. A comparative study is shown in Fig. 5.5 for a) r_a =25 µm and b) r_a=12.5 µm, where deflection decreases for lower actuation layer radius value. It is observed from Fig. 5.6 that at centre the deflection is maximum and at the boundary it becomes zero. Reduction in bias causes decremented deflection. The above plate deflection characteristics exhibit 13.8nm and 10.2nm deflection at device structural parameters [2] for SiC and Si_3N_4 actuation layer based device respectively. Cavity height for the structure taken as reference [2] is 500nm but only 2.8% of gap separation is used for full swing mode deflection.

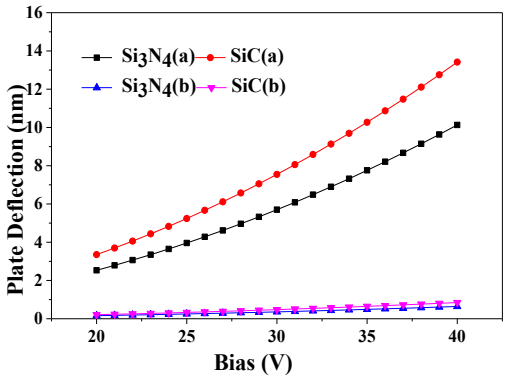

Fig. 5.5 Plate deflection with change in bias voltage for a) r_a=25 µm b) r_a=12.5 µm

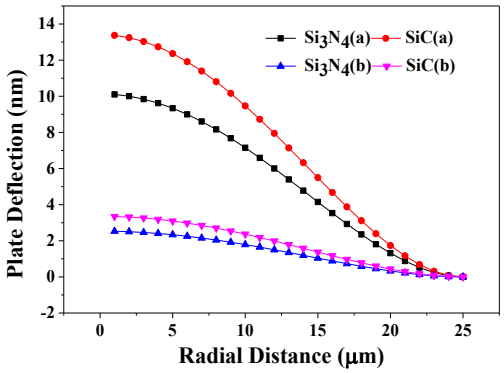

Fig. 5.6 Deflection with change in radial distance for a) V_{dc}=40 V b) V_{dc}=20 V

5.3 Actuation layer deflection of a non-insulated CMUT using membrane model

Extensive advancement of material science induces various materials to in MEMS that follows the basic requirements [4-8]. These materials are metals like Ni, Al, non-metals like Si, Ge, GaAs, polymers like SU8, polymide like diamond, SiC, Si_3N_4 , SiO_2 [9-11]. Based on certain parameters like Young modulus, residual stress, material density, displacement also changes in the device. Actuating material with low residual stress and high Young's modulus improves the deflection and becomes capable enough to produce high frequency ultrasound wave. Plate deflection model

doesn't suit always for evaluating peak deflection. In the context displacement can be modeled under static bias by involving Mason's expression. While analysing with Mason's expression the actuation layer is considered as membrane throughout the analytical modeling.

5.3.1 Analysis of membrane deflection in non-insulated structure using Mason's analysis

Mechanical behavior of actuation layer of CMUT can be executed by consideration of Mason's analysis [12]. Expression of motion of actuation layer under tension will be,

$$\frac{\left(Y_a + T_a\right) t_a^{\,3}}{12\left(1-\sigma_a^{\,2}\right)} \nabla^4 w_m - T_a \nabla^2 w_m - P + t_a \rho_a \frac{\partial^2 w_m}{\partial t^2} = 0 \tag{5.30}$$

Here t_a is actuation layer thickness, w_m is displacement of actuation layer involving membrane model , T_a is Tension of actuation layer, ρ_a is material density of actuating material. Displacement of actuation layer under static bias is derived here and as $t_a^3 \to 0$, hence (5.30) can be written as

$$T_a \left(\frac{d^2 w_m}{dr^2} + \frac{1}{r} \frac{dw_m}{dr} \right) - t_a \rho_a \frac{\partial^2 w_m}{\partial t^2} + P = 0 \tag{5.31}$$

Under static bias (5.31) becomes,

$$\frac{d^2 w_m}{dr^2} + \frac{1}{r} \frac{dw_m}{dr} + P \,/\, T_a = 0 \tag{5.32}$$

As r is the radial distance measured from centre, multiplying both side of (5.32) by r^2, (5.33) is achieved.

$$r^2 \left(\frac{d^2 w_m}{dr^2} \right) + r \left(\frac{dw_m}{dr} \right) = - \left(\frac{P}{T_a} \right) r^2 \tag{5.33}$$

Let $r = e^z$ then $z = logr$. Assuming $\frac{d}{dZ} = D$, so $r \frac{dw_m}{dr} = Dw_m$ and $r^2 \frac{d^2 w_m}{dr^2} = D(D-1) w_m$. Considering $C_1 + C_2 z$ as complementary function, where C_1 and C_2 are constants. Hence the solution can be written as ,

$$\left[D\left(D-1\right)+D\right]w_m=-\frac{P}{T_a}e^{2z} \tag{5.34}$$

The particular integral,

$$\text{PI}=\frac{1}{D^2}\left[\frac{-P}{T_a}e^{2z}\right]=-\frac{-P}{T_a}e^{2z}\frac{1}{(D+2)^2}=\frac{-P}{4T_a}e^{2z}\left\{1-2\times\frac{D}{2}+.....\right\} \tag{5.35}$$

$$\text{The particular integral}=\frac{-P}{4T_a}e^{2z} \tag{5.36}$$

The general solution becomes,

$$w_m(z)=CF+PI=\left(C_1+C_2z\right)-\frac{P}{4T_a}e^{2z} \tag{5.37}$$

Putting the value of z in (5.37) is expressed by,

$$w_m(r)=\left(C_1+C_2\log r\right)-\frac{P}{4T_a}r^2 \tag{5.38}$$

Displacement $w(r)$ will be maximum at $r=0$. Multiplying both side of (5.38) by r the equation becomes,

$$C_2-\frac{P}{2T_a}r^2=0$$

$$\Rightarrow C_2=0 \tag{5.39}$$

Displacement $w_m(r)$ will be 0 at the boundary of the actuation layer at $r=r_a$ as diameter of top electrode is matched with the actuation layer. Putting this boundary condition at (5.38), the expression is represented as,

$$C_1=\frac{P}{4T_a}r_a^{\,2} \tag{5.40}$$

Hence, putting the values of (5.39) and (5.40) in (5.38), it becomes,

$$w_m\left(r\right)=\frac{P}{4T_a}r_a^{\,2}-\frac{P}{4T_a}r_a^{\,2}=\frac{P}{4T_a}\left(r_a^{\,2}-r^2\right) \tag{5.41}$$

If maximum displacement is $w_{m(\max)}$, then at $r=0$,

$$w_{m(\max)}=\frac{P}{4T_a}\left(r_a^{\,2}-0\right)=\frac{P}{4T_a}r_a^{\,2} \tag{5.42}$$

Pressure P is derived from electrostatic force under static bias condition. P_{bias} generated in non-insulated CMUT excluding fringing is expressed from (4.13),

$$P_{bias} = F_{bias}/A = \frac{1}{2A}\frac{V_{dc}^{\,2}C_a^{\,2}}{C_g^{\,2}\left(\frac{C_a}{C_g}+1\right)^2}\left[\varepsilon_g\frac{\pi r_e^{\,2}}{t_g^{\,2}}\right] \tag{5.43}$$

Putting the value of (5.43) in (5.42), peak displacement at the centre of the actuation layer under static bias for non-insulated element excluding fringing effect becomes,

$$w_{m_{bias}} = \left(\frac{1}{8AT_a}\right)\times\frac{V_{dc}^{\,2}C_a^{\,2}r_a^{\,2}}{\left(\frac{C_a}{C_g}+1\right)^2 C_g^{\,2}}\times\left[\left(\frac{\varepsilon_g\pi r_e^{\,2}}{t_g^{\,2}}\right)\right] \tag{5.44}$$

On the other hand, $P_{f_{bia}}$ generated in non-insulated CMUT including fringing is expressed from (4.14),

$$P_{f_{bias}} = F_{f_{bias}}/A = \frac{1}{2A}\frac{V_{dc}^{\,2}C_{af}^{\,2}}{C_{gf}^{\,2}\left(\frac{C_{af}}{C_{gf}}+1\right)^2}\left[\varepsilon_g\frac{\pi r_e^{\,2}}{t_g^{\,2}}+\frac{\varepsilon_g r_e}{\left(\frac{16\pi r_e}{t_g}-1\right)}\times\frac{16\pi r_e}{t_g^{\,2}}\right]. \tag{5.45}$$

Substituting (5.45) in (5.42), peak displacement at centre under static bias for non-insulated element including fringing effect becomes,

$$w_{mf_{bias}} = \left(\frac{1}{8AT_a}\right)\times\frac{V_{dc}^{\,2}C_{af}^{\,2}r_a^{\,2}}{\left(\frac{C_{af}}{C_{gf}}+1\right)^2 C_{gf}^{\,2}}\times\left[\left(\frac{\varepsilon_g\pi r_e^{\,2}}{t_g^{\,2}}\right)+\left(\frac{\varepsilon_g r_e}{\left(\frac{16\pi r_e}{t_g}\right)-1}\right)\times\left(\frac{16\pi r_e}{t_g^{\,2}}\right)\right] \tag{5.46}$$

Investigation of fringing effect upon displacement enhancement is calculated by,

$$E_m = \frac{w_{mf_{bias}} - w_{m_{bias}}}{w_{m_{bias}}}\times 100\% \tag{5.47}$$

Enhancement in displacement for a cell with SiC actuation layer instead of Si_3N_4 is

$$E_{m\_SiC} = \left(\frac{w_{mf_{bias(SiC)}} - w_{mf_{bias(Si_3N_4)}}}{w_{mf_{bias(Si_3N_4)}}} \right) \times 100\% \quad (5.48)$$

Here $w_{mf_{bias(SiC)}}$ is the displacement of SiC based non-insulated element and the same for Si_3N_4 actuation layer based is $w_{mf_{bias(Si_3N_4)}}$. These two expressions are calculated from (5.46) by substituting the value of $F_{f_{bias(SiC)}}$ and $F_{f_{bias(Si_3N_4)}}$ respectively in (5.45). Electrostatic force $F_{f_{bias(SiC)}}$ is generated in the device for involving SiC as actuation layer and that same involving Si_3N_4 generates electrostatic force as $F_{f_{bias(Si_3N_4)}}$. Both values of electrostatic force are calculated from $C_{eqf(SiC)}$ and $C_{eqf(Si_3N_4)}$ using (3.8) putting relative dielectric constant as 9.7 and 7.5 respectively in (4.7). Calculation of membrane displacement for Si_3N_4 and SiC actuation layer was done by considering residual stress as 80 MPa and that of SiC is 30 MPa.

5.3.2 FEM Simulation

The PZFlex FEM analysis was carried out to evaluate the actuation layer displacement behaviour. Three different geometries of capacitive element have considered for the FEM model. Considering same cross sectional area circular, square and hexagonal shapes are studied which has shown in Fig. 5.7. During vibrating mode device actuation layer deforms into a corresponding shape. The actuation layer displacement profile is shown in Fig. 5.8.

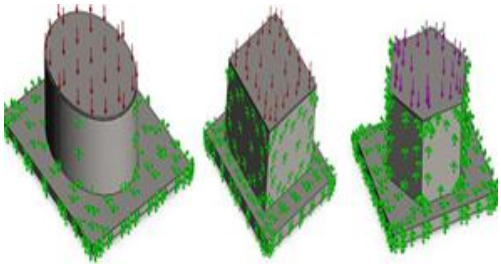

Fig. 5.7 FEM models of dissimilar membrane profile

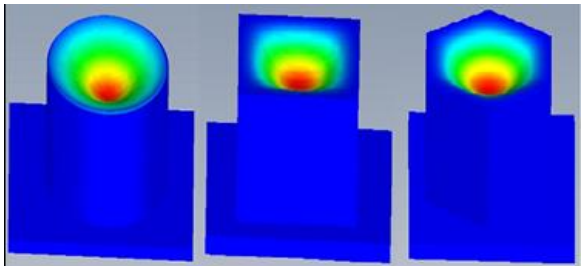

Fig. 5.8 FEM model magnitude distribution of the proposed structures

It is observed that circular structure is providing higher actuation layer displacement followed by hexagonal actuation layer and lastly square actuation layer. The FEM result justifies the analysis of circular shape which shown in Fig. 5.9.

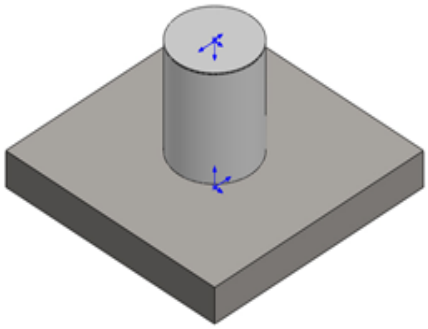

Fig. 5.9 CMUT with circular shape model

Meshed geometry of the simulated structure is shown in Fig. 5.10. The red arrows show the application of uniform electrostatic force along with all boundary conditions. The model consists of three parts: substrate, base, and actuation layer. The green symbols on the substrate are fixtures, which were added on the substrate only. Here time domain analysis is involved to evaluate the actuation layer displacement profile which shows maximum displacement at the centre as shown in Fig. 5.11. Outcome of analytically modelled data including fringing effect is validated with the results depicted by FEM model. Actuation layer displacement behaviour for non insulated and insulated structure is carried out in the following sections.

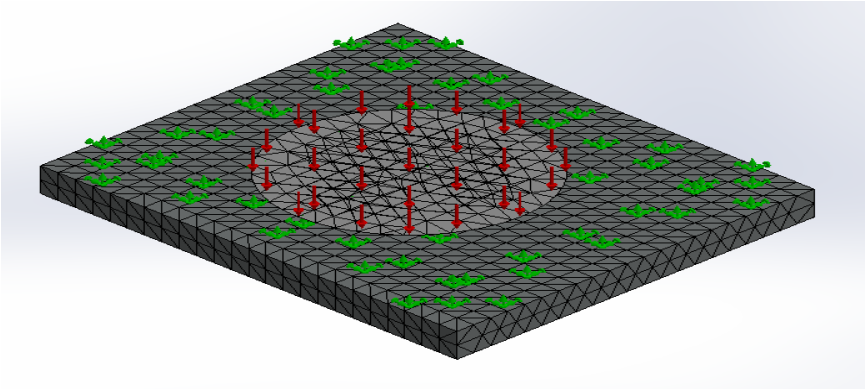

Fig. 5.10 Isometric view of the meshed geometry

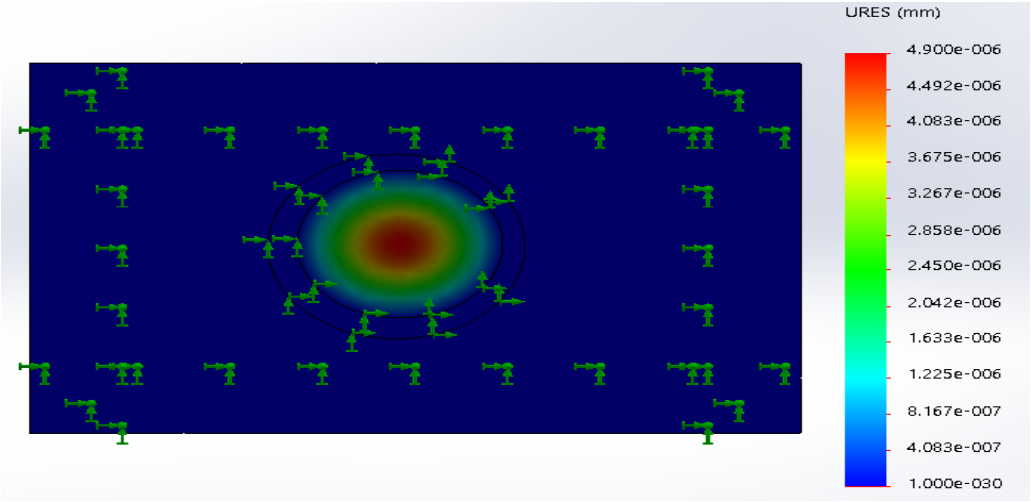

Fig. 5.11 Displacement profile of the simulated geometry

5.3.3 Comparative study between plate and actuation layer displacement for Si_3N_4 / SiC actuation layer based non-insulated cell

Figures 5.12 and 5.13 show a comparative study of displacement plot with change in actuation layer radius and radial position as measured from centre of the structure. Increasing actuation layer radius enhances the displacement as shown in Fig. 5.12. At the centre of the device displacement is maximum and more we move towards the boundary it gets reduced. This phenomenon is seen in the characteristic study of Fig. 5.13, where at zero radial distance, displacement is maximum for both plate and membrane model. Figures 5.14 and 5.15 exhibit the variation of displacement for changing cavity height and actuation layer thickness. Increasing air gap separation and actuation layer thickness enhances the distance between two oppositely charged electrodes and generated capacitance decreases. Simultaneously low valued electrostatic force is generated in the device which is not capable of generating large valued displacement. Difference in displacement involving membrane model between SiC and Si_3N_4 based element gets larger while plotted against actuation layer thickness compared to cavity height. Figures 5.12-5.15 depict that utilization of SiC as actuation layer material is obviously a good choice for its excellent performance over Si_3N_4. Compared to plate displacement profile, membrane model provides impressive value of displacement.

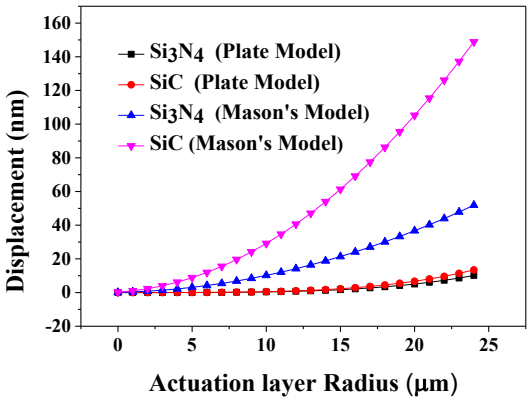

Fig. 5.12 Displacement with changing actuation layer radius

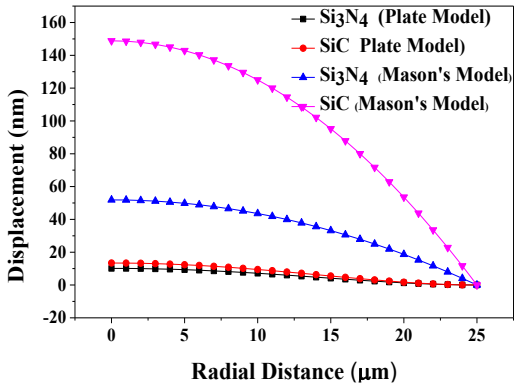

Fig. 5.13 Displacement with increasing radial distance

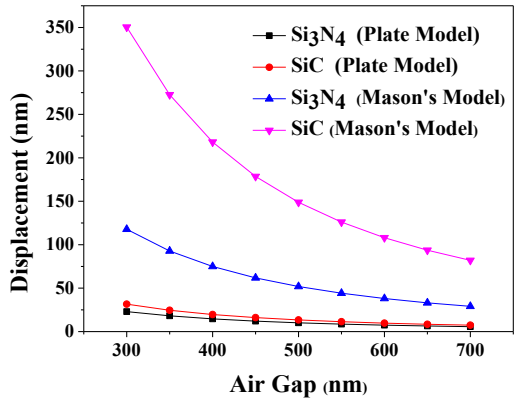

Fig. 5.14 Displacement with changing cavity height

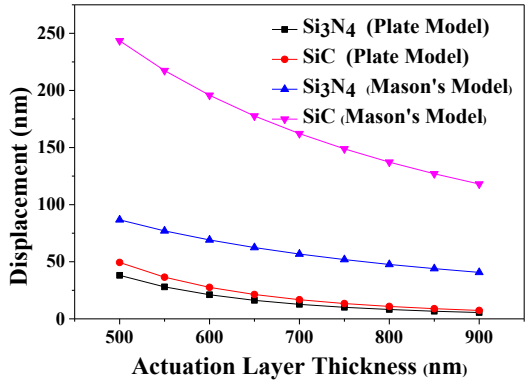

Fig. 5.15 Displacement with changing actuation layer thickness

5.3.4 Effect of fringing in Si_3N_4 / SiC actuation layer based non-insulated cell

Performance of SiC as actuation layer material for enhancement in device capacitance and electrostatic force is already discussed in section 3.5 and 4.3.2 respectively. Restoring force of actuation layer is a linear function of its displacement. In consideration with enhanced device capacitance and force of SiC actuation layer based capacitive structure instigates to perform a comparative study of displacement with Si_3N_4 based counterpart. Enhancement due to SiC actuation layer is also accomplished in this section.

Figure 5.16 shows the behavior of actuation layer displacement due to change in electrode radius. Increase in actuation layer radius gives a rise in device capacitance, subsequent to which electrostatic force also gets enhanced. Enhanced electrostatic force generates large valued displacement. Displacement of actuation layer is solely dependent upon the actuation layer's residual stress, Young's

modulus, material density and many more. Lower tensile stress, higher Young's modulus permits SiC to perform better than Si_3N_4. effect of fringing is also profound for SiC based device. Difference between E_m of SiC and Si_3N_4 gets enhanced for higher actuation layer radius as shown in Fig. 5.17. Average value of E_m is 11.79% and 15.19% for Si_3N_4 and SiC respectively. Enhancement of displacement in SiC cell against actuation layer radius is plotted in Fig. 5.18. Impressive enhancement is observed over Si_3N_4 cell due to involvement of SiC as actuation layer material. Average E_{m_SiC} of 218% is achieved when plotted against actuation layer radius.

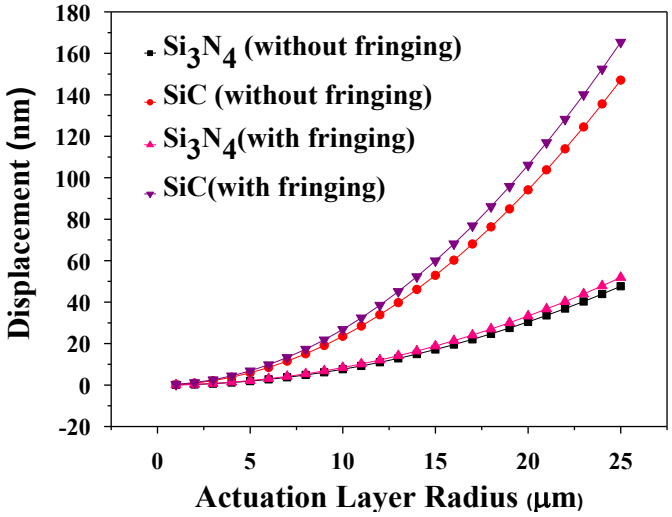

Fig. 5.16 Actuation layer displacement due to variation in actuation layer radius

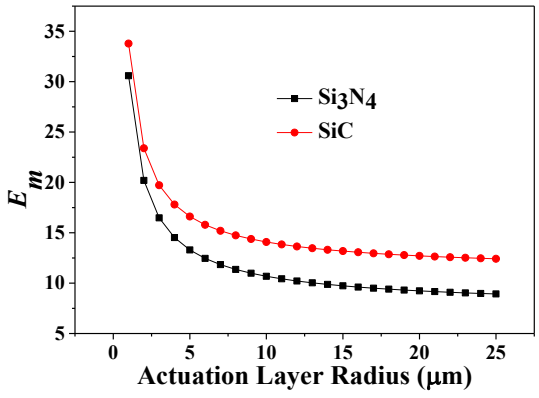

Fig. 5.17 E_m for varying actuation layer radius

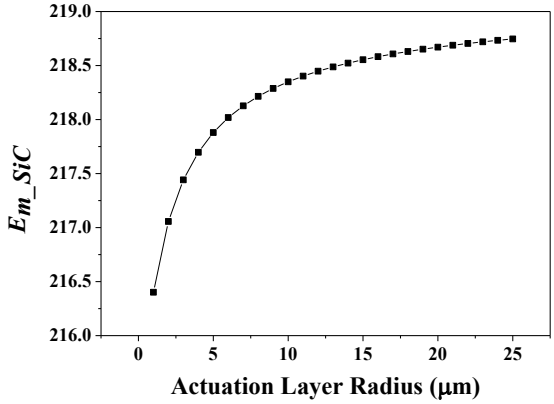

Fig. 5.18 E_{m_SiC} for varying actuation layer radius

Figure 5.19 depicts the variation of actuation layer displacement for varying cavity gap. Equivalent device capacitance in non-insulated structure is a series combination of air gap and actuation layer capacitance. Increase in cavity gap makes two parallel electrodes far apart from each other. This enhanced gap reduces the capacitance and simultaneously decrement of electrostatic force occurs. Reduction in force is the prime factor of reduced displacement. Due to circular structure the flux lines generated in the device bends near the edges of the electrodes and gets benefitted from fringing field effects. These fringing field lines enhance the electrostatic force and cause enhancement of displacement which is quite evident from Fig. 5.20. Effect of fringing has greater impact upon SiC actuation layer and displacement also enhances due to its unique properties which were discussed earlier. Average value of E_m is 9.09% and 12.53% for Si_3N_4 and SiC respectively. Figure 5.21 generates an average E_{m_SiC} of 219.9% when cavity gap is considered as variable.

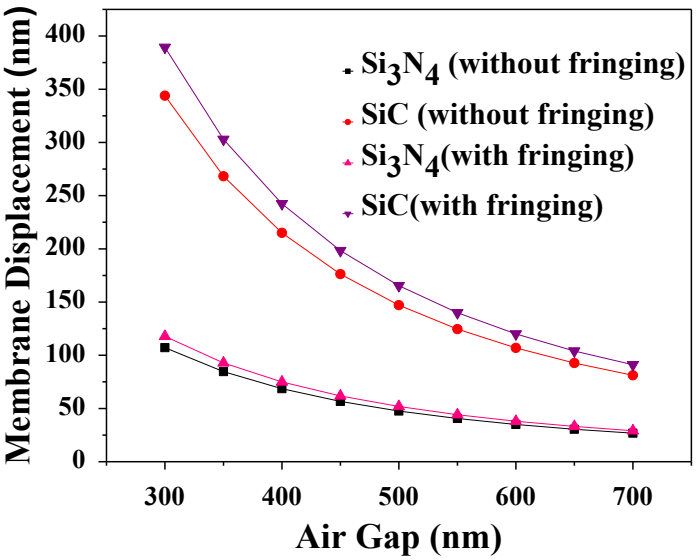

Fig. 5.19 Actuation layer displacement due to variation in cavity gap

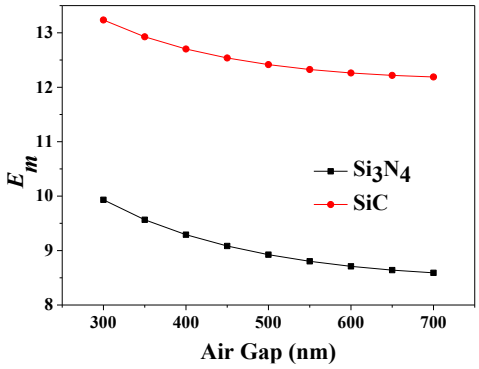

Fig. 5.20 E_m for varying cavity gap

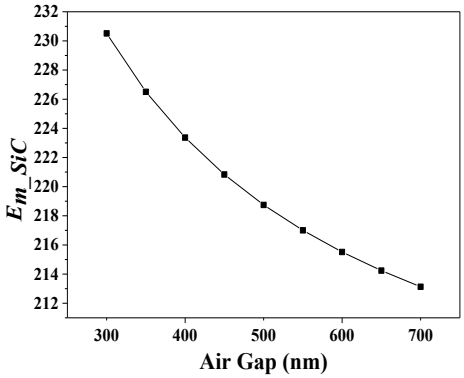

Fig. 5.21 E_{m_SiC} for varying cavity gap

Increase in actuation layer thickness affects actuation layer displacement in same manner as cavity gap does. Figure 5.22 shows the variation of actuation layer displacement with respect to actuation layer thickness. Fringing effect quite evident in SiC cell as depicted in Fig. 5.23. Enhancement in displacement of SiC cell in comparison with Si_3N_4 is shown in Fig. 5.23, where average value of E_m are 8.79% for Si_3N_4 and 12.31% for SiC. Figure 5.24 generates an average E_{m_SiC} of 219.9% when displacement is dependent of varying actuation layer thickness. Figure 5.25 exhibits a parabolic opening up nature of actuation layer displacement when plotted against static bias. Increase in bias give a rise to device capacitance which acts as a prime initiator to enhance the generated electrostatic force and displacement. A constant enhancement of displacement is observed as a effect of fringing in Fig. 5.26. As discussed earlier enhancement in SiC involving fringing model is quite larger compared to Si_3N_4.

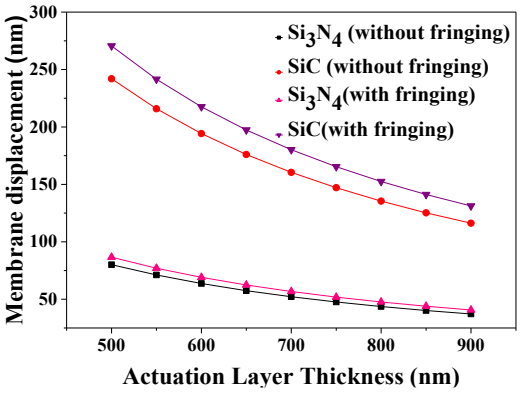

Fig. 5.22 Actuation layer displacement due to variation in actuation layer thickness

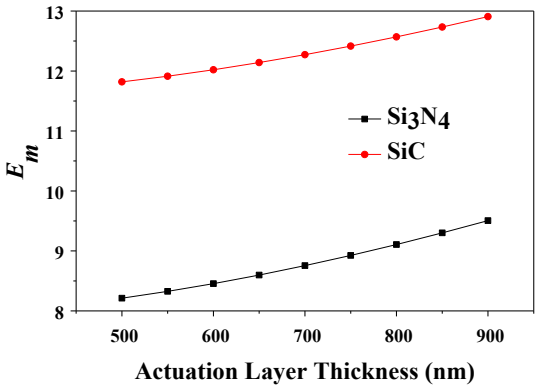

Fig. 5.23 E_m for varying actuation layer thickness

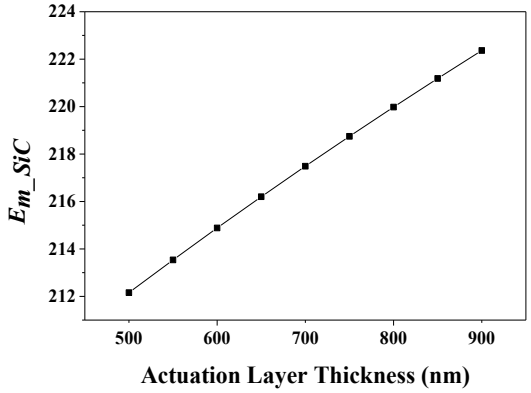

Fig. 5.24 E_{m_SiC} for varying actuation layer thickness

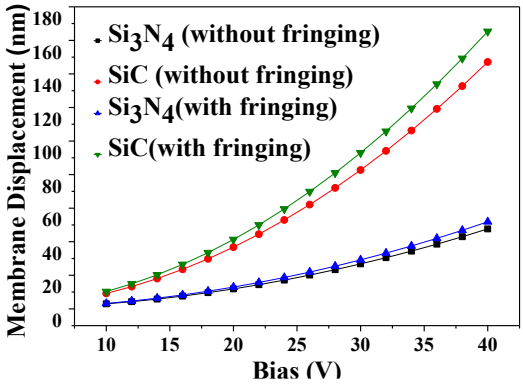

Fig. 5.25 Actuation layer displacement due to variation in bias

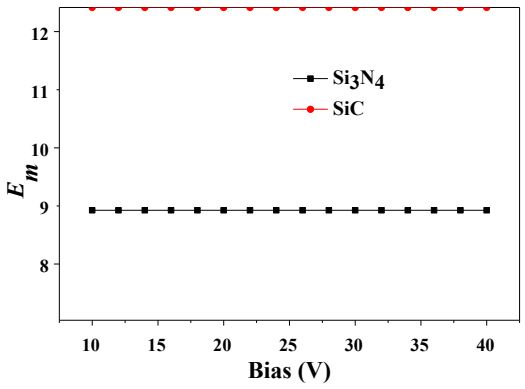

Fig. 5.26 E_m for varying bias

5.4 Displacement profile analysis of insulated cell

The presence of the insulation layer as in Fig.4.15 permits the patterning of the upper electrode above it which increases the overall capacitance and electrostatic force of the device as already analyzed in secs. 3.6.3 and 4.4.2. Inclusion of insulation layer has a deep impact upon the transducer due to excellence in device capacitance and displacement.

5.4.1 Analytical force model of insulated element

Analyzing the results discussed in section 5.3.2, one conclusion can be drawn that usage of SiC actuation layer improves the displacement. An analytical modeling of insulated CMUT (shown in Fig. 4.15) with SiC actuation layer is discussed in this section.

Actuation layer displacement of insulated cell excluding fringing is expressed from (5.44) and becomes,

$$w'_{m_{bias}} = \left(\frac{1}{8AT_a}\right) \times \frac{V_{dc}{}^2 C_i{}^2 r_a{}^2}{\left(\frac{C_i}{C_g}+1\right)^2 C_g{}^2} \times \left[\left(\frac{\varepsilon_g \pi r_e{}^2}{t_g{}^2}\right)\right] \tag{5.49}$$

Substituting device generated electrostatic force with fringing as expressed in (4.16), in (5.46) the expression of actuation layer displacement for insulated cell will be,

$$w'_{mf_{bias}} = \left(\frac{1}{8AT_a}\right) \times \frac{V_{dc}{}^2 C_{if}{}^2 r_a{}^2}{\left(\frac{C_{if}}{C_{gf}}+1\right)^2 C_{gf}{}^2} \times \left[\left(\frac{\varepsilon_g \pi r_e{}^2}{t_g{}^2}\right) + \left(\frac{\varepsilon_g r_e}{\left(\frac{16\pi r_e}{t_g}\right)-1}\right) \times \left(\frac{16\pi r_e}{t_g{}^2}\right)\right] \tag{5.50}$$

Investigation of fringing effect upon displacement enhancement for insulated device is calculated by,

$$E'_m = \left(\frac{w'_{mf_{bias}} - w'_{m_{bias}}}{w'_{m_{bias}}}\right) \times 100 \tag{5.51}$$

Enhancement in displacement due to insulation layer is derived as,

$$E''_i = \left(\frac{w'_{mf_{bias}} - w_{mf_{bias}}}{w_{mf_{bias}}}\right) \times 100 \tag{5.52}$$

5.4.2 Enhancement of displacement profile in insulated structure

Figure 5.27 shows an exponential decaying of actuation layer displacement nature with increase in gap thickness. It is quite evident displacement enhances by large percentage due to inclusion of insulation layer. In accordance to this phenomenon, the enhanced characteristics are clearly plotted in Fig. 5.28. Maintaining the gap thickness within the specified range enhances the displacement value by 50% compared to the CMUT structure without insulation layer. Similarly Fig. 5.29 shows the parabolic nature of actuation layer displacement due to variation of actuation layer radius. An average E''_i of 62% occurs in SiC based CMUT with insulation layer as shown in Fig. 5.30.

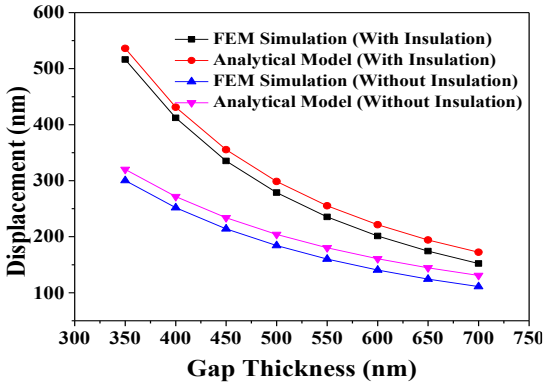

Fig. 5.27 Comparative analysis of actuation layer displacement due to variation of actuation layer thickness

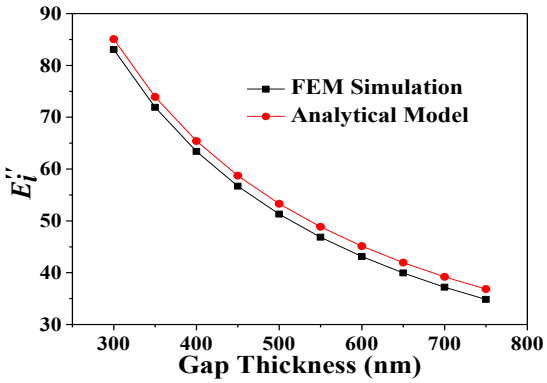

Fig. 5.28 Enhancement in displacement for the variation of gap thickness

In consideration with the dimension of the device comparable to the gap separation between the capacitive plates the diameter is kept as 110 µm for generating high frequency ultrasound wave that can be involved for enhanced penetration by high pressure transmission and better signal to noise ratio.

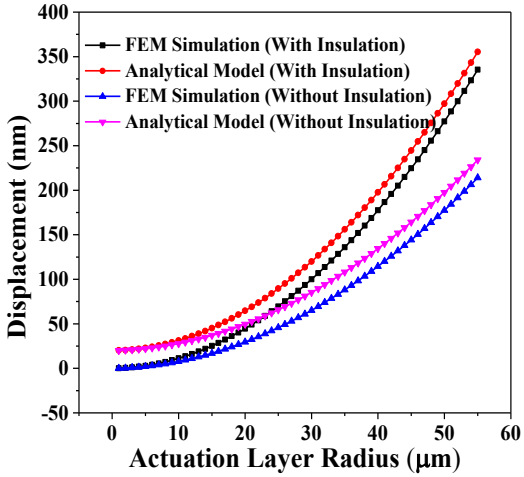

Fig. 5.29 Comparative analysis of actuation layer displacement due to variation of actuation layer radius

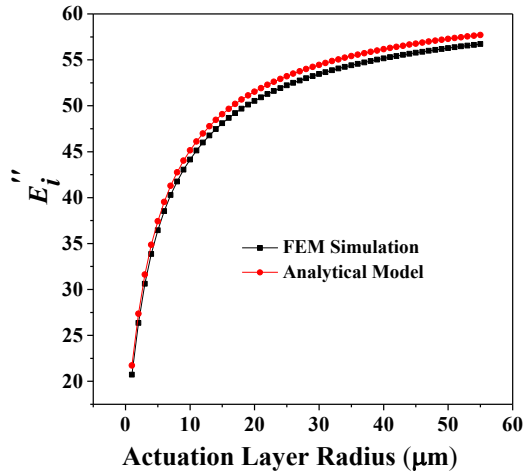

Fig. 5.30 Enhancement in displacement for the variation of actuation layer radius

Figure 5.31 shows variation of actuation layer displacement with the bias. Certain increase in bias increases the actuation layer displacement more for the structure with insulation layer. An average $E_i^{''}$ of 62% enhancement in displacement occurs when characterised against bias. According to the characteristics of displacement shown in Fig. 5.31, the actuation layer displacement is nearly 400 nm for a 2 µm actuation layer. In consequent to this fact Fig. 5.32 also shows that due to increase in

gap thickness actuation layer displacement reduces while impressive displacement takes place by keeping the gap thickness between the range of 350 nm-500 nm. Fig. 5.33 shows a plot of $E_i^{''}$ with respect to actuation layer thickness.

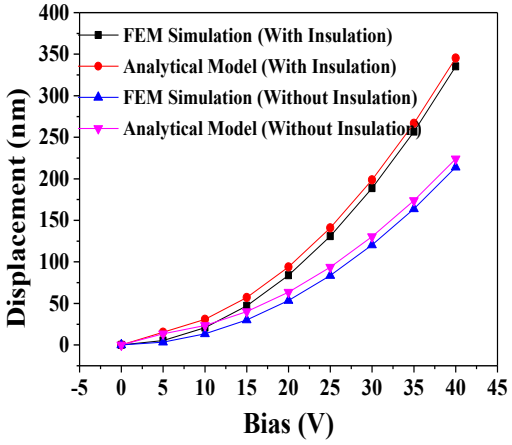

Fig. 5.31 Comparative analysis of actuation layer displacement due to variation of bias

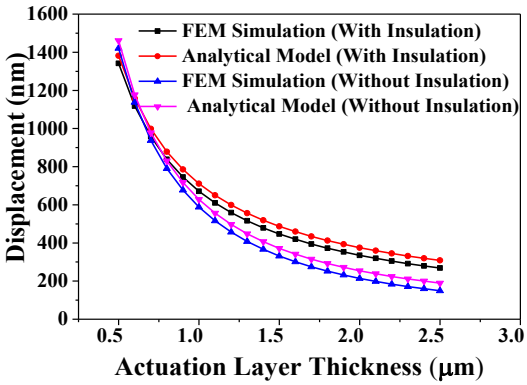

Fig. 5.32 Comparative analysis of actuation layer displacement due to variation of actuation layer thickness

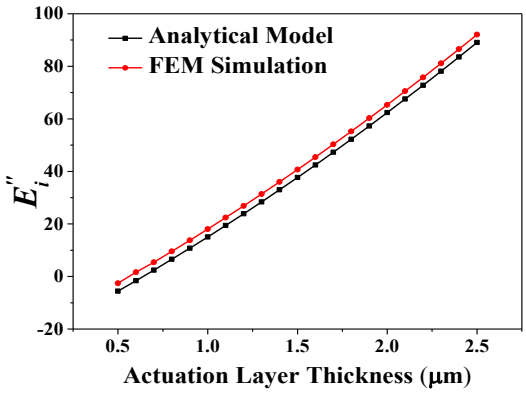

Fig. 5.33 $E_i^{''}$ with change in actuation layer thickness

A comparative study of enhancement in displacement due to variation of various CMUT parameters is shown in Table 5.1. Keeping any one of these structural parameters variable all others are maintained constant. An average 50% enhancement of displacement occurs in insulated cell compared to non insulated counterpart. As depicted in Table 5.1 maximum enhancement takes place due to change in applied bias. Effect of actuation layer radius and cavity gap upon displacement enhancement is moderate and minimum when actuation layer thickness is concerned.

Table 5.1 Enhancement in displacement due to variation of various CMUT parameters

Bias (V)	Actuation layer radius (μm)	Actuation layer thickness (μm)	Gap separation (nm)	% enhancement in displacement due to insulation layer
Variable	55	2	450	59
40	Variable	2	450	49
40	55	Variable	450	39
40	55	2	Variable	52

5.4.3 Analysis of fringing effect in insulated CMUT

In this section effect of fringing is analyzed for insulated device. Bending of flux lines at the boundary of the electrodes enhances the capacitance and electrostatic force. This enhanced capacitance and electrostatic force certainly affect the displacement. Based on variation of various structural parameters characteristic study of displacement is carried out in this section. Figure 5.34 exhibits the variation of actuation layer displacement with actuation layer radius for various actuation layer thicknesses. Displacement holds a directly proportional relationship with electrode radius, thus shows a parabolic opening up nature. Another phenomenon is also observed from the given characteristic that is reduction in actuation layer thickness increases the displacement. Effect of fringing is profound for lower electrode radius and approximately similar enhancement is noticed all along the considered range of electrode radius for various thickness of actuation layer. An average $E_m^{'}$ of 12% is attained form the characteristic study plotted in Fig. 5.35. Figure 5.36 shows a decreasing nature of actuation layer displacement with respect to air gap. Appreciable amount of displacement enhancement takes place due to fringing. An average $E_m^{'}$ of 11.54%, 11.33% and 12.11% is produced from Fig. 5.37 for a) t_i =500 nm b) t_i =350 nm c) t_i =750 nm.

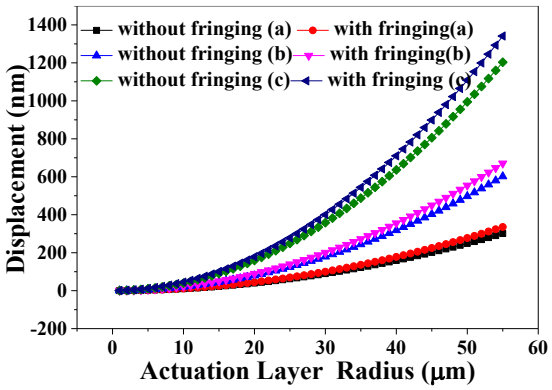

Fig. 5.34 Actuation layer displacement for varying actuation layer radius for a) t_a =2 µm b) t_a =1 µm c) t_a =0.5 µm

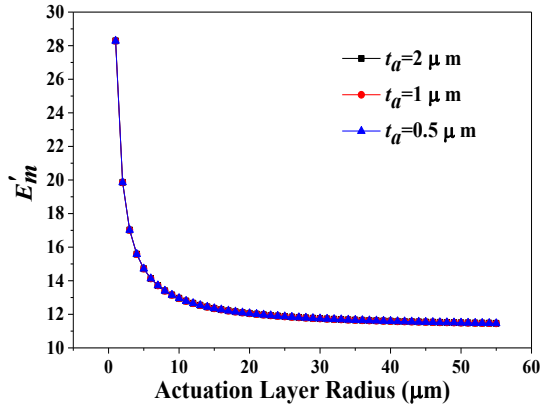

Fig. 5.35 $E_m^{'}$ for varying actuation layer radius

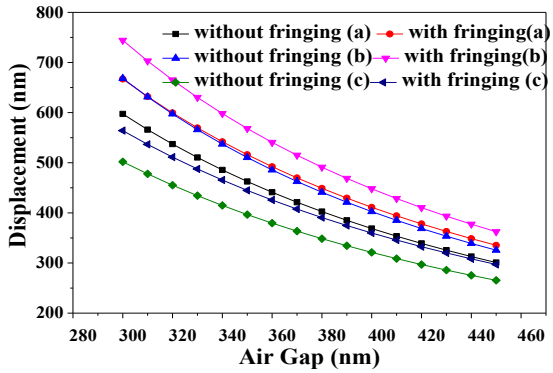

Fig. 5.36 Actuation layer displacement for varying air gap for a) t_i =500 nm b) t_i =350 nm c) t_i =750 nm

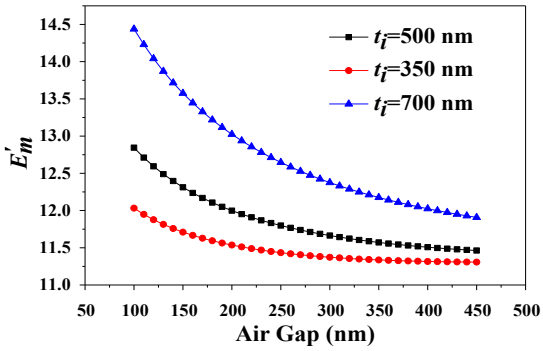

Fig. 5.37 $E_m^{'}$ for varying air gap

Dielectric material used for insulation layer is a prime deciding factor for displacement generation in insulated device. Utilization of insulation layer also has great impact upon electrical safety. Involvement of material having higher relative dielectric constant enhances displacement in large manner as depicted in Fig. 5.38. Displacement has a non-linear relationship with applied bias. This occurrence is also observed here as lower bias generates low valued displacement and vice versa. A constant enhancement is observed for all the three considered cases of a) V_{dc}=40 V b) a) V_{dc}=20 V c) V_{dc}=60 V. An average $E_m^{'}$ of 11.46% is noted from the characteristic shown by Fig. 5.39.

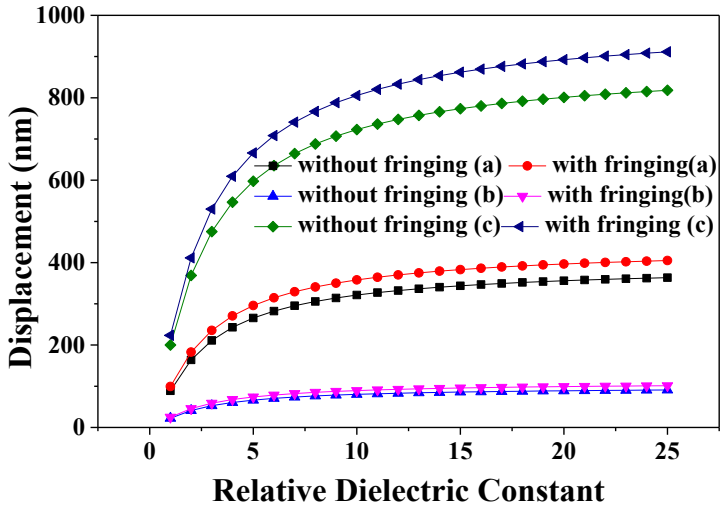

Fig. 5.38 Displacement for varying material permittivity for a) V_{dc} =40 V b) a) V_{dc} =20 V c) V_{dc} =60 V

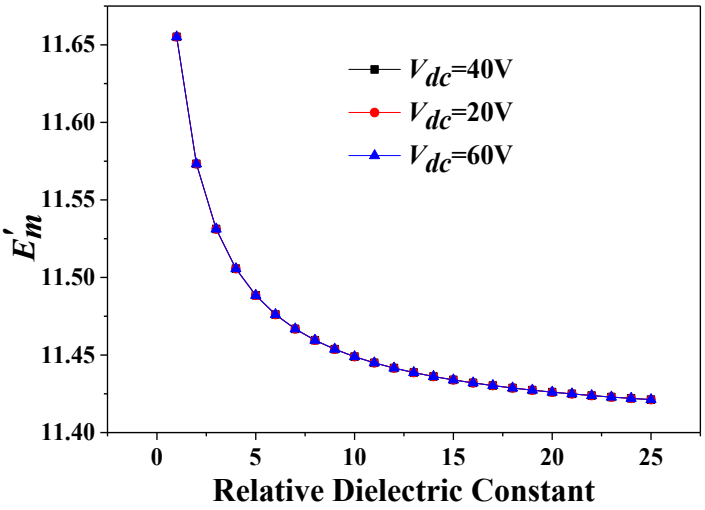

Fig. 5.39 $E_m^{'}$ with respect to various material permittivity

A combinational effect of actuation layer radius and gap thickness upon displacement is plotted in Fig. 5.40 against varying insulation thickness. Certainly increase in insulation thickness decreases device capacitance as its directly dependent upon combinational effect of gap and insulation capacitance. Subsequent to this decrement of displacement occurs in the device. While studying the combinational effect of actuation layer radius and gap thickness upon displacement then a unique fact is observed that; gap thickness acts as a main deciding factor of actuation layer displacement. Though displacement enhances for increasing actuation layer radius still noticeable displacement doesn't take place for 65µm actuation layer

radius as gap thickness is quite larger compared to reference one [14]. Enhancement due to fringing is shown in Fig. 5.41. An average $E_m^{'}$ of 11.35%, 11.78% and 11.30% is produced from the study for a) r_a=55 µm, t_g=450 nm b) r_a=27.5 µm, t_g=300 nm c) r_a=65 µm, t_g=600 nm respectively.

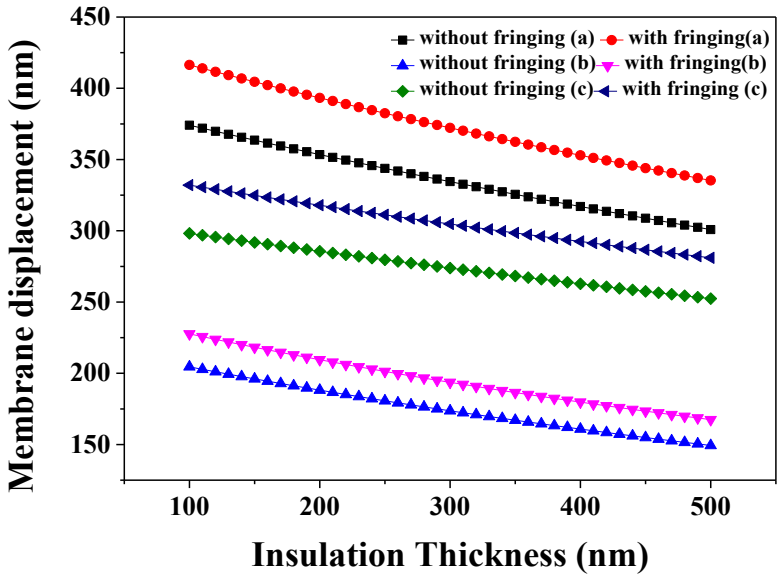

Fig. 5.40 Displacement for varying insulation thickness for a) r_a=55 µm, t_g=450nm b) r_a=27.5 µm, t_g=300 nm c) r_a=65 µm, t_g=600 nm

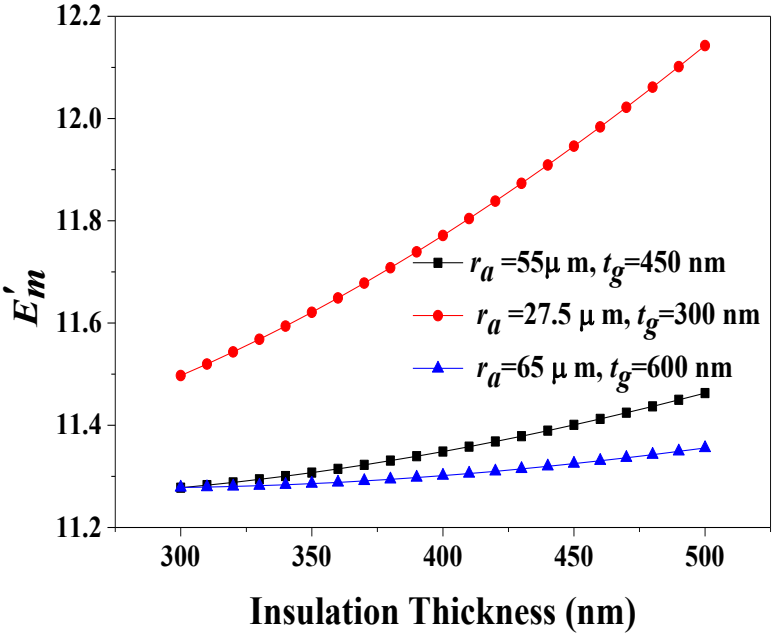

Fig. 5.41 $E_m^{'}$ for variation in insulation thickness

Figures 5.42-5.44 show 3D plot of actuation layer displacement with respect to various structural parameters. Dependency of displacement upon those parameters is also evident in these 3D figures which are depicted earlier. Figure 5.42 shows that at maximum value of actuation layer radius and material permittivity displacement becomes highest. Increasing nature of actuation layer displacement due to increases of both parameters is noticed in the figure. In contrast to this as increase in insulation thickness reduces displacement hence according to Fig. 5.43 maximum displacement is achieved at minimum insulation thickness and maximum actuation layer radius. Figure 5.44 shows, maximum displacement is attained for maximum actuation layer radius and bias.

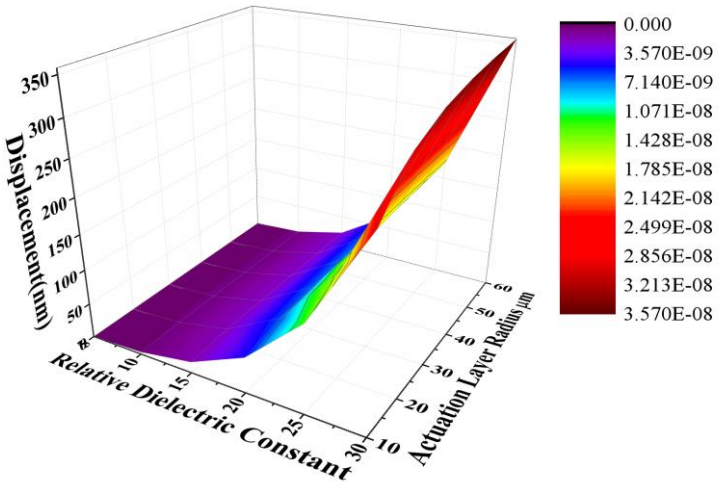

Fig. 5.42 Variation of displacement with simultaneous change in r_a and K

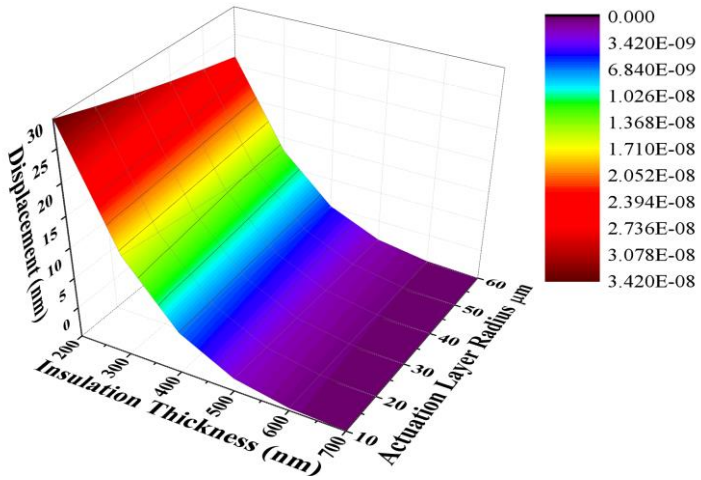

Fig. 5.43 Variation of displacement with simultaneous variation in r_a and t_i

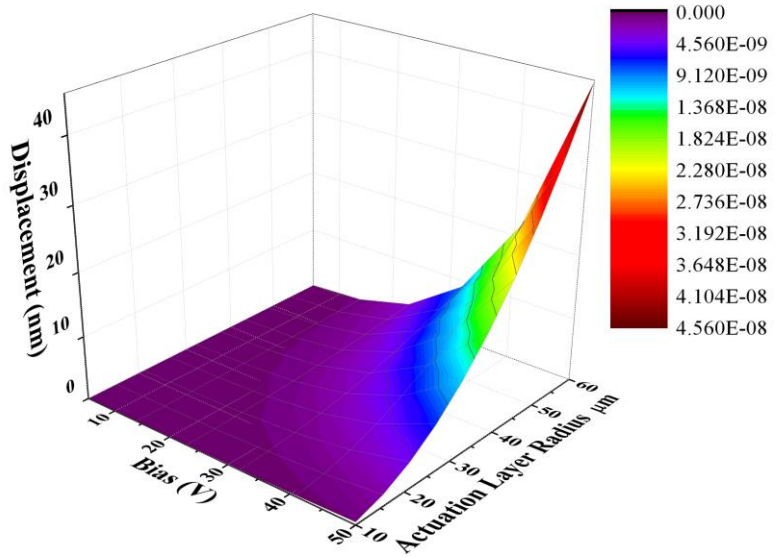

Fig. 5.44 Variation of displacement with simultaneous change in r_a and V_{dc}

5.5 Influence of HfO_2 upon actuation layer displacement

Insulating material having high dielectric constant has proved to be an excellent choice to enhance device capacitance and electrostatic force from sections 3.9 and 4.5. In this context displacement will certainly enhance by its involvement. Keeping this in mind influence of HfO_2 is taken care of in this section. Various insulation thickness is considered during usage of HfO_2 and enhancement is calculated with respect to 500nm Si_3N_4 [13]. Enhancement due to HfO_2 insulating layer is calculated as, $E''_{HfO_2} = \left(\frac{w'_{mf_{bias}(HfO_2)} - w'_{mf_{bias}(Si_3N_4)}}{w'_{mf_{bias}(Si_3N_4)}} \right) \times 100$, where $w'_{mf_{bias}(Si_3N_4)}$ is the actuation layer displacement generated by structure having 500 nm Si_3N_4 layer and $w'_{mf_{bias}(HfO_2)}$ is measured as displacement generated from structure having HfO_2 insulation layer of various thickness within a range of 500nm to 50 nm.

Figure 5.45 shows a comparative study of actuation layer displacement for change in actuation layer radius for the same input pulse between HfO_2 and Si_3N_4 isolation for various HfO2 thicknesses. Average E''_{HfO_2} for 500 nm, 300 nm, 200 nm, 100 nm and 50 nm is 20.41%, 24.71%, 26.86%, 29.15% and 30.35% respectively is

depicted in Fig. 5.46. Increasing gap separation between two electrodes reduces the attraction force between them , thus displacement decreases.

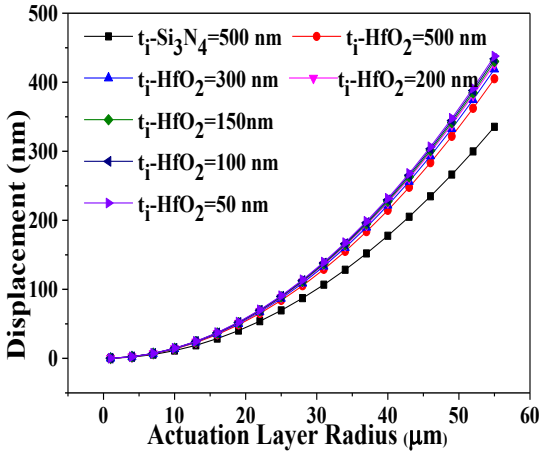

Fig. 5.45 Comparative analysis of displacement with actuation layer radius for HfO_2 and Si_3N_4 insulation

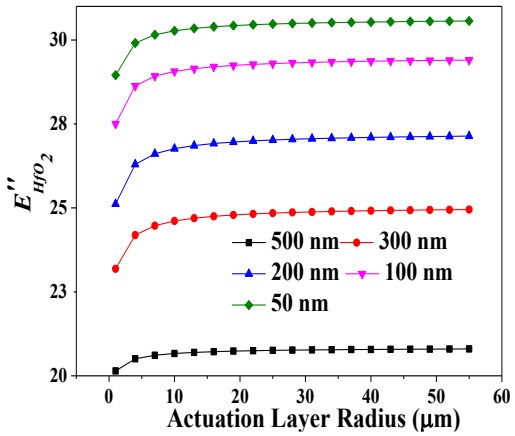

Fig. 5.46 E''_{HfO_2} with changing actuation layer radius for varying actuation layer thickness

Noticeable improvement in displacement takes place in Fig. 5.47 due to involvement of HfO_2. For 500 nm Si_3N_4 insulation thickness and 450 nm gap separation the displacement is 330 nm whereas for HfO_2 the displacement becomes 381.4nm and for 50 nm HfO_2 thickness the 401.3 nm. Average E''_{HfO_2} for 500 nm, 300 nm, 200 nm, 100 nm and 50 nm is 29.21%, 36.73%, 40.36%, 44.25% and 47.35% respectively is depicted in Fig. 5.48.

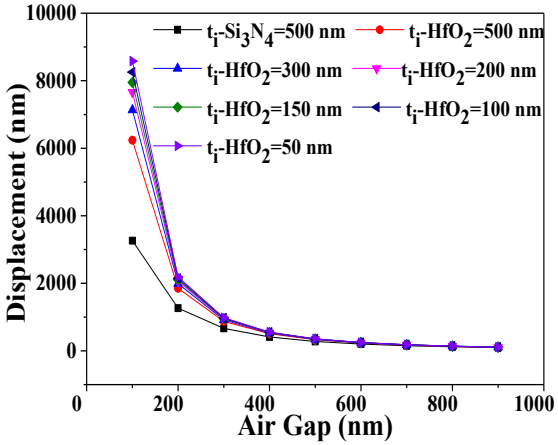

Fig. 5.47 Comparative analysis of displacement with air gap for HfO_2 and Si_3N_4 insulation

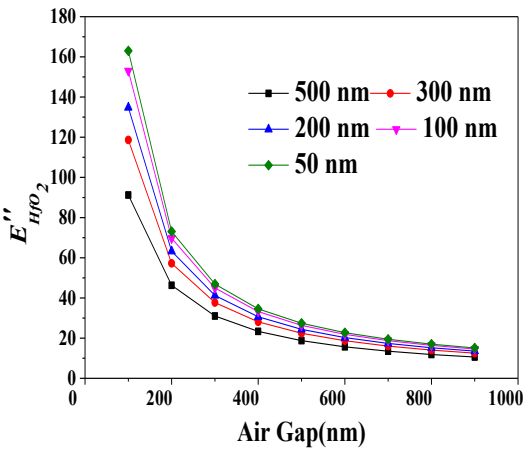

Fig. 5.48 E''_{HfO_2} for varying air gap

Figure 5.49 signifies the enhancement of displacement due to increase in insulation thickness along with the involvement of high-K material. The graph shows that, in case of PECVD Si_3N_4, the displacement changes from 335 nm to 429 nm only by reducing the insulation thickness from 500 nm to 50 nm. Maintaining the exact condition for HfO_2 the displacement changes from 402 nm to 438 nm which is almost same for Ta_2O_3. Fig. 5.50 exhibits a comparative study of displacement profile between Si_3N_4 and HfO_2 insulation layer of different thickness. It is quite evident from the figure that, at 50 nm HfO_2 thickness maximum displacement of 438 nm is generated. Whereas, Si_3N_4 of 500 nm dimension produces displacement of 335 nm.

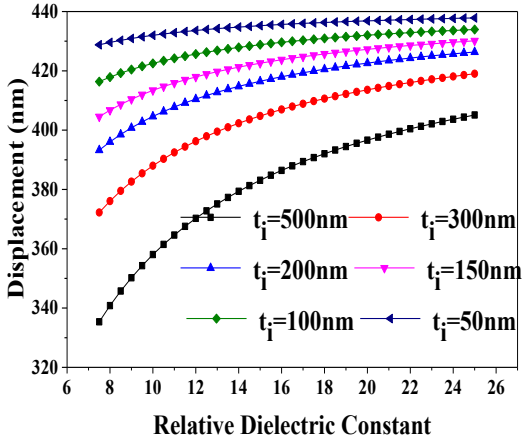

Fig. 5.49 Comparative analysis of displacement for varying relative dielectric constant with different insulation thickness

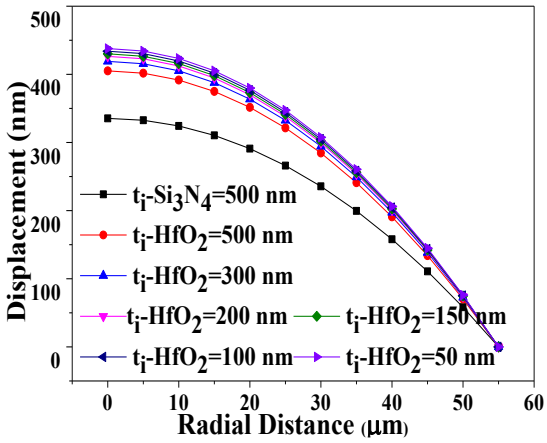

Fig. 5.50 Comparative analysis of displacement profile for HfO_2 and Si_3N_4 insulation

Figure 5.51 depicts the variation of displacement concerning the change in applied potential given for biasing of the CMUT. The central displacement of the CMUT forms a directly proportional relationship with the square of the applied bias. Variation of the electrostatic force is apparent that it intensifies from zero, which supports the logic of generating attraction force between two electrodes and simultaneously pulls down the actuation layer towards the substrate. As a result, displacement shows a parabolic opening up type characteristic due to given applied bias. Figure 5.52 shows the enhancement of displacement due to HfO_2 insulation layer of various thicknesses with respect to Si_3N_4 insulation. A constant enhancement is observed all along the considered range of bias voltage. Average E''_{HfO_2} for 500

nm, 300 nm, 200 nm, 100 nm and 50 nm is 20.79%, 24.95%, 27.13%, 29.49 % and 30.56% respectively is depicted in Fig. 5.52. In Table 5.2, a comparative analysis is done among various CMUT structure. Undoubtedly involvement of high-K material enhances the displacement and appreciable enhancement is observed for reduced insulation thickness. Maximum percentage of full swing actuation layer vibration is achieved by involving HfO_2.

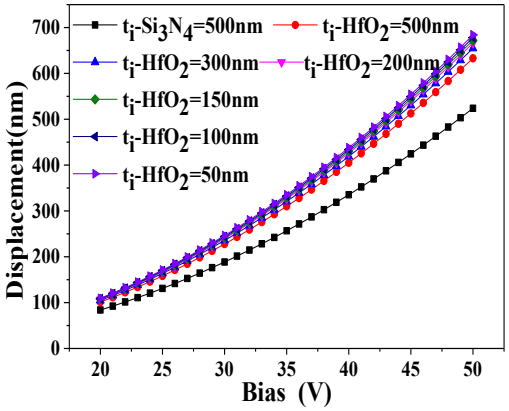

Fig. 5.51 Comparative analysis of displacement for change in bias between Si_3N_4 isolation and HfO_2 of various thickness

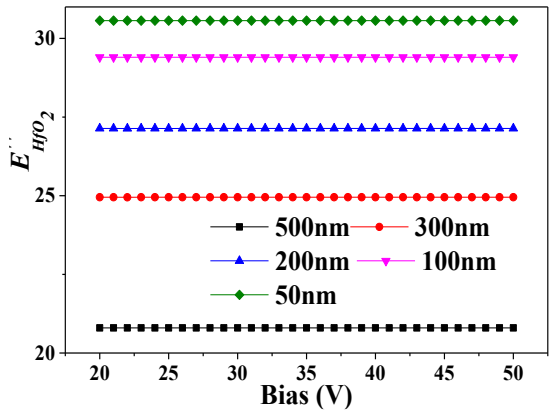

Fig. 5.52 E''_{HfO_2} for varying bias

Table 5.2 Comparative analysis of Displacement among various CMUT structure

CMUT Type	Electrode Radius (μm)	Type of Layers	Material Permittivity	Thickness of each Layer (nm)	Displacement (nm)	%usage of gap thickness
SiC based CMUT with HfO_2 insulation Layer	55	HfO_2	25	500	405	90
		air	1	450		
SiC based CMUT [13]	55	Si_3N_4	7.5	500	335	75
		air	1	450		
Si_3N_4 based CMUT [14]	22	Si_3N_4	7.5	400	93	62
		air	1	150		
		Si_3N_4	7.5	250		
Diamond Based CMUT [15]	22	Diamond	5.7	1 000	125	8
		SiO_2	3.9	230		
		air	1	1570		
Polymer Based CMUT [16]	50	SU8	3.2	670	82	27
		air	1	300		
		SU8	4.5	2400		

5.6 Summary

An improved displacement modeling is derived in this chapter. Deflection of actuation layer is modeled by plate and actuation layer modeling. Mason's analysis is considered for analyzing the actuation layer modeling. Impressive result for peak displacement is achieved from membrane model, which allows to consider actuation layer as actuation layer for both insulated and non-insulated structure. Overall influence of fringing effect is carried out for various types of CMUT structure. Insulation layer has deeper insight upon displacement compared to non-insulated element. Performance of SiC as excellent actuation layer is studied for non-insulated element where impressive enhancement in displacement is observed compared to Si_3N_4 actuation layer. Fringing effect is more profound for SiC based non-insulated device than Si_3N_4 counterpart. Inclusion of HfO_2 as insulation layer improves the device displacement than Si_3N_4 insulation.

References

[1] I. O. Wygant, M. Kupnik and B. T. Khuri-Yakub, "Analytically calculating actuation layer displacement and the equivalent circuit model of a circular CMUT cell," *IEEE Ultrasonics Symposium*, pp. 2111-2114, 2008.

[2] R. Maity , N.P. Maity, R.K. Thapa, S. Baishya, " Investigation of Si_3N_4 as an Excellent Actuation layer Material for MEMS Ultrasonic Transducers", *Applied Mechanics and Materials*, vol.45 , pp. 567-571, 2017.

[3] S.Timoshenko and S. Woinowsky-Krieger, "Theory of Plates and Shells", 2nd ed., New York, NY: McGraw Hill, 1959.

[4] R. Pratap and A. Kumar," Material selection for MEMS devices", *Indian Journal of Pure and Applied Physics*, vol. 45, pp.358, 2007.

[5] Z. Mehmood, I. Haneef, and F. Udrea, "Material selection for Micro-Electro-Mechanical-Systems (MEMS) using Ashby's approach," *Materials & Design,* vol. 157, pp. 412-430, 2018.

[6] A. Fleischman, S. Roy, C. Zorman, M. Mehregany, and L. Matus, "Polycrystalline silicon carbide for surface micromachining," *Proceedings of Ninth International Workshop on Micro Electromechanical Systems*, pp. 234-238. 1996.

[7] A. C. Hoogerwerf, G. S. Durante, R. J. James, M.-A. Dubois, O. Dubochet, and M. Despont, "Silicon carbide pressure sensors for harsh environments," *20th International Conference on Solid-State Sensors, Actuators and Microsystems & Eurosensors,* pp. 2154-2157, 2019.

[8] L. Pakula, H. Yang, H. Pham, P. French, and P. Sarro, "Fabrication of a CMOS compatible pressure sensor for harsh environments," *Journal of Micromechanics and Microengineering,* vol. 14, no. 11, pp. 1478-1485, 2004.

[9] V. Rajaraman, L. Pakula, H. Pham, P. Sarro, and P. French, "Robust wafer-level thin-film encapsulation of microstructures using low stress PECVD silicon carbide," *IEEE 22nd International Conference on Micro Electro Mechanical Systems*, pp. 140-143, 2009.

[10] H. Zhang, H. Guo, Y. Wang, G. Zhang, and Z. Li, "Study on a PECVD SiC-coated pressure sensor," *Journal of Micromechanics and Microengineering,* vol. 17, no. 3, pp. 426-431, 2007.

[11] M. A. Fraga, "Comparison between the piezoresistive properties of a-SiC films obtained by PECVD and magnetron sputtering," *Materials Science Forum*, vol. 679, pp. 217-220, 2011.

[12] Shailendra Kumar Tiwari, B. S. Satyanarayana, A. Gopalkrishna Pai and Kunal K.Trivedi, "Circular capacitance micro machined ultrasonic transducer", *Defence Science Journal*, vol. 59, pp. 627-632, 2019.

[13] Q. Zhang, P. Cicek, K. Allidina, F. Nabki, and M. N. El-Gamal, "Surface Micromachined CMUT Using Low-Temperature Deposited SiC Actuation layer s for Above-IC Integration", *IEEE Journal of Microelectromechanical System,* vol. 23, no. 2, pp.482-493, 2014.

[14] A. Logan and J. T. W. Yeow, "Fabricating capacitive micromachined ultrasonic transducers with a novel silicon-nitride-Based wafer bonding process," *IEEE Transactions on Ultrasonics, Ferroelectrics, and Frequency Control*, vol. 56, no. 5, pp. 1074-1084, 2009.

[15] A. M. Cetin and B. Bayram, "Diamond-Based Capacitive Micromachined Ultrasonic Transducers in Immersion", *IEEE Transactions on Ultrasonics, Ferroelectrics, and Frequency Control*, vol. 60, no. 2, pp. 414-420, 2013.

[16] Carlos D. Gerardo, Edmond Cretu and Robert Rohling, "Fabrication and testing of polymer-based capacitive micro machined ultrasound transducers for medical imaging", *Microsystems & Nano engineering*, vol. 19, no. 4, pp.1-12, 2018.

CHAPTER

6

Collapse Voltage and Coupling Factor

6.1 Introduction

Vast application of ultrasound includes all kind of sensing and actuating application. Imparted ultrasound needs to be detected from the source through coupling medium. Various types of coupling medium exist, such as solid for measuring wafer temperature, liquid for NDE and medical proposes and gaseous for air coupled application [1-4]. Piezo electric transducer suffers from impedance mismatch for fluid coupled applications. MUTs are extensively engaged as air transducer with largest dynamic range and equally for acoustic application [5-9].

To employ the device at optimal operating point, collapse voltage of a capacitive element is an important parameter. Performance of the MUT is determined by the operating bias applied to it. Considering various behaviour of the membrane under static conditions different operating modes exist such as collapsed mode and conventional mode [10]-[12]. Compared to conventional mode, electromechanical coupling factor is quite larger in collapsed mode. In collapsed mode, actuation layer collapses onto the substrate and is capable of generating and detecting of ultrasound in more efficient manner than conventional one. Inconsideration with all these aspects, accurate knowledge of evaluation of collapse voltage is essential. In this chapter an analytical modeling is carried out by involving electromechanical model.

Figure 6.1 shows the schematic diagram of CMUT at collapsed condition. Application of bias along with signal causes vibration in the actuation layer. An equivalent amount of current is given to an external load when the actuation layer is subjected to an acoustic field in biased condition. The device converts electrical energy into mechanical form during transmission and functions in the opposite manner during reception. The amount of transmitted mechanical energy

to the stored energy in the device is thus defined by electromechanical conversion or coupling coefficient [13]. Based on this coupling factor, characterisation of transducer is done. Keeping this in mind evaluation of collapse voltage and coupling factor has chosen to be an important parameter for CMUT design.

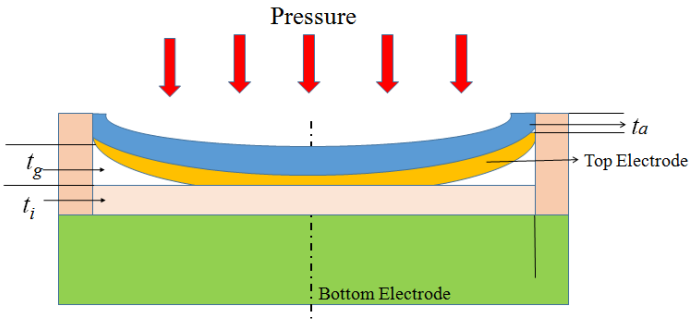

Fig. 6.1 Schematic diagram of CMUT at collapse condition

6.2 Significance of collapse voltage

During transmission mode actuation layer of CMUT element vibrates under the influence of electrostatic force as a signal is applied. Moreover, due to force the actuation layer vibrates twice the frequency of applied signal. A larger bias than signal is thus needed to make the device vibrate at the first harmonic. Applied bias generates electrostatic force which pulls the actuation layer towards the substrate and gets balanced by mechanical restoring force of the actuation layer. Above a certain bias imbalance takes place between these restoring and electrostatic force, thus compels the actuation layer to fall down upon the substrate. Bias at which this phenomenon occurs is considered as collapse voltage. It is desired to maintain bias voltage less than this collapse voltage for proper functioning of CMUT. Collapse voltage is an important parameter of this device as maximum efficiency is attained by operating the transducer close to this collapse voltage.

6.3 Electro-mechanical model of a CMUT element

In this section an electromechanical model is proposed for modeling of collapse voltage. Purpose of simplified analysis is done by adopting several approximations like parallel capacitive plates are straight, absence of fringing effect, and restoring force of actuation layer expressed as a linear function of displacement.

Moreover, CMUT is operating in vacuum and all conductors and contacts to be perfect. Any loading of the actuation layer is neglected. Modeling of collapse voltage is calculated by first order electromechanical model shown in Fig. 6.2. This model neglects the curvature of actuation layer thus bending electric field lines at the edge of actuation layers are also ignored. This electromechanical model consists of a spring, mass and a parallel plate capacitor. Spring constant is calculated by the actuation layer bending stiffness and electrostatic force that acts upon it.

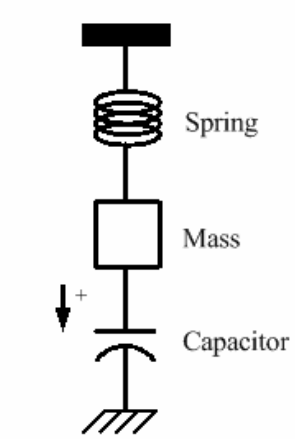

Fig. 6.2 First order lumped electro-mechanical model of CMUT

In this model spring represents the restoring force of actuation layer results from the resistance its residual stress, mass accounts for the mass of the actuation layer and capacitor represents device generated the electrostatic force.

6.3.1 Analytical modeling of collapse voltage

The resultant of capacitor and the spring forces actuates mass, thus the expression will be

$$F_{CAPACITOR} + F_{SPRING} = F_{MASS} \tag{6.1}$$

Thus individual derivation for capacitor forces and spring forces are required to interpret the effect on the mass force. For insulated cell direct capacitance is a series combination of C_i and C_g, hence equivalent capacitance $C_{eq}^{'}$ is expressed as (3.10). Considering large displacement X_a in the direction as shown in Fig. 6.2. $C_{eq}^{'}$ can be expressed for electromechanical model by,

$$\frac{1}{C_{eq}^{'}} = \frac{1}{\frac{\varepsilon_g A}{\left(t_g - X_a\right)}} + \frac{1}{\frac{\varepsilon_i A}{t_i}},$$

$$\therefore C_{eq}^{'} = \frac{\varepsilon_i \varepsilon_g A}{\varepsilon_i \left(t_g - X_a\right) + \varepsilon_g t_i} \tag{6.2}$$

Here ε_g is the permittivity of gap, ε_i is the permittivity of insulator, A is area of the capacitor plate, t_i is thickness of insulator, t_g is separation of capacitor plate at rest.

Force exerted by the capacitor

It can be calculated by differentiating the potential energy of the capacitor with respect to position of the mass.

$$F_{CAPACITOR} = -\frac{du}{dX_a} \tag{6.3}$$

where u is the potential energy of the capacitor and unbiased CMUT is can be thought as a simple capacitor, where the stored energy is

$$u = \frac{1}{2} C_{eq}^{'} v(t)^2 \tag{6.4}$$

Here $v(t)$ is the total voltage across the capacitor.

Substituting (6.4) in (6.3),

$$F_{CAPACITOR} = -\frac{d}{dX_a}\left(\frac{1}{2} C_{eq}^{'} v(t)^2\right) = -\frac{1}{2} v(t)^2 \left\{\frac{d}{dX_a}\left[\frac{\varepsilon_i \varepsilon_g A}{\varepsilon_i \left(t_g - X_a\right) + \varepsilon_g t_i}\right]\right\} \tag{6.5}$$

$$F_{CAPACITOR} = \frac{\varepsilon_i^{\,2} \varepsilon_g A\, v(t)^2}{2\left[\varepsilon_i \left(t_g - X_a\right) + \varepsilon_g t_i\right]^2} \tag{6.6}$$

Force due to spring:

Restoring force of spring enhances with the increase of displacement due to directly proportional relationship between them. Spring constant can there by expressed in terms of bending stiffness and device generated electrostatic force for variation in capacitance. So,

$$F_{SPRING} = -K_a X_a \tag{6.7}$$

where K_a is the spring constant and is expressed in terms of Young's modulus of actuation layer Y_a, actuation layer thickness t_a, actuation layer radius $A = \pi r_e^2 = \pi r_a^2$ and Poisson ratio of actuation layer material σ_a

$$K_a = \frac{16 Y_a {t_a}^3}{{r_a}^2 \left(1 - {\sigma_a}^2\right)} \tag{6.8}$$

Force due to the mass

Mass is represented as $F = ma$; where a is acceleration of the body and m is the mass of the actuation layer, thus the equation in terms of displacement will be,

$$F_{MASS} = m \frac{d^2 X_a}{dt^2} \tag{6.9}$$

where $m = 1.84 \pi {r_a}^2 \rho_a t_a$ and ρ_a is material density of actuation layer. Substituting (6.6), (6.7) and (6.9) in (6.1), the expression becomes,

$$m \frac{d^2 X_a}{dt^2} = \frac{{\varepsilon_i}^2 \varepsilon_g A \, v(t)^2}{2\left[\varepsilon_i \left(t_g - X_a\right) + \varepsilon_g t_i\right]^2} - K_a X_a \tag{6.10}$$

Static bias analysis

Considering device under static bias condition, time dependent signal is neglected. Assuming $v(t) = V_{dc}$ and neglecting mass of actuation layer due to its negligible thickness (6.10) is expressed as,

$$K_a X_a = \frac{{\varepsilon_i}^2 \varepsilon_g A {V_{dc}}^2}{2\left[\varepsilon_i \left(t_g - X_a\right) + \varepsilon_g t_i\right]^2} \tag{6.11}$$

$$\Rightarrow V_{dc} = \sqrt{\frac{2 K_a X_a \left[\varepsilon_i \left(t_g - X_a\right) + \varepsilon_g t_i\right]^2}{{\varepsilon_i}^2 \varepsilon_g A}} \tag{6.12}$$

Simplifying the expression (6.12), (6.13) is achieved

$$V_{dc} = \sqrt{\frac{2 K_a X_a}{{\varepsilon_i}^2 \varepsilon_g A}} \left[\varepsilon_i \left(t_g - X_a\right) + \varepsilon_g t_i\right] \tag{6.13}$$

Let, $\sqrt{\frac{2K_a}{\varepsilon_g A}} = Q$, then (6.13) becomes,

$$V_{dc}=\mathrm{Q}X_a^{\frac{1}{2}}\left[\left(t_g+\frac{\varepsilon_g}{\varepsilon_i}t_i\right)-X_a\right]$$

$$\Rightarrow V_{dc}=\mathrm{Q}X_a^{\frac{1}{2}}\left(t_g+\frac{\varepsilon_g}{\varepsilon_i}t_i\right)-\mathrm{Q}X_a^{\frac{3}{2}} \tag{6.14}$$

Now differentiating V_{dc} with respect to displacement and equating as $\frac{dV_{dc}}{dX_a}=0$, therefore,

$$\frac{dV_{dc}}{dX_a}=\frac{Q}{2}\left[\frac{1}{X_a}\left(t_g+\frac{\varepsilon_g}{\varepsilon_i}t_i\right)-3\sqrt{X_a}\right]=0 \tag{6.15}$$

$$\Rightarrow \frac{1}{X_a}\left(t_g+\frac{\varepsilon_g}{\varepsilon_i}t_i\right)-3\sqrt{X_a}=0 \tag{6.16}$$

Multiplying both side of (6.16) with $\sqrt{X_a}$, following equations are attained

$$\left(t_g+\frac{\varepsilon_g}{\varepsilon_i}t_i\right)-3\sqrt{X_a}=0$$

$$X_a=\frac{1}{3}\left(t_g+\frac{\varepsilon_g}{\varepsilon_i}t_i\right) \tag{6.17}$$

Putting this value of X_a into equation (6.14) and solving for V_{dc}, expression of collapse voltage $V_{collapse}$ is achieved,

$$V_{collapse}=\sqrt{\frac{8K_a\left(t_g+\frac{\varepsilon_g}{\varepsilon_i}t_i\right)^3}{27\varepsilon_g A}} \tag{6.18}$$

6.3.2 Effect of various structural parameters upon collapse voltage

In Fig 6.3 variation of actuation layer's spring constant and collapse voltage are plotted with change in actuation layer radius. Increase in radius reduces the spring constant which also affects the collapse voltage as it holds a linear relationship with spring constant. Moreover decrement in actuation layer thickness decreases the collapse voltage value as shown in Fig. 6.4.

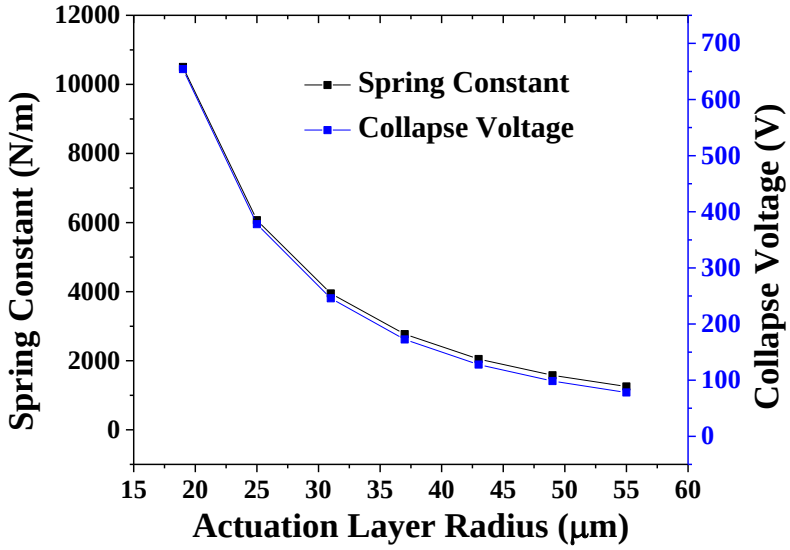

Fig. 6.3 Variation of collapse voltage and spring constant for various actuation layer radius

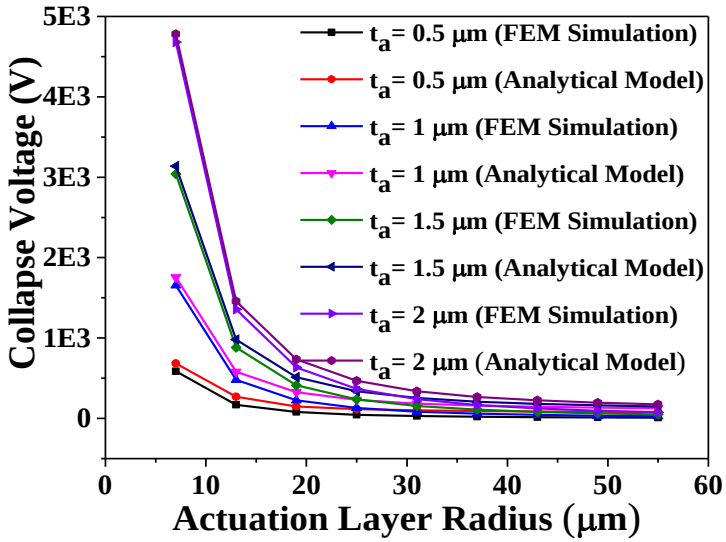

Fig. 6.4 Variation of collapse voltage for changing actuation layer radius due to different values of actuation layer thickness

Figure 6.5 depicts a nonlinear increment of spring constant with actuation layer thickness. Increment in thickness increases stiffness thus reduces displacement. This reduction in displacement makes the actuation layer to collapse at higher voltage. Figure 6.6 signifies this phenomenon in distinct manner and exhibits parabolic increment of collapse voltage with actuation layer thickness.

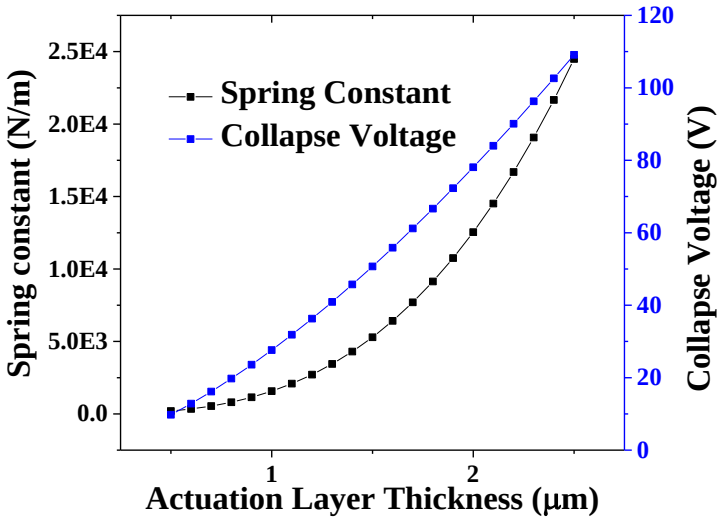

Fig. 6.5 Variation of spring constant and collapse voltage for changing actuation layer thickness

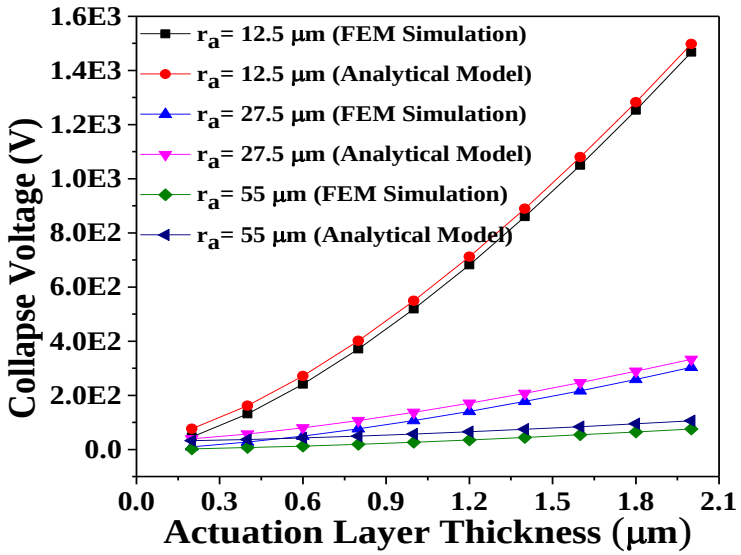

Fig. 6.6 Variation of collapse voltage for changing actuation layer thickness due to different values of actuation layer radius

It is observed from Fig. 6.7 that with the increase in insulator thickness, collapse voltage also increases linearly. As electrostatic force and displacement of the actuation layer both decreases hence collapse point will be reached at a higher bias. While dependency of collapse voltage is examined with gap thickness, similar effect is seen as it is for insulation thickness as shown in Fig. 6.8.

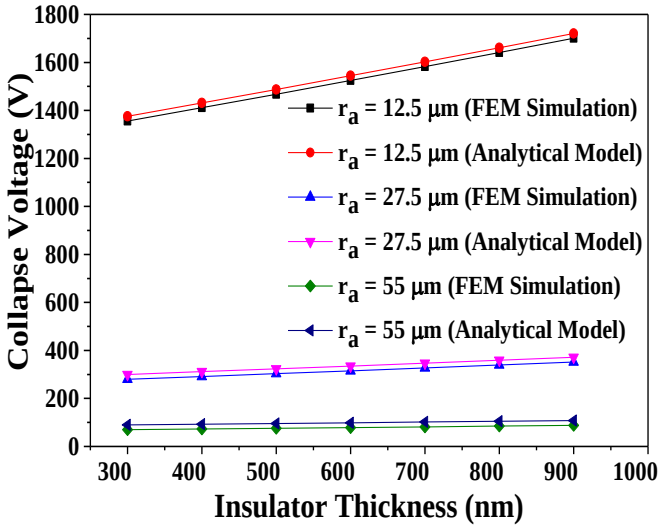

Fig. 6.7 Variation of collapse voltage for change in insulator thickness due to different values of actuation layer radius

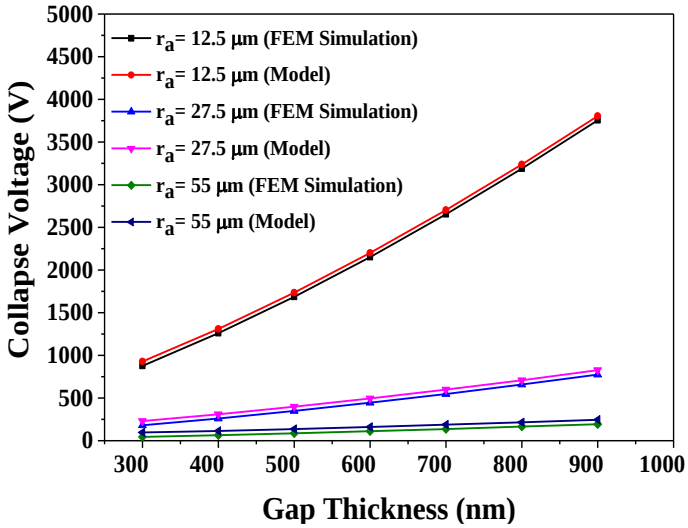

Fig. 6.8 Variation of collapse voltage for changing gap thickness due to different values of actuation layer radius

6.4 Analytical modeling of collapse voltage with fringing field effect

Considering fringing effect, the total capacitance of gap is C_{gf} and that of insulation layer is C_{if} expressed in (3.11). Considering X_a as large displacement for electromechanical model, (3.6) be rewritten as,

$$C_{gf} = \varepsilon_g \left[\left(\frac{\pi r_e^2}{t_g - X_a} \right) + r_e \ln \left\{ \left(\frac{16\pi r_e}{t_g - X_a} \right) - 1 \right\} \right] \tag{6.19}$$

Now the equivalent capacitance due to fringing, The series capacitance of the insulation and the air gap capacitances is denoted by C'_{eqf} . Therefore modified (3.12) for electromechanical model is written as,

$$C'_{eqf} = \frac{\left(C_{if}\right)\times r_e\left(\ln\left[-1+\frac{16\pi r_e}{t_g - X_a}\right]+\frac{\pi r_e}{t_g - X_a}\right)\varepsilon_g}{C_{if} + r_e\left(\ln\left[-1+\frac{16\pi r_e}{t_g - X_a}\right]+\frac{\pi r_e}{t_g - X_a}\right)\varepsilon_g} \tag{6.20}$$

$$F_{f_{CAPACITOR}} = -\frac{1}{2}v(t)^2\frac{d}{dX_a}\left(\frac{C_{gf}\times C_{if}}{C_{gf}+C_{if}}\right) \tag{6.21}$$

$$= \frac{r_e\left\{\pi r_e + t_i\ln\left(\frac{16\pi r_e}{t_i}-1\right)\right\}\left\{\pi r_e + \ln\left(\frac{16\pi r_e}{t_g - X_a}-1\right)\left(t_g - X_a\right)\right\}\varepsilon_g\varepsilon_i}{t_i\left\{\pi r_e + \ln\left(\frac{16\pi r_e}{t_g - X_a}-1\right)\left(t_g - X_a\right)\right\}\varepsilon_g + \left\{\pi r_e + \ln\left(\frac{16\pi r_e}{t_i}-1\right)t_i\right\}(t_g - X_a)\varepsilon_i} \tag{6.22}$$

Force exerted by the capacitor

As, $\frac{d}{dX_a}\left(\frac{C_{gf}\times C_{if}}{C_{gf}+C_{if}}\right) = \frac{\left(C_{if}\right)^2}{\left(C_{gf}+C_{if}\right)^2}\frac{dC_{gf}}{dX_a}$, hence,

$$F_{f_{CAPACITOR}} = \frac{\left(C_{if}\right)^2 v(t)^2}{2\left(C_{gf}+C_{if}\right)^2}\frac{\pi r_e^2\varepsilon_g}{\left(t_g - X_a\right)^2}\left(\frac{16\left(t_g - X_a\right)}{16\pi r_e - t_g + X_a}+1\right) \tag{6.23}$$

Here, force due to spring and mass is same as derived in (6.7) and (6.9). Substituting (6.7), (6.9) and (6.23) , (6.1) is rewritten as (6.24)

$$m\frac{d^2X_a}{dt^2} = \frac{\left(C_{if}\right)^2 v(t)^2}{2\left(C_{gf}+C_{if}\right)^2}\frac{\pi r_e^2\varepsilon_g}{\left(t_g - X_a\right)^2}\left(\frac{16\left(t_g - X_a\right)}{16\pi r_e - t_g + X_a}+1\right) - K_aX_a \tag{6.24}$$

Static bias analysis

Considering the device under static bias, the time dependence in voltage will be neglected and assuming $v(t) = V_{dc}$ and neglecting mass portion of the thin actuation layer, (6.24) is represented as

$$K_a X_a = \frac{\left(C_{if}\right)^2 V_{dc}^2}{2\left(C_{gf}+C_{if}\right)^2}\frac{\pi r_e^2 \varepsilon_g}{\left(t_g - X_a\right)^2}\left(\frac{16\left(t_g - X_a\right)}{16\pi r_e - t_g + X_a}+1\right) \tag{6.25}$$

Solving (6.25) for V_{dc}, (6.26) is attained

$$V_{dC} = \sqrt{\frac{2K_a X_a}{\pi r_e^2 \varepsilon_g}}\left(t_g - X_a\right)\frac{C_{gf}+C_{if}}{C_{if}}\sqrt{\frac{(t_g - X_a) - 16\pi r_e}{16\pi r_e + 15(t_g - X_a)}} \tag{6.26}$$

$$= Q\sqrt{X_a}\left(t_g - X_a\right)\left(1+\frac{C_{gf}}{C_{if}}\right)\sqrt{\frac{(t_g - X_a) - 16\pi r_e}{16\pi r_e + 15(t_g - X_a)}} \tag{6.27}$$

Here, $Q = \sqrt{\frac{2K_a}{\pi r_e^2 \varepsilon_g}}$. Now differentiating V_{dc} with respect to displacement, (6.28) is attained

$$\frac{dV_{dc}}{dX_a} = \frac{Q}{2A_1\sqrt{X_a}}\left(\begin{array}{l} A_1^2\left(1+\frac{C_{gf}}{C_{if}}\right)(t_g - X_a) - 2A_1^2\left(1+\frac{C_{gf}}{C_{if}}\right)X_a \\ -\frac{256\pi r_e\left(1+\frac{C_{gf}}{C_{if}}\right)(t_g - X_a)X_a}{(16\pi r_e + 15(t_g - X_a))^2} - \frac{2\pi r_e^2 X_a \varepsilon_g}{C_{if}(t_g - X_a)^2} \end{array}\right) \tag{6.28}.$$

Now implying $\frac{dV_{dc}}{dX_a} = 0$,

$$A_1^2\left(1+\frac{C_{gf}}{C_{if}}\right)\left(t_g - X_a\right) - 2A_1^2\left(1+\frac{C_{gf}}{C_{af}}\right)X_a - \frac{256\pi r_e\left(1+\frac{C_{gf}}{C_{if}}\right)\left(t_g - X_a\right)X_a}{\left(16\pi r_e + 15\left(t_g - X_a\right)\right)^2} - \frac{2\pi r_e^2 X_a \varepsilon_g}{C_{if}\left(t_g - X_a\right)^2} = 0$$

$$\Rightarrow A_1^2\left(t_g - X_a\right) - 2A_1^2 X_a - \frac{256\pi r_e\left(t_g - X_a\right)X_a}{\left(16\pi r_e + 15\left(t_g - X_a\right)\right)^2} - \frac{2\pi r_e^2 X_a \varepsilon_g}{C_{if}\left(t_g - X_a\right)^2}\left(\frac{C_{if}}{C_{gf}+C_{if}}\right) = 0 \tag{6.29}$$

Here $A_1 = \left[t_i + \left(\frac{\varepsilon_g r_e^2\left(t_i + 16\right)}{C_{if}}\right)\right]$, $X_a = \frac{1}{3}\left(\frac{.0207 \times t_i}{\left(A_1 + 1\right)}\right)$

The expression (6.29) results multiple solutions of root, hence considering the optimized solution of X_a, (6.27) is expressed as ,

$$V_{f_{COLLAPSE}} = \sqrt{\frac{K_a X_a}{256\pi r_e \varepsilon_g X_a}}\left(t_g - X_a\right)\frac{C_{if}+C_{gf}}{C_{if}} \tag{6.30}$$

6.4.1 Analysis of fringing effect upon collapse voltage

Figure 6.9 plots the effect of fringing upon variation of collapse voltage with actuation layer radius. Fringing effect is profound for lower actuation layer radius and higher thickness. Above 25µm radius collapse voltage becomes almost constant. Enhancement of device capacitance enhances due to fringing effect. Enhanced capacitance increases generated electrostatic force which causes simultaneous improvement in displacement. This improved displacement led the actuation layer collapse at comparatively lower voltage than excluding fringing effect. Fig. 6.10 depicts fringing effect has insightful effect upon collapse voltage with a combinational effect of increase in insulation thickness and decrease in actuation layer radius. Incremented capacitance leads to reduction in collapse voltage by 11.03%.

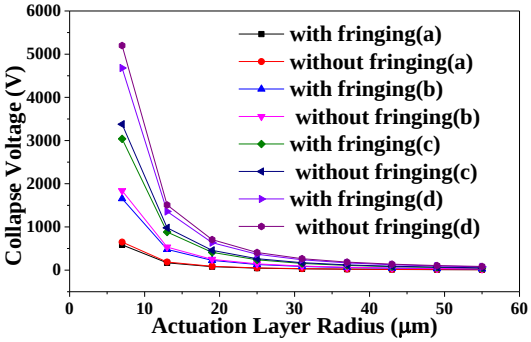

Fig. 6.9 Variation of collapse voltage for changing actuation layer radius for a) t_a =0.5 µm, b) t_a =1 µm, c) t_a =1.5 µm, d) t_a =2 µm

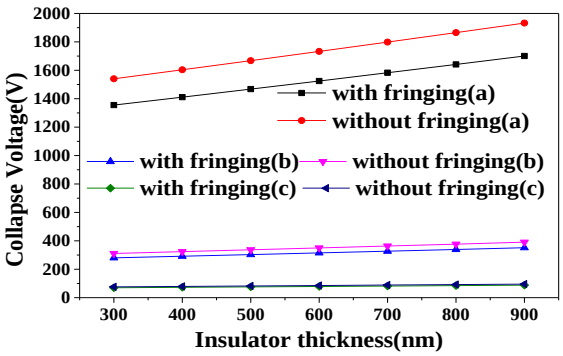

Fig. 6.10 Variation of collapse voltage for changing insulation thickness for a) r_a =12.5 µm b) r_a =27.5 µm, c) r_a =55 µm

Figures 6.11 and 6.12 show the variation of collapse voltage with actuation layer and gap thickness respectively. Increase in actuation layer thickness enhances stiffness thus decreases displacement. Due to fringing effect displacement enhances in the device which causes lower collapse voltage compared to device without fringing effect. Fringing capacitance increases with gap thickness, this enhanced device capacitance is quite responsible to make the actuation layer collapsed at 11.02% lower voltage than the value calculated excluding fringing effect. The fringing has no effects on the maximum displacement the actuation layer can attain before collapse but the collapse takes place at a lower bias as fringing effects increases the electrostatic force of the actuation layer.

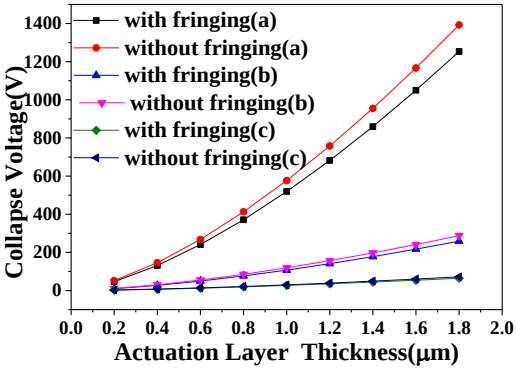

Fig. 6.11 Variation of collapse voltage for changing actuation layer thickness for a) r_a =12.5 μm b) r_a =27.5 μm, c) r_a =55 μm

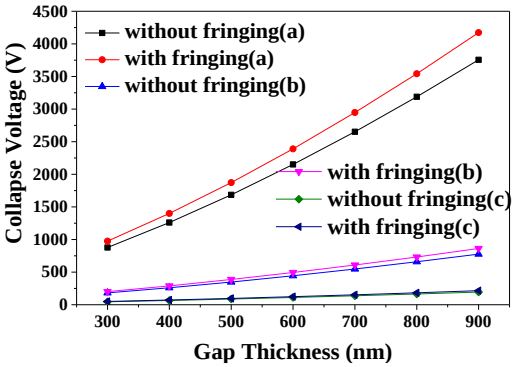

Fig. 6.12 Variation of collapse voltage for changing gap thickness for a) r_a =12.5 μm b) r_a =27.5 μm, c) r_a =55 μm

6.5 Coupling Coefficient

The dimensionless factor, also known as the coupling coefficient, is a measure of the transducer's ability to convert one type of energy into another and is an important characterisation parameter. Coupling coefficients are affected by the stress distribution, electric field, and shape of the piezo element, in addition to the kind of material. The ratio of converted to total energy in one vibration cycle of the transducer is the square of this value. We next proceed to find the device's lumped electromechanical equivalent circuit, as shown in Fig. 6.13, with the device's electrical impedance in parallel with the electrical analogue of the actuation layer's mechanical impedance. In the equivalent circuit Z_{em} can be represented by a series combination of an inductor L_{em} corresponding to the mass of the actuation layer and a capacitor C_{em} corresponding to the mechanical compliance.

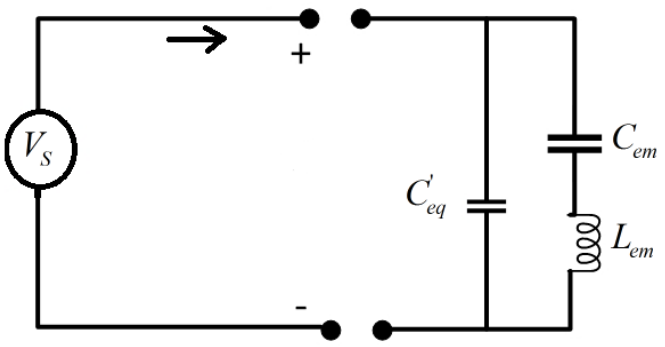

Fig. 6.13 CMUT equivalent model in the transmitting mode

$C_{eq}^{'}$ is in parallel with the series combination of L_{em} and C_{em}. Here

$$L_{em} = 1.446 \times \left(\frac{\rho_a t_a A}{\phi_1^2} \right) \tag{6.31}$$

and

$$C_{em} = \phi_1^2 \times \left[\frac{0.9568}{8\pi P_r t_a} \right] \tag{6.32}$$

Both in (6.31) and (6.32) ϕ is the transformation factor of the cell and P_r is the residual stress. In the circuit series capacitance of the device and electrical equivalence of the actuation layer is represented by

$$C_s = \left\{ \left(C_{em} \times C_{eq}^{'} \right) / C_{em} + C_{eq}^{'} \right\} \tag{6.33}$$

when the actuation layer is in free vibration, the inductor generates a sinusoidal current with a peak value of $I_{\max}$ in resonance with the input signal, producing the greatest kinetic energy as,

$$E_{tot} = (KE)_{\max} = \frac{1}{2} L_{em} I_{\max}^2 \tag{6.34}$$

The kinetic energy is zero at maximum displacement, and the maximum energy is stored in the device capacitance in electrical form as,

$$EE = \left(\frac{C_s}{C_{eq}^{'}} \right) \frac{1}{2} L_{em} I_{\max}^2 \tag{6.35}$$

The dynamic coupling factor can be easily calculated using

$$k_w = \sqrt{EE / E_{tot}} = \sqrt{C_s / C_{eq}^{'}} \tag{6.36}$$

Expression of coupling coefficient excluding fringing field effect becomes,

$$k_w = \sqrt{\frac{\varepsilon_g A V_{dc}^2}{\varepsilon_g A V_{dc}^2 + 26.28 \times (P_r t_a d_{eff}^3)}} \tag{6.37}$$

where $d_{eff} = \left(t_g + \frac{\varepsilon_g}{\varepsilon_i} t_i \right)$.

6.5.1 Variation of coupling factor under influence of structural parameters

Figures 6.14 and 6.15 show the variation of coupling factor with respect to effective gap and insulation thickness respectively. Increase in gap and insulation thickness decreases the electrostatic force which reduces the displacement. Reduced displacement causes reduction in energy conversion and as a consequence coupling factor decreases.

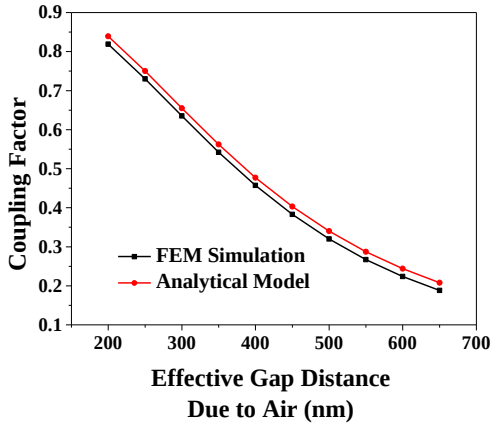

Fig. 6.14 Coupling factor with change in effective gap distance due to air gap

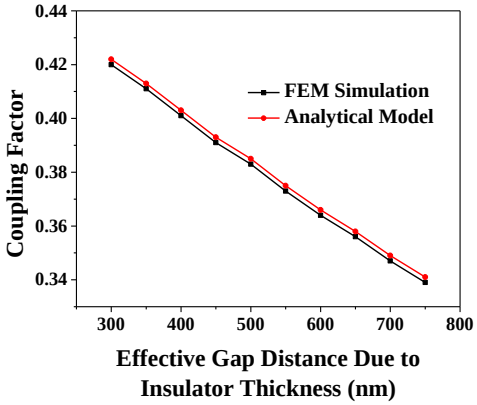

Fig. 6.15 Coupling factor with change in effective gap distance due to insulator thickness

Application of bias results in columbic force between metalized actuation layer and Si substrate, subsequent to which actuation layer gets attracted towards the bottom electrode. Increase in this bias enhances the attraction force between them and simultaneously linear increment of displacement occurs. Enhanced displacement converts energy in proportionate manner and as a result increase in coupling factor takes place with respect to change in applied bias as depicted in Fig. 6.16. Variation in coupling factor with respect to residual stress is plotted in Fig. 6.17.

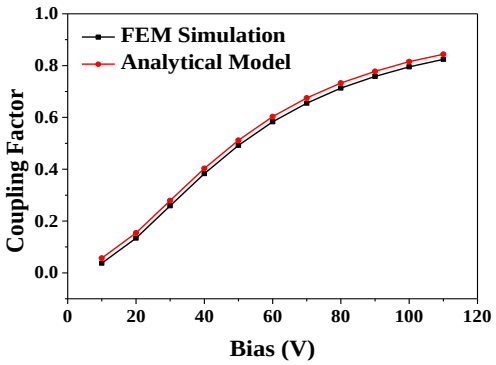

Fig. 6.16 Coupling factor with applied bias

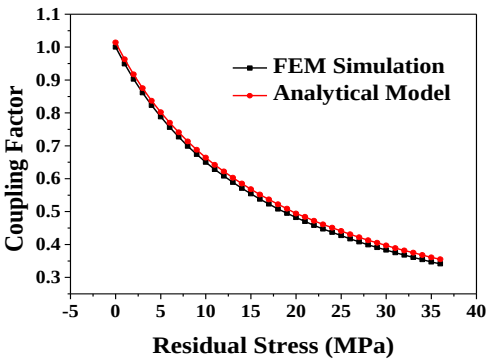

Fig. 6.17 Coupling factor with residual stress

Coupling factor holds inversely proportional relationship with residual stress of actuation layer. Increase in residual stress enhances stiffness thus displacement of actuation layer decreases resulting decrement of coupling factor. Figures 6.18 and 6.19 depict the variation of coupling factor with respect to change in actuation layer radius and its thickness respectively. Displacement increases with actuation layer radius and decreases with actuation layer thickness. As a result coupling factor increases when plotted with actuation layer radius and decreases against actuation layer thickness.

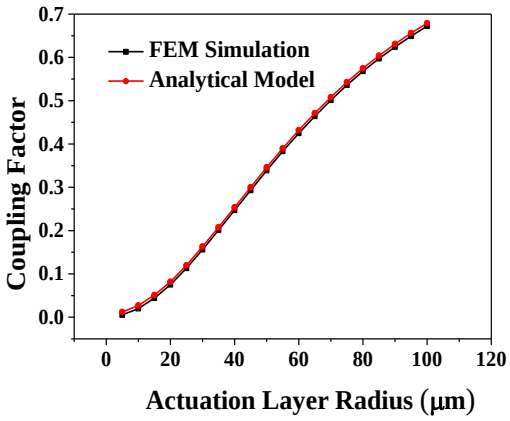

Fig. 6.18 Coupling Factor with actuation layer radius

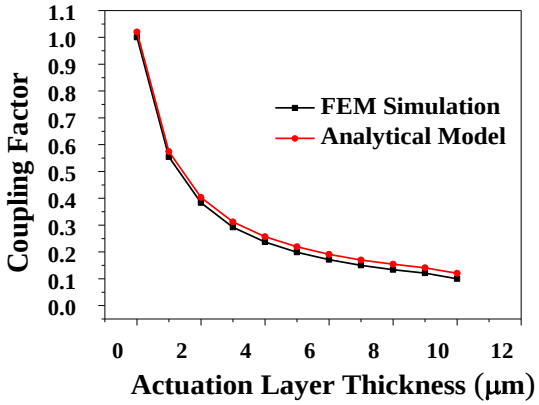

Fig. 6.19 Coupling Factor with actuation layer thickness

Figure 6.20 shows the combinational effect of actuation layer radius and gap separation upon collapse voltage. Combinational effect of bias voltage and actuation layer radius is exhibited in Fig 6.21. Increase in actuation layer radius and reduced gap thickness can improve coupling factor as shown in Fig. 6.20 whereas increase of bias can also improve the factor. For both these cases increase in actuation layer radius and bias leads the coupling factor towards unity. Figs. 6.22 depicts the dual effect of actuation layer and insulation thickness upon coupling factor and Fig. 6.23 shows the same of residual stress and actuation layer radius upon coupling factor. Decrease in actuation layer, insulation thickness can improve the coupling factor whereas device having high actuation laye radius and actuation layer of low residual stress material have high coupling factor. Considering all these characteristics

moderate values of structural parameters should be taken so that device should not collapse at low voltage and have high coupling factor.

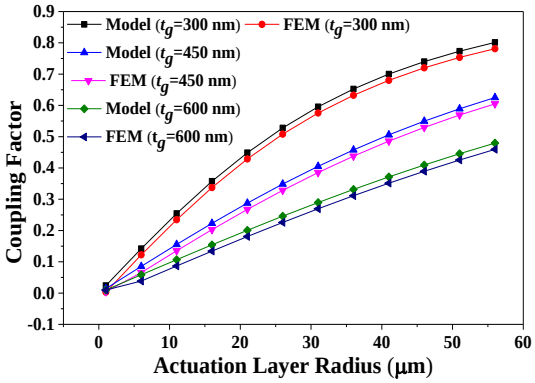

Fig. 6.20 Comparative analysis of coupling factor for combinational effect of r_a and t_g

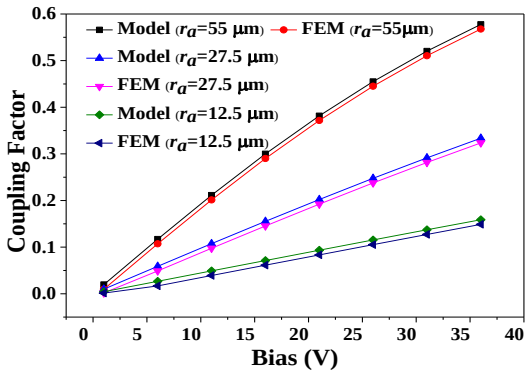

Fig. 6.21 Comparative analysis of coupling factor for combinational effect of V_{dc} and t_g

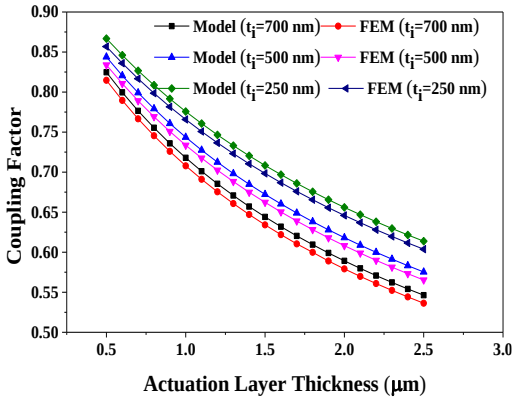

Fig. 6.22 Comparative analysis of coupling factor for combinational effect of t_a and t_i

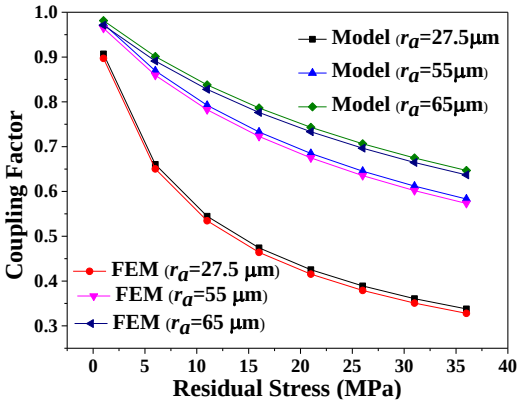

Fig. 6.23 Comparative analysis of coupling factor for combinational effect of r_a and P_r

6.6 Influence of HfO_2 upon collapse voltage and coupling factor

Insulating material having high dielectric constant has proved to be an excellent choice to enhance device displacement. In this context effect of HfO_2 is investigated upon collapse voltage and coupling factor. Various insulation thickness is considered during usage of HfO_2 and enhancement is calculated with respect to 500 nm Si_3N_4. Increase in the radius of the actuation layer the collapse voltage decreases as there is a decrement in a thickness of the insulation thickness and actuation layer respectively in Figs. 6.24 and 6.25. As per the graphs shown here the involvement of high-K insulation reduces the collapse voltage along with the insulation and actuation layer thickness. As the radius of the actuation layer grows,

the displacement of the actuation layer grows as well. On low voltage, this means the actuation layer will collapse very quickly. For a 55 µm radius and a 2 µm actuation layer thickness, the collapse voltage was found to be 75.8 V in this case. Whereas due to a decrease in actuation layer thickness the collapse voltage value decreases. Analyzing Fig. 6.24 for insulation thickness 500 nm involving Si_3N_4 the collapse voltage is 78.07 V at 55µm actuation layer radius and keeping all these parameters unchanged only using HfO_2 the collapse voltage reduces and becomes 67.7 V, but for 50nm insulation thickness the collapse voltage again reduces at 63.8V. As shown in Fig.6.25 at 1.5 µm actuation layer thickness the collapse voltage is 49.2 V, at lastly for 0.5 µm the collapse voltage is 9.5 V for Si_3N_4, but keeping actuation layer thickness same as earlier, only for HfO_2 is 43.9 V and 4.3 V when all other parameters are kept unchanged.

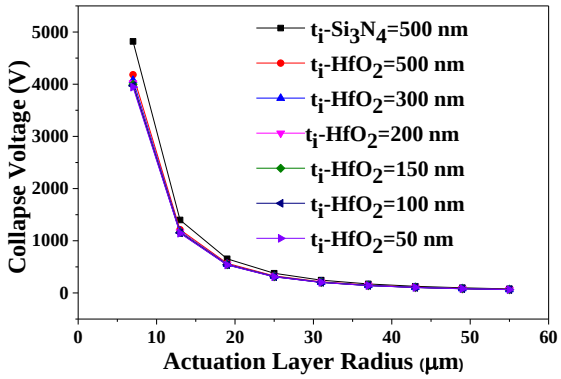

Fig. 6.24 Comparative analysis of collapse voltage with respect to actuation layer radius

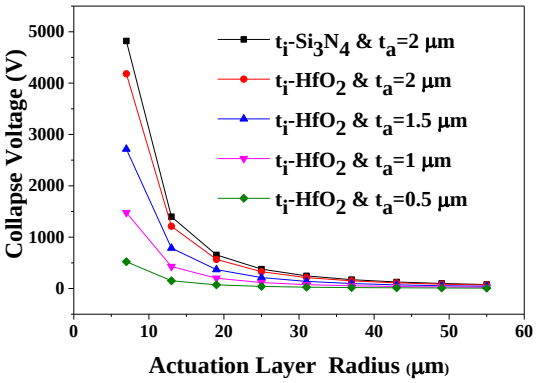

Fig. 6.25 Comparative analysis of collapse voltage with respect to actuation layer radius

The actuation layer displacement decreases as the gap distance increases under constant bias, reducing the relaxing effect of the actuation layer. When shown in Fig. 6.26, as the vacuum gap thickness increases, the collapse voltage increases as well, but as the insulation thickness decreases due to the presence of high–K material, the collapse voltage decreases. The characteristic graph also shows that the collapsed voltage grows linearly with the increase in vacuum gap thickness. As the electrostatic force of the actuation layer decreases, as predicted by analytical results, and as the same phenomenon occurs in the case of actuation layer displacement, the collapse point will be reached at a higher bias voltage, implying that the actuation layer will not collapse at lower voltages. At 450 nm gap separation, the collapse voltage for

Si_3N_4 with insulation thickness of 500 nm is 78.07 V, while the collapse voltage for HfO_2 is 67.2 V. If HfO_2 is employed as an insulator, the collapse voltage is reduced to 63.3 V by reducing the insulation thickness. The actuation layer displacement decreases as the insulator thickness increases at constant bias, reducing the relaxing effect of the actuation layer. The increase in collapse voltage is caused by increasing insulator thickness, as seen in Fig. 6.27. The collapse voltage increases linearly with the increase in insulator thickness, according to this particular study. According to analytical results, the electrostatic force and displacement of the actuation layer decrease with insulator thickness, therefore the collapse point will be achieved at a higher bias voltage, indicating that the actuation layer will not collapse at lower voltages.

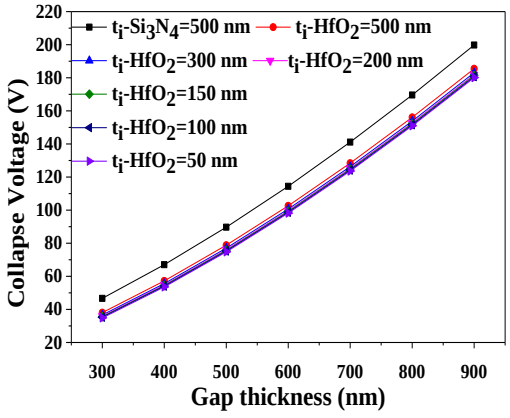

Fig. 6.26 Comparative analysis of collapse voltage for change in gap thickness

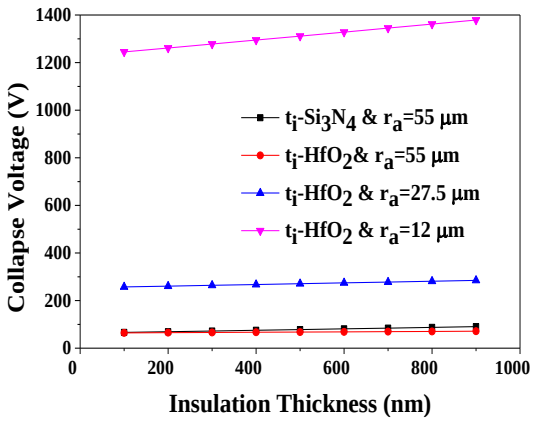

Fig. 6.27 Comparative analysis of collapse voltage with insulation thickness

Fig. 6.28 shows the comparative analysis of coupling factor due to increasing bias. Introducing HfO_2 as insulation layer enhances displacement in comparison with Si_3N_4 isolation resulting improvement in coupling factor. It is quite evident that decreasing the actuation layer thickness also causes increment of coupling factor. As involvement of HfO_2 enhances displacement of the device hence its quite obvious the enhancement of coupling factor will also take place. Enhancement due to HfO_2 insulating layer is calculated as, $E_{k_w} = \left(\frac{k_{w(HfO_2)} - k_{w(Si_3N_4)}}{k_{w(Si_3N_4)}} \right) \times 100$, where $k_{w(Si_3N_4)}$ is the coupling factor for insulated structure having 500 nm Si_3N_4 layer and $k_{w(HfO_2)}$ is the

coupling factor for insulated structure having HfO_2 insulation layer of various thickness within a range of 500 nm to 50 nm.

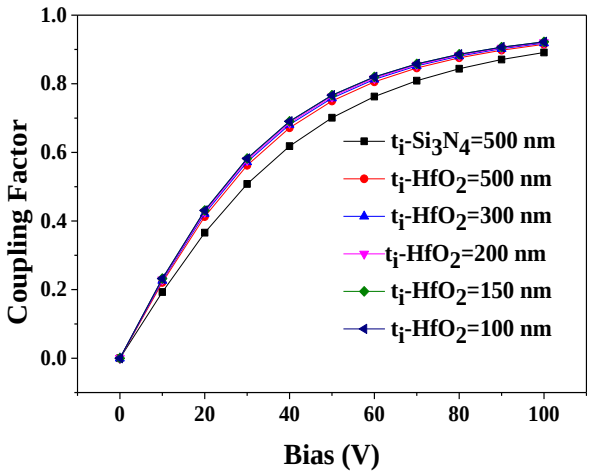

Fig. 6.28 Comparative analysis of coupling factor for change in bias between HfO_2/ Si_3N_4 isolation for various HfO_2 thickness

Figure 6.29 depicts the variation of coupling factor with variation in residual stress. Involvement of HfO_2 isolation has noticeable impact upon coupling factor compared with Si_3N_4 isolation. Enhanced displacement in HfO_2 isolation yields larger coupling factor than Si_3N_4 isolation. With residual stress increment, coupling factor shows non-linear decrement pattern. Increase in residual stress creates adverse effect upon displacement which results reduction in coupling factor. Figure 6.30 shows average E_{k_w} of 4.65%, 6.78%, 7.69%, 8.55% and 8.97% for considering dimension of 500 nm, 300 nm, 200 nm, 100 nm and 50 nm insulation thickness HfO_2.

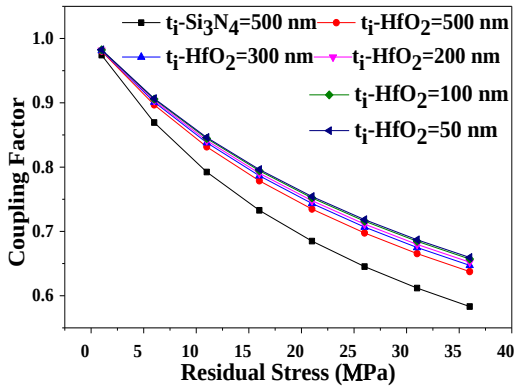

Fig. 6.29 Comparative analysis of coupling factor for change in residual stress between Si_3N_4 isolation and HfO_2 of various thickness

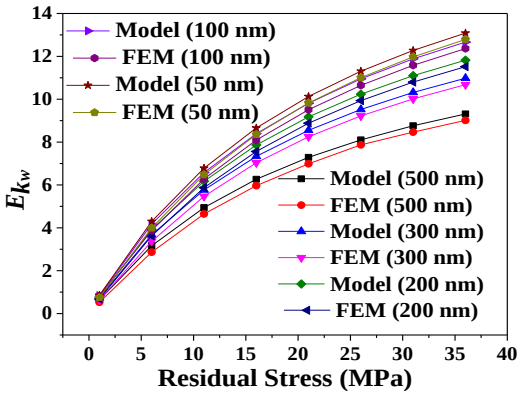

Fig. 6.30 E_{k_w} with respect to residual stress

Figure 6.31 illustrates a comparison of coupling factor for changes in gap thickness for the same input pulse between HfO_2 and Si_3N_4 isolation for various HfO_2 thicknesses for the same input pulse. Though coupling factor reduces for increasing gap thickness but usage of HfO_2 enhances the factor compared to Si_3N_4 isolation. Figure 6.32 shows E_{k_w} with respect to gap thickness where average E_{k_w} of 3.75%, 4.73%, 6.69%, 7.55% and 8.07% for considering dimension of 500 nm, 300 nm, 200 nm, 100 nm and 50 nm insulation thickness HfO_2.

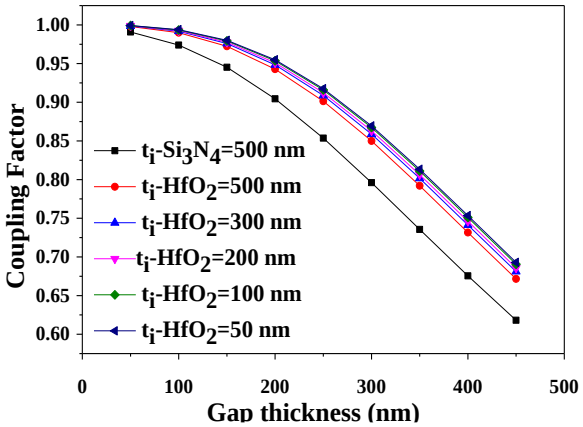

Fig. 6.31 Comparative analysis of coupling factor for change in gap thickness Si_3N_4 isolation and HfO_2 of various thickness

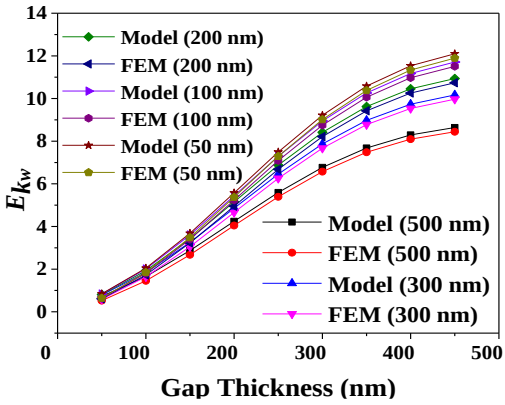

Fig. 6.32 E_{k_w} with respect to gap thickness

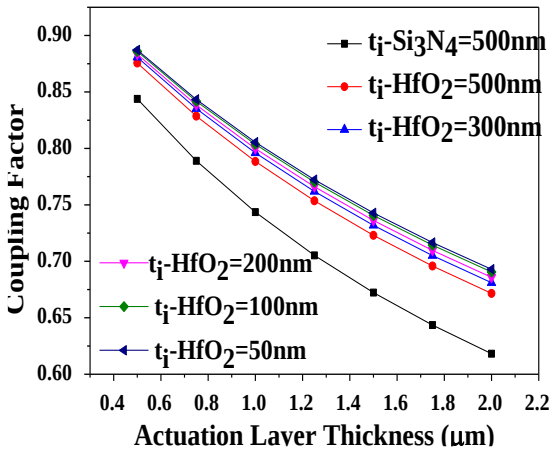

Fig. 6.33 Comparison of coupling factor for change in actuation layer thickness between Si_3N_4 isolation and HfO_2 of various thickness

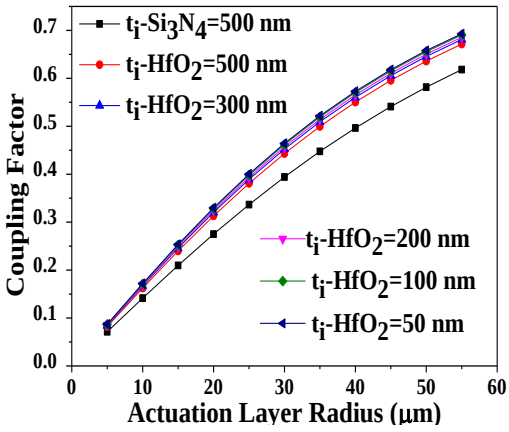

Fig. 6.34 Comparison of coupling factor for change in actuation layer radius between Si_3N_4 isolation and HfO_2 of various thickness

6.7 Summary

Modeling of collapse voltage and coupling factor is carried over for an insulated CMUT structure with SiC is investigated here. Factors that influence displacement are also responsible for determining the collapse voltage and coupling factor. Collapse voltage decreases due to enhanced displacement. Introduction of fringing effect enhances the capacitance thus collapse voltage decreases but coupling factor increases. The inclusion of an insulation layer increased the coupling factor, improved device sensitivity, and made the CMUT ready to function safely in both high voltage and high temperature environments. The insulation layer aids in the CMUT's ability to produce high-resolution images at a minimal cost. Such discoveries could help to develop medical imaging on a broad scale.

References

[1] G. R. Lockwood, D. H. Turnbull, D. A. Christopher, and F. S. Foster, “Beyond 30 MHz Applications of high-frequency ultrasound imaging”, *IEEE Engineering in Medicine and Biology Magazine*, vol. 15, no. 6, pp. 60-71, 1996.

[2] F. Levent Degertekin, J. Pei, B. T. Khuri-Yakub, and K. C. Saraswat, "In situ acoustic temperature tomography of semiconductor wafers," *Applied physics letters*, vol. 64, no. 11, pp. 1338-1340, 1994.

[3] F. L. Degertekin and B. Khuri-Yakub, "Hertzian contact transducers for nondestructive evaluation," *The Journal of the Acoustical Society of America*, vol. 99, no. 1, pp. 299-308, 1996.

[4] R. M. White, "Generation of elastic waves by transient surface heating," *Journal of Applied Physics*, vol. 34, no. 12, pp. 3559-3567, 1963.

[5] S. P. Kelly, R. Farlow, and G. Hayward, "Applications of through-air ultrasound for rapid NDE scanning in the aerospace industry," *IEEE Transactions on Ultrasonics, Ferroelectrics, and Frequency Control*, vol. 43, no. 4, pp. 581-591, 1996.

[6] M. Gachagan, G. Hayward, S. P. Kelly, and W. Galbraith, "Characterization of air-coupled transducers," *IEEE Transactions on Ultrasonics, Ferroelectrics, and Frequency Control*, vol. 43, no. 4, pp. 678-689, 1996.

[7] G. Hayward and A. Gachagan, "An evaluation of 1–3 connectivity composite transducers for air-coupled ultrasonic applications," *The Journal of the Acoustical Society of America*, vol. 99, no. 4, pp. 2148-2157, 1996.

[8] W. Manthey, N. Kroemer, and V. Magori, "Ultrasonic transducers and transducer arrays for applications in air," *Measurement Science and Technology*, vol. 3, no. 3, p. 249, 1992.

[9] D. W. Schindel and D. A. Hutchins, “Applications of micromachined capacitance transducers in air-coupled ultrasonics and nondestructive evaluation," *IEEE Transactions on Ultrasonics, Ferroelectrics, and Frequency Control*, vol. 42, pp. 51-58, 1995.

[10] O. Oralkan, A.S. Ergun, J.A. Jhonson, M. Karaman *et al*. "Capacitive micromachined ultrasonic transducers: next-generation arrays for acoustic imaging?," *IEEE Transactions on Ultrasonics, Ferroelectrics, and Frequency Control*, vol. 49, no. 11, pp. 1596-1610, 2002.

[11] O. Oralkan, B. Bayram, G.G. Yaralioglu, A.S. Ergu,"Experimental characterization of collapse-mode CMUT operation," *IEEE Transactions on Ultrasonics, Ferroelectrics, and Frequency Control*, vol. 53, no. 8, pp. 1513-1523, 2006.

[12] K. K. Park, O. Oralkan and B. T. Khuri-Yakub, "A comparison between conventional and collapse-mode capacitive micromachined ultrasonic transducers in 10-MHz 1-D arrays," *IEEE Transactions on Ultrasonics, Ferroelectrics, and Frequency Control*, vol. 60, no. 6, pp. 1245-1255, 2013.

[13] G. G. Yaralioglu, A. S. Ergun, B. Bayram, E. Haeggstrom and B. T. Khuri-Yakub, "Calculation and measurement of electromechanical coupling coefficient of capacitive micromachined ultrasonic transducers," *IEEE Transactions on Ultrasonics, Ferroelectrics, and Frequency Control*, vol. 50, no. 4, pp. 449-456, 2003.

CHAPTER

7

Frequency Response and Mechanical Impedance

7.1 Introduction

CMUT transmits ultrasonic sound wave in the surrounding medium. In comparison with piezoelectric transducer bandwidth of transmitted wave is quite larger for MEMS capacitive transducer. Practical potential of ultrasound can be harnessed by efficient launching upon the subject of incidence. MUT capacitive transducers also detect ultrasound waves for sensing or actuating applications. During transmission and detection ultrasound needs to be done through coupling medium [1-2]. Coupling medium can be of solid, liquid and gaseous form. Piezoelectric transducers suffers from impedance mismatch while involved for executing and detecting ultrasound in liquid medium but fit well during ultrasonic investigation in solid. This limitation of impedance mismatch with the fluid of interest can easily be overcomed by the engagement of CMUT [3-5]. Usage of piezoelectric transducer is not suitable also for generating ultrasound in air medium due to its quite smaller acoustic impedance (400 Kg/m^2s) compared to that of piezoelectric materials which execute ultrasonic vibration of 30×10^6 Kg/m^2s [6]. In this context capacitive MUT is accepted unanimously for its lower mechanical impedance and better coupling with medium of interest and wider bandwidth. Geometrical shape of single capacitive transducer acts as prime deciding factor of device performance and compatibility among other cells [7-8]. Various membrane shapes like hexagonal, square and circular are investigated in many research works [9-13]. Vibration of device membrane occurs due to electrostatic attraction force between two electrodes. Variation of the separation between two electrodes can be expressed as a function of time. Under static bias condition metalized SiC actuation

layer gets attracted towards Si substrate due to coulomb attraction force. Application of signal along with this bias results vibration in respect to applied frequency thus generates ultrasonic waves. In this chapter mechanical impedance and frequency response [14-17] is modeled and analysed to evaluate primary and secondary resonances for circular membrane based insulated element.

7.2 Analytical modeling of dynamic displacement using Mason's circular membrane Model

This analytical modeling of dynamic response of the device is derived by Mason's equations. Mechanical behavior of actuation layer of CMUT can be executed by consideration of Mason's analysis [18]. Expression of motion of actuation layer will be,

$$\frac{\left(Y_a + T_a\right) t_a^{\,3}}{12\left(1-\sigma_a^{\,2}\right)} \nabla^4 w \; - T_a \nabla^2 w \; - P \; + t_a \rho_a \frac{\partial^2 w}{\partial t^2} = 0 \tag{7.1}$$

Dynamic response of actuation layer can be expressed as (7.2) by considering $\nabla^2 w \; = \left(\frac{d^2 w}{dr^2} + \frac{1}{r}\frac{dw}{dr} \right)$ and $t_a^3 \to 0$, due to thin stretched membrane under a constant pressure over the surface hence equation (7.1) can be rewritten as

$$T_a \left(\frac{d^2 w}{dr^2} + \frac{1}{r}\frac{dw}{dr} \right) - t_a \rho_a \frac{\partial^2 w}{\partial t^2} + P = 0 \tag{7.2}$$

When an alternating voltage of variation $e^{j\omega t}$ is superimposed on the static bias, ultrasonic energy will be coupled to the surrounding medium being proportional to the amplitude of the vibration of the membrane created, then (7.2) will be

$$\left(\frac{d^2 w_{signal}}{dr^2} + \frac{1}{r}\frac{dw_{signal}}{dr} \right) + \frac{\omega^2 \rho_a t_a}{T_a} w_{signal} + \frac{P_{signal}}{T_a} = 0 \tag{7.3}$$

Here w_{signal} is the displacement of actuation layer due to application of signal, ω is radial frequency, P_{signal} is the pressure due to application of signal along with bias. Expression of P_{signal} is derived from $F'_{f_{signal}}$ acting on device area A, $F'_{f_{signal}}$ where force generated in insulated cell considering fringing effect.

$$P_{signal} = \frac{F'_{f_{signal}}}{A} = \frac{V_{ac} V_{dc} {C_{if}}^2}{A {C_{gf}}^2 \left(\frac{C_{if}}{C_{gf}} + 1 \right)^2} \left[\varepsilon_g \frac{\pi {r_e}^2}{{t_g}^2} + \frac{\varepsilon_g r_e}{\left(\frac{16\pi r_e}{t_g} - 1 \right)} \times \frac{16\pi r_e}{{t_g}^2} \right] \tag{7.4}$$

Let $\frac{\omega^2 \rho_a t_a}{T_a} = k^2$ and $\rho_a t_a = \rho_s$ is the surface density of the actuation layer, hence $k = \omega \left(\frac{\rho_s}{T_a} \right)^{1/2} = \frac{\omega}{\upsilon}$, $\upsilon = \left(\frac{T_a}{\rho_s} \right)^{1/2}$ is the velocity of propagation of wave on the suspended actuation layer and the tension of the actuation layer can be expressed as $T_a = P_r t_a$, so (7.4) becomes,

$$\frac{d^2 w_{signal}}{dr^2} + \frac{1}{r} \frac{dw_{signal}}{dr} + k^2 w_{signal} + \frac{P_{signal}}{T_a} = 0 \tag{7.5}$$

Multiplying the whole equation by r^2 and excluding the term $\left(\frac{P}{T_a} \right) r^2$, the equation is expressed by Bessel's differential equation as,

$$r^2 \frac{d^2 w_{signal}}{dr^2} + r \frac{dw_{signal}}{dr} + \left\{ (kr)^2 - 0 \right\} w_{signal} = 0 \tag{7.6}$$

Solution of the above equation is expressed by,

$$w_{signal} = A J_0(kr) + B K_0(kr)$$

where J_0 is the Bessel function of zeroth order of the first kind , K_0 is the Bessel function of second kind. Taking w_{signal} as common from (7.5), then (7.7) is obtained,

$$\left[\frac{d^2}{dr^2} + \frac{1}{r} \frac{d}{dr} + k^2 \right] w_{signal} = \frac{P_{signal}}{T_a} \tag{7.7}$$

$$w_{signal} = -\left[-\frac{P_{signal}}{T_a} k^2 \left\{ 1 + \frac{1}{k^2} \frac{d^2}{dr^2} + \frac{1}{rk^2} \frac{d}{dr} + ... \right\} \right] \tag{7.8}$$

As differentiation of constant term becomes zero, so above equation becomes,

$$w_{signal} = -\frac{P_{signal}}{T_a k^2}.$$

The solution of (7.5) can be obtained by substituting the value of $T_a k^2$ and combining both the cases that is

$$w_{signal} = AJ_0(kr) + BK_0(kr) - \frac{P_{signal}}{(\omega^2 \rho_a t_a)} \tag{7.9}$$

Here P_{signal} is considered as a constant and only w_{signal} is a function of time. At $r = 0$, $K_0 = \propto$ giving $B = 0$. Deflection of actuation layer is maximum at the center and becomes zero at the edge of the layer. The deflection tends to zero as the actuation layer is considered to be rigidly fixed at the edges so $w_{signal} = 0$ when $r = r_a$, solving the constant A, the expression becomes,

$$A = \frac{P_{signal}}{\left\{\left(\omega^2 \rho_a t_a\right) J_0\left(\frac{\omega}{\upsilon} r_a\right)\right\}} \tag{7.10}$$

Displacement of actuation layer is given by,

$$w_{signal}(r) = \frac{P_{signal}}{\omega^2 \rho_a t_a}\left\{\frac{J_0\left(\frac{\omega}{\upsilon} r\right)}{J_0\left(\frac{\omega}{\upsilon} r_a\right)} - 1\right\} \tag{7.11}$$

7.3 Analysis of Resonance Frequency Response Profile

The frequency response characteristic of the device is modeled and analyzed to evaluate the primary and the secondary resonance. Displacement at radial position from the center is given by (7.11) . Displacement of actuation layer at the center can be written as,

$$w_{signal}(r) = \frac{P_{signal}}{\omega^2 \rho_a t_a}\left\{\frac{J_0\left(\frac{\omega}{\upsilon} r\right)}{J_0\left(\frac{\omega}{\upsilon} r_a\right)} - 1\right\} \tag{7.12}$$

The standard expression for the Bessel function is ,

$$J_0(x) = 1 - \frac{x^2}{2^2} + \frac{x^4}{2^2.4^2} - \frac{x^6}{2^2.4^2.6^2} + ...$$

$$J_1(x) = \frac{x}{2} - \frac{x^3}{2^2} + \frac{x^5}{2^2.4^2.6} - .....$$

Using the above formula and putting the value $J_0(ka_e)$ the following three cases can be considered.

CASE 1: Considering the first two terms of the Bessel function of the first kind (7.12) becomes,

$$w_{signal}(0) = \frac{P_{signal}}{\omega^2 \rho_a t_a}\left[\frac{1}{1-\frac{k^2 r_a{}^2}{4}} - 1\right] \tag{7.13}$$

For resonance, differentiating (7.13) with respect to the ω and equating to zero (7.14) is obtained

$$\frac{dw_{signal}(0)}{d\omega} = \frac{P_{signal}}{\omega^2 \rho_a t_a}\left[\frac{\left(1-\frac{k^2 r_a{}^2}{4}\right)\left(\frac{2k^2 r_a}{4}\frac{dk}{d\omega}\right)}{\left(1-\frac{k^2 r_a{}^2}{4}\right)^2}\right] - \frac{P_{signal}}{\omega^2 \rho_a t_a}\left[\frac{\left(\frac{k^2 r_a{}^2}{4}\right)\left(\frac{-2k r_a{}^2}{4}\frac{dk}{d\omega}\right)}{\left(1-\frac{k^2 r_a{}^2}{4}\right)^2}\right] + \frac{\frac{k^2 r_a{}^2}{4} - 2P_{signal}}{1-\frac{k^2 r_a{}^2 \omega^3 \rho_a t_a}{4}} \tag{7.14}$$

Simplifying (7.14) for resonance, (7.15) is attained.

$$\frac{\left(4-k^2 r_a{}^2\right)\left(2k r_a{}^2 \frac{dk}{d\omega}\right) - \left(k^2 r_a{}^2\right)\left(-2k r_a{}^2 \frac{dk}{d\omega}\right)}{4-k^2 r_a{}^2} = \frac{2}{\omega}\left(k^2 r_a{}^2\right) \tag{7.15}$$

As, $k = \omega\sqrt{\frac{\rho_a}{P_r}} = \omega x$ the equation becomes,

$$\left[\frac{\left(4-\omega^2x^2{r_a}^2\right)\left(2\omega x{r_a}^2x\right)-\pm\left(\omega^2x^2{r_a}^2\right)\left(-2\omega x^2r_ax\right)}{4-\omega^2x^2{r_a}^2}\right]=\left[\frac{2}{\omega}(\omega^2x^2{r_a}^2)\right] \tag{7.16}$$

Resulting in $\omega^2x^2{r_a}^2=0$, hence this analysis shows no roots are possible resulting in no resonance frequencies.

CASE 2: Considering the first three terms of the Bessel function of the first kind the 7.12 becomes

$$\omega(0)=\frac{P_{signal}}{\omega^2\rho_at_a}\left[\frac{1-\left(1-\frac{k^2{r_a}^2}{4}+\frac{k^4{r_a}^4}{64}\right)}{1-\frac{k^2{r_a}^2}{4}+\frac{k^4{r_a}^4}{64}}\right] \tag{7.17}$$

Differentiating with respect to ω

$$\begin{aligned}\frac{dw(0)}{d\omega}=&\frac{P_{signal}}{\omega^2\rho_at_a}\left[\frac{\left(1-\frac{\omega^2x^2{r_a}^2}{4}+\frac{\omega^4x^4{r_a}^4}{64}\right)\left(\frac{2\omega x^2{r_a}^2}{4}-\frac{4\omega^3x^4{r_a}^4}{64}\right)}{\left(1-\frac{\omega^2x^2{r_a}^2}{4}+\frac{\omega^4x^4{r_a}^4}{64}\right)^2}\right]\\&-\frac{P_{signal}}{\omega^2\rho_at_a}\left[\frac{\left(\frac{\omega^2x^2{r_a}^2}{4}-\frac{\omega^4x^4{r_a}^4}{64}\right)\left(\frac{-2\omega x^2{r_a}^2}{4}+\frac{4\omega^3x^4{r_a}^4}{64}\right)}{\left(1-\frac{\omega^2x^2{r_a}^2}{4}+\frac{\omega^4x^4{r_a}^4}{64}\right)^2}\right]\\&+\left(\frac{\frac{\omega^2x^2{r_a}^2}{4}-\frac{\omega^4x^4{r_a}^4}{64}}{1-\frac{\omega^2x^2{r_a}^2}{4}+\frac{\omega^4x^4{r_a}^4}{64}}\right)\left(\frac{-2}{\omega^3}\right)\left(\frac{P_{Signal}}{\rho_at_a}\right)\end{aligned} \tag{7.18}$$

At resonance assuming $\omega^2x^2{r_a}^2=p$, the equation $-\frac{2p^2}{64}+p-6=0$ yields double roots as ,

$$\omega_0=\frac{2\sqrt{2}}{r_a}\sqrt{\frac{P_r}{\rho_a}} \tag{7.19}$$

$$\omega_{01}=\frac{\sqrt{24}}{r_a}\sqrt{\frac{P_r}{\rho_a}} \tag{7.20}$$

This analysis shows two roots are possible, resulting in two resonance frequencies. They are ω_0, the primary resonance frequency and ω_{01}, the secondary resonance frequency. The former is termed in literature as the primary resonance frequency and the later as the secondary resonance which arises for the higher bending modes of the membrane.

CASE 3: Considering the first four terms of the Bessel function of the first kind the equation 7.12 becomes,

$$\omega(0) = \frac{P_{Signal}}{\omega^2 \rho_a t_a} \left[\frac{\left(\frac{k^2 r_a^{\,2}}{4} - \frac{k^4 r_a^{\,4}}{64} + \frac{k^6 r_a^{\,6}}{2304} \right)}{1 - \frac{k^2 r_a^{\,2}}{4} + \frac{k^4 r_a^{\,4}}{64} - \frac{k^6 r_a^{\,6}}{2304}} \right] \tag{7.21}$$

Differentiating and for resonance

$$\begin{aligned} &\frac{2}{\omega}\left[\frac{k^2 r_a^2}{4} - \frac{k^4 r_a^4}{64} + \frac{k^6 r_a^6}{2304} - \frac{k^4 r_a^4}{16} + \frac{k^6 r_a^6}{64 \times 4} - \frac{k^8 r_a^8}{2304 \times 8} + \frac{k^6 r_a^6}{64 \times 4} \right] \\ &+ \frac{2}{\omega}\left[- \frac{k^8 r_a^8}{64 \times 64} + \frac{k^{10} r_a^{10}}{64 \times 2304} - \frac{k^8 r_a^8}{2304 \times 4} + \frac{k^{10} r_a^{10}}{2304 \times 64} - \frac{k^{12} r_a^{12}}{(2304)^2} \right] \\ &= \frac{2kr_a^2}{4}\frac{dk}{d\omega} - \frac{4k^3 r_a^4}{64}\frac{dk}{d\omega} + \frac{6k^5 r_a^6}{2304}\frac{dk}{d\omega} \end{aligned} \tag{7.22}$$

The equation can be written as,

$$\left[\frac{-2p^2}{2304} + \frac{2p^{32}}{2304 \times 16} - \frac{2p^4}{2304 \times 576} \right] = \left[\frac{-4}{16} + \frac{6p}{576} \right] \tag{7.23}$$

Since p has 4 roots , so ω have 4 possible values of resonance frequencies.

7.4 Analytical modeling of mechanical impedance

The electro-mechanical equivalent circuit of CMUT comprises of an electrical part, a transformer, and a mechanical part. The electrical part includes the resistance and the capacitance of the CMUT as a capacitor, and the mechanical port includes the mechanical impedance, the loss resistance and the acoustic load impedance. The description of the acoustic impedance of the membrane is fundamental for the correct calculation of the model. For that reason the focus is in the following on the detailed

derivation of the acoustic impedance of the membrane Z_m. The effective mechanical impedance of the membrane is a ratio of the impressed pressure and the average velocity of the surface which is found to be nearly 30% less than centre displacement of the membrane. By consideration of Mason's analysis, the equation of membrane displacement of a circular membrane can be expressed as a function of the radial position measured from the centre by the (7.17), where the primary resonance frequency is given by (7.19)

Considering for the whole circular membrane, to evaluate the volume velocity through the device, or to integrate the velocity given by $\dot{w}(r,t)$ over the surface,

$$V_{total} = \int_0^{r_a} \left(\dot{w}(r,t) \right) (2\pi r) dr = 2\pi \int_0^{r_a} \left(\dot{w}(r,t) \right) r dr = j2\pi\omega \int_0^{r_a} w(r) r dr \tag{7.24}$$

The average velocity at the surface will be given by as,

$$V_{average} = \frac{j2\pi\omega}{\pi r_a^{\,2}} \int_0^{r_a} w(r) r dr = \frac{j2}{r_a^{\,2}} \frac{P_{signal}}{\omega \rho_a t_a} \left[\frac{1}{J_0(kr_a)} \int_0^{r_a} r J_0(kr) dr - \int_0^{r_a} r dr \right] \tag{7.25}$$

Employing the well-known integral, $\int r J_0(kr) dr = \frac{J_1(kr)}{k}$, the integral becomes,

$$V_{average} = \frac{2j}{r_a^{\,2}} \frac{P_{signal}}{\omega \rho_a t_a} \left[\frac{r_a J_1(kr_a)}{k J_0(kr_a)} - \frac{r_a^{\,2}}{2} \right] = \frac{j P_{signal}}{r_a \omega \rho_a t_a} \left[\frac{2J_1(kr_a) - a_e k J_0(kr_a)}{k J_0(kr_a)} \right] \tag{7.26}$$

The effective mechanical impedance (Z_m) of the membrane is defined as,

$$Z_m = \frac{P_{signal}}{V_{average}} = \left[\frac{-j\omega \rho_a t_a k r_a J_0(kr_a)}{2J_1(kr_a) - k r_a J_0(kr_a)} \right] \tag{7.27}$$

Since $\frac{1}{j} = -j$ therefore,

$$Z_m = \left[\frac{-j\omega \rho_a t_a k r_a J_0(kr_a)}{2J_1(kr_a) - k r_a J_0(kr_a)} \right] \tag{7.28}$$

This equation gives the mechanical impedance of a circular membrane as a function of frequency and its physical properties. Its unit is $kgm^{-2}\,\sec^{-1}$.

7.5 Analysis of dynamic response and mechanical impedance under the influence of various structural parameters

Application of bias applied to the capacitor causes an electrostatic force generation between them. This force leads the movement of top electrode towards bottom one which is restricted by the residual stress of actuation layer. This electrostatic force generates sufficient amount of pressure and depends upon square of voltage. This voltage $v(t) = V_{dc} + V_{ac} cos\omega t$, where V_{dc} is the bias and V_{ac} is the signal. As, $v(t)^2 = V_{dc}^2 + 2(V_{dc}V_{ac})c\,\mathrm{os}\,\omega t + V_{ac}^2 c\,\mathrm{os}^2\,\omega t$, so first harmonic depends on $V_{dc}V_{ac}$ and $V_{ac}^2 \cos^2 \omega t$ is responsible for the second harmonic, which is quite less compared to the bias.

Variation of displacement profile with frequency for device having 110 µm diameter is shown in Fig. 7.1. The device shows maximum peak displacement at 1.5 MHz with analytical modeling, which is exactly same as simulated profile. Further validation can be also done with the resemblance of resonance of the fabricated structure [13] under AC actuation, where resonance is observed at 1.62 MHz. Maximum displacement shown at resonance is 50 Å which is validated by simulation result and matched with displacement shown in the fabricated structure [19]. It is observed that CMUT has multiple resonances which is quite evident from the figure. Maximized amplitude is observed at first resonance which has sole dependency upon membrane material and structural properties. Another resonance is observed at 2.43 MHz where amplitude of displacement gets lower compared to first resonance. At primary resonance energy transmission takes place and image is formed at secondary resonance. 3 dB bandwidth of CMUT having 49 Å peak displacement at lower cut off frequency f_L 1.48 MHz and higher cut off frequency 1.63 MHz is depicted from Fig. 7.2. Hence at 1.55 MHz resonant frequency 3dB bandwidth of 0.15 MHz is again validated by experimental result [19]. Figure 7.3 shows the 3D variation of displacement with respect to frequency and actuation layer radius. Displacement of the actuation layer gets maximised at the centre of the device. This analytical value of resonance frequency and 3 dB bandwidth matches with experimental results where SiC actuation layer based CMUT was taken into consideration and various device

parameters were evaluated. In Table 7.1 a comparative analysis is depicted between the dynamic response attained by analytical, simulation and experimental result [19].

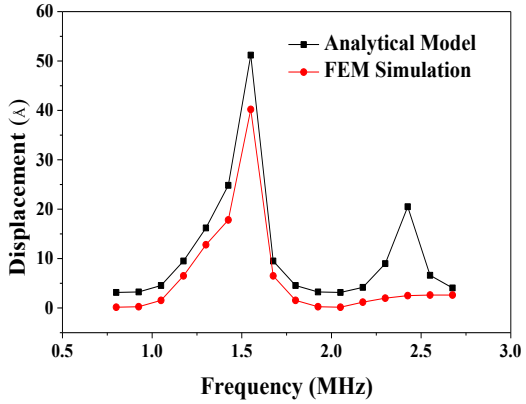

Fig. 7.1 Frequency response of 110µm actuated membrane

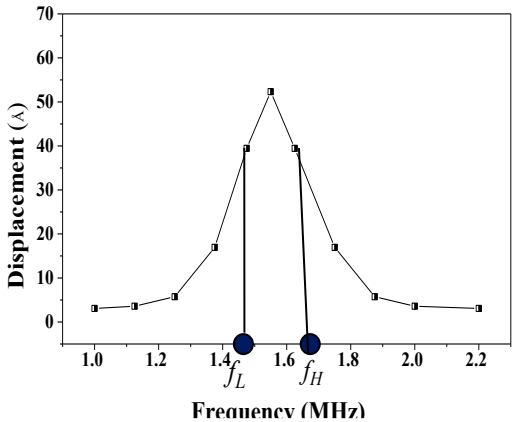

Fig 7.2 3dB bandwidth of CMUT

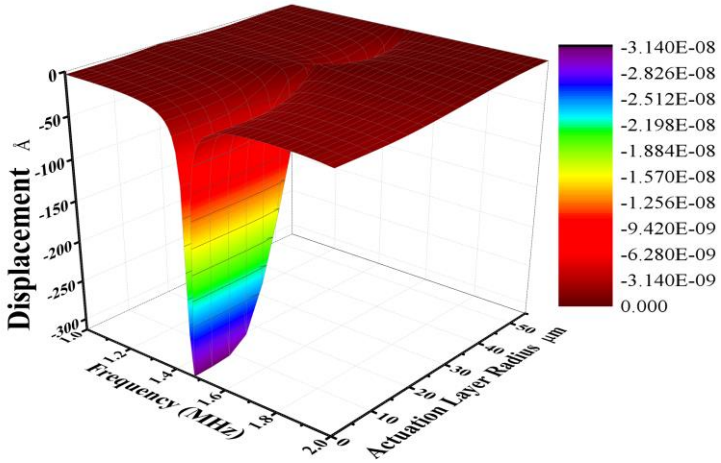

Fig. 7.3 3D Frequency response of 110µm actuated membrane

Table 7.1 Percentage of difference between analytical and experimental data

Parameter	**Analytical**	**Simulation**	**Experimental**	**% of difference with respect to experimental**
Resonance Frequency	1.55 MHz	1.55 MHz	1.62 MHz	4.5 %
3 dB bandwidth	0.15 MHz	0.15 MHz	0.15 MHz	0%

Figure 7.4 shows the comparative study of frequency profile of Si_3N_4 insulation based element with that of HfO_2 insulation based element. Usage of high-K insulation enhances peak displacement without making any change in the

resonance frequency. Figure 7.5 shows the comparative study of frequency response among various material used for actuation and insulation. Keeping the actuation layer material fixed, frequency response is studied involving insulation layer as Si_3N_4 and HfO_2. Its quite evident from both the Figs. 7.4 and 7.5 that, increase in material permittivity enhances the peak displacement whereas resonance frequency increases with the usage of Si_3N_4. As resonance increases with increase in residual stress, hence larger residual stress of Si_3N_4 enhances the resonance. Moreover, it is observed that device used for medical imaging operates at MHz frequency range that requires the device dimension to be in micrometer range. In consideration with this fact CMUT will be the most relevant choice for medical applications.

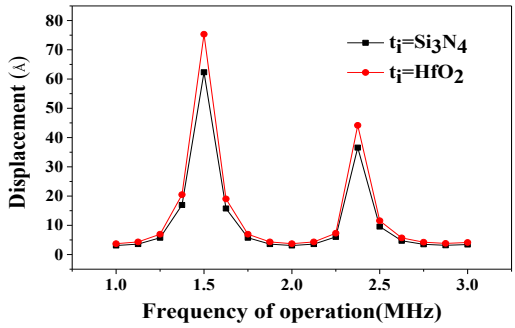

Fig. 7.4 Comparison of frequency profile for the same input pulse between HfO_2 Vs. Si_3N_4 isolation

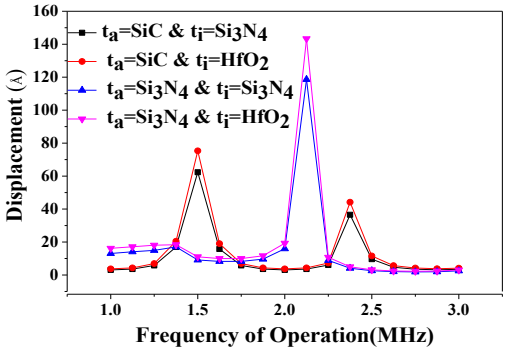

Fig. 7.5 Comparison of frequency profile for change in insulating and structural material for the same input pulse

Figures 7.6 and 7.7 show the frequency profile for various actuation layer radius and actuation layer thickness. Reduction in actuation layer radius compels the device to resonate at lower frequency compared to increased one is evident from Fig. 7.6. Figure 7.7 shows that increase in actuation layer thickness causes reduction in peak displacement and vice versa but keeps the resonance frequency unchanged. Figure 7.8 shows exactly same variation as shown in Fig. 7.7. Reduction in insulation thickness enhances displacement of the device hence in Fig. 7.8 increased peak displacement is noticed at resonance.

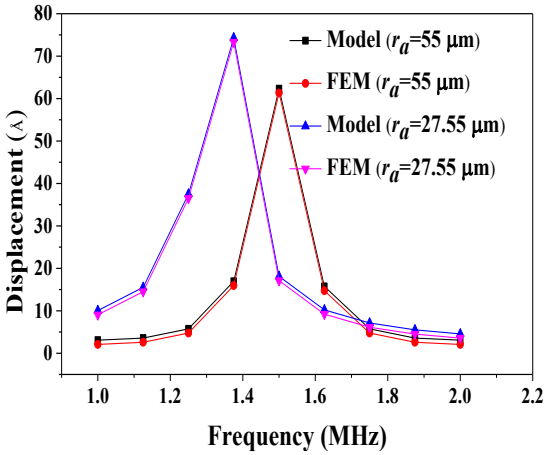

Fig. 7.6 Comparison of frequency profile for various actuation layer radius

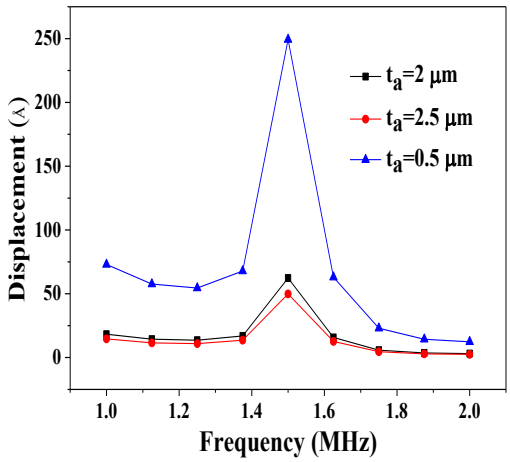

Fig. 7.7 Comparison of frequency profile for various actuation layer thickness

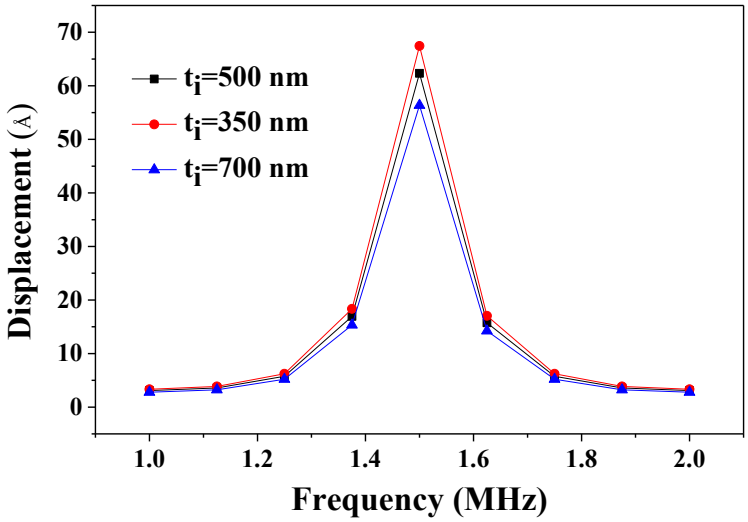

Fig. 7.8 Comparison of frequency profile for various insulation thickness

Under uniform pressure variation of primary or the fundamental resonance with respect to residual stress and actuation layer radius is exhibited in Figs. 7.9 and 7.10 respectively. Displacement of actuation layer is modeled using Mason's model which depicts the prediction of primary resonance upon residual stress and actuation layer radius. Residual stress of actuation layer remains unchanged with variation of bias and structural parameter hence observable amount of displacement is not observed while displacement is plotted due to effect of signal.

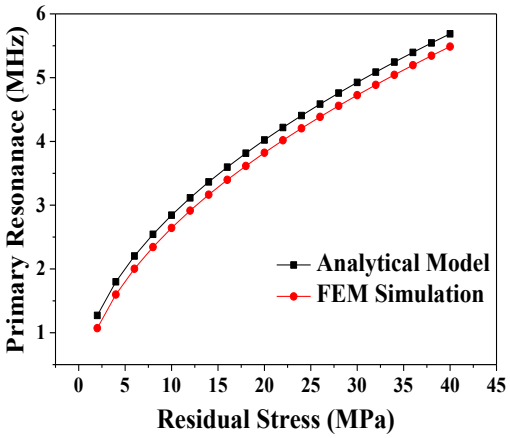

Fig. 7.9 Primary resonance with respect to residual stress

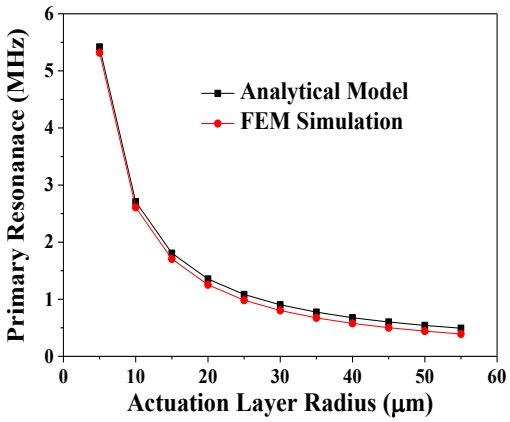

Fig. 7.10 Primary resonance with respect to actuation layer radius

Changes in residual stress and bias thus cannot be taken into consideration while small actuation layer displacement is taken into account. Figs. 7.9 and 7.10 shows the change in primary resonance with respect to residual stress of actuating material and actuation layer radius . Increasing residual stress enhances primary resonance frequency whereas increase in actuation layer radius reduces the same. Displacement of actuation layer depends on various factors as electrostatic force generated due to the presence of ac and dc component creates an pressure which is one of the influencing parameters. Figures 7.11 - 7.15 shows behaviour of actuation layer displacement for varying structural parameters. Increase in actuation layer, gap and insulation thickness reduces the displacement of the device as device capacitance and force gets decreased. Figures 7.11 and 7.12 show the variation of dynamic displacement with change in bias and gap thickness respectively. Increase in bias causes enhancement in displacement as pressure generated due to application of signal enhances is shown in Fig. 7.11. Increase in gap separating between two electrodes reduces the pressure generated in the device while signal is applied. This results decrement of displacement in parabolic manner due to increase in gap separation as shown in Fig. 7.12. Increase in actuation layer and insulation thickness also exhibits similar nature of variation of displacement which is depicted in Figs. 7.13 and 7.14 respectively. Figure 7.15 shows the displacement profile with respect to radial position which depicts maximum displacement occurs at the centre of actuation layer and gets diminished while approaching towards boundary.

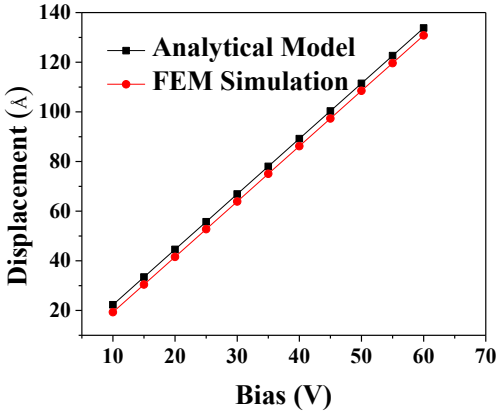

Fig. 7.11 Displacement with respect to bias

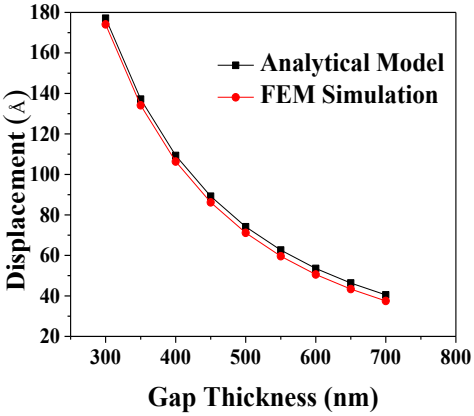

Fig. 7.12 Displacement with respect to gap separation

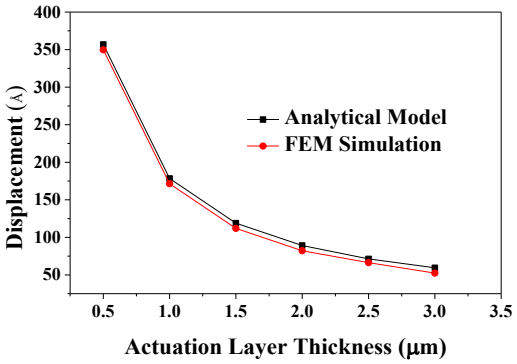

Fig. 7.13 Displacement with actuation layer thickness

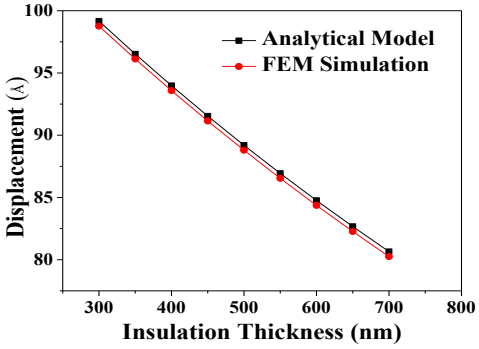

Fig. 7.14 Displacement with respect to insulation thickness

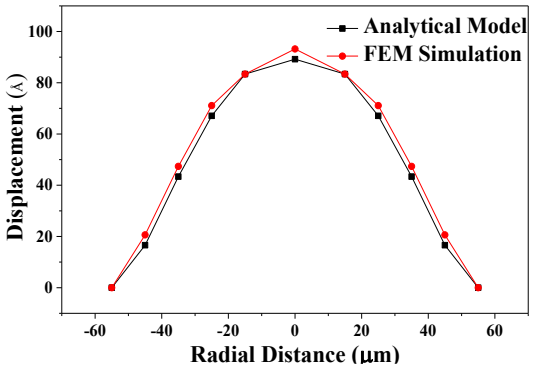

Fig. 7.15 Displacement with radial distance

At the centre of actuation layer, ratio of pressure to velocity derives the mechanical impedance. Variation of mechanical impedance can thus be calculated by attaining the displacement with a known pressure load as shown in Fig. 7.16. Minimum impedance is achieved at device resonance frequency. Figure 7.17

presents matching of impedance is achieved at 55 µm radius with air impedance of 413 kg/m^{2}s. Increase in radius results reduction in device resonance frequency.

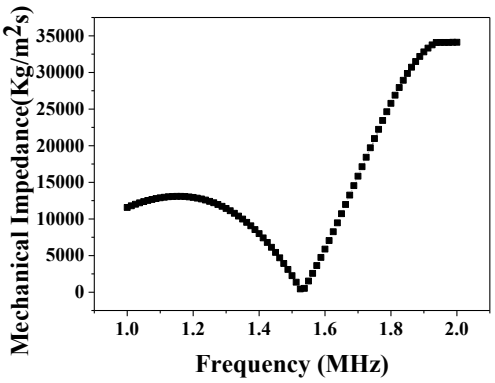

Fig. 7.16 Impedance profile with respect to frequency

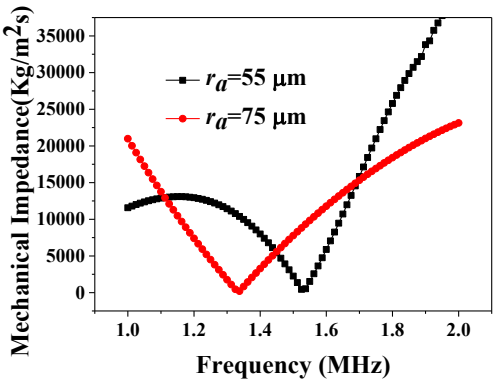

Fig. 7.17 Comparative analysis of impedance profile for various actuation layer radius

Figure 7.18 depicts a comparative study of impedance profile for change of actuation layer thickness. Increase in insulation thickness increases mechanical impedance which will certainly transform less energy to medium of interest. Properties of structural material also have great impact upon mechanical impedance as shown in Fig. 7.19. Figure 7.20 shows 3D plot of mechanical impedance with frequency and actuation layer radius.

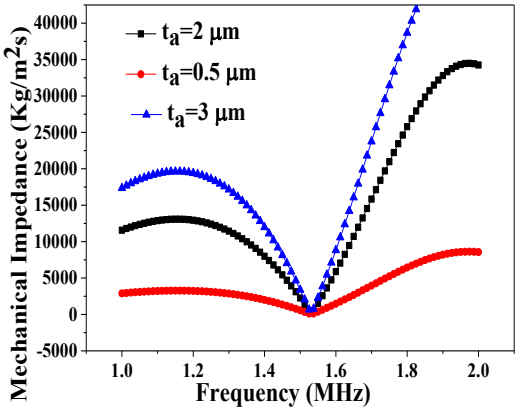

Fig. 7.18 Comparative analysis of impedance profile for various actuation layer thickness

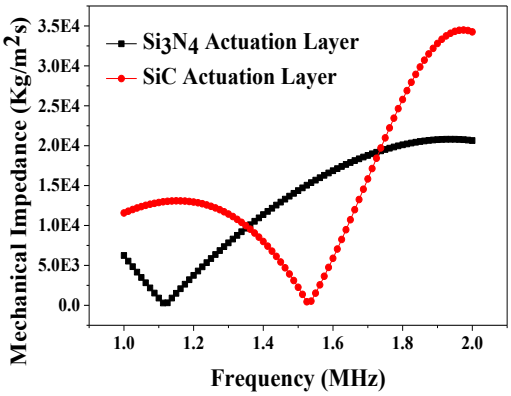

Fig. 7.19 Comparative analysis of impedance profile between SiC and Si_3N_4 actuation layer

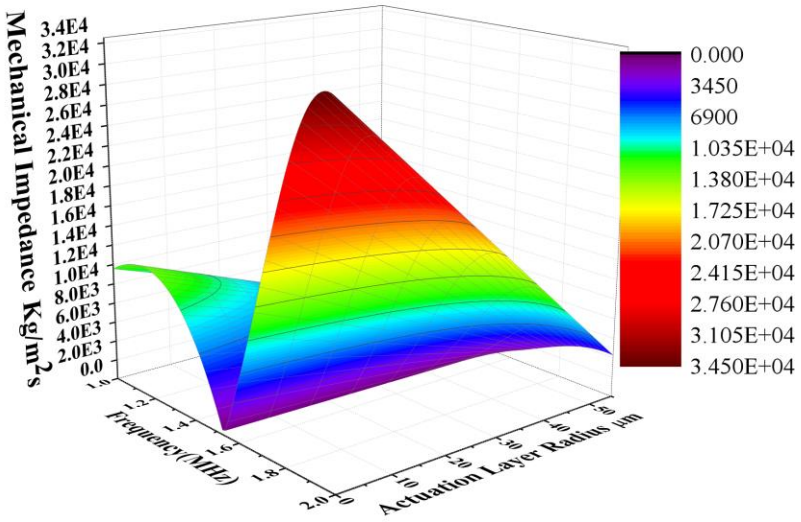

Fig. 7.20 3D plot of impedance profile with actuation layer radius

In Fig. 7.21 a 3D plot of mechanical impedance with frequency and actuation layer thickness is shown. As discussed increase in thickness of actuation layer increases mechanical impedance as stiffness of the membrane enhances thus decreases the displacement. Increment of actuation layer radius increases displacement which results decrease in mechanical impedance. Enhanced displacement allows maximum ultrasound wave energy transformation from device to surrounding medium .

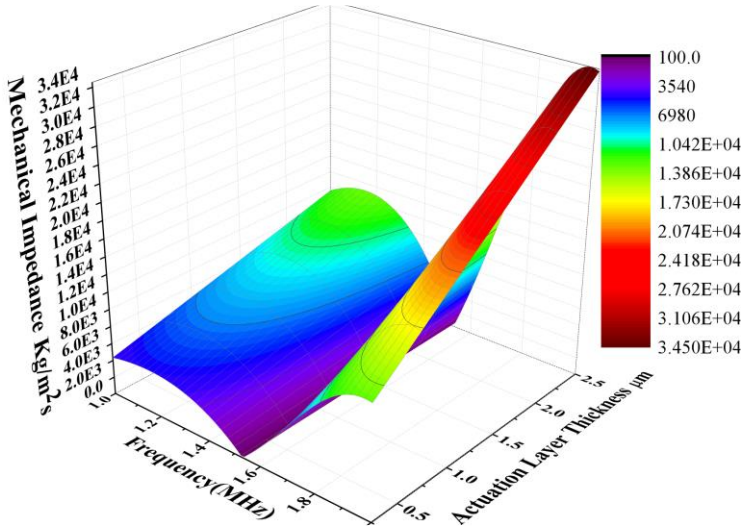

Fig. 7.21 3D plot of impedance profile with actuation layer thickness

7.6 Summary

Dynamic response and impedance profile of CMUT element has been analytically modeled considering Mason's model for circular shaped device. Theoretical results are validated with simulation result and established good agreement with published experimental results. Derived analytical model exhibits the presence of multiple resonances for capacitive element. Between primary and secondary resonance, prime consideration will be for primary one due to its increased peak value displacement compared to secondary counterpart. Device resonance also resembles with published experimental result. Matched impedance with air makes the device a suitable one for acoustic medium. Regardless, this insulated element diminishes the search of perfect matching layer for maximum transmission of ultrasound in the surrounding medium as required for piezoelectric material.

References

[1] P. M. Grant and R. S. Withers, "Recent advances in analog signal processing, " *IEEE Transactions on Aerospace and Electronic Systems*, vol. 26, no. 5, pp. 818-849, 1990.

[2] L. F. Degertekin, J. Pei, B. T. Khuri-Yakub, and K. C. Saraswat, "In situ acoustic temperature tomography of semiconductor wafers," *Applied Physics Letters*, vol. 64, pp. 1338-1340, Mar. 1994.

[3] L. F. Degertekin and B. T. Khuri-Yakub, "Hertzian contact transducers for nondestructive evaluation," *The Journal of the Acoustical Society of America.*, vol. 99, pp. 299-308, Jan. 1996.

[4] R. M. White, "Generation of elastic waves by transient surface heating," *Journal of Applied Physics*, vol. 34, pp. 3559-3567, 1963.

[5] J. P. Monchalin, J. D. Aussel, R. Heon, C. K. Jen, A. Boudreault, and R. Bernier, "Measurement of in-plane and out-of-plane ultrasonic displacements by optical heterodyne interferometry," *Journal of Nondestructive Evaluation ,* vol. 8, pp. 121-133, 1989.

[6] M.-H. Noroy, D. Royer, and M. Fink, "The laser-generated ultrasonic phased array: analysis and experiments," *The Journal of the Acoustical Society of America.*, vol. 94, pp. 1934-1943, 1993.

[7] A. Ergun, Y. Huang, X . Zhuang, O . Oralkan, GG .Yaralıoglu, B.T. Khuri Yakub, "Capacitive Micromachined Ultrasonic Transducers:fabrication Technology", *IEEE Transactions on Ultrasonics, Ferroelectrics, and Frequency Control*, vol 52, pp 2242–2258, 2005

[8] M . Rahman, J . Hernandez, S. Chowdhury ,"An Improved Analytical Method to Design CMUTs with Square Diaphragms", *IEEE Transactions on Ultrasonics, Ferroelectrics, and Frequency Control*, vol 60, pp 834–845, 2013

[9] R. Maity, R. K. Thapa, S. Baishya, "Membrane Displacement Behavior of Capacitive Micromachined Ultrasonic Transducers under Static Bias", *Advanced Materials Research,* vol 816, pp 892-896, 2013

[10] R. Maity, N. P. Maity, R. K. Thapa, S. Baishya," Analysis of Frequency Response Behaviour of Capacitive Micromachined Ultrasonic Transducers", *Journal of Computational and Theoratical Nanoscience*, vol 12 , pp 3492-3494, 2015

[11] R. Maity, N. P. Maity, R. K. Thapa, S. Baishya, "Analytical Characterization and Simulation of a 2-D Capacitive Micromachined Ultrasonic Transducer Array Element" , *Journal of Computational and Theoratical Nanoscience,* vol 12, 3692-3696, 2015

[12] B Bayram, G. Yaralioglu, M Kupnik, A Ergun, O. Oralkan, A. Nikoozadeh, B. Khuri Yakub, "Dynamic analysis of capacitive micromachined ultrasonic transducers," *IEEE Transactions on Ultrasonics, Ferroelectrics, and Frequency Control*, vol. 52, no. 6, pp. 2270–2275, 2005.

[13] G. G. Yaralioglu, A. S. Ergun, and B. T. Khuri-Yakub, "Finite-element analysis of capacitive micromachined ultrasonic transducers," *IEEE Transactions on Ultrasonics, Ferroelectrics, and Frequency Control*, vol. 52, no. 12, pp. 2185–2198, 2005.

[14] B. Ma, C. Chang, H.K. Oguz, K. Firouzi, B.T. Khuri Yakub, "Multi-parameter optimization of vented CMUTs for airborne applications, " *IEEE International Ultrasonics Symposium (IUS)*, pp. 1–4 , 2017.

[15] N. Apte, K.K. Park, B.T. Khuri Yakub, "Finite element analysis of CMUTs with pressurized cavities," *IEEE International Ultrasonics Symposium, Dresden, Germany,* pp. 979–982, 2012.

[16] N. Apte, K. Park, A. Nikoozadeh, B. T. Khuri Yakub, "Bandwidth and sensitivity optimization in CMUTs for airborne applications," *IEEE International Ultrasonics Symposium, Chicago*, pp. 166–169, 2014.

[17] O. Wygant, K. Mario, "Analytically Calculating Membrane Displacement and the equivalent Circuit Model of a Circular CMUT Cell", *IEEE International Ultrasonics Symposium* ,pp. 167-170, 2008.

[18] S.K. Tiwari, B. S. Satyanarayana, A. Gopalkrishna Pai and Kunal K. Trivedi, "Circular capacitance micro machined ultrasonic transducer", *Defence Science Journal*, vol. 59, p. 627,2019.

[19] Q. Zhang, P. Cicek, K. Allidina, F. Nabki, and M. N. El-Gamal, "Surface Micromachined CMUT Using Low-Temperature Deposited SiC Actuation layer s for Above-IC Integration", *IEEE Journal of Micro electromechanical Systems,* vol. 23, no. 2, pp.482-493, 2014.

CHAPTER

8

Conclusion and Future Work

8.1 Conclusion

This research work elaborates the performance of circular shaped SiC based CMUT. Various device parameters is analytically modeled and validated by FEM simulation. To analyse the performance of SiC CMUT, initially device capacitance , electrostatic force , displacement are studied for non-insulated CMUT. Need of insulation layer also examined under the influence of various device parameters. In consideration with all these facts, SiC based insulated element proves its potency compared to non-insulated CMUT.

An improved model was taken into account considering fringing field capacitance as the flux lines bends near the ages and the comparable actuation layer width of the capacitive cell to its cavity gap raises the effect of fringing in the device and necessitates the use of a capacitance correction factor. The effect of changing gap and membrane thickness on the fringing fields has been determined using a study of the total capacitance of a CMUT cell for computing the displacement profile and electrostatic force. The Landau technique for simulating the fringing field in CMUT is the subject of this investigation. With this novel method, Mason's modelling for calculating actuation layer displacement is carried out. PZFlex SolidWorks data is also used to validate the analytical result of displacement. With the fringing field effect, there has been a lot of agreement. It is possible to get a 15% reduction in error on average.

For proper adjustment of the structural characteristics of the device and material properties for a given bias state, the otherwise unwanted fringing effect, which increases the electrostatic field, is used. In comparison to Si_3N_4, SiC membrane reveals to be a superior material with superior mechanical and electrical

properties. The ability to create ultrasonic waves was demonstrated by the performance of an insulated CMUT structure with SiC as the structural material. The use of an insulating layer improves device sensitivity and allows the CMUT to operate safely in high voltage and high temperature environments. The insulation layer aids in the CMUT's ability to produce high-resolution images at a minimal cost. Such discoveries could help to develop medical imaging on a broad scale.

For insulating thicknesses ranging from 500 nm to 50 nm, a comprehensive comparison of HfO_2 isolation and Si_3N_4 is carried out. It is also possible can use the ALD deposition process to incorporate HfO_2 for low-temperature manufacturing with an isolation thickness of less than 100nm. When compared to PECVD Si_3N_4, CMUT outperforms PECVD Si_3N_4 in every way. This increase in CMUT parameters will undoubtedly make it more sensitive in high-frequency applications as well as in the acoustic medium. The coupling coefficient is nearly 0.67 in this case, and it's higher for actuation layers that are thinner but have a bigger diameter. In terms of actuating material, SiC is far superior to Si_3N_4 as a structural layer in bigger displacement and high-frequency applications.

This research work also investigates the modelling of collapse voltage and coupling factor for an insulated CMUT structure made of SiC. The collapse voltage and coupling factor are determined by the same factors that effect displacement. Because of the increased displacement, the value of the collapse voltage drops. Increase in fringing field capacitance lowers the collapse voltage while the coupling factor rises. The addition of an insulating layer improve device sensitivity and makes the CMUT safe to use in high voltage and high temperature situations. The CMUT's capacity to produce high-resolution images at a low cost is aided by the insulating layer. Such breakthroughs could aid in the development of medical imaging on a large scale.

Mason's model for circular shaped devices was used to model the dynamic response and impedance profile of the CMUT element. Theoretical findings are supported by simulation results, which show good agreement with reported experimental findings. As stated by experimental results SiC CMUT of 110 µm diameter resonates at 1.62 MHz with 3 dB bandwidth of 0.15 MHz. This value

differs by 4.5% when resonance frequency is taken into consideration. While 3 dB bandwidth is concerned then both experimental and analytical values completely match with each other. In this context simulated results also shows perfect match with analytical result. Multiple resonances is present in the derived analytical model for the vented capacitive element. Primary resonance has a larger peak value displacement than secondary resonance, thus will be given priority over secondary resonance. The resonance of the device is also consistent with previously published experimental results. The device's matched impedance to air and water makes it ideal for both acoustic and air mediums. Regardless, the search for a perfect matching layer for maximal ultrasonic transmission in the surrounding medium, as required for piezoelectric material, is reduced by this insulated element.

A comparative analysis is carried out in Table 8.1 considering various structures of non-insulated and insulated cell. Keeping the basic dimensions of fabricated structure same this analysis is done. For non-insulated one Si_3N_4 and SiC actuation layer is used in separate manner and in insulated structure insulation layer is altered by HfO_2 instead of Si_3N_4. Table 8.1 clearly depicts that CMUT structure having SiC as actuation layer and HfO_2 as insulation layer has the potential to generate high frequency ultrasonic sound and fittest one to get involved in air and acoustic application. As per the tabular representation SiC based device with HfO_2 insulation generates appreciable results compared to rest three structures. In Table 8.2 a comparative analysis of percentage improvement in CMUT parameters are depicted with respect to Si_3N_4 based non-insulated structure. As documented in Table 8.2, percentage improvement in device capacitance, electrostatic force, displacement and other device parameters are quite impressive for SiC based HfO_2 insulated structure. Taking this into account this specific structure of the research work establishes its novelty in all aspect.

Table 8.1 Comparative study of CMUT parameters for various structures

CMUT Type	Device capacitance (pF)	Electrostatic Force(μN)	Displacement(nm)	Collapse Voltage(V)	Coupling Factor	Resonant Frequency (MHz)	Impedance (Kg/m^2-s)	Dynamic displacement (Å)
Si_3N_4 based non-insulated	0.123	119	68.1	84	0.43	1.12	908.62	42.7
SiC based non-insulated	0.133	161	214	80	0.47	1.52	558.94	49.4
SiC based Si_3N_4 insulation	0.166	253	335	78	0.61	1.55	524.44	61.6
SiC based HfO_2 insulation	0.183	305	405	67	0.67	1.55	524.44	74.3

Table 8.2 Percentage improvements in parameters in comparison with Si_3N_4 based non-insulated

CMUT Type	% enhancement in Device capacitance	% enhancement in Electrostatic Force	% enhancement in Displacement	% decrement in Collapse Voltage	% enhancement in Coupling Factor	% enhancement in Resonant Frequency	% decrement in Impedance	% enhancement in Dynamic Displacement
SiC based non-insulated	8.13	35.29	214	5	9.30	33.92	62.55	15
SiC based Si_3N_4 insulation	34.95	112	391	7.69	41.86	38.39	73.25	44
SiC based HfO_2 insulation	48.78	156	494	25.37	55.81	38.39	73.25	74

8.2 Future Work

The CMUT is still in its infancy, and it will require more research in order to improve. An improved membrane shape, as well as finiteness of actuation layer radius should be included in the analytical modelling. During the calculation, the piston-like assumption should be removed. Furthermore, observing the dynamic behaviour of CMUT cells necessitates the use of time-dependent finite element

analysis by fourth order differential form. However, a single CMUT cell finite element analysis in this research work. As a result, analysis in arrays form should be addressed in the future to provide a deeper insight into the auditory domain of CMUTs. In the future, a complete CMUTs device must be completed in order to have a successfully working device on which experimental tests can be conducted.

Introduction

Micro electro mechanical system (MEMS) is a collection of microdevices that connects mechanical and electronic components and is made in sizes ranging from micrometres to millimetres using batch-processing technologies compatible with integrated circuits (ICs). These systems can detect, control, and respond on a micro-scale and perform individually or in clusters to generate macro-scale effects. MEMS has been hailed as a game-changing technology since the mid 1970s, bringing up new possibilities in chemical, physiological, and biological sensors and actuators. MEMS technology is based on IC fabrication techniques, but its test approaches are significant. MUTs are of piezoelectric and capacitive types. For many years, piezoelectric micromachined ultrasonic transducers (PMUTs) have been developed and widely used in clinical imaging in recent years. It frequently employs lead-zirconate-titanate (PZT) film for sensing or actuating. In the scientific world, capacitive micromachined ultrasonic transducers (CMUTs) have evolved as a response to the inadequacies of piezoelectric transducers. Fabrication of this device can be performed by surface micromachining technique or involving fusion bonding process at high temperature. Square, circular or hexagonal geometry is included for constructing the diaphragm of a typical CMUT, which is supported on a fixed bottom electrode. Working of this transducer is based on capacitive action where the structure performs as a variable capacitor and the top electrode acts as a diaphragm and is free to move or deform against the bottom electrode. As a result, variation in capacitance takes place due to a change in distance between these two electrodes. Hence it can be considered as a capacitor cell that consists of a thin moveable film suspended upon a vacuum gap. The top electrode of the device sometimes becomes metal coated and is used as one of the electrodes for the capacitor. During transmitting mode, resonance takes place due to the application of bias along with superimposed desired signal to the geometry. Consequently, an electrostatic force is generated which causes the diaphragm to vibrate and create ultrasonic vibration in the surrounding medium. During the receiving mode, the device gets exposed to the incident ultrasound wave, and as a result, deformation

takes place in the diaphragm towards the fixed bottom electrode due to sound pressure. As the distance between the top and bottom electrodes change, so variation in capacitance occurs. The change in capacitance is then transformed to an equivalent electrical signal by a suitable microelectronic circuit. To employ the device at the optimal operating point, collapse voltage of a capacitive element is an important parameter. Performance of the MUT is determined by the operating bias applied to it. Considering various behaviour of the membrane under static bias condition, different operating modes exist such as collapsed mode and conventional mode. In comparison with piezoelectric transducer, bandwidth of transmitted wave is quite larger for MEMS capacitive transducer. Practical potential of ultrasound can be harnessed by efficient launching upon the subject of incidence. MUT capacitive transducers also detect ultrasound waves for sensing or actuating applications. During transmission and detection ultrasound travels through coupling medium. Coupling medium can be of solid, liquid, and gaseous form. The tiny moveable capacitor plate and the air cavity reduce the acoustic impedance for capacitive ultrasonic transducer and perform better in liquid or air-coupled applications.

Objective

The use of ultrasound in acoustic and air mediums necessitates a perfect match of impedance between the source and the surrounding environment. For collecting high-intensity images of internal organs, a high-frequency ultrasound pulse is necessary. In this case, CMUT outperforms PZT transducers in terms of meeting all of these objectives. According to current miniaturization trends, device design must be done in the micro dimension. CMUT exist in two types such as insulated and non-insulated structure. Membrane patterning beneath the top electrode in non-insulated CMUT, causes the electrodes to be spaced apart, resulting in a reduction in device capacitance. To overcome this constraint, an insulated structure for generating high frequency ultrasonic waves is proposed, as it comprises an insulation layer with a smaller dimension than the membrane, patterned below the top electrode. In comparison to a non-insulated device, this insulating layer lowers the effective gap separation and increases direct device capacitance. Furthermore, this layer protects

patients from electrical risks and ensures their safety. Increased device capacitance is projected to result in increased membrane peak displacement. Following that, there occurs a reduction in impedance mismatch. The device's high coupling factor makes it ideal for transmitting ultrasonic waves in an air medium. In this case, an insulated CMUT is an excellent choice since increased membrane displacement leads to a higher coupling factor.

The circular shaped capacitive element has the maximum displacement among various hexagonal, rectangular, and square geometries. As a result, the use of an insulated circular CMUT is considered in this research. Moreover, electric field lines bend at the edges of the circular shaped plates resulting fringing field effect in the device. An improved model of device capacitance is used to express the excess capacitance in the device that causes the fringing effect. The excess fringing capacitance will undoubtedly improve device performance by increasing membrane displacement and coupling efficiency. Subsequent to this, the device attains the capability to convey maximum energy to the surrounding medium.

One of the most critical performances determining factors for CMUT is the structural material employed. As device capacitance is proportional to the dielectric constant of the insulating material, using a high-K material improves device performance. In this research work hafnium oxide (HfO_2) is engaged as an insulating material due to its high relative dielectric constant. Insolvent silicon carbide (SiC) as an actuation layer can enhance device performance by enhancing the penetration as it necessitates high-valued pressure transmission. Due to the high Young's modulus and low residual stress, SiC is expected to be one of the fittest materials for therapeutic application and medical imaging. Though silicon nitride (Si_3N_4) is used as membrane material in many devices still SiC is a better choice for its unique material properties. Displacement of the SiC layer is modeled by Mason's model and plate model where lower valued residual stress and higher valued Young's modulus acts as an influencing factor to enhance displacement compared to Si_3N_4 membrane. All the analytical results are validated by FEM simulation and consideration of displacement model is also done based on the result achieved by FEM simulation.

In this regard, the following objectives are carried out.

i. To determine the equivalent capacitance and the electrostatic force of attraction with the inclusion of fringing fields.

ii. To analyze the displacement profile by considering the plate and membrane vibration at static bias.

iii. To analyze the frequency response profile under dynamic vibration.

iv. To analyze the impedance profile.

v. To validate the analytical model outcomes with FEM simulations.

Summary of results

In chapter 1, the familiarization of MEMS, its application, and various types of MEMS are discussed. A brief discussion is included to prove the competency of CMUT over PZT transducer.

In chapter 2, a review of CMUT is elaborated, where fabrication technologies adopted for MEMS device design are discussed. The existence of various geometrical shapes of the membrane and their performances are depicted. The vast application of this capacitive transducer is also documented.

In chapter 3, the Landau technique for simulating the fringing field implication in CMUT is discussed. This approach is used to determine the capacitances of the actuation layer, gap, and insulation. SiC as a structural material makes the CMUT more capable of being produced with the smallest thermal budget. An average 4.32% enhancement in device capacitance takes place due to the involvement of SiC as an actuation layer instead of Si_3N_4 in non-insulated CMUT. The addition of an insulating layer improves device capacitance by 26% and allows the CMUT to operate safely in high-voltage applications while being stable in high temperatures. The insulation layer is extremely beneficial in allowing CMUT to generate high-simulation results which validate the Landau and Lifschitz approach for modeling the fringing field effect. Due to this fringing effect, an average 14.3% enhancement of device capacitance takes place. The performance of CMUT is improved in every aspect when HfO_2 is used as an insulation layer instead of Si_3N_4. This enhancement

in CMUT characteristics will undoubtedly make the device fit for high-frequency applications and also allow it to be used in an acoustic medium.

In chapter 4, improved analytical modeling of the electrostatic force is carried out. This analysis deals with Landau's technique for modeling the electrostatic force considering the fringing field capacitance in CMUT. Analytical data is validated by FEM simulation. The overall impact of fringing field is observed in electrostatic force in almost all types of capacitive device structure like non-insulated and insulated CMUT. An average 14.8% enhancement in electrostatic force occurs in an insulated cell due to the fringing effect and 27% enhancement in electrostatic force is attained when compared with non-insulated counterpart. Based on the performance of insulated CMUT structure with SiC as structural material seems to be quite capable of generating high frequency ultrasound waves due to appreciable amount of force generation. A comparative study between HfO_2 isolation and Si_3N_4 is done rigorously for insulation thickness from 500 nm to 50 nm. Reduction in insulation thickness and usage of HfO_2 enhances device electrostatic force by 24.6%.

In chapter 5, an improved displacement modeling is derived. Deflection of actuation layer is modeled by plate and actuation layer modeling. Mason's analysis is considered for analyzing the actuation layer modeling. Impressive result for peak displacement is achieved from Mason's analysis, which allows considering actuation layer as a membrane for both insulated and non-insulated structures. The insulation layer has deeper insight into displacement compared to non-insulated elements. The performance of SiC as an excellent actuation layer is studied for the non-insulated element where impressive enhancement in displacement is observed compared to Si_3N_4 actuation layer. Fringing effect is more profound for SiC based non-insulated devices than Si_3N_4 counterparts. Inclusion of HfO_2 as an insulation layer improves the device displacement by 20.79% than Si_3N_4 insulation of 500 nm thickness.

In chapter 6, modeling of collapse voltage and coupling factor is carried over for an insulated CMUT structure with SiC. Factors that influence displacement are also responsible for determining the collapse voltage and coupling factor. Collapse voltage decreases due to enhanced displacement. The introduction of the fringing effect enhances the capacitance thus collapse voltage decreases but the coupling

factor becomes 0.61. Involvement of HfO_2 as an insulation layer generates coupling factor of 0.67 maintaining the same dimension.

In chapter 7, the dynamic response and impedance profile of the CMUT element has been analytically modeled considering Mason's model for circular shaped device. Theoretical results are validated with simulation results and established a good agreement with published experimental results. The derived analytical model exhibits the presence of multiple resonances for capacitive elements. Between primary and secondary resonance, prime consideration will be for primary one due to its increased peak value displacement compared to secondary counterpart. Device resonance of 1.55 MHz by analytical modeling also resembles with 1.62 MHz which is a published experimental result. Matched impedance with air makes the device a suitable one for acoustic medium. Regardless, this insulated element diminishes the search for a perfect matching layer for maximum transmission of ultrasound in the surrounding medium as required for piezoelectric material.

In chapter 8, a comparative analysis is carried out considering various structures of non-insulated and insulated cell. Keeping the basic dimensions of fabricated structure the same this analysis is done. For non-insulated one Si_3N_4 and SiC actuation layer is used separately and for insulated structure, insulation layer is altered by HfO_2 instead of Si_3N_4. The analysis depicts that CMUT structure having SiC as actuation layer and HfO_2 as insulation layer is the best in all aspects among these four structures as percentage enhancement of device parameters is quite impressive compared to all others.